2017

TUNABLE NANOCOMPOSITE MEMBRANES FOR WATER REMEDIATION AND SEPARATIONS

Sebastián Hernández Sierra
University of Kentucky, sebaccano@gmail.com
Author ORCID Identifier:
http://orcid.org/0000-0002-7513-5511
Digital Object Identifier: https://doi.org/10.13023/ETD.2017.042

STUDENT AGREEMENT:

I represent that my thesis or dissertation and abstract are my original work. Proper attribution has been given to all outside sources. I understand that I am solely responsible for obtaining any needed copyright permissions. I have obtained needed written permission statement(s) from the owner(s) of each third-party copyrighted matter to be included in my work, allowing electronic distribution (if such use is not permitted by the fair use doctrine) which will be submitted to UKnowledge as Additional File.

I hereby grant to The University of Kentucky and its agents the irrevocable, non-exclusive, and royalty-free license to archive and make accessible my work in whole or in part in all forms of media, now or hereafter known. I agree that the document mentioned above may be made available immediately for worldwide access unless an embargo applies.

I retain all other ownership rights to the copyright of my work. I also retain the right to use in future works (such as articles or books) all or part of my work. I understand that I am free to register the copyright to my work.

REVIEW, APPROVAL AND ACCEPTANCE

The document mentioned above has been reviewed and accepted by the student's advisor, on behalf of the advisory committee, and by the Director of Graduate Studies (DGS), on behalf of the program; we verify that this is the final, approved version of the student's thesis including all changes required by the advisory committee. The undersigned agree to abide by the statements above.

Sebastián Hernández Sierra, Student

Dr. Dibakar Bhattacharyya, Major Professor

Dr. Thomas D. Dziubla, Director of Graduate Studies

TUNABLE NANOCOMPOSITE MEMBRANES FOR WATER REMEDIATION AND SEPARATIONS

DISSERTATION

A dissertation submitted in partial fulfillment of the
requirements for the degree of Doctor of Philosophy in the
College of Engineering
at the University of Kentucky

By
Sebastián Hernández Sierra

Lexington, Kentucky

Director: Dr. Dibakar Bhattacharyya, Alumni Chair Professor of Chemical Engineering

Lexington, Kentucky

2017

ABSTRACT OF DISSERTATION

TUNABLE NANOCOMPOSITE MEMBRANES FOR WATER REMEDIATION AND SEPARATIONS

Nano-structured material fabrication using functionalized membranes with polyelectrolytes is a promising research field for water pollution, catalytic and mining applications. These responsive polymers react to external stimuli like temperature, pH, radiation, ionic strength or chemical composition. Such nanomaterials provide novel hybrid properties and can also be self-supported in addition to the membranes.

Polyelectrolytes (as hydrogels) have pH responsiveness. The hydrogel moieties gain or lose protons based on the pH, displaying swelling properties. These responsive materials can be exploited to synthesize metal nanoparticles in situ using their functional groups, or to immobilize other polyelectrolytes and biomolecules. Due to their properties, these responsive materials prevent the loss of nanomaterials to the environment and improve reactivity due to their larger surface areas, expanding their range of applications.

The present work describes different techniques used to create nanocomposites based on poly(vinylidene fluoride) (PVDF) hollow fiber and flat sheet membranes, both thick sponge-like and thin. Due to their hydrophobicity, hollow fiber membranes were hydrophilized by a water-based green process of cross-linking polyvinylpyrrolidone (PVP) onto their surface. Commercial hydrophilic and hydrophilized lab-prepared membranes were subsequently functionalized with a poly(acrylic acid) (PAA) hydrogel through free radical polymerizations. This work advanced membrane functionalization, specifically flat sheet membranes, from lab-scale to full-scale by modifications of the polymerization procedures. The hydrogel functionalized membranes by redox polymerization showed an expected responsive behavior, represented by permeability variation at various pH values ($4.0 \leq pH \leq 9.0$), from 53.9 to 3.4 L/(m^2·h·bar) and a change in effective pore size from 222 to 111 nm, being 3800 L/(m^2·h·bar) and 650 nm the former permeability and pore size values of the non-functionalized membrane. Then, throughout a double ion exchange of sodium/iron and a subsequent reduction, bimetallic Fe/Pd nanoparticles were synthesized in-situ. Similarly, it was possible to use the reacted accelerants of the redox polymerization

to synthesize Fe^0 nanoparticles.

These hydrogel-membrane systems with Fe/Pd nanoparticles were studied throughout the reduction of trichloroethylene (TCE). This work has demonstrated an effective improvement in TCE reduction by the variation of the supporting membrane types and the functionalization (polymerization and nanoparticle synthesis) processes. The TCE normalized dechlorination rates (k_{sa}) are 3 times greater and 8 times for hollow fiber and sponge-like flat sheet membranes, respectively, than previous studies. For membrane supported Fe/Pd nanoparticles by redox functionalization, the dechlorination rates are similar to previous works in flat sheet membranes; and for the redox polymerized hydrogel, the dechlorination rates are the highest results with 1.3 times greater than the rates of solution-phase nanoparticles and 10 times the rate values of the membranes. All supports showed nonsignificant nanoparticle loss (up to 1%). Up to 80% of reduction was achieved within 2 hours with chloride production near to stoichiometric values (3:1), demonstrating absence of intermediates.

As an extension of the membrane functionalization, it was possible to immobilize Outer membrane protein F precursor (OmpF) from *Escherichia coli* within the PVDF membrane pore structure, using layer-by-layer (LbL) assembly of polyeletrolytes. This LbL technique allows to reuse the membranes numerous times, having reproducibility and greater selective rejections of uncharged (organic species) over charged solutes (small ions) than similar functionalized membranes without OmpF: 1.7 times and 2.0 times higher for Organic/$CaCl_2$ and Organic/NaCl, respectively. Additionally, the permeability of OmpF-membranes is almost double of the non-OmpF: 2.6 to 1.5 L/(m^2·h·bar).

KEYWORDS: hydrogel, reactive nanocomposite membranes, dechlorination, biomimetic membranes, selective separation.

Sebastián Hernández S.
Student's Signature

3/14/2017
Date

TUNABLE NANOCOMPOSITE MEMBRANES FOR WATER REMEDIATION AND SEPARATIONS

By

Sebastián Hernández Sierra

Dibakar Bhattacharyya, PhD
Director of Dissertation

Thomas D. Dziubla, PhD
Director of Graduate Studies

Ser feliz es una actitud ante la vida que cada uno decide

ACKNOWLEDGEMENTS

First and foremost, I would like to thank Prof. Dibakar Bhattacharyya for his substantial support and insightful guidance through these years. Thank you for encouraging and believe in me throughout my time at UK. Your passion and knowledge in engineering and life make me want to be a better person every day. I have been fortunate to meet you and have you as advisor, with our critical discussions and also informal conversations, teaching me all aspects of engineering and water technologies.

I would like to thank my doctoral committee members for providing me help insight and for improving this research. Dr. David Allan Butterfield for his perceptive observations in theoretical aspects of these research. Prof. Thomas Dziubla for providing technical support on nanoparticle, membrane and hydrogel characterizations, and Prof. John Balk for joining this committee after time and help me in material characterizations through the Electron Microscopy Center. Dr. Lindell Ormsbee for his support and help in the practical aspects of this research and Dr. Bruce Hinds for his contributions at the beginning of this process. Additionally, Dr. Anne-Frances Miller for accepting to be part of my doctoral committee, appointed by The Graduate School, her comments about this research are most welcome.

I would like to thank Dr. Yinan Wei for her support and insightful help in biochemistry fundamentals and Xinyi Zhang for material supply and characterization, Dr, Shi Lei and Dr. Rong Wang for their help and support in hollow fiber membrane technology. Dr. Dali Qian and specially Dr. Nicolas Briot for his support in the microscopy center and being always available, Tricia Coakley and John May in Environmental Research Training Laboratory (ERTL) at University of Kentucky (UK) for their analytical

assistance, Dr. Yang-Tse Cheng, Dr. Stephen Rankin, Dr. J. Zach Hilt, Dr. Andrew Morris, and Dr. Brad Berron, thank you all for sharing the instruments and resources in your labs.

I also want to thank and acknowledge my previous and current lab mates: Li Xiao, Noah Meeks, Minghui Gui, Ruo He, Andrew Tomaino, Andrew Colburn, Douglas Davenport, Hongyi Wan, Anthony Saad, Ashish Aher, Alani Johnson, Saiful Islam, Michael Detisch, Rupam Sarma and Madison Sloan. Special thanks to Joe Papp, Cassandra Porter and Jonathan Murphy, who worked with me on this project throughout their undergraduate studies. I would like to convey my thankfulness to my classmates and office mates at UK. Thanks to the NIEHS SRP people, especially Dr. Bernhard Hennig, Dr. Ljiljana Rajic, and Dr. Brad Newsome.

I would like to thank my friends, those I met here and those from my country. I want especially to thank Caterina for her love, help and support these years. Finally, I also want to thank my family, but especially my mother Luz Elena and my uncle Juan, who are always loving, patient and the big support in my life and my decisions.

This research is supported by the by the National Institute of Environmental Health Sciences (NIH-NIEHS-SRC) of the National Institutes of Health under Award Number P42ES007380. The content is solely the responsibility of the authors and does not necessarily represent the official views of the National Institutes of Health. I also want to acknowledge the significant contributions of the Singapore Membrane Technology Centre and Nanostone Water Inc. towards the joint development of hollow fiber and full-scale membranes, and the Center of Membrane Sciences and KY NSF EPSCoR Membrane Pillar.

TABLE OF CONTENTS

LIST OF TABLES

LIST OF FIGURES

1 INTRODUCTION

The development of new-generation materials that extend the industrial applications of polymeric membrane processes will require high levels of control of the characteristics of the base polymeric support layer, as well as, its corresponding surface and pore structure properties. Membrane processes provide a highly flexible separation technique for selective solute separation/concentration, and permeate water recycling and reuse. Although membrane processes such as, Reverse Osmosis (RO), Nanofiltration (NF), Ultrafiltration (UF), and Microfiltration (MF) have provided many successful applications ranging from high quality water production to material recovery, the incorporation of responsive macromolecules or nanoparticles (NPs) in macro-porous membranes should add immense value in the area of water treatment.

This chapter starts with a discussion about the relevance of current technological and scientific developments in nanocomposite and responsive/reactive membrane technologies, particularly in water remediation. Then, the general and the specific objectives are presented showing the importance of the research work contained in this dissertation. Part of this introduction has been published (Hernández, Saad, Ormsbee, & Bhattacharyya, 2016). Literature review and background information is given in Chapter 2. The experimental methods and the materials used are in Chapter 3. Chapter 4 outlines the importance of functionalization of membranes with polyelectrolytes and how these materials can be used to effectively change membrane properties. The subsequent Chapter 5 describes the synthesis of metallic Fe/Pd NPs and their characterization within synthetic membranes. How metallic NPs can be used for catalytic reduction of chlorinated organics is discussed in Chapter 6, using trichloroethylene (TCE) as a model pollutant. Finally in

Chapter 7, an extension of this polyelectrolyte membrane functionalization is developed in order to immobilize outer membrane protein F (OmpF) or “porins” channels using layer-by-layer (LbL) assembly technology in order to selective separate non-charged molecules from ions in solution.

1.1 NANOCOMPOSITE AND RESPONSIVE MEMBRANES FOR WATER TREATMENT

Research has done across multiple disciplines in order to develop technologies to adhere to the need of higher quality water and more effective selective separations. Figure 1.1 shows some existing and emerging technologies for water/wastewater treatment. Membranes are proving to be effective in meeting such objectives, specifically: selective separation of small molecules, separations in various environmental conditions, enhanced durability, simultaneous separation and reaction processes, and selectively removing components from difficult mixtures (Geise et al., 2010). Some of these objectives can be addressed from established technologies using nanomaterials, biological nanostructures or by adoption of concepts from physicochemical and biological systems.

In specific, polymeric membranes are a very important segment in water treatment. Polymeric membrane technology has gained significant interest for water treatment applications because of its high flexibility, broad range of pore sizes and structure, simple manufacturing processes and low associated costs (Merkel et al., 2002; M. M. Pendergast & Hoek, 2011; Vijay et al., 2006).

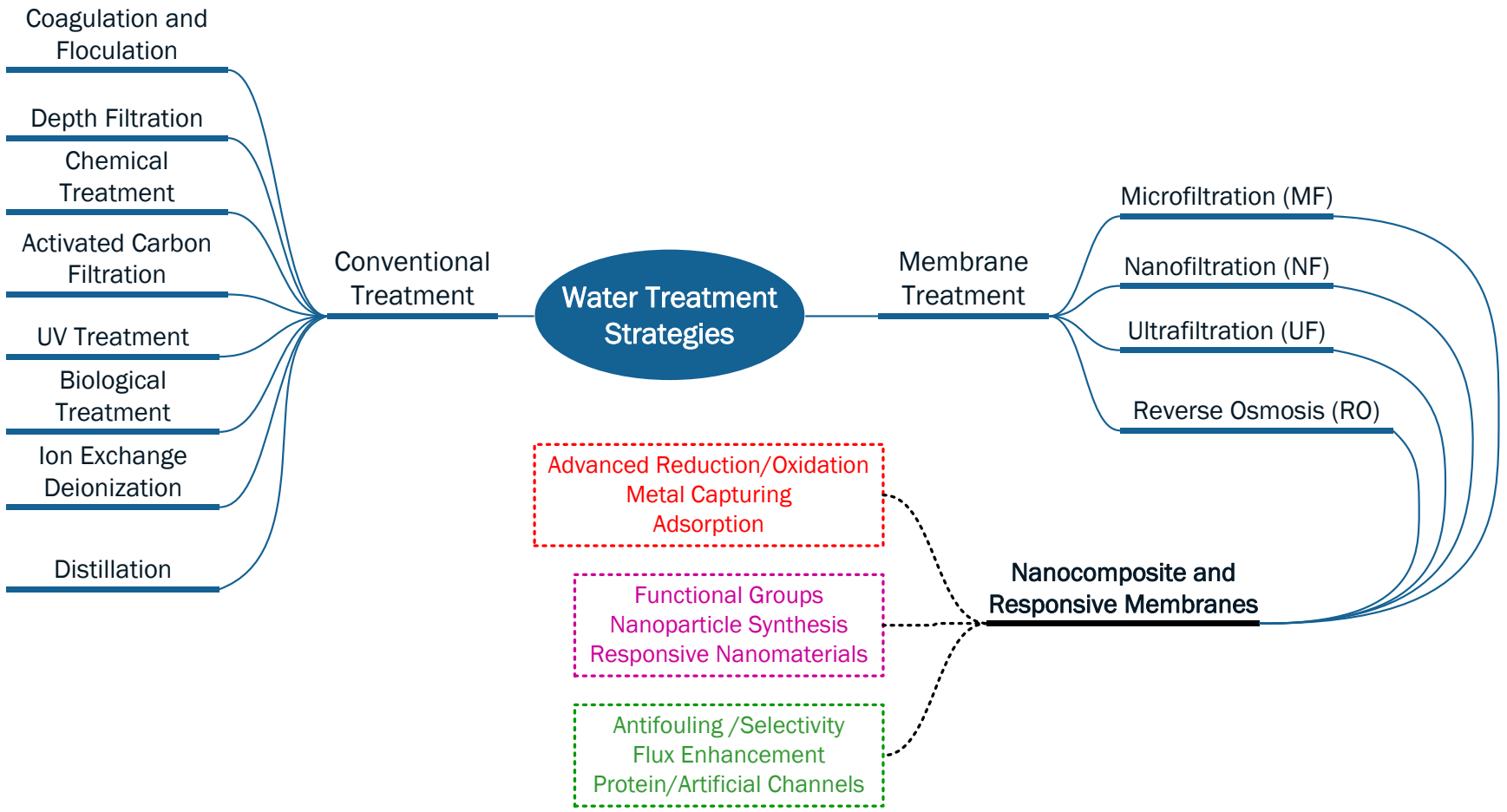

Figure 1.1. Conceptual Map of water treatment strategies currently used in industry (solid lines) and emerging applications (dash lines). Reprinted from (Hernández, Saad, et al., 2016). Copyright (2016) Elsevier.

The main innovational goals consist of simultaneously obtaining high selectivity and high permeability at low costs, combining reactions within the pore structures to avoid further downstream unit operations, avoiding membrane fouling, and increasing membrane physical durability (Lai, Groth, Gray, & Duke, 2014; M. M. Pendergast & Hoek, 2011). These polymeric membranes are fabricated using improved or novel materials mixed with inorganic, organic and/or bio-synthesized nanomaterials. Responsive and/or nanoscale materials can be added or in-situ synthesized onto the porous surface of commercial membranes to obtain functionalized, responsive, and reactive membranes (Ulbricht, 2006).

1.2 OBJECTIVES

Despite the aforementioned tremendous advances in environmental technologies, especially using functionalized membranes, it is necessary to investigate the functional material used as support of different moieties and the functions that can be engineered on its surface.

Essentially, the present work intends to improve the functionalization aspects of polymeric membranes using polyelectrolytes and reactive bimetallic nanoparticles, in a way to improve the elimination of chlorinated organics in water.

Specifically, this study attempts to use nanocomposite membranes in the remediation of water contaminated with TCE. The polyelectrolyte functionalization is then exploited through an LbL technique in order to immobilize non-specific bio-based protein channels (OmpF porins). This work includes characterization of the immobilized and non-immobilized NPs and OmpF, the hydrogel produced and the membranes by different

morphological, spectral and physicochemical techniques during each stage of the processes used. The specific objectives are depicted below.

For improvement of polyelectrolyte functionalization in membranes:

- To synthesize a hydrogel of acrylic acid (AA) by a redox polymerization using an iron salt as accelerant of the process.

- To functionalize flat sheet (FS) hydrophilized microfiltration poly(vinylidene fluoride) (PVDF) membranes by the abovementioned redox polymerization of AA-based hydrogel within the membrane pore.

- To characterize PVDF hydrophobic sponge-like hollow fiber (HF) membranes made in-lab by thermal induced phase separation (TIPS).

- To develop a method of a post-casting hydrophilization of the HF membrane fabricated, by cross-linking of polyvinylpyrrolidone (PVP) on the surface, and the subsequent evaluation through contact angle measurements and surface energy calculations on the fabricated membrane.

- To functionalize the "sponge-like" PVDF membranes, HF and FS types, by thermal induced polymerization of poly(acrylic acid) (PAA) hydrogel within the membrane pores.

For improvement of bimetallic nanoparticle synthesis in membranes:

- To synthesize in situ iron NPs by using the remaining ferric and ferrous ions from the exhausted accelerant ($FeCl_2 \cdot 4H_2O$) used in the redox polymerization of AA within the PVDF membranes

- To in situ synthesize Fe/Pd NPs within the PAA functionalized membrane and the hydrogel structure along with the size and shape characterization of the produced NPs by diverse physical chemistry methods and image analysis.

For dechlorination in water:

- To evaluate the surface catalyzed dechlorination reactions in aqueous solutions of the Fe/Pd nanoparticle functionalized hydrogel and membranes using trichloroethylene (TCE) as model compound.

For immobilization of non-specific bio-based protein channels (OmpF):

- To immobilize OmpF porins within the pores of PVDF membranes through LbL assembly.

- To compare the selective separation performance between LbL membranes with OmpF and without OmpF through rejection of various model organic solutes in solution with inorganic salts.

2 BACKGROUND

Polymers and polymer networks have many tunable properties that can selectively response to external stimuli. Responsive polymers can react to various stimuli including variations in temperature, pH, light, ionic strength, and chemical composition, which enable their use for a wide range of important applications (Bhattacharyya, Schäfer, Wickramasinghe, & Daunert, 2013; Roy, Cambre, & Sumerlin, 2010; Stuart et al., 2010).

On the other hand, nanocomposites, depending on their nature, can generate hybrid inorganic-organic or protein-polymer biomimetic interactions within the membranes. These nanocomposites provide novel properties such as antibacterial activity, surface electrical charge, hydrophilicity, reactivity (catalysis), enhanced flux and selectivity (rejection), thermal, mechanical and chemical strength.

This chapter provides an overview of the literature studies on nanocomposite membranes. It begins focusing in membranes containing crosslinked polyions (hydrogels), and metallic nanoparticles with an emphasis in iron and iron/palladium. Finally, it is discussed the layer-by-layer (LbL) methodology that utilizes these polyions and its applications in immobilization of different moieties such as bio-based protein channels. Part of this literature review has been published (Hernández, Saad, et al., 2016).

2.1 RESPONSIVE MATERIALS

The current use and future potential of polymeric stimuli-responsive materials cut across various disciplines. From being able to mimic biological processes to induce selective separations across membrane structures, these smart materials are one of the most important current research topics.

Recent advances in materials surface science have led to the creation of many smart surface designs where interfacial properties are controlled by external stimuli, see Figure 2.1. These smart surfaces are mostly based on using stimuli-responsive materials to form self-assembled monolayers and polymer thin films. There are various methods for producing polymer films and depositing them on substrate surfaces. Methods include spin coating, plasma deposition, chemical and electrochemical reactions, chemical vapor deposition, LbL assembly, etc. Recently, polymers have been tethered to the membrane surface in a controlled manner to create polymer films, and are known as polymer brushes (Azzaroni, Brown, & Huck, 2007; Husson, 2012; Mendes, 2008; Q. Yang & Wickramasinghe, 2012). Polymers can be attached via anchor sites on the membrane surface or within membrane pores, either by physical adsorption or covalently, to create polymer brushes. They differ from conventional solution casted polymer coatings by their defined, stretched chain conformation due to side chain steric demands, which causes rod-like or helical conformations and lead to responsive surfaces that can respond to external stimuli, depending on the polymers used (Husson, 2012; Kastantin & Tirrell, 2011; Rudick & Percec, 2007; Schlüter & Rabe, 2000; Sergiy, 2007; Q. Yang & Wickramasinghe, 2012; Zehm et al., 2011; H. Zhang, Qu, & He, 2015). Polymer brushes are covalently attached by either the "grafting-to" or the "grafting from" method. In the "grafting to" method, an end-functionalized polymer in solution reacts onto a desired substrate surface.

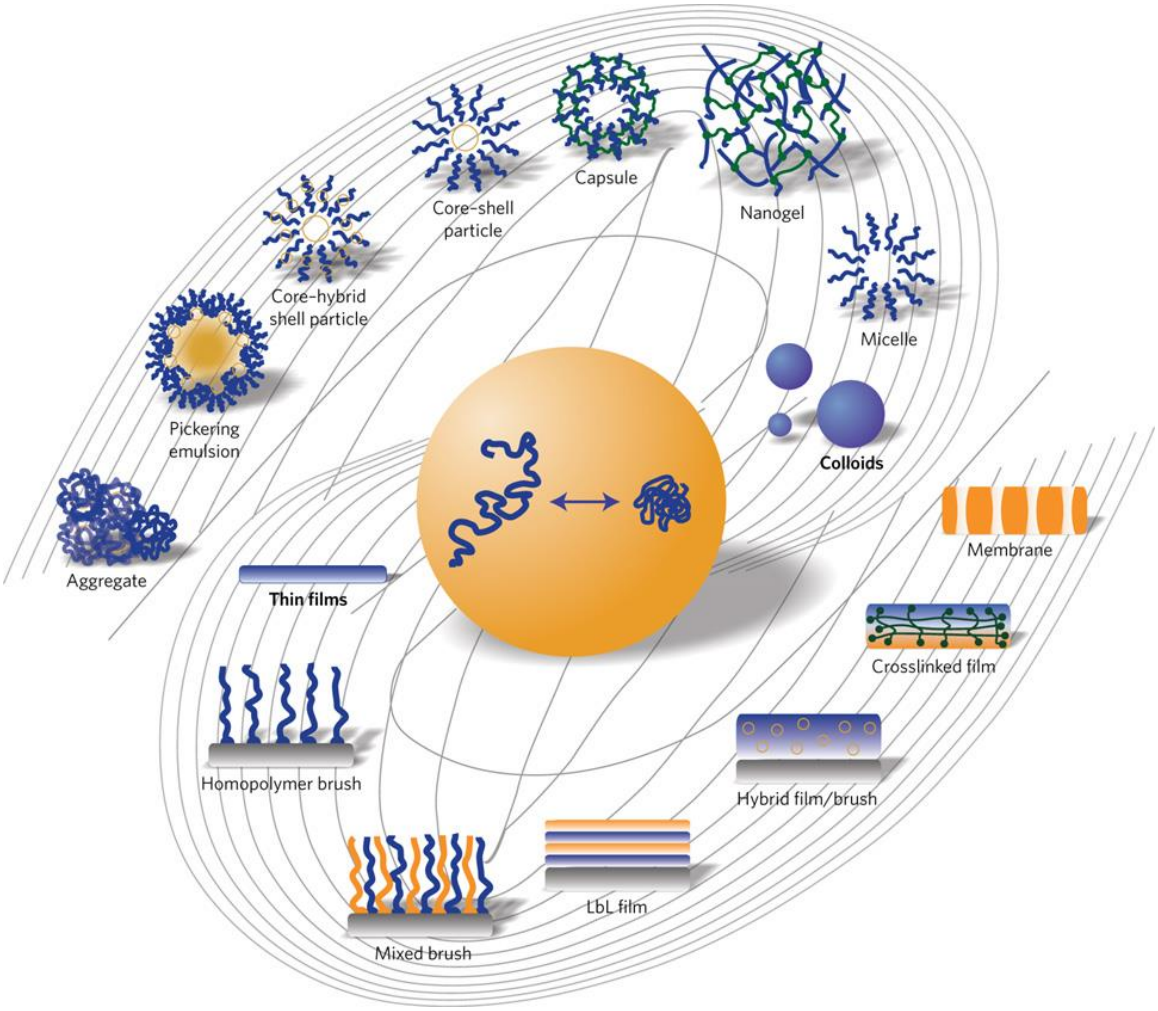

Figure 2.1. Nanostructured stimuli-responsive polymer materials. Reprinted with permission from (Stuart et al., 2010). Copyright (2010) Macmillan Publishers Limited.

The “grafting-from” method is sometimes considered more advantageous because monomers are polymerized onto initiators already anchored on the surface, thereby reducing steric hindrance of neighboring bonded chains (Husson, 2012; Kastantin & Tirrell, 2011; Mendes, 2008; Rudick & Percec, 2007; Schlüter & Rabe, 2000; Q. Yang & Wickramasinghe, 2012; Zehm et al., 2011; H. Zhang et al., 2015). As depicted in Figure 2.2, Adrus and Ulbricht describe a method of functionalizing membrane pores with responsive polymers via in-situ polymerization, using UV light as an initiator for the polymerization of N-isopropylacrylamide (NIPAm) within the pores via the grafting-from technique, ultimately creating pores that are reactive to external stimuli (Adrus & Ulbricht, 2012). Grafting of stimuli-responsive lower critical solution temperature (LCST) segments, binary brushes, block copolymers, and photo-chromic segments are also shown in Figure 2.3 (F. Liu & Urban, 2010).

Surface-initiated atom transfer radical polymerization (ATRP) was used to grow polymer nanolayers on the membrane surface, and polymer chain density and polymerization time were varied in order to optimize produced water treatment performance (Wandera, Himstedt, Marroquin, Wickramasinghe, & Husson, 2012). Higher polymer chain density and longer polymerization times lead to membranes with more stable flux, whereas lower chain density and shorter polymerization times lead to higher instantaneous flux, but do not completely eliminate flux decline due to fouling. Figure 2.4 show that higher chain density leads to lower, more stable trans-membrane water flux. By varying polymer coating structural properties, the membrane surface can be modified to optimize both permeate flux and flux decline due to fouling for separation of oil emulsion from produced water (Wandera et al., 2012).

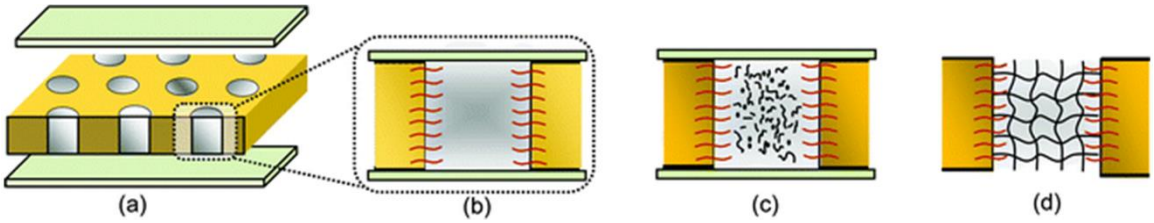

Figure 2.2. Membrane pore functionalization with responsive polymer; (a) and (b) membrane filled with reaction mixture, and equilibration, (c) in-situ polymerization is initiated by UV (d) hydrogen created within the membrane pore. Reprinted with permission from (Adrus & Ulbricht, 2012). Copyright (2012) Royal Society of Chemistry.

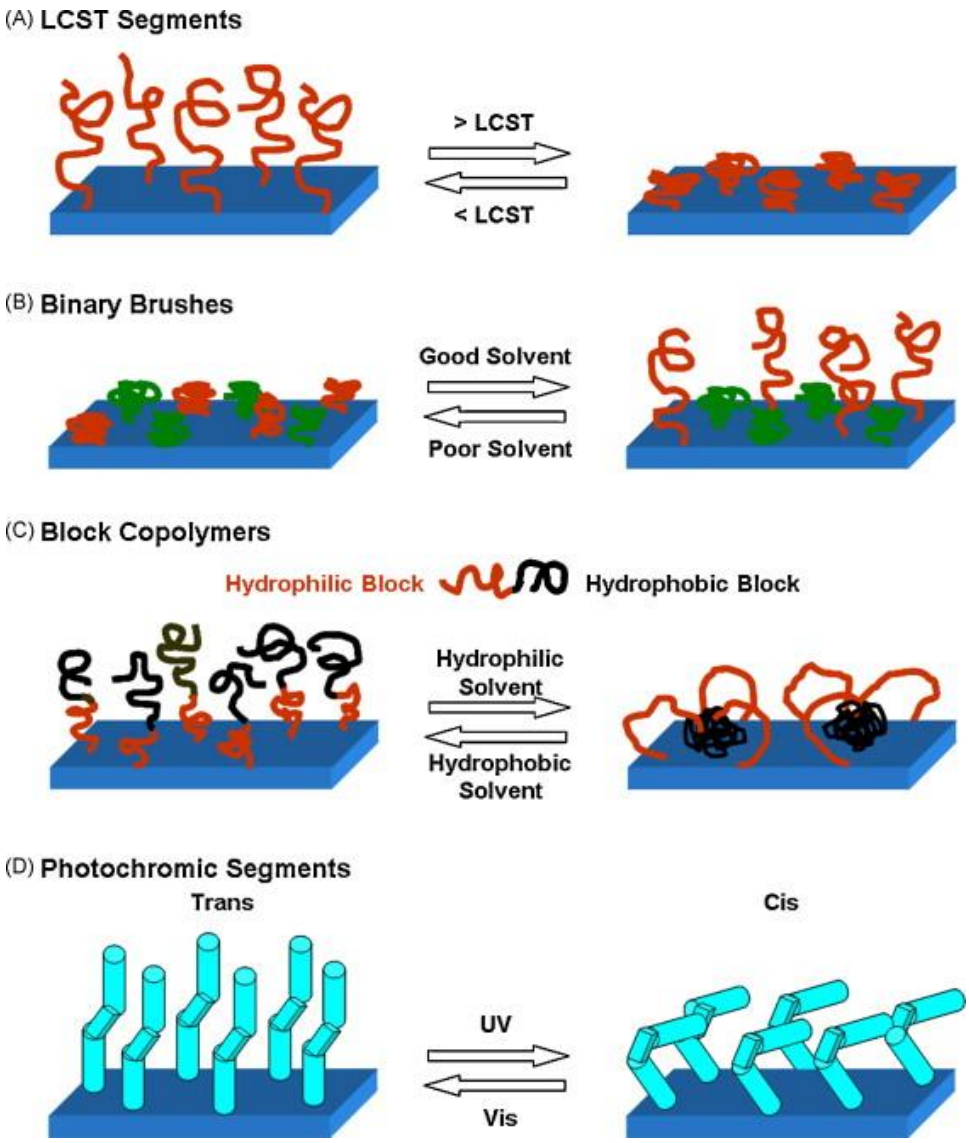

Figure 2.3. Grafting of stimuli-responsive: (A) LCST segments, (B) binary brushes, (C) block copolymers, and (D) photo-chromic segments. Reprinted with permission from (F. Liu & Urban, 2010). Copyright (2014) Elsevier.

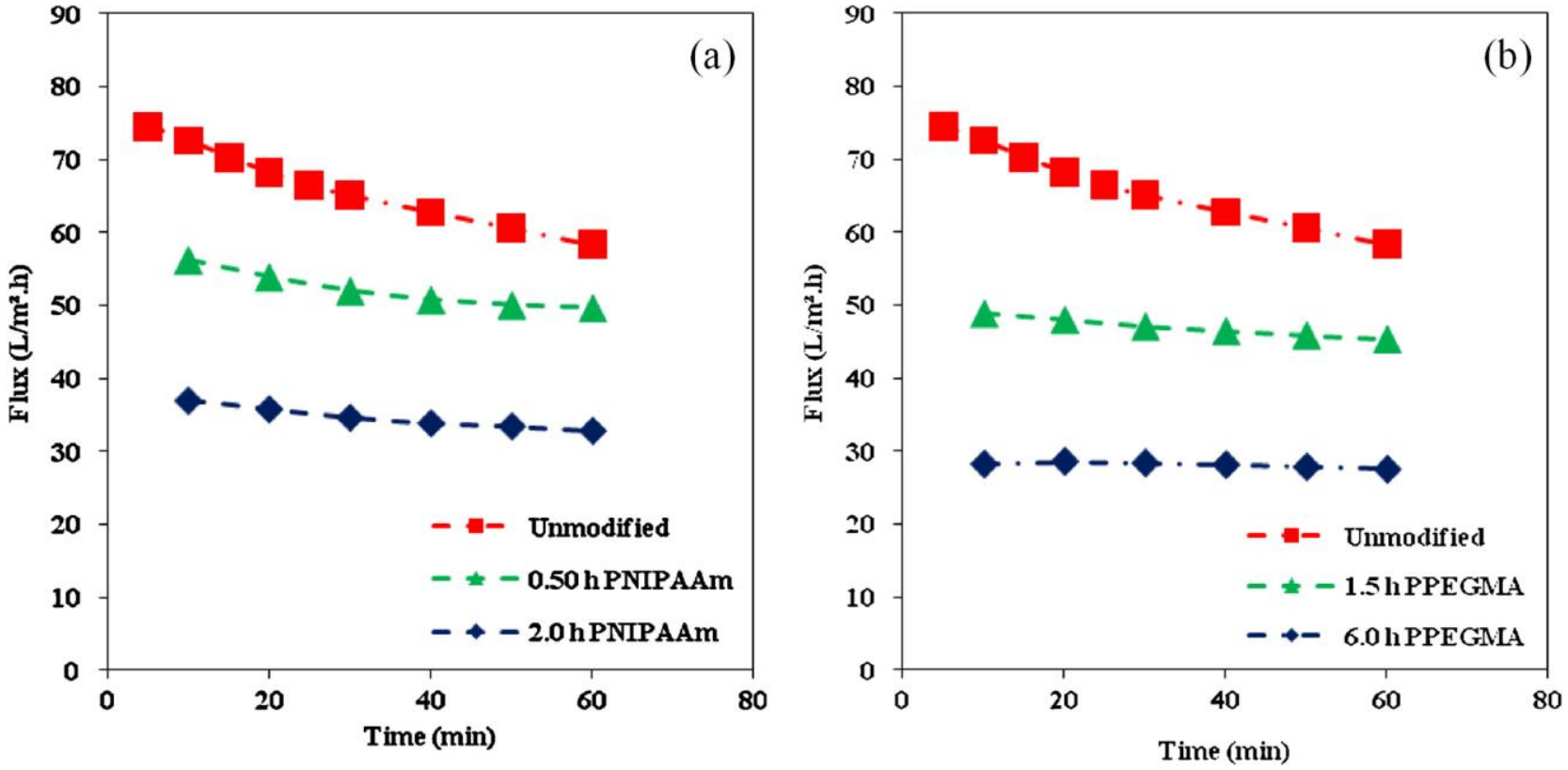

Figure 2.4. (a) Produced water flux of an unmodified membrane (5 kDa Hydrosart membrane), membrane modified by PNIPAm for 0.5 h and PPEGMA for 3 h, and membrane modified by PNIPAm for 2 h and PPEGMA for 3 h. (b) Produced water flux of an unmodified membrane (5 kDa Hydrosart membrane), membrane modified by PPEGMA for 1.5 h and PNIPAm for 1 h, and membrane modified by PPEGMA for 6 h and PNIPAm for 1 h. All experiments conducted at 210 kPa and 45 °C. Reprinted with permission from (Wandera et al., 2012). Copyright (2012) Elsevier.

The application of polymer films to surfaces enables the formation of materials that are responsive to a variety of external stimuli, targeting chemical and biological species that interact with a particular responsive location or by mass and mass/heat transfer from the bulk solution (Darvishmanesh, Qian, & Wickramasinghe, 2015). Therefore these responsive materials can be used for a multitude of industrial purposes. Some of these are outlined below.

2.1.1 Temperature Responsive Surfaces

Thermo-responsive polymers are polymers that have been known to display a miscibility gap in temperature-composition diagrams; they are known as either LCST or UCST (upper critical solution temperature) polymers depending on whether this gap exists above a certain temperature (LCST polymers) or below a certain temperature (UCST polymers) (Husson, 2012; Rackaitis, Strawhecker, & Manias, 2002; Tauer, Gau, Schulze, Völkel, & Dimova, 2009; Yim et al., 2004).

The most common temperature responsive hydrogel is poly(N-isopropylacrylamide), or PNIPAm, because of the phase transition it experiences from its hydrophilic state to hydrophobic state at its LCST of around 32 °C. This transition occurs due to alterations in the hydrogen bonding interactions of the amide group (Yim et al., 2004) – this makes it applicable to physiological processes (Adrus & Ulbricht, 2012). By increasing temperature, the polymer side chains undergo property changes that hinder the hydrogen bonds that enabled favorable interaction with water molecules. Therefore, manipulating the side chains and their properties can effectively alter the LCST of a polymer. The polymer's LCST value can be controlled by adding hydrophobic branches,

hydrophobic/hydrophilic balance in the polymer, or manipulating the length of the hydrophobic side chains (Rackaitis et al., 2002).

The ability to control the hydrophobicity of a polymer with slight variations in temperature is important for water treatment applications for several reasons. First, it enables selective control over water permeability through the membrane (L. Xiao et al., 2014). Second, temperature responsive polymers have also been used to functionalize membranes with reactive nanoparticles (NPs) in order to enhance membrane reactivity (L. Xiao et al., 2014). Zero-valent metal, such as iron NPs have recently received considerable attention for the remediation of chlorinated compounds in groundwater (Varanasi, Fullana, & Sidhu, 2007). Fe and Fe/Pd NPs have been immobilized in poly(acrylic acid)-*co*-PNIPAm (PAA-*co*-PNIPAm)-functionalized membranes for the remediation of trichloroethylene (TCE) in water (Smuleac, Varma, Sikdar, & Bhattacharyya, 2011; L. Xiao et al., 2014). Slight variations in temperature affects not only NP reactivity by affecting the reaction rate constant, but can also affect adsorption of hydrophobic/hydrophilic species; as temperature is increased above the polymer's LCST, transition to the hydrophobic state caused increased TCE adsorption onto the membrane surface because of the hydrophobic nature of this solute (Li Xiao, Isner, Hilt, & Bhattacharyya, 2012). Figure 2.5 demonstrates the increase in TCE adsorption percentage onto a PNIPAm-PAA hydrogel from 30% to 65% as temperature is increased above the LCST because of enhanced hydrophobicity (Li Xiao et al., 2012).

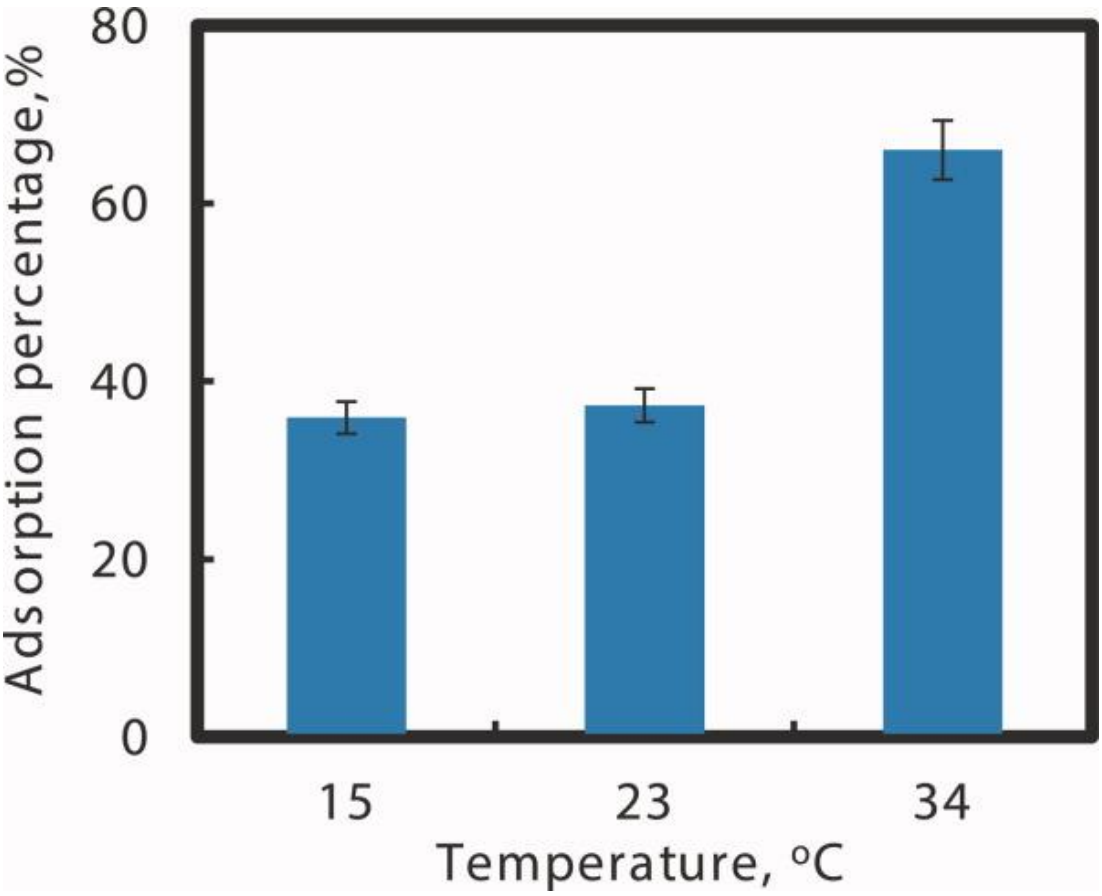

Figure 2.5. Normalized TCE (trichloroethylene) adsorption through temperature responsive PNIPAm-PAA hydrogel below LCST (15 and 23°C) and above LCST (34°C), feed concentration: 0.2 mM TCE in water, 20 mL, pH = 6.8. Reprinted with permission from (Li Xiao et al., 2012). Copyright (2012) Elsevier.

Water can also oxidize the Fe NPs and decrease reactivity. By controlling the hydrophilicity of the polymeric membrane, water content within the membrane pores can be controlled, thereby allowing for selective tuning of the reduction reaction (Li Xiao et al., 2012). Varying temperature affects NP reactivity because as we know, reaction kinetics are a function of temperature, and also affects diffusivity through the membrane as shown in the Wilke-Chang equation (Wilke & Chang, 1955).

Xiao et al. studied TCE dechlorination using Fe/Pd nanoparticles (1.5 wt. % Pd relative to Fe) in a PNIPAm-PAA hydrogel matrix above and below the LCST to verify the effect of temperature on reaction rate constant. The surface area normalized rate constant for the dechlorination reaction (k_{sa}) increased by a factor of three, from 0.0156 to 0.0411 L/(m^2·h) (LMH), due to a temperature increase of only a few degrees above the LCST (Li Xiao et al., 2012). Figure 2.6 shows how TCE concentration versus time changes during the dechlorination reaction by Fe/Pd NPs in a PNIPAm-PAA hydrogel at 30 °C and 34 °C (Li Xiao et al., 2012).

2.1.2 pH Responsive Properties

Membranes and surfaces can also be functionalized with polymers that display pH responsiveness, also called hydrogels. By having ionizable functional groups that have the ability to gain or lose protons based on the surrounding pH, such polymer chains can be collapsed or extended based on fluctuation of hydrophobic volume (swelling) caused by generated electrostatic repulsions (F. Liu & Urban, 2010). Functional groups such as amino and amine groups in polymer chains with pKa values around 5 will lose their protons in basic pH conditions and are responsible for the responsive behavior (Q. Zhang et al., 2008).

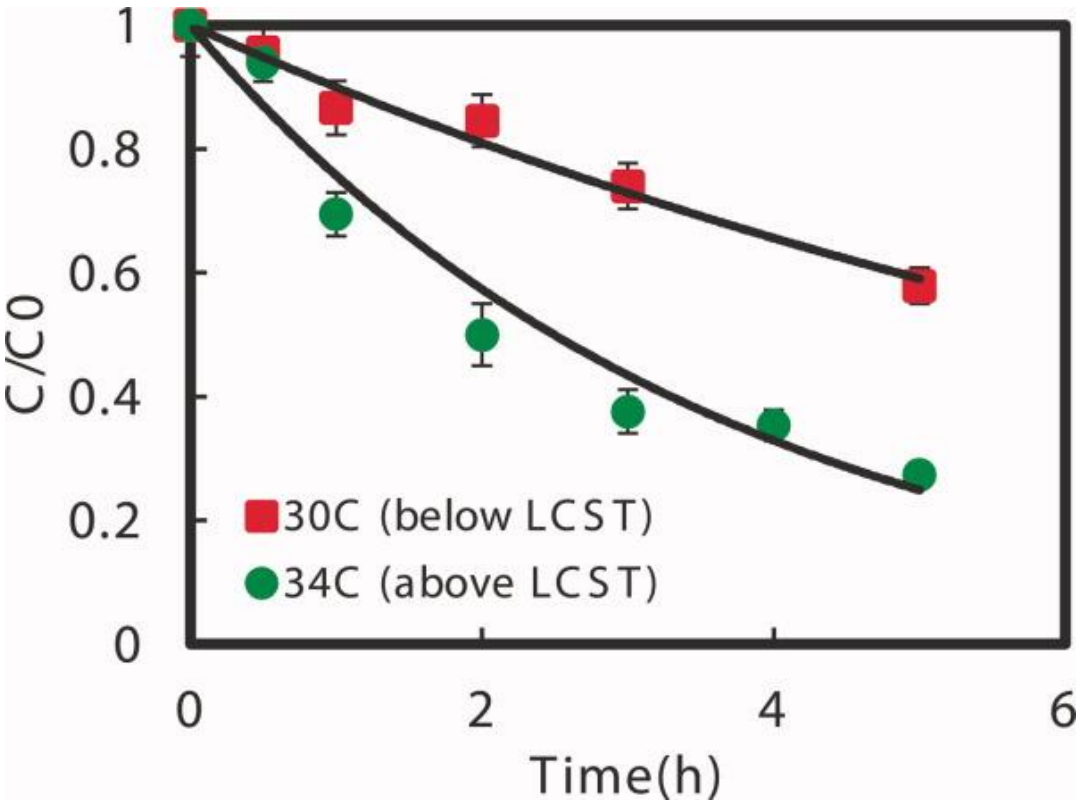

Figure 2.6. Batch dechlorination of TCE with 70 nm Fe/Pd NPs (Pd = 1.5 wt. %) immobilized in Poly(NIPAm-AA) hydrogel at 30°C (below LCST) and 34 °C (above LCST). Vol. = 43 mL, pH = 6.8; initial TCE concentration: 30 mg/L, iron loading amount: 0.3 g/L. Reprinted with permission from (Li Xiao et al., 2012). Copyright (2012) Elsevier.

Figure 2.7 demonstrates the physical response of a pH responsive polymer when subjected to pH values above and below its pKa (Q. Zhang et al., 2008). The swelling behavior of a hydrogel can be predicted by first-order or second-order kinetics. This behavior has an increment in the mesh size of the polymer, which is a parameter of cross-linking density by calculating the average distance of neighbor polymer chains between two cross-linked points (Katime et al., 1996; N. A. Peppas & S. L. Wright, 1996; A. Thakur, R. K. Wanchoo, & P. Singh, 2011b).

The fabrication of pH responsive polymers that display high hydrophilicity at low pH values is important for water treatment applications. In the past little research was done on wettability of surfaces based on pH responsive membranes that display such characteristics. A novel pH responsive surface was created by a poly(N-N'-dimethylaminoethyl methacrylate) (PDMAEMA) thin film on silicon substrates. This homopolymer can be prepared via surface-initiated atom transfer radical polymerization. The polymer is deprotonated at high pH and protonated at low pH, thereby allowing it to interact with anionic substances through electrostatic attraction (Q. Zhang et al., 2008). Since membrane fouling properties and solute rejection are correlated with membrane surface charge, coating membranes with a polymer that can be selectively deprotonated are able to significantly enhance anti-fouling properties while maintaining high solute rejection (Sagle et al., 2009). Lowering the surface free energy of the membrane, which lowers the interfacial interactions with foulant molecules, can also significantly reduce membrane fouling (Y. Li et al., 2014).

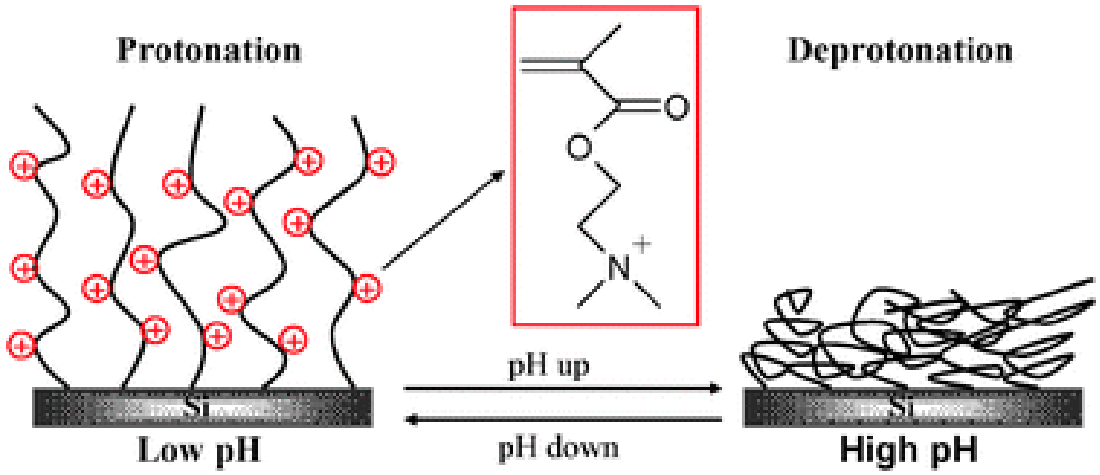

Figure 2.7. pH responsive behavior of PDMAEMA above and below pKa, characterized by deprotonation of the amine group at high pH, thereby reducing repulsion between chains and allowing for higher water permeability. Reprinted with permission from (Q. Zhang et al., 2008). Copyright (2008) Royal Society of Chemistry.

Our group have reported the functionalization of poly(vinylidene fluoride) PVDF with PAA to create pH responsive membranes onto which iron and iron oxide NPs can be immobilized for water remediation (M. Gui, Ormsbee, & Bhattacharyya, 2013; M. Gui et al., 2015; Hernandez, Papp, & Bhattacharyya, 2014; Smuleac, Bachas, & Bhattacharyya, 2010b; Smuleac et al., 2011; J. Xu & Bhattacharyya, 2007). PAA can be transformed into the ionized state at environmental pH values above its pKa ($4.3 \leq pKa \leq 4.9$). Membrane functionalization with PAA enables selective pore size tunability and therefore control over water permeability through the membrane. Figure 2.8 shows the effect of environmental pH on water flux and permeation through a PVDF-PAA membrane (M. Gui et al., 2013). The PAA functionalization is made by free radical polymerization using strong oxidants (e. g. persulfate) at 70 – 90 °C depending on the cross-linker used (ethylene glycol (EG); N,N′- methylenebis (acrylamide) (MBA), etc.), or starting at room temperature using metallic salts as accelerants (redox reactions) and antioxidants, such as ascorbic acid, to control the reaction process (Hernandez et al., 2014; Smuleac et al., 2010b).

Full-scale PVDF-PAA flat sheet membranes (1×91 m and 70 μm of PVDF thickness, 45-55% porosity and backing fabric for stability) and membrane modules (0.465 m^2 of surface area) were recently developed by joint work with the industry, see Figure 2.9. The polymerization in solution process at industrial scale is similar to the reported bench-scale studies using EG as cross-linker with a lower amount of acrylic acid (AA) to reduce the viscosity of the solution and shorter polymerization times (M. Gui, V. Smuleac, L. E. Ormsbee, D. L. Sedlak, & D. Bhattacharyya, 2012b; Seteni, Ngila, Sikhwivhilu, Moutloali, & Mamba, 2013; Smuleac et al., 2010b).

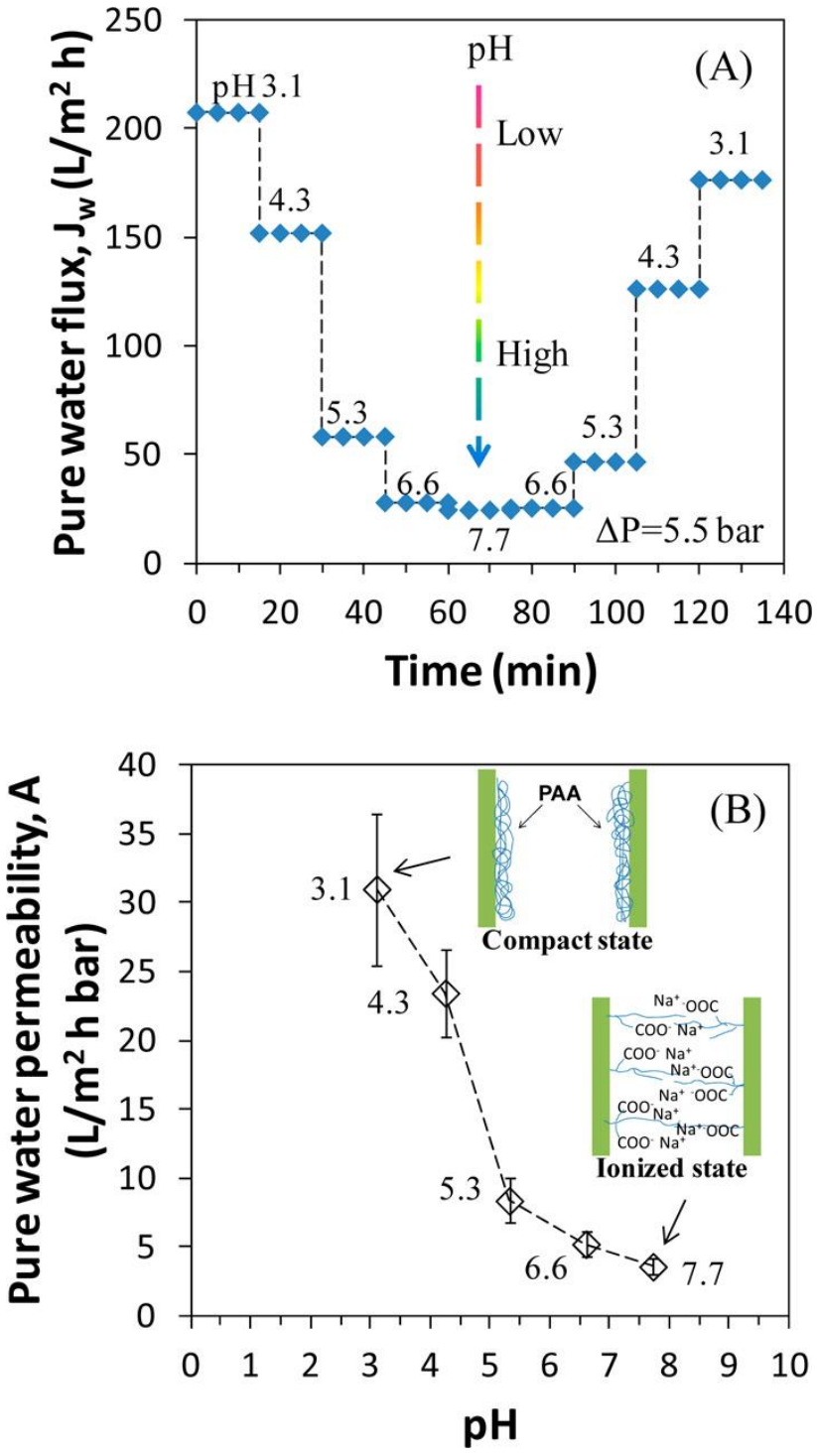

Figure 2.8. pH responsive behavior of poly acrylic acid (PAA) functionalized bench-scale PVDF membranes is demonstrated by water permeation tests. (A) Water flux is determined at 5.5 bar and (B) pure water permeability. Thickness of PVDF membranes: 125 μm. Reprinted with permission from (M. Gui et al., 2013). Copyright (2013) American Chemical Society.

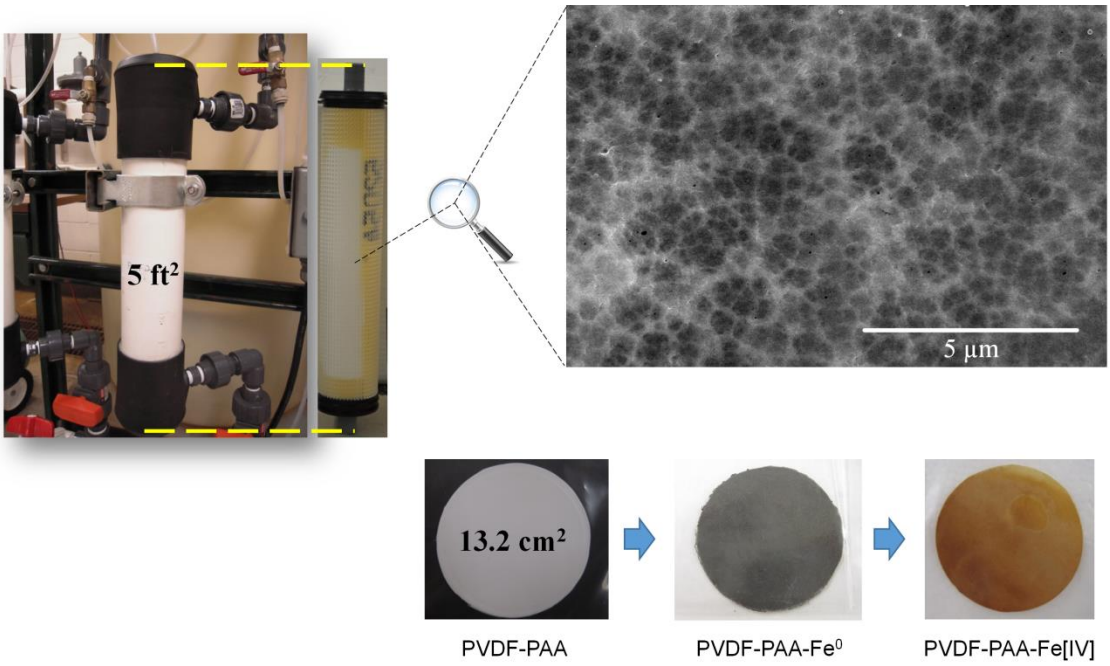

Figure 2.9. Top: Full-scale PVDF-PAA Functionalized Membrane and Module (Nanostone Water Inc.). Bottom: PVDF-PAA functionalization with zero-valent iron and iron oxide NPs. Reprinted from (Hernández, Saad, et al., 2016). Copyright (2016) Elsevier.

Pure water permeabilities of these full-scale membranes can vary from 1355 to 383 (LMH/bar), when the pH increased from acidic to neutral (3.0-7.3), and have a constant flux at different temperatures at same pH (see insert in Figure 2.10), whereas the modules can go from around 320 to 230 (LMH/bar) when the pH goes from 4.0 to 9.0, as depicted in Figure 2.11A (M. Gui et al., 2013; M. Gui et al., 2015; L. Xiao et al., 2014). These full-scale membranes and modules have also been post-functionalized with iron and iron oxide NPs (Figure 2.9) for degradation and metal capture studies and with PNIPAm to get both temperature and pH responsive behaviors, see Figure 2.10 (M. Gui et al., 2013; M. Gui et al., 2015; L. Xiao et al., 2014).

Other studies have reported the fabrication of smart fiber membranes for gravity-driven oil-water separations by depositing poly(methyl methacrylate)-block-poly(4-vinylpyridine) (PMMA-*b*-P4VP) pH responsive copolymer fibers on stainless steel mesh (J. J. Li, Zhou, & Luo, 2015). The pH responsiveness allows for switchable wetting states of the membrane from a superhydrophobic/superoleophilic to superhydrophilic/underwater superoleophobic state. By wetting the membrane with acidic water, the smart fiber membrane switches from allowing oil to selectively pass through the membrane with high separation efficiency, to allowing water to selectively pass through the membrane with similar high efficiency (J. J. Li et al., 2015). High flux, gravity driven flow with switchable wettability for many cycles makes the smart fiber-pH responsive membrane cost-effective and appropriate for large-scale oil recovery and water purification applications (J. J. Li et al., 2015).

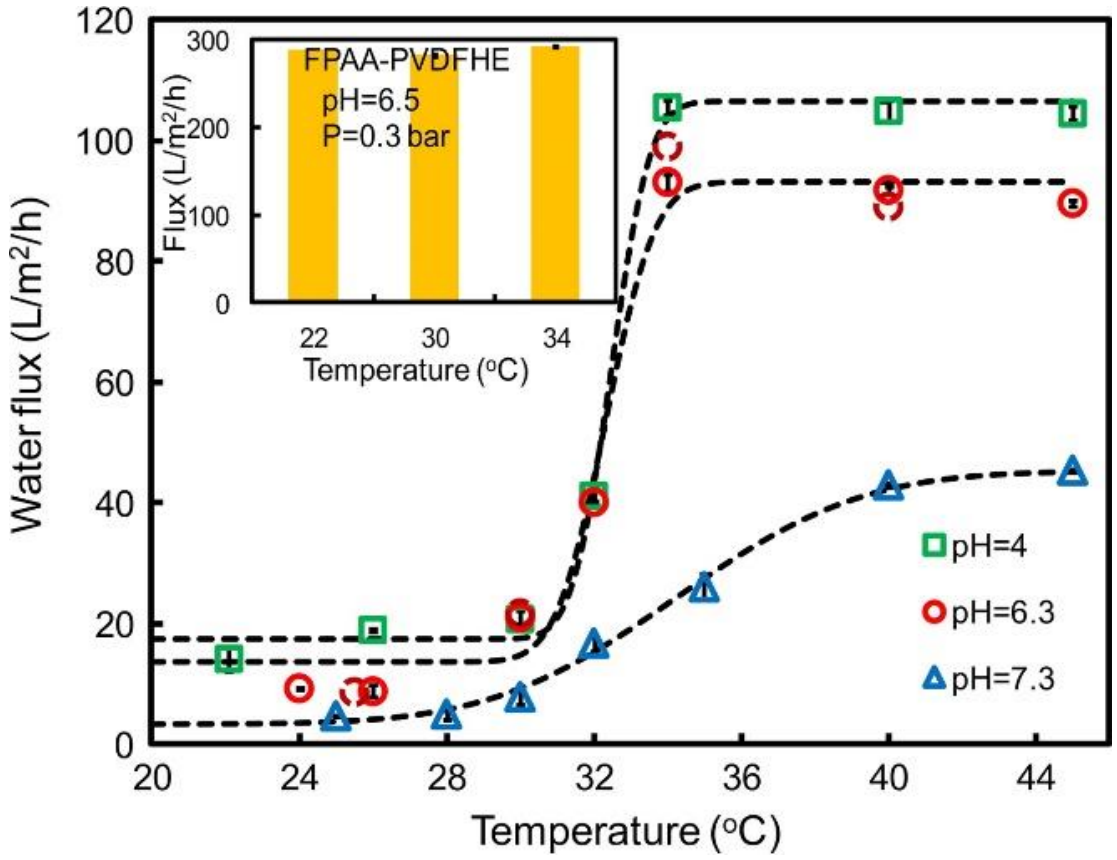

Figure 2.10. pH and temperature responsive behavior of PAA-*co*-PNIPAm functionalized full-scale PVDF membranes is demonstrated by water permeation tests. Water flux is determined at 0.3 bar. Sharp flux transition is seen at 32 °C. Insert shows flux behavior of membrane without PNIPAm constant pH of 6.5. Reprinted with permission from (L. Xiao et al., 2014). Copyright (2014) Elsevier.

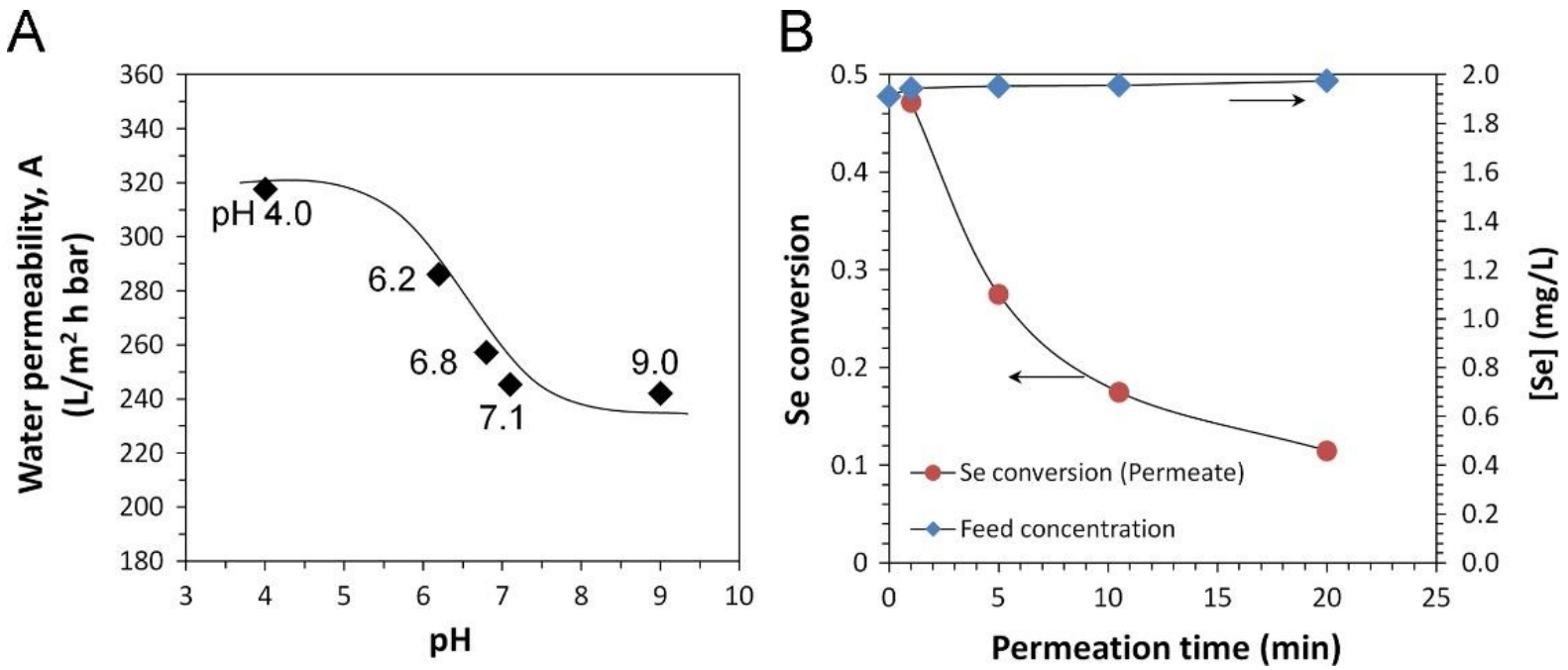

Figure 2.11. Full-scale PVDF-PAA membrane module water flux and reactivity in selenium oxyanion removal. (A) Water permeability with pH at 25 °C; (B) selenium removal results by passing synthetic selenium solution through iron immobilized module convectively, $[Fe]_0$ = 0.68 g, $[Se(VI)]_0$ = 1.00±0.05 mg/L, $[Se(IV)]_0$ = 1.00±0.05 mg/L (2.0±0.1 mg/L in total) in synthetic feed solution. pH = 6.2, J_w = 110.4 LMH and τ = 1.2 s. Effective membrane area: 0.465 m^2. In the pH responsive study, water flux was measured after being stabilized for 15 min. Reprinted with permission from (M. Gui et al., 2015). Copyright (2015) Elsevier.

2.1.3 Other responsive properties

Electromagnetic responsiveness can also be achieved by incorporating photo-sensitive molecules that rearrange based on ionization upon exposure to electromagnetic irradiation; photo-induced polymer chains can expand/shrink because of the reversible exchange of electrostatic repulsion between ionic states (F. Liu & Urban, 2010). Molecular structures of photo-responsive monomers have the ability to isomerizes, dimerize, and ionize given a certain irradiation, either inducing a change in charge or conformation. Structures of some photo-responsive monomers are shown in Figure 2.12 at various wavelengths (F. Liu & Urban, 2010).

Much like membranes functionalized with temperature and pH responsive polymers which can be varied to control effective pore diameter and therefore control both transmembrane flux and size-selective exclusion of particles, the use of superparamagnetic NPs can also be used to achieve the same phenomena due to their instantaneous response to an electric field (Q. Yang, Himstedt, Ulbricht, Qian, & Ranil Wickramasinghe, 2013). By varying the magnetic field orientation, the NPs cause the grafted poly(2-hydrocyethyl methacrylate) polyHEMA chains to extend, thereby reducing water flux through the membrane (Himstedt, Yang, Qian, Ranil Wickramasinghe, & Ulbricht, 2012). Increasing the magnetic field and therefore decreasing pore diameter and reducing permeation of larger particles can enable a nano-valve character. Yang et al. also grafted polyHEMA onto thin film composite polyamide NF membranes and attached superparamagnetic Fe_3O_4 NPs to obtain magneto-responsive membranes for salt rejection with antifouling properties (Q. Yang et al., 2013). Membrane rejection of $CaCl_2$ and $MgSO_4$ was measured in dead-end filtration mode both in the absence and presence of an oscillating magnetic field (Q. Yang

et al., 2013). Both permeate flux and salt rejection was greater in the presence of the magnetic field, and was also greater with increased magnetic NP density (Q. Yang et al., 2013). However, permeate flow decreases with increased grafting and NP density, thereby implying that the trade-off between permeate flow and membrane performance can be optimized for the desired application (Q. Yang et al., 2013).

Schacher et al. have reported the use of block copolymers displaying responsiveness to more than one stimulus to create functionalized membranes and surfaces that are controllable by multiple environmental factors (Schacher, Rudolph, Wieberger, Ulbricht, & Muller, 2009). They demonstrated that for PDMAEMA, both pH and temperature can be independently varied with significant resulting effects on the transmembrane water flux (Schacher et al., 2009).

2.2 NANOCOMPOSITE MEMBRANES

In water treatment applications, it is important for membranes to have a determined hydrophilicity and surface structure, as well as high durability with regard to physicochemical and mechanical stability. Pore size and porosity are also important considerations in membrane separation processes. A nanocomposite membrane is a hybrid material that can contain nanoscale inorganic and/or organic solid phases in a porous structure. These nanoscale materials give or enhance membrane properties that would otherwise not be satisfied by the polymer alone (J. Yin & Deng, 2015). They can be classified based on the materials selected and their properties, or their fabrication method.

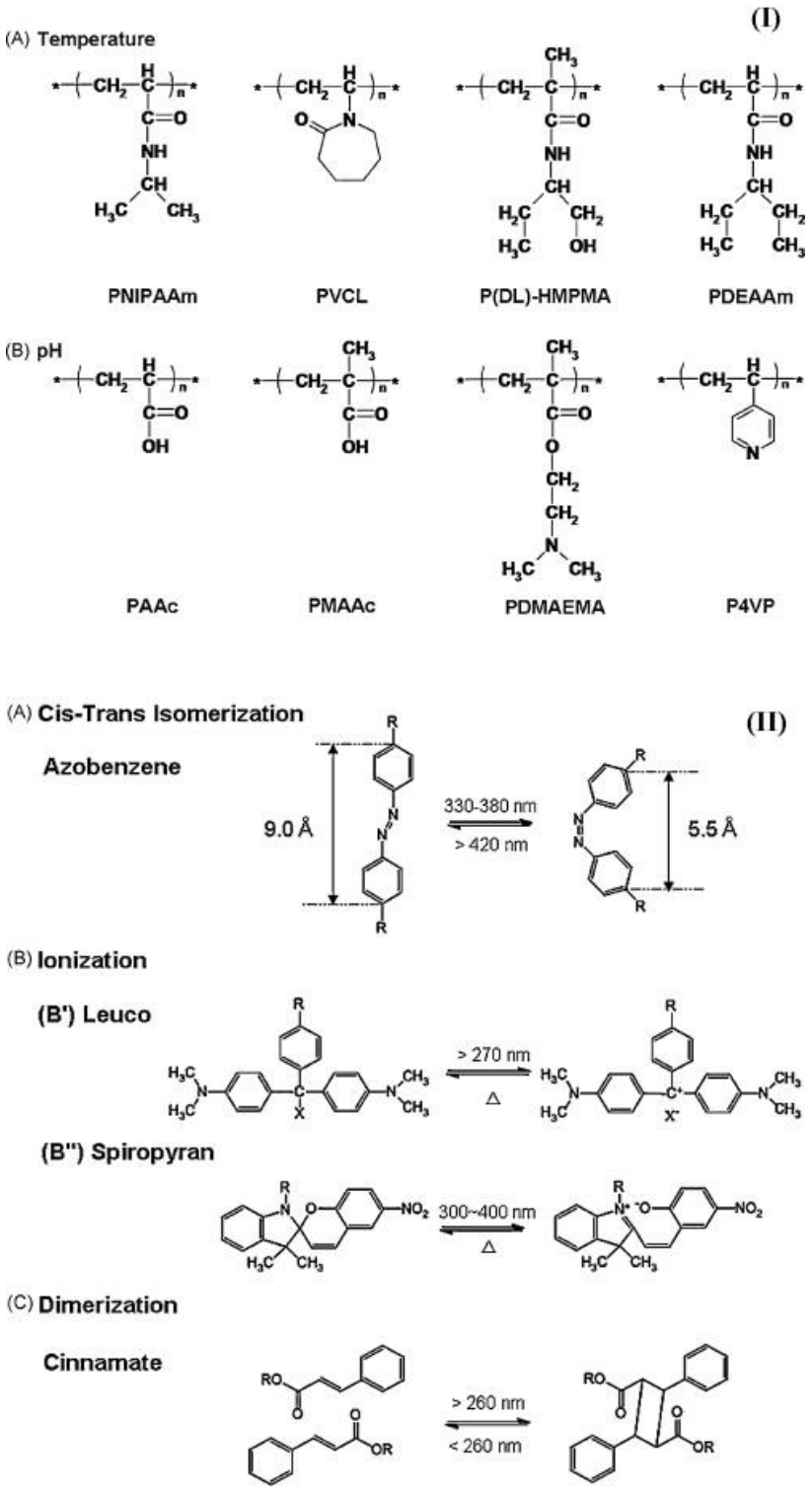

Figure 2.12. Examples of molecular structures of photoresponsive monomers: cis-trans isomer of azobenzene (A); ionization monomers of leucos (B') of spiropyran (B"); dimerization of monomer of cinnamate (C). Reprinted with permission from (F. Liu & Urban, 2010). Copyright (2010) Elsevier.

Nanomaterials can affect several properties, including mechanical strength and thermal stability (Paul & Robeson, 2008; Z.-l. Xu, Yu, & Han, 2009). They have enhanced membrane separations by providing various new functionalities such as antifouling properties, permeability, and selectivity. Many different materials are used in nanocomposite membranes to enhance water purification, including carbon-based nanotubes (CNTs), graphene and graphene oxide (GO), silica and zeolites, metal and metal oxides, functional polymers and dendrimers, and more recently biological nanomaterials (Savage & Diallo, 2005; Y.-x. Shen, Saboe, Sines, Erbakan, & Kumar, 2014). Because the field of nanocomposite membranes is immense and growing, covering all its components is a complex task. This section presents a broad classification of existing nanocomposite membranes, focusing on metal, metal oxides and polymer-silica functionalized membranes for catalytic and adsorptive applications in water treatment.

2.2.1 Membrane Fabrication with Nanofillers

The casting of nanocomposite membrane covers all manufacturing processes related to the incorporation of nanomaterials into the membrane structure starting from mixing of nanofillers with the polymer solution before membrane fabrication (Figure 2.13). Either flat sheet or hollow fiber membranes are fabricated by phase inversion (PI): thermal induced phase separation (TIPS) and non-solvent induced phase separation (NIPS). Nanofillers can considerably strengthen the mechanical properties of the polymers, such as fatigue and tensile resistances with a significant decrease in loading using nanoscale materials with large aspect ratios (length/thickness).

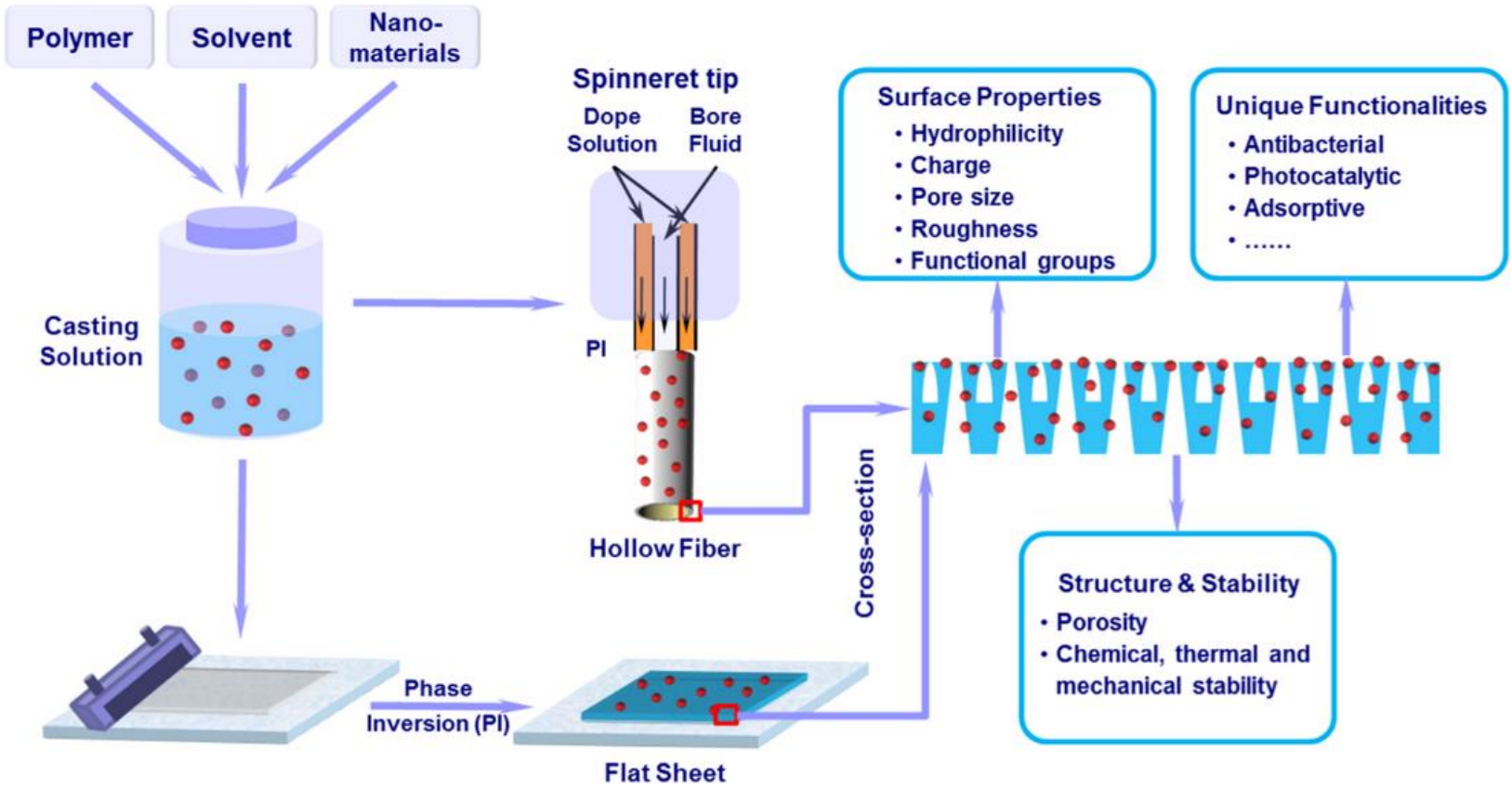

Figure 2.13. Fabrication of conventional nanocomposite membranes through the phase separation process and the main effects of nanofillers on final products. Reprinted with permission from (J. Yin & Deng, 2015). Copyright (2015) Elsevier.

The other main property that can be modified by nanomaterials is the glass transition temperature, T_g, and its increase or decrease is subjected by the interaction between the membrane matrix and the NPs (Paul & Robeson, 2008). Among the nanomaterials that change membrane structure are CNTs and nanoclays with aspect ratios from 100 to 1000 (Paul & Robeson, 2008; Sinha Ray & Okamoto, 2003; Tjong, 2006). The mechanical performance of CNTs have shown excellent reinforcement with higher Young´s modulus and tensile strength while both, CNT and nanoclays (including silica), can have changes in T_g < 10 °C at low NP incorporation (below 10 wt. %) (Paul & Robeson, 2008). These casted nanocomposite membranes, also called mixed matrix membranes, have shown enhanced and modified properties, besides the mechanical and thermal, due to the increase in the specific surface areas and the quantum interactions between the polymer and the particles (Goh, Ng, Lau, & Ismail, 2014).

2.2.2 Thin-film Membranes

Thin-film membranes created by interfacial polymerization (TFC's) have advanced the field of membranes in water applications ranging from water desalination to water softening to various industrial water reuse applications. Emerging areas also include addition of nanomaterials (silica, zeolites, etc.) to further improve flux behavior and selectivity. For example, inorganic silica increases the T_g when it is introduced into the thin film, but this silica nanofiller simultaneously increases pore size and porosity of the membrane (Jadav & Singh, 2009). In other applications, zeolite-polyamide and Zn_2GeO_4-polyamide TFN (thin film nanocomposites) membranes, for example, have demonstrated enhanced performance in reverse osmosis (RO) and forward osmosis (FO) applications

(Kurth, Burk, & Green, 2013; Low, Liu, Shamsaei, Zhang, & Wang, 2015; Ma, Wei, Liao, & Tang, 2012).

2.2.3 Functionalization of Commercial Membranes

Nanocomposite membranes can be casted with ready-made nanomaterials, either in the polymer matrix, the top layer (thin-film membrane) or any other combination. Post-manufacture modification on the other hand, relates to a procedure that incorporates various nanomaterials into the structure of a membrane fabricated previously, usually a commercial one. Different methods such as hydrogel functionalization, grafting polymerization or LbL deposition are applied, some of them already discussed in section 2.1 due to their responsive properties. In most cases, these modifications are followed by in situ syntheses or encapsulation of nanomaterials. This feature could give more flexibility in membrane design to fulfill certain applications by tailoring specific particle size and functionalities. Additionally, it allows better conformation and distribution of the nanomaterial, avoiding aggregation, mixing problems and losses. As discussed in section 2.1.2, recent studies use commercial membranes with well-known performance and reliability to incorporate these type of nanomaterials (M. Gui et al., 2013; M. Gui et al., 2015; L. Xiao et al., 2014).

2.2.4 Metal and Metal Oxide Immobilized Membranes

Conventionally, inorganic particles are used to increase the selectivity and improve the porous structure and mechanical strength of the membrane. These particles prevent the formation of macrovoids, forming more connections throughout the membrane structure that gives compaction resistance at high pressures. With the increase in NP synthesis, the

inorganic materials (metal and metal oxides) have provided similar to better mechanical and thermal performances, enhancing or adding other properties such as chemical reactivity, electromagnetic and optical activity and high surface area to volume ratio, with much less material used. To have an idea, in a 5 nm cubic particle almost 40% of the atoms are on the surface with a surface area 4 x 10^6 times greater than a 27 cm cube (Hanemann & Szabó, 2010). Some of these properties enable the nanocomposite membrane to be used in various applications such as catalysis, chemical reduction/oxidation, sorption, sensing, antibacterial activity or hydrophilization (Sarkar, Guibal, Quignard, & SenGupta, 2012).

2.2.4.1 Metal Oxide Nanocomposite Membranes

Metal and metal oxide NPs alone or in combination with carbon-based or silica-based nanomaterials can improve the membrane performance and responsive characteristics, also adding more functionalities (Hanemann & Szabó, 2010; Vatanpour, Madaeni, Moradian, Zinadini, & Astinchap, 2012). The most used metal oxides in membranes include alumina (Al_2O_3), magnetite (Fe_3O_4), silica (SiO_2), titania (TiO_2), and zirconia (ZrO_2). Due to its importance in membrane functionalization, silica will be presented in section 2.2.6. These oxides are used principally in polyether sulfone (PES) and cellulose acetate (CA) membranes to increase pore size and hydrophilicity and hence, improving fouling resistance. Figure 2.14 demonstrates higher pure water flux with alumina, titania and zirconia NPs, having similar sizes (175, 135 and 204 nm in average, respectively), with a better performance of alumina NPs regardless that their size is in the middle.

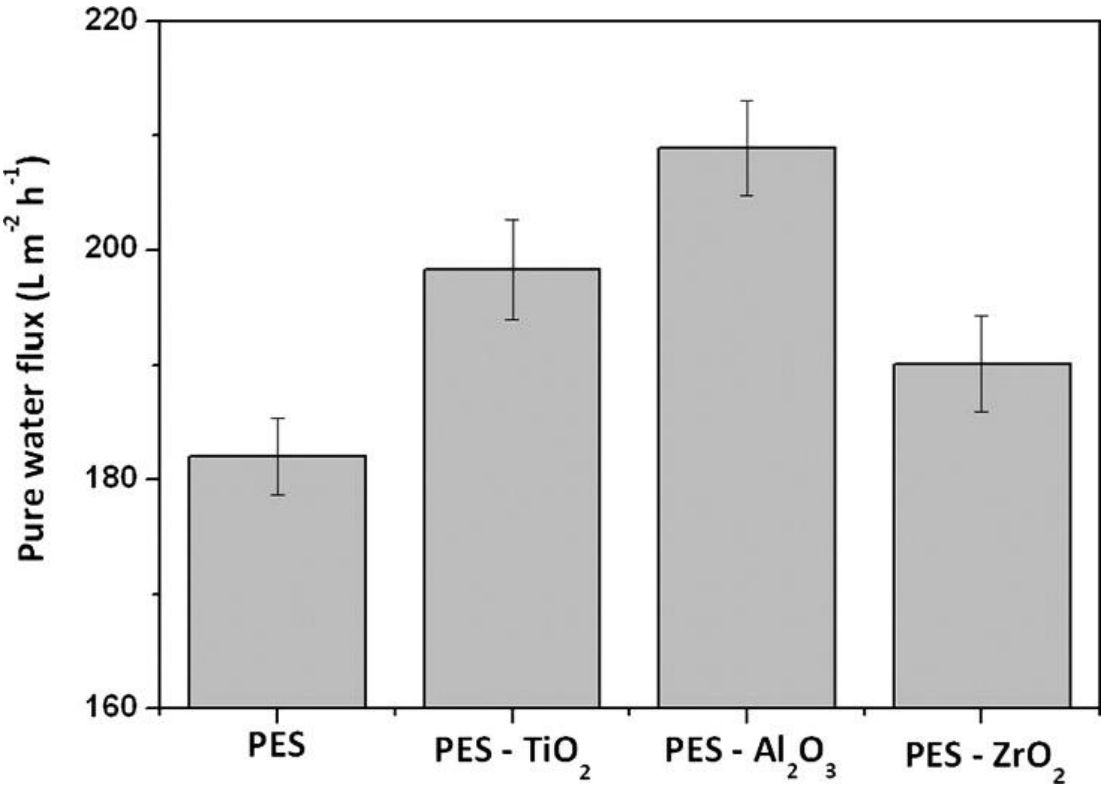

Figure 2.14. Effect of metal oxide loading on the pure water flux in PES membranes. Reprinted with permission from (María Arsuaga et al., 2013). Copyright (2013) Elsevier.

This behavior causes an increment in the contact angle in ascending order: zirconia < titania < alumina (Arthanareeswaran & Thanikaivelan, 2010; María Arsuaga et al., 2013). Alumina decreases membrane thickness by 30-50% and show structural changes from finger-like to sponge-like structure (María Arsuaga et al., 2013; Maximous, Nakhla, Wan, & Wong, 2010).

In PVDF ultrafiltration (UF) membranes, alumina can improve fouling resistance and retain oil and suspended solids, both less than 1 mg/L after filtration. This gives a retention of chemical oxygen demand (COD) and total organic carbon (TOC) of more than 90% (L. Yan, Hong, Li, & Li, 2009). Titania NPs in UF modify the membrane surface, decreases pore size, roughness and unfortunately flux. However, flux decline over time is not as drastic as original UF membranes and can be recovered after a non-chemical wash (Cao, Ma, Shi, & Ren, 2006; María Arsuaga et al., 2013; Oh, Kim, & Lee, 2009). Due to its nature and photocatalytic activity, titania has been suitable for bactericidal treatment in UF, RO membranes and organic degradation of pollutants (Dussan Garzón et al., 2010; Kwak, Kim, & Kim, 2001; Ngang, Ooi, Ahmad, & Lai, 2012; Rahimpour, Madaeni, Taheri, & Mansourpanah, 2008).

Zirconia like alumina, slightly decreases membrane thickness and shows structural changes in membranes (Arthanareeswaran & Thanikaivelan, 2010; María Arsuaga et al., 2013; Maximous et al., 2010). Other metal oxides, like Ag_2O and ZnO in polysulfone (PS) and PVDF, or MnO_2 in PES membranes have similar results to those obtained by the previous discussed. With a very low concentration of Ag_2O NPs (0.001 to 0.1 wt. %), PS membrane surfaces are smoother with improved hydrophilicity, 60% higher pure water flux and 99% rejection of NaCl (Al-Hobaib, AL-Sheetan, Shaik, Al-Andis, & Al-Suhybani,

2015). For PS/ZnO membranes, they have shown changes into a more sponge-like structure, higher hydrophilicity and more closed surfaces. PVDF/ZnO membranes can achieve 100% water flux recovery after physical cleaning with stable flux in long-term operations, doubled water permeability and modify pore structure (Alhoshan, Alam, Dass, & Al-Homaidi, 2013; S. Liang, Xiao, Mo, & Huang, 2012). Hydrous MnO_2 addition to UF membranes of PES improved their antifouling property and increased pure water flux by more than 12 times compared to PES alone, with almost complete flux recovery after a simple wash (Jamshidi Gohari et al., 2014). Additionally, ZnO has anti-electrostatic and antibacterial functions and MnO_2 has also been used in heavy metal adsorption (Jamshidi Gohari, Lau, Matsuura, Halakoo, & Ismail, 2013; T. Xu & Xie, 2003). MgO is other metal oxide that has also been used as a biocidal against Gram-positive and Gram-negative bacteria and spores due to electrostatic forces that bind the bacteria surface (Stoimenov, Klinger, Marchin, & Klabunde, 2002).

2.2.4.2 Silver Nanocomposite Membranes

Pure metal NPs have purposes similar to metal oxide NPs in membranes (hydrophilicity, biofouling resistance, salt rejection). For example, calcium nanocomposite membranes have shown rejections, despite low selectivity, greater than 99% for divalent ions such as Mg^{2+}, Cu^{2+}, Ca^{2+}, Ni^{2+}, Zn^{2+} and Cd^{2+} with permeabilities between 6.7 and 4.9 LMH/bar at pH 6.5. In long-term operations at pH 2.0 (70 hours), lower rejection values ($\approx$ 95% for Ni^{2+}) and constant fluxes were obtained (Qin et al., 2016). Additionally, metal NP implementation provides antimicrobial and catalytic functionalities. Copper, selenium and silver have been studied as antimicrobial agents with Ag being the most documented (Akar, Asar, Dizge, & Koyuncu, 2013; Dasari et al., 2012; Hoek, Ghosh, Huang, Liong, &

Zink, 2011). Table 2.1 shows a small summary of various nanocomposite membrane studies involving silver.

Notably, most research is done in UF, NF, RO and FO membranes with the Ag NPs either added before casting or synthesized in the polymer blend by reduction of $AgNO_3$. The main problem with these applications is silver leaching, as high as almost 90 %, which can decrease or complete eliminate their antibacterial property. In CA-Ag hollow fiber membranes, Ag NPs (0.001 – 0.1 wt. % loading) are synthesized during the spinning by reduction with *N, N*-dimethyl-formamide (DMF) and they were tested in batch mode for bacterial resistance only (Chou, Yu, & Yang, 2005). For poly(acrylonitrile-*co*-acrylic acid)-silver (PAN-*co*-PAA-Ag) membranes, Ag NPs with a loading between 0.07 and 0.35 wt. % were synthesized in the polymer blend by reduction with DMF or $NaBH_4$ before casting (Jewrajka & Haldar, 2011).

Other polymers used are: PVDF functionalized with PAA and subsequent immobilization of Ag NPs, and PVDF with Ag^+ ions exchanged into NaY zeolites (J.-H. Li, Shao, Zhou, Li, & Zhang, 2013; Liao, Yu, Zhao, Wang, & Luo, 2011). Poly(lactic acid) (PLA) containing sepiolite (5 wt. %) functionalized with Ag and Cu NPs (26 wt. % both) (Dasari et al., 2012); polyamide (PA) in RO systems with silver coating on the membrane and/or spacers showing more lasting antimicrobial activity when the NPs are on the spacer; A NF membrane of PA with higher rejection and effective antibiofouling activity on the TFN has also obtained (S. Y. Lee et al., 2007; H. L. Yang, Lin, & Huang, 2009).

Table 2.1. Polymer-silver nanocomposite membrane antibacterial activities and metal leaching. Reprinted from (Hernández, Saad, et al., 2016). Copyright (2016) Elsevier.

Polymeric Material	Nanocomposite fabrication	Antibacterial activity (wt. % of Ag)	Silver Leaching (% of initial loading)	Functionality study	References
CA	Blending – Phase Inversion	≥ 0.005	40	Antibacterial	(Chou et al., 2005)
PAN-*co*-PAA	Blending – Phase Inversion	≥ 0.14	7 – 9	Antibacterial Antifouling	(Jewrajka & Haldar, 2011)
PAN	Phase Inversion – Layer-by-layer assembly	0.01	0.01	Antibacterial Antifouling Permeability	(X. Liu et al., 2013)
PS	Blending – Phase Inversion Phase Inversion – Reduction	0.22-2.0	10 – 40	Antibacterial Antifouling Permeability Antivirus	(Y. Liu, Rosenfield, Hu, & Mi, 2013; Mollahosseini, Rahimpour, Jahamshahi, Peyravi, & Khavarpour, 2012; Taurozzi et al., 2008; Zodrow et al., 2009)
PES	Blending – Phase Inversion	2.0	(73 – 89)*	Antibacterial Antifouling Permeability	(Basri, Ismail, & Aziz, 2011; Basri et al., 2010; Sawada et al., 2012; M. Zhang, Zhang, De Gusseme, & Verstraete, 2012)

CA: Cellulose Acetate; PAN: Polyacrylonitrile; PAA: Poly(acrylic acid); PS: Polysulfone; PES: Polyether sulfone; *Without using polyvinylpyrrolidone (PVP) and 2, 4, 6-triaminopyrimidine (TAP).

Polyacrylonitrile (PAN) on the other side, has the lowest leaching of all membranes due to encapsulated NPs throughout the LbL procedure (X. Liu et al., 2013). PS and PES membranes can be regenerated by addition of NPs recovering their antibacterial property, but silver leaching remains considerably high (Y. Liu et al., 2013; Mollahosseini et al., 2012; M. Zhang et al., 2012; Zodrow et al., 2009). Taurozzi et al. found that these Ag NPs are more effective when they are put into a less porous membrane, which can result in increased permeability with a minor decrease in rejection due to a "macrovoid broadening", as well as larger pore density and pore sizes (Taurozzi et al., 2008). In PES membranes, silver leaching is reduced by addition of polyvinylpyrrolidone (PVP) and 2, 4, 6-triaminopyrimidine (TAP) (57 to 63%) or by grafting acrylamide into the PES polymer chain (Basri et al., 2011; Basri et al., 2010; Sawada et al., 2012).

2.2.4.3 In Situ Synthesis of NPs

Traditionally, most studies related to inorganic NPs are carried out by sol-gel synthesis before incorporating them into the blend before casting the membranes. However, the possibility of in situ synthesis avoids NP aggregation and transmigration, increases membrane selectivity, allows high NP concentration, NP regeneration and possible membrane reuse (M. Gui et al., 2013; X. Li, Sotto, Li, & Van der Bruggen, 2017; Sahiner, Butun, Ozay, & Dibek, 2012; Thomas, Namdeo, Murali Mohan, Bajpai, & Bajpai, 2007; J. Zhang, Xu, & Kumacheva, 2004). For example, due to their magnetic properties, Fe (or Fe/Pd bimetallic) NPs tend to agglomerate rapidly in water (Lu, Salabas, & Schuth, 2007; K. Yin, Lo, Dong, Rao, & Mak, 2012), thus reducing their reactivity. Various techniques have been employed to control particle size, e.g., soluble dispersing agents such as polymers (Feng He & Zhao, 2008; Leng et al., 2009; Lu et al., 2007), surfactants (Y. T.

Wei et al., 2012; B. W. Zhu, Lim, & Feng, 2008) or protective coating (Dong & Lo, 2013; Lu et al., 2007; W. Wang, Zhou, Jin, & Li, 2010).

To achieve this goal in membranes, functional polymers are used to disperse metal and metal oxide NPs by in situ processes. These polymers (hydrogels or microgels) give more properties to the nanocomposite membranes in addition to the ones given by NPs alone. Some of these properties are: chemical and mechanical stability, higher reactivity, selectivity and functionality, regenerability, hydrophilic favorability, and lower costs (Sarkar et al., 2012). As shown in Figure 2.15 and discussed in section 2.1, responsive/functional polymers can be polymerized on the membrane surface to use their functional groups and load metallic water-soluble salts, by ion exchange for example (Stage 1). Then form the desired NPs through exchange reactions (for semiconductor NPs), reducing agents or oxidations (Stage 2) (J. Zhang et al., 2004).

An example of this process is shown in Figure 2.16. Here, hydrogels are immersed in a NaCl solution (5–10 wt. %) at high pH to ionize the carboxyl group (COOH to COO^--Na^+). The next step is an ion exchange using a solution containing Fe^{2+} ions in anoxic conditions at a pH slightly above the pKa of the ferrous salt in order to avoid reincorporation of H^+ ions. The Fe^0 nanoparticle formation (black hydrogel) is then established via sodium borohydride or by other greener chemical reduction (Li Xiao et al., 2012).

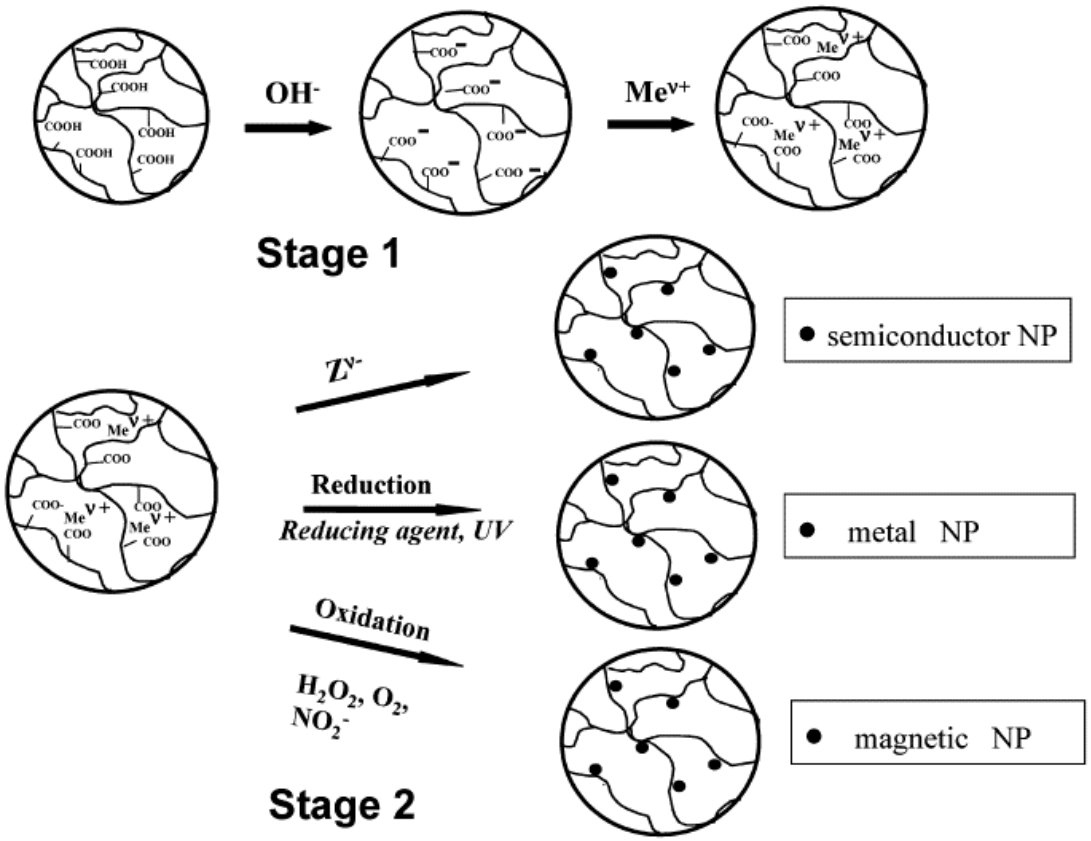

Figure 2.15. Schematic of hydrogel or microgel-based synthesis of semiconductor, metal, and magnetic nanoparticles. Reprinted with permission from (J. Zhang et al., 2004). Copyright (2004) American Chemical Society.

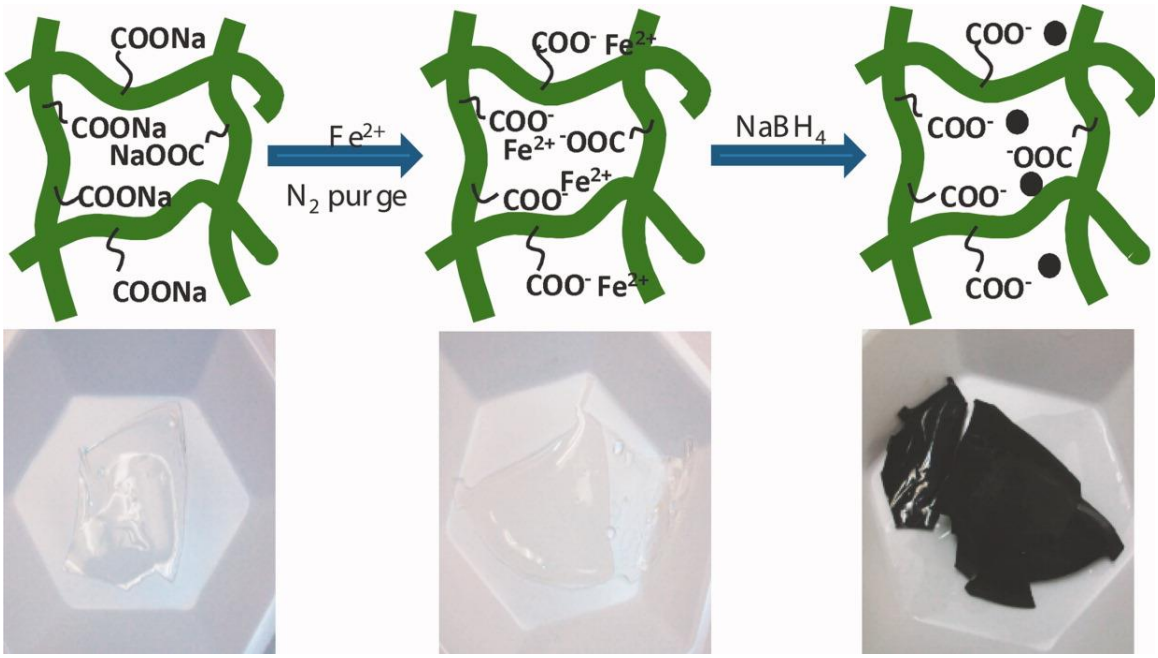

Figure 2.16. Schematic of direct formation of Fe^0 nanoparticles in PAA-*co*-PNIPAm hydrogel network (top) and the corresponding digital images (bottom). Reprinted with permission from (Li Xiao et al., 2012). Copyright (2013) John Wiley & Sons, Inc.

2.2.4.4 Iron and Iron Oxide Immobilized Reactive Membranes

Another commonly used metal in nanocomposite membranes is iron due to its reductive/oxidative and magnetic properties, and because iron is abundant and relatively non-toxic. Iron oxides like other oxides improve the properties previously discussed (Alam, Dass, Ghasemi, & Alhoshan, 2013; Z.-Q. Huang et al., 2008). Additionally, iron oxides like magnetite or ferrite, are used as selective barrier when they are subjected to an electromagnetic field, deforming surface layers and pore structure (e. g. switch "on-off" nanochannels to permeation), as discussed in section 2.1.3 (Csetneki, Filipcsei, & Zrínyi, 2006; Daraei et al., 2013; Jian, Yahui, Yang, & Linlin, 2006).

Iron oxides can be used as adsorbents of metallic ions and for selective degradation of toxic organic compounds. Among the metal ions adsorbed, copper can be removed up to 75% at low concentrations with an additional 85% rejection of copper salt in a PES membrane functionalized with polyaniline/Fe_3O_4 NPs (Daraei et al., 2012). These NPs have additionally shown adsorption of Cr(VI) ions of about 200mg/g (Han et al., 2013); and for the removal of lead, Gholami et al. used Fe_3O_4 NPs too in a NF membrane of polyvinyl chloride/CA with a concentration of about 0.1 wt. % (Gholami, Moghadassi, Hosseini, Shabani, & Gholami, 2014).

Full-scale microfiltration (MF) membranes (PVDF-PAA post functionalized with zero-valent iron/iron oxide NPs) have removed selenium up to 91.4% from pure water, as shown in Figure 2.11B, while from a coal-fired power plant scrubber water, only 21.8% conversion is achieved due to dissolved salts and metal ions interference (M. Gui et al., 2015). Figure 2.17 illustrates the reduction process of metals from their ions (e. g. selenite/selenate) when the membrane module is operated by convective flow.

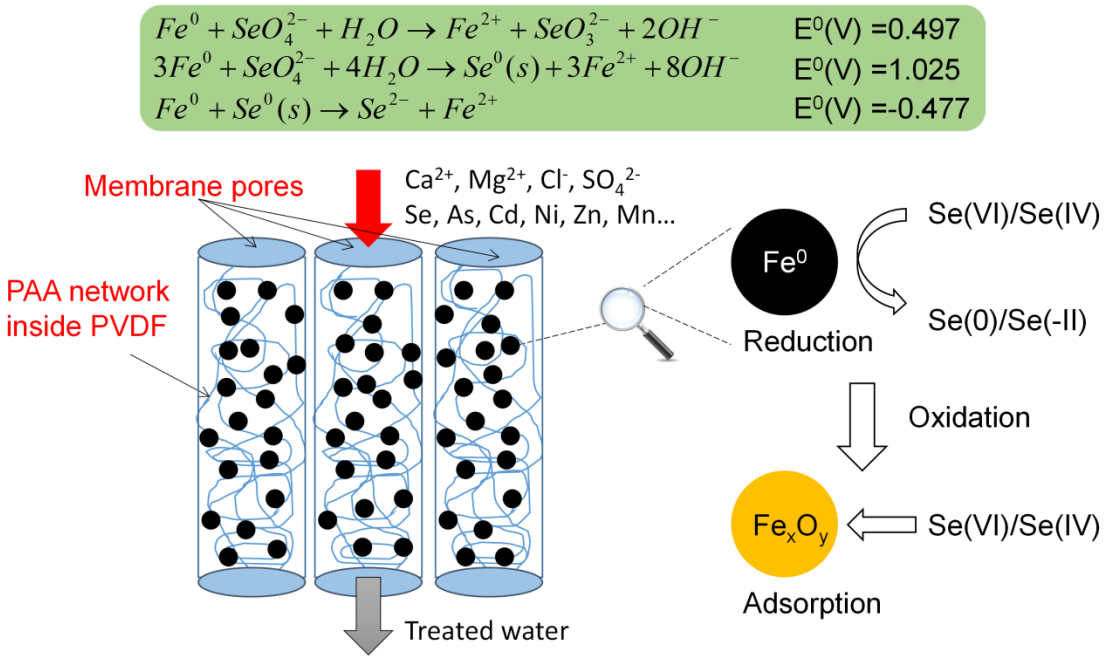

Figure 2.17. Selenium and other toxic metal reduction by iron functionalized membranes. Reprinted from (Hernández, Saad, et al., 2016). Copyright (2016) Elsevier.

The contaminant removal is calculated based on its residence time (τ) in the membrane bulk phase since the flow under pressure makes mass transfer by diffusion negligible (M. Gui et al., 2015):

$$\tau = \left(A_m d \varepsilon_S (1 - \Phi) - {m_{Fe}}/{\rho_m}\right) Q \tag{2.1}$$

where A_m is the membrane top-surface area, ε_S is the porosity of the polymer membrane (without NPs), d is the thickness of the membrane excluding the supporting material, m_{Fe} and ρ_m are the mass and density of loaded NPs in the membrane, Q is the water flow rate. Φ is the gel volume fraction of the functionalized membrane:

$$\Phi = \frac{(W - W_0)/\rho_{gel}}{A_m d \varepsilon_S} \tag{2.2}$$

where W_0 and W are the weights of the membrane before and after functionalization with the hydrogel, respectively and ρ_{gel} is the hydrogel density.

In the degradation of chlorinated organic compounds in water, iron oxide has demonstrated its effectiveness in heterogeneous Fenton reactions (Dussan Garzón et al., 2010; Keenan & Sedlak, 2008). This reaction process takes place on the iron oxide particle surface and is based on the generation of hydroxyl radicals ($OH^{\bullet}$) or ferryl ions (Fe(IV)) in presence of hydrogen peroxide at low to near-neutral pH values. Their reactivity toward TCE oxidation has been investigated in both batch and convective flow. Figure 2.18 shows that depending on the NP loading, H_2O_2 concentration and contact time, a complete oxidation of TCE can be achieved (M. Gui et al., 2013; Minghui Gui et al., 2012b).

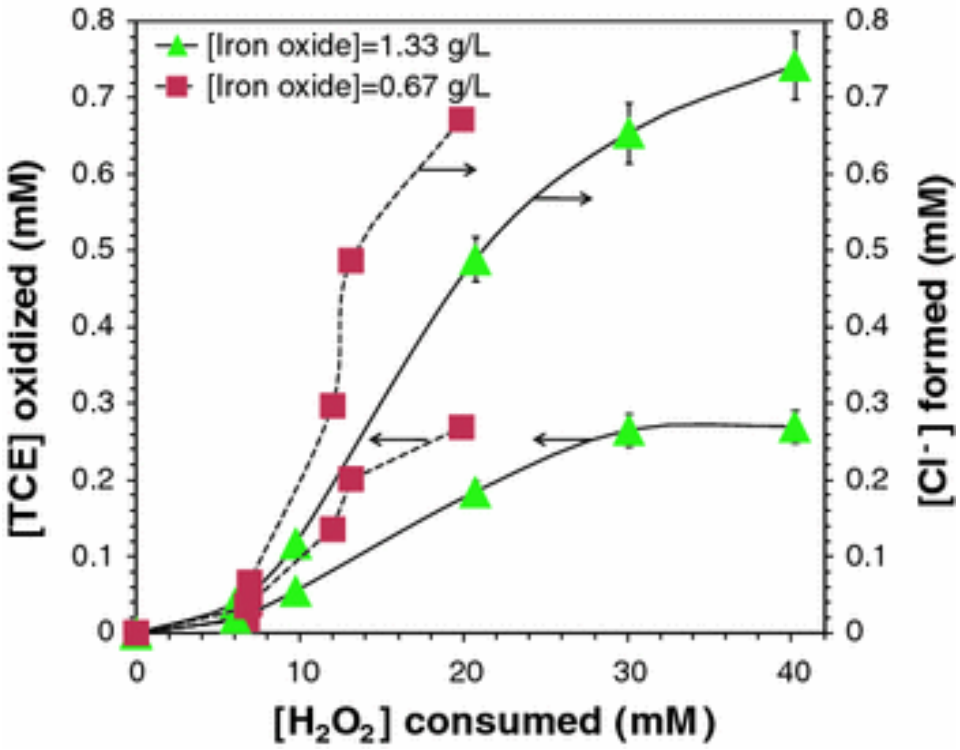

Figure 2.18. TCE decay and chloride (Cl^-) formation with H_2O_2 consumption in the iron oxide/H_2O_2 membrane system. $[TCE]_0$ = 0.270 mM, $[H_2O_2]_0$ = 41.4 mM, total volume V = 20 mL. pH 6.95 at t = 0 and pH 4.6 at t = 48 h. $[Cl^-\ formed]_{max}$ = 0.810 mM. Reprinted with permission from (Minghui Gui et al., 2012b). Copyright (2004) American Chemical Society).

Zero-valent iron and other metal NPs have also been studied and implemented for chlorinated organic compounds through reductive pathways as shown in Equation (2.3) (Crane & Scott, 2012; F. He, Zhao, & Paul, 2010; C.-C. Huang, Lo, & Lien, 2012; Lewis, Smuleac, Xiao, & Bhattacharyya, 2012; H. Liu, Wang, Wang, & Li, 2013; Y. Liu & Lowry, 2006; Y. Liu, S. A. Majetich, R. D. Tilton, D. S. Sholl, & G. V. Lowry, 2005; Thompson, Chisholm, & Bezbaruah, 2010; S. Xiao et al., 2009):

$$mFe^0 + RCl_m + mH^+ \rightarrow mFe^{2+} + RH_m + mCl^- \quad (2.3)$$

with RCl_m as the chlorinated organic compound. For a more rapid and complete reductive dechlorination, a second metal is often added, resulting in creation of bimetallic NPs. In these systems, the former metal (Fe, Mg, Sn, etc.) is an electron donor that generates hydrogen gas via a corrosion reaction to degrade the organic compound, and the latter metal promotes the reactivity through hydrogenation, acting as a catalyst.

Numerous bimetallic systems that are designed to dechlorinate toxic chlorinated organic compounds have been reported in literature, (O'Carroll, Sleep, Krol, Boparai, & Kocur, 2013), including: Fe/Cu (Chun, Baer, Matson, Amonette, & Penn, 2010; N. Zhu et al., 2010), Fe/Ni (Parshetti & Doong, 2009; Tee, Bachas, & Bhattacharyya, 2009) or Fe/Pd (Lien & Zhang, 2007; Nagpal, Bokare, Chikate, Rode, & Paknikar, 2010; X. Wang, Chen, Liu, & Ma, 2008; W. Yan, Herzing, Li, Kiely, & Zhang, 2010; M. Zhang, He, Zhao, & Hao, 2011; B. W. Zhu & Lim, 2007). Among these, the Fe/Pd bimetallic system has emerged as the most efficient and most commonly used system for dechlorination of various chlorinated organics due to its low activation barrier (Lien & Zhang, 2007). These Fe/Pd NPs have been synthesized in PVDF membranes after being functionalized with

non-toxic PAA and PAA-*co*-PNIPAm hydrogels via free radical polymerization to pick up iron (II) and iron (III) by ion exchange. Iron is either reduced with polyphenols from green tea extract (which act as both reducing and capping agents) or $NaBH_4$ (see Figure 2.16) (Lewis et al., 2012). The polyphenol-reduced Fe NPs (20-30 nm) maintained excellent activity and great longevity (Smuleac et al., 2011; Smuleac, Xiao, & Bhattacharyya, 2013). PVDF membranes were in addition modified by surface dehydrofluorination in order to create active double bonds to obtain covalent grafting of PAA onto the membrane surface (L. Xiao, Davenport, Ormsbee, & Bhattacharyya, 2015). Relative to pristine PVDF membranes, covalently attached PAA on dehydrofluorinated membranes (Def-PVDF) cause an increase in permeability from 964 to 1474 LMH/bar. Variations in the solution pH show an effect on both water permeability and solute retention in a reversible fashion.

Fe/Pd NPs immobilized in these membranes show consistent TCE and 2, 2′-dichlorobiphenyl (DiCB) dechlorination (L. Xiao et al., 2015; J. Xu & Bhattacharyya, 2008). The apparent rate constant for the dechlorination reaction can be acquired from Equation (2.4).

$$k_{obs} = k_{sa} a_s \rho_m \tag{2.4}$$

Here, a_S represents the surface area of NPs, k_{sa} is the surface-area-normalized rate constant, reported to have values from 8.1×10^{-4} to 0.15 LMH, (M. Gui et al., 2013; M. Gui et al., 2015; Hernandez et al., 2014; L. Xiao et al., 2015; L. Xiao et al., 2014; Li Xiao et al., 2012; J. Xu & Bhattacharyya, 2007, 2008).

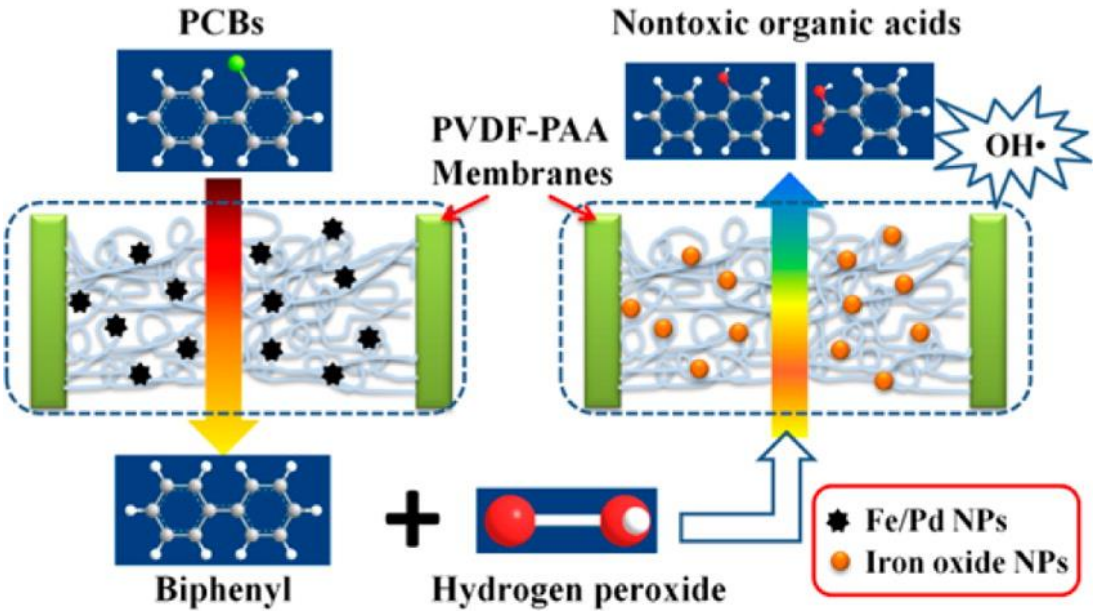

Figure 2.19. Combined PCB degradation scheme by reductive and oxidative pathways using PVDF-PAA membranes with Fe/Pd NPs for the dechlorination of PCBs and H_2O_2/iron oxide NPs for the oxidation of biphenyl. Reprinted with permission from (M. Gui et al., 2013). Copyright (2013) American Chemical Society.

However, the reductive pathway leads to the complete removal of chlorine atoms without ring scission (e.g., PCBs→biphenyl). Therefore, a combined pathway based on the functionalized membranes can be used to convert PCBs into biphenyl, followed by an oxidative treatment to degrade the biphenyl to non-chlorinated degradation products, as shown in Figure 2.19. For oxidative pathway, iron/iron oxide (core-shell system), ferrihydrite and magnetite NPs are synthesized through the controlled oxidation of iron NPs (with air/H_2O_2) (M. Gui et al., 2013).

Iron can also be deposited inside membrane pores by using a diffusion cell to synthesize metal nanotubes with a highly reactive surface area (50 m^2/g). About 95% dechlorination is reached in 1 hour for a metal loading of 1 mg/L Fe nanotubes doped with 2.5 wt. % Pd (Zahran, Prodromidis, Bhattacharyya, & Bachas, 2012). Additionally, PAA and PAA-*co*-PNIPAm hydrogels with Fe/Pd NPs have demonstrated a three-fold increase in TCE degradation reactivity, and reduced the degradation time of DiCB from 6 h to 2 h with Cl^- generation (Hernandez et al., 2014; Li Xiao et al., 2012).

2.2.5 Biomimetic Membranes

Biological membranes that nature offers are more impressive than synthetic membranes, functionalized or not, with higher selectivity, resistance to fouling, and regenerative capabilities, see Figure 2.20. Thus, incorporating bio-structures into synthetic membranes, such as protein channels (porins), CNTs or GO could potentially increase stimulus-responsive behavior, rejection and selectivity while attaining larger fluxes than other highly selective membranes.

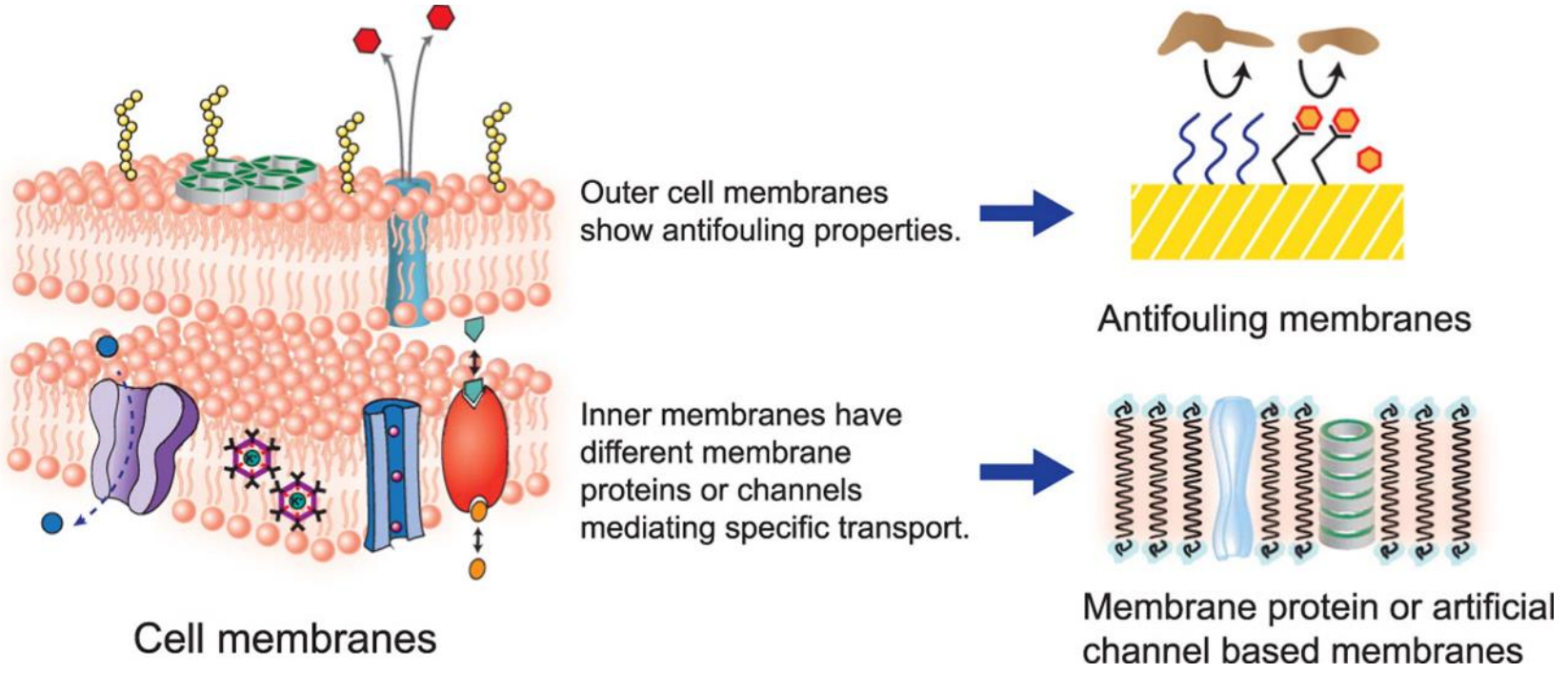

Figure 2.20. Biological membrane separation and antifouling strategies of a gram-negative bacterial organism. The membrane bilayers allow mass transfer of water, gases and solutes by solution diffusion and carrier mediated diffusion. These membranes also have antifouling strategies to prevent unwanted protein deposition on their surface and attachment by other microorganisms. Reprinted with permission from (Y.-x. Shen et al., 2014). Copyright (2014) Elsevier

In the case of porins, among other channels, are transmembrane passive pores conformed by cylindrical β-barrel proteins with a pore going through the middle of their structure (Y.-x. Shen et al., 2014). Some porins are monomers, while others, including the Outer membrane protein F (OmpF), form trimers that come from the outer membrane of Gram-negative *Escherichia coli*.

OmpF are an advantageous choice for the incorporation into membranes for several reasons. It has been shown to have a slight selectivity for cations over anions, although it functions principally as a non-specific port (Kojima & Nikaido, 2013; Nikaido, 1981; Nikaido & Rosenberg, 1983; Nikaido, Rosenberg, & Foulds, 1983; Saint et al., 1996; Schirmer & Phale, 1999). Gross physicochemical properties like size and charge of the solute rather than specific molecular shape and atomic composition dictate how OmpF rejects (Kojima & Nikaido, 2013). With an hourglass shape with ~2 nm diameter at its opening and ~0.7 x 1.1 nm at its most constricted region, the monomeric pores of OmpF could reject charged (large ions, such as nitrates or phosphates) and neutral molecules around this same size, which include sucrose at a hydrated diameter of approximately 1.0 nm (Nikaido & Vaara, 1985). Furthermore, both *in vivo* and *in vitro* studies have revealed OmpF's pH responsive behavior, suggesting changes in pore size at a pKa of 7.2 (Benz, Janko, & Lauger, 1979; Buehler & Rosenbusch, 1993; Schindler & Rosenbusch, 1978; Todt & McGroarty, 1992; Todt, Rocque, & McGroarty, 1992).

Such inherent stimulus-responsiveness including that OmpF are sensitive to magnetic fields, property that could be applied for channel alignment, can be tactful in simultaneous biofilm cleaning and separation of multiple sizes of molecules (Klara et al., 2016). Permeability through the central channel in porins depends on the size and charge

of a molecule. For example, small metabolites can transport through porins but large polysaccharides cannot. To use porins in the construction of artificial membranes, the protein needs to be incorporated with proper alignment and protected from denaturation. The LbL-assembly is potentially a good method for the incorporation of proteins. This technique has shown a 25-fold increase of immobilized biomolecules with insignificant distortion of the biomolecule (Butterfield, Bhattacharyya, Daunert, & Bachas, 2001; Smuleac, Butterfield, & Bhattacharyya, 2006).

Studies thus far on OmpF have been done with entire *E. coli* cell *in vivo* or with porins isolated and immobilized within block-copolymer or lipid vesicles and deposited on porous supports in maintained vesicle form, or ruptured into a lipid bilayers (Kumar, Grzelakowski, Zilles, Clark, & Meier, 2007; Y. X. Shen et al., 2015; H. Wang et al., 2012; M. Wang et al., 2015). However, these vesicles or lipid bilayers have proven to be quite unstable environments that cannot handle the high pressures utilized in industrial processes, like reverse osmosis (RO). Membranes with vesicles containing aquaporins have poorly rejected inorganic salts, with only one research group achieving 98% rejection (H. Wang et al., 2012). Falling short of 100% rejection is likely attributed to defects in the bilayers because the vesicles are not crosslinked together and the porins may not be aligned. Even with perfect block-copolymer or lipid bilayer, protein stability is still a major concern (Werber, Osuji, & Elimelech, 2016). Immobilizing biomolecules within already-existing membrane pores and then crosslinking the charged residues of these molecules could increase mechanical stability and longevity.

On the other hand, CNTs or GO have been incorporated into almost all type of membranes. Other than having antifouling properties, they can selectively separate water

from salt ions and enhance permeability (Das, Ali, Hamid, Ramakrishna, & Chowdhury, 2014; Huiqing Wu, Tang, & Wu, 2014). CNTs can be vertically aligned by addition of other fillers or on a nanocomposite membrane (Figure 2.21).

Both materials present almost no-friction to water flux, showing enhancements in various orders of magnitude compared to RO and with the advantage of lower energy consumptions (Das et al., 2014; Hinds, 2012; Q. Xu et al., 2015). Moreover, it is relatively easy to functionalize the CNTs or GO surfaces with metal and metal oxide NPs and then incorporate them onto a porous membrane surface or onto a TFN. Crumpled GO for example, has been assembled with encapsulated TiO_2 and Ag NPs for enhancing water flux, antifouling (organic and biological), photocatalytic degradation and antibacterial activity (Jiang et al., 2015). On the other hand, TFN membranes were synthesized by interfacial polymerization containing a layer of modified multi-walled CNTs and another layer of Ag NPs that enhanced water permeability and hydrophilicity with simultaneous antibacterial and antifouling capabilities (E.-S. Kim, Hwang, Gamal El-Din, & Liu, 2012). Metal-organic frameworks have also been applied as templates for enhancing porosity and flux (J. Y. Lee, Tang, & Huo, 2014; Sorribas, Gorgojo, Tellez, Coronas, & Livingston, 2013).

2.2.6 Polymer – Silica Composite Membranes

Silica is often considered a nanofiller along with zeolites and metal/metal oxide NPs (Mahajan, Burns, Schaeffer, & Koros, 2002). In fact, SiO_2 NPs are commonly generated in situ through sol-gel techniques mixed with polymers to obtain hybrid nanocomposites, including membranes (W. Chen et al., 2010; Hanemann & Szabó, 2010; X. Huang et al., 2015).

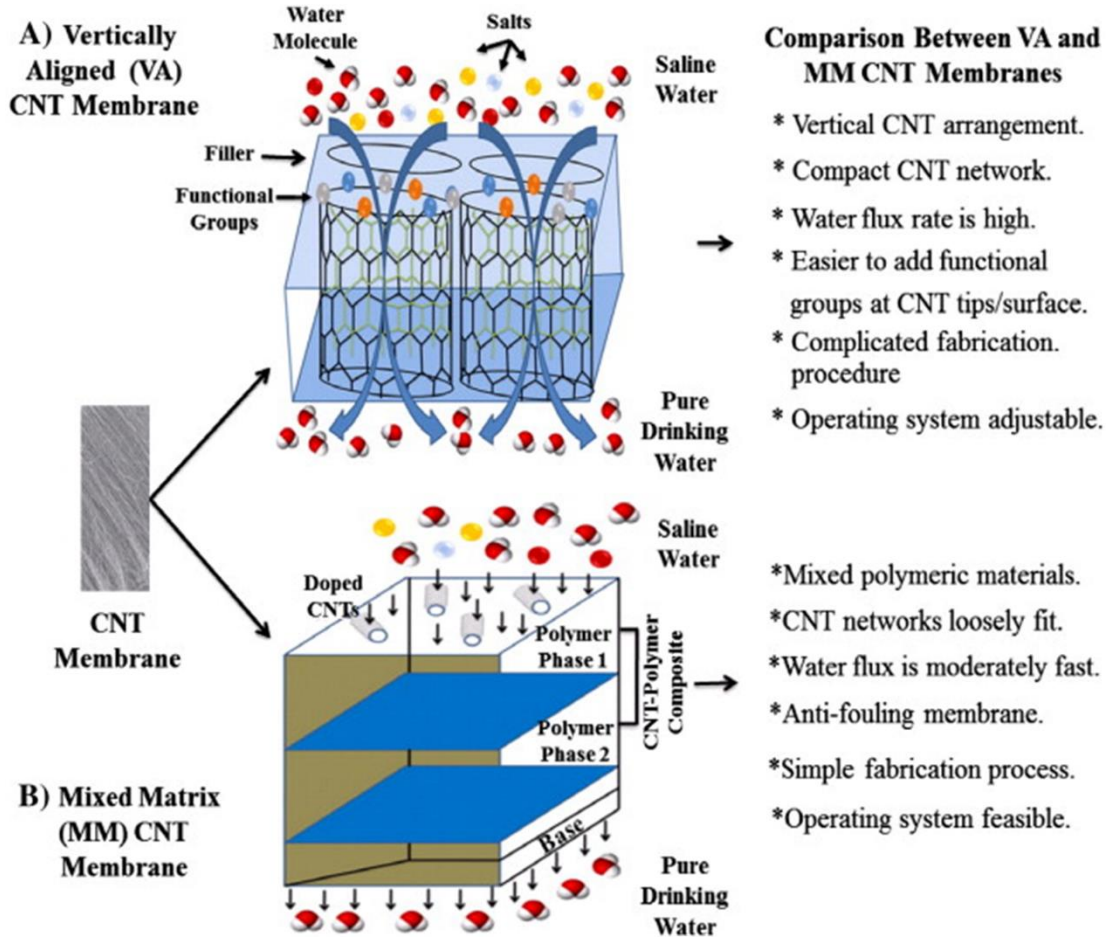

Figure 2.21. A prototype of CNT membrane. Shown are trapping of salts and movement of water molecules from saline water through (A) single-walled CNT, and (B) mixed matrix CNT membranes. Reprinted with permission from (Das et al., 2014). Copyright (2014) Elsevier.

Silica brings about great advantages because it can be used as a flux enhancer and antifouling material (Merkel et al., 2002; M. M. Pendergast & Hoek, 2011; M. T. M. Pendergast, Nygaard, Ghosh, & Hoek, 2010). Layered silicates (nanoclays) have produced nanocomposites with numerous properties, such as mechanical, thermal, tensile, optical, ionic and biocidal (Nigmatullin, Gao, & Konovalova, 2008; Sinha Ray & Okamoto, 2003; Tjong, 2006). Chen et al. also showed the enhanced permeability in CA membranes by in situ synthesis of silica NPs within the polymer blend. Then, the NPs were extracted in the phase inversion process forming the pores and improving membrane permeability (W. Chen et al., 2010). Yin et al. obtained improved results in hydrophilicity, roughness and zeta potential by increasing the concentration of mesoporous silica NPs in TFN membranes. These SiO_2 NPs allowed higher salt rejections of about 64% increase when the silica particles were left inside the membrane (see Figure 2.22a). Even if the silica NPs are non-porous (Figure 2.22c), they have better rejection than when the NPs were removed (Figure 2.22b) (J. Yin, Kim, Yang, & Deng, 2012).

Silica nanofillers have also been used as precursors of ordered mesoporous carbons (OMCs) to increase water permeability simultaneously with a decrease in biofouling (E.-S. Kim & Deng, 2011). Silica also can support metallic NPs in catalyzed reactions, capture metal ions or perform selective separations thanks to the modification of its surface by generation of several reactive sites. This process, called silylation, can be carried out not only in silica, but also in alumina, ferric oxide, titania, and zirconia (Flesch et al., 2005; Lewis et al., 2012; Thomas et al., 2007; Hao Wu, Mansouri, & Chen, 2013; G. Zhang et al., 2013).

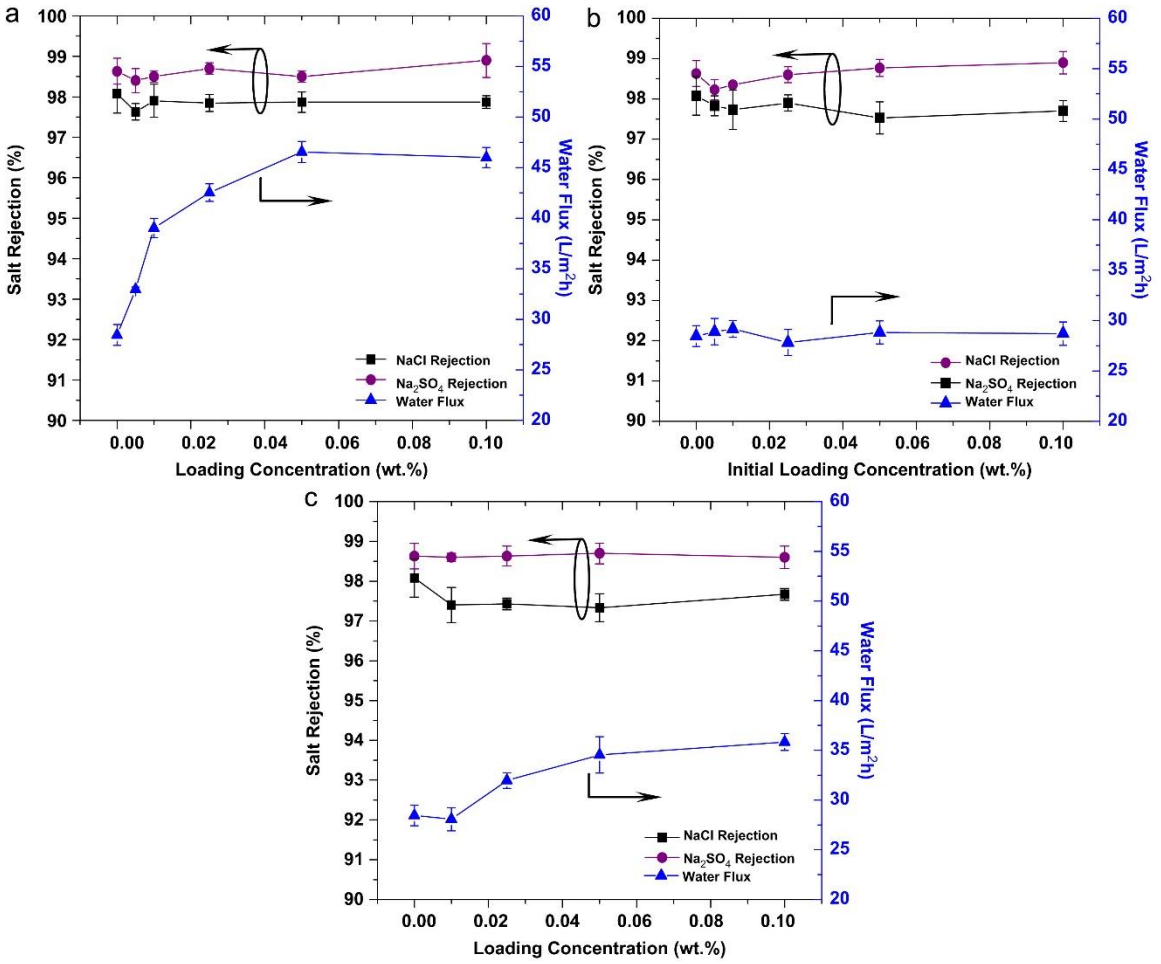

Figure 2.22. Membrane water flux and salt rejection of (a) porous silica; (b) removed porous silica before the interfacial polymerization); and (c) non-porous silica. The experiments were performed on 20.4 bar at 25 °C. Base membrane: polysulfone. Reprinted with permission from (J. Yin et al., 2012). Copyright (2012) Elsevier.

The process is depicted in Figure 2.23; the reaction takes place on the surface of the particle (SiO_2) with a silylating agent previously hydrolyzed (in this case 3-(Triethoxysilyl) propionitrile, TESPN) to form a functionalized SiO_2 NP by condensation of polysilanes (Lewis et al., 2012; Ritchie & Bhattacharyya, 2001). The resulting particles have functional groups that allow different types of functionalization such as NPs synthesis or grafting polymerization.

Within the applications of functionalized silica are the capture of metallic ions in water. Meeks et al. synthesized zero-valent iron and iron oxide NPs in order to degrade TCE via reductive and oxidative processes, respectively (N. D. Meeks, Smuleac, Stevens, & Bhattacharyya, 2012). By performing double ion exchange with NaOH and ferric chloride on modified silica with sulfonated silanes, the particles were formed after reduction with sodium borohydride and subsequent oxidation (see Figure 2.24a). The other method used is employing ascorbic acid as a "green" reducing agent to synthesize bimetallic Fe/Pd NPs (Figure 2.24b). The excess of ascorbic acid prevents oxidation and NP aggregation while it is oxidized (N. D. Meeks et al., 2012).

In other study, mercury and silver are adsorbed almost completely in a PS membrane functionalized with carbon core/silica thin shell NPs containing free-thiol silanes (3.7%) (Noah D. Meeks, Davis, Jain, Skandan, & Bhattacharyya, 2013). In Figure 2.25, convective flow shows high sorption capacity and accessibility due to dispersion of silica NPs within the membrane matrix. (Noah D. Meeks et al., 2013). Similarly, Ladhe et al. functionalized CA and PS membranes with NPs of silica/free-thiol silanes. These groups are more selective to silver ions than calcium or copper with high metal capture capacity (around 2 mmol Ag per g. Silica) (Ladhe, Frailie, Hua, Darsillo, & Bhattacharyya, 2009).

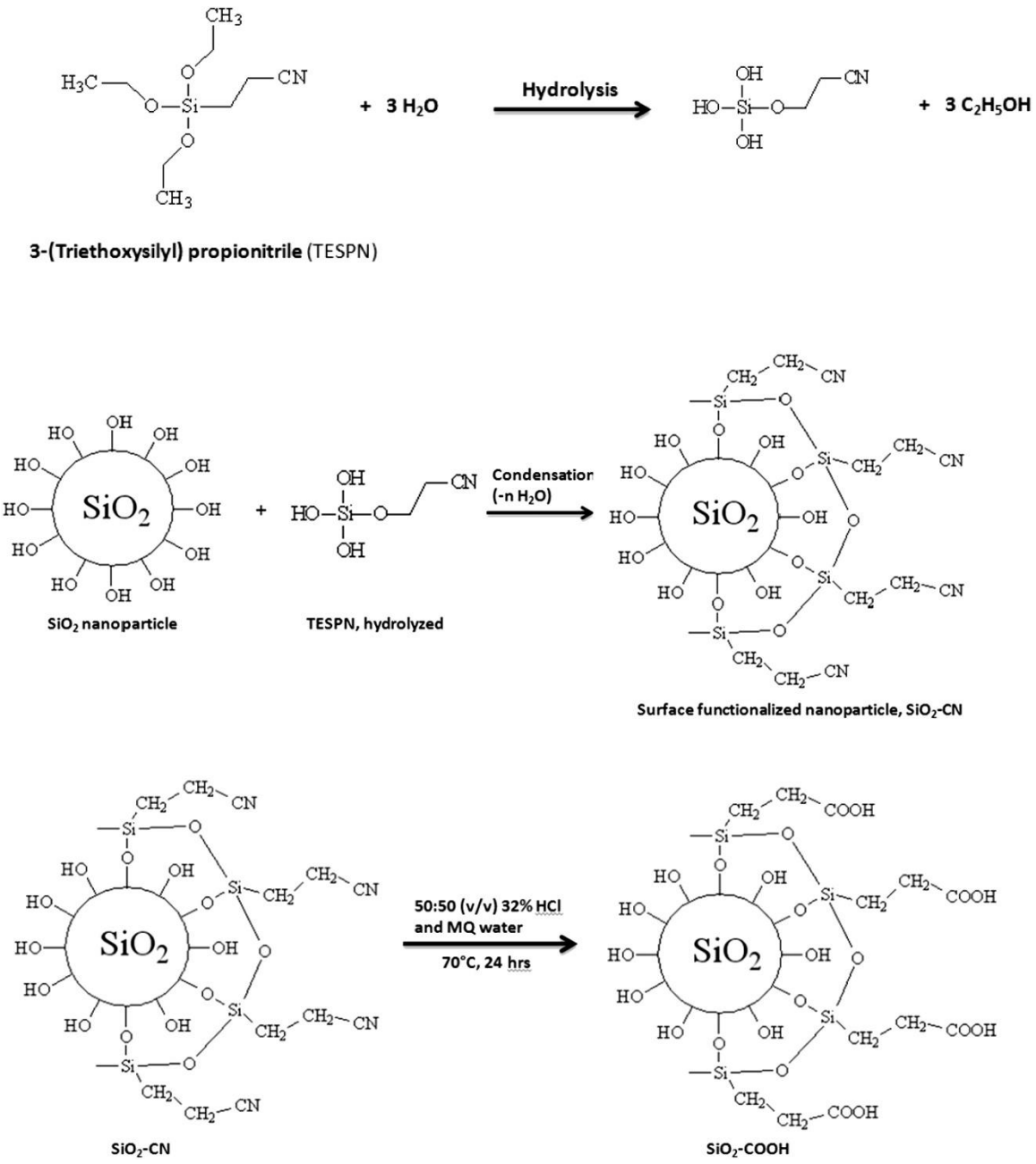

Figure 2.23. Schematic diagram of surface functionalization of SiO_2. Reprinted with permission from (Hao Wu et al., 2013). Copyright (2013) Elsevier.

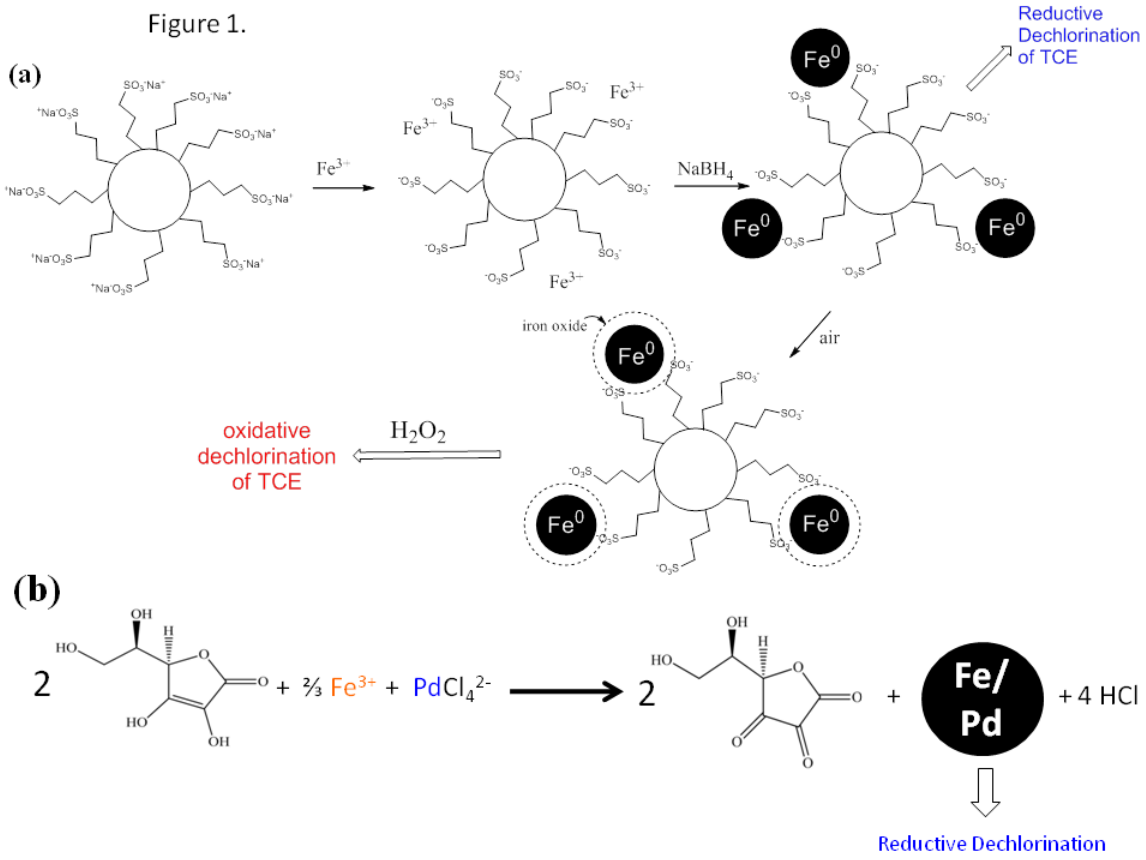

Figure 2.24. Schematic of various Fe and Fe/Pd nanoparticle syntheses. (a) Silica-gel based synthesis of zero-valent iron nanoparticles for reductive dechlorination or iron/iron oxide nanoparticles for oxidative dechlorination. (b) "Green" synthesis of bimetallic particles using ascorbic acid as reducing agent. Reprinted with permission from (N. D. Meeks et al., 2012). Copyright (2012) American Chemical Society.

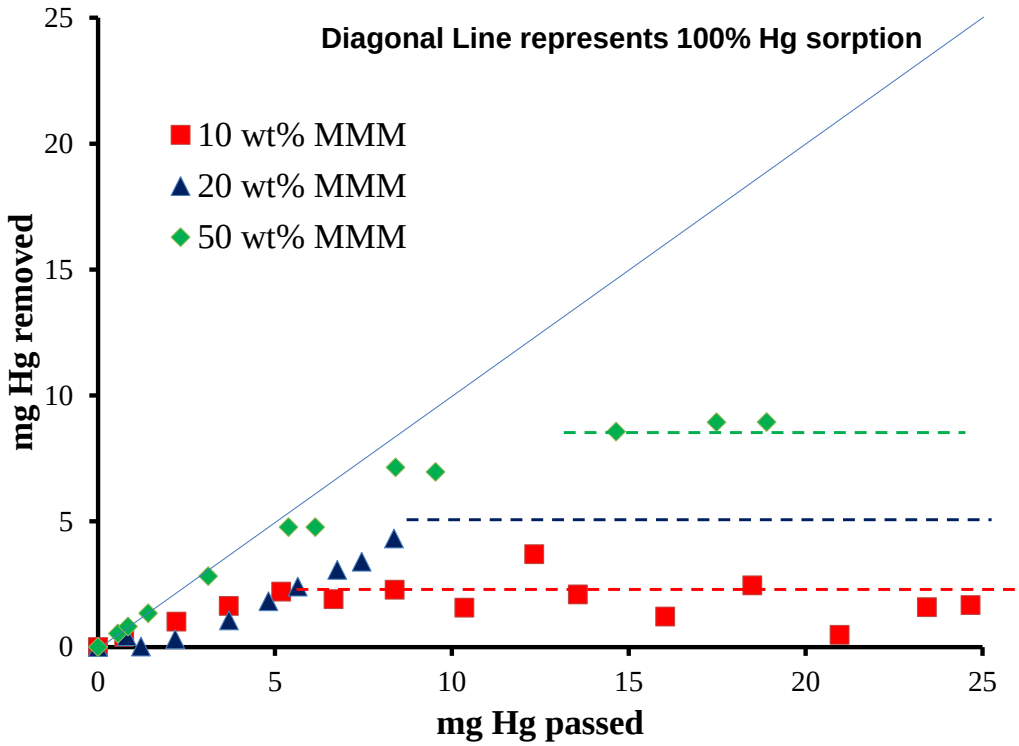

Figure 2.25. Removal of mercury using a mixed-matrix membrane platform (polysulfone/silica). Dotted lines represent maximum mercury capacity of thiol groups for each sorbent loading. Reprinted with permission from (Noah D. Meeks et al., 2013). Copyright (2013) John Wiley & Sons, Inc.

3 MATERIALS AND EXPERIMENTAL METHODS

This chapter describes the materials, membrane functionalization, experimental methods, equipment and set-up used, analytical methods and statistical methods used. Parts of this chapter are published or submitted (Hernández, Lei, Rong, Ormsbee, & Bhattacharyya, 2016; Hernandez et al., 2014; Porter, Hernández, Zhang, Wei, & Bhattacharyya, 2017).

3.1 MATERIALS

All chemicals used in this work were of reagent grade and used as received. Basic materials for all experiments are described first followed by materials for membranes or specific experiments. In all cases, deionized ultra-filtered water (DIUF) was used, membranes surface areas were based on the outer surface (10.9 cm^2 on average) for hollow fiber membranes (HF) and the top surface area (17.3 cm^2) for flat sheet membranes (FS), respectively. The active area of flat sheet membranes was always 13.2 cm^2.

Acrylic acid (AA, 99%), potassium tetrachloropalladate (II) (K_2PdCl_4, 98%), sodium borohydride ($NaBH_4$, 99.99%), 1, 2 dibromoethane (EDB, 99+ %) (Sigma-Aldrich, St. Louis. MO, USA), ammonium persulfate ($(NH_4)_2S_2O_8$) (APS) (EM Science for Merck KGaA, Darmstadt, Germany); ferrous chloride tetrahydrate ($FeCl_2{\cdot}4H_2O$), ascorbic acid (AH_2), trichloroethylene (TCE = 99.9+ %), sodium hydroxide (NaOH) solution, sodium chloride (NaCl), sulfuric acid (H_2SO_4) solution and nitric acid (Fisher Scientific, Fair Lawn, NJ, USA); N, N'- methylenebisacrylamide (MBA or NMBA >99%), isopropanol (IPA, 99.9%) (Acros, New Jersey, NJ, USA).

3.1.1 Membranes and materials used in membrane synthesis

Polyvinylidene fluoride polymer (PVDF) (Solef® 1015, MW = 516,000) (Solvay, France) and dibutyl phthalate (DBP) (EM Science for Merck KGaA, Darmstadt, Germany) for HF synthesis (HPVDF). Polyvinylpyrrolidone (PVP) (MW = 40,000) (Polysciences Inc., Warrington, PA, USA). Track-etched 50 nm polycarbonate membranes (PC50) (Whatman-Tisch Scientific, USA). FS hydrophilized PVDF membranes with 0.65 μm pore size and 125 μm thickness (MPVDF) (DVPP Millipore Corporation). Commercial scale FS hydrophilized PVDF membranes: 0.40 μm pore size and 200 μm thickness, sponge-like (SPVDF) (125 μm PVDF thickness and 75 μm backing), and 50 kDa cut-off (PV200), both produced in collaboration with Nanostone Water, Inc., USA.

3.1.2 Materials for Layer-by-Layer Functionalization

AA 98% extra pure and stabilized, MBA for electrophoresis, 99+% (ACROS ORGANICS, France and Belgium, respectively); potassium persulfate (KPS) (EM SCIENCE, Germany); poly(allylamine hydrochloride) (PAH) (ALDRICH, Japan); poly(styrene sulfonic acid) (PSS), M.W. 75,000, 30% w/v aq. sol. (Alfa Aesar, USA); purified OmpF from E. coli;

3.1.3 Materials for OmpF Extraction

E.coli BL21(DE3) (NEB, USA); Valeric Acid (99%); Coomassie blue R-250, Ammonium persulfate (APS) (Sigma-Aldrich, USA); sodium dodecyl sulfate (SDS), polyacrylamide, Tris-HCl, N,N,N′,N′-Tetramethylethylenediamine (TEMED) (Bioworld ,

USA); ethanol (95%), acetic acid (glacial) (VWR, USA); protein marker, bicinchoninic acid (BCA) assay (Thermofisher, USA).

3.2 EXPERIMENTAL METHODS

The procedures made to most of the membranes are depicted in Figure 3.1 and described next. Some variants of this process are described in further sections such as the hydrophilization of HF membranes, the functionalization by redox polymerization, and the layer-by-layer (LbL) functionalization, etc. All the quantities are molar percent based on the amount of monomer, unless it is indicated. All measurements were done by triplicate, calculating the respective deviations and standard errors of the means.

3.2.1 General Membrane Functionalization and Nanoparticle Synthesis

The membrane functionalization is made by free radical polymerization of AA (monomer) in the PVDF porous surface by dipping or using vacuum to partially pull the monomer solution through the membrane to ensure pores were completely filled: AA (10 or 20 wt. % aqueous solution), MBA as cross-linker (1.0 mol % of AA) and APS or KPS as initiator (1.0 mol % of AA). Membranes were sandwiched and clipped between two plastic sheets and two Teflon or glass plates at 70-80 °C for 1 h in a N_2 atmosphere (M. Gui et al., 2013). After this, the membranes were washed several times with DIUF, dried and weighed.

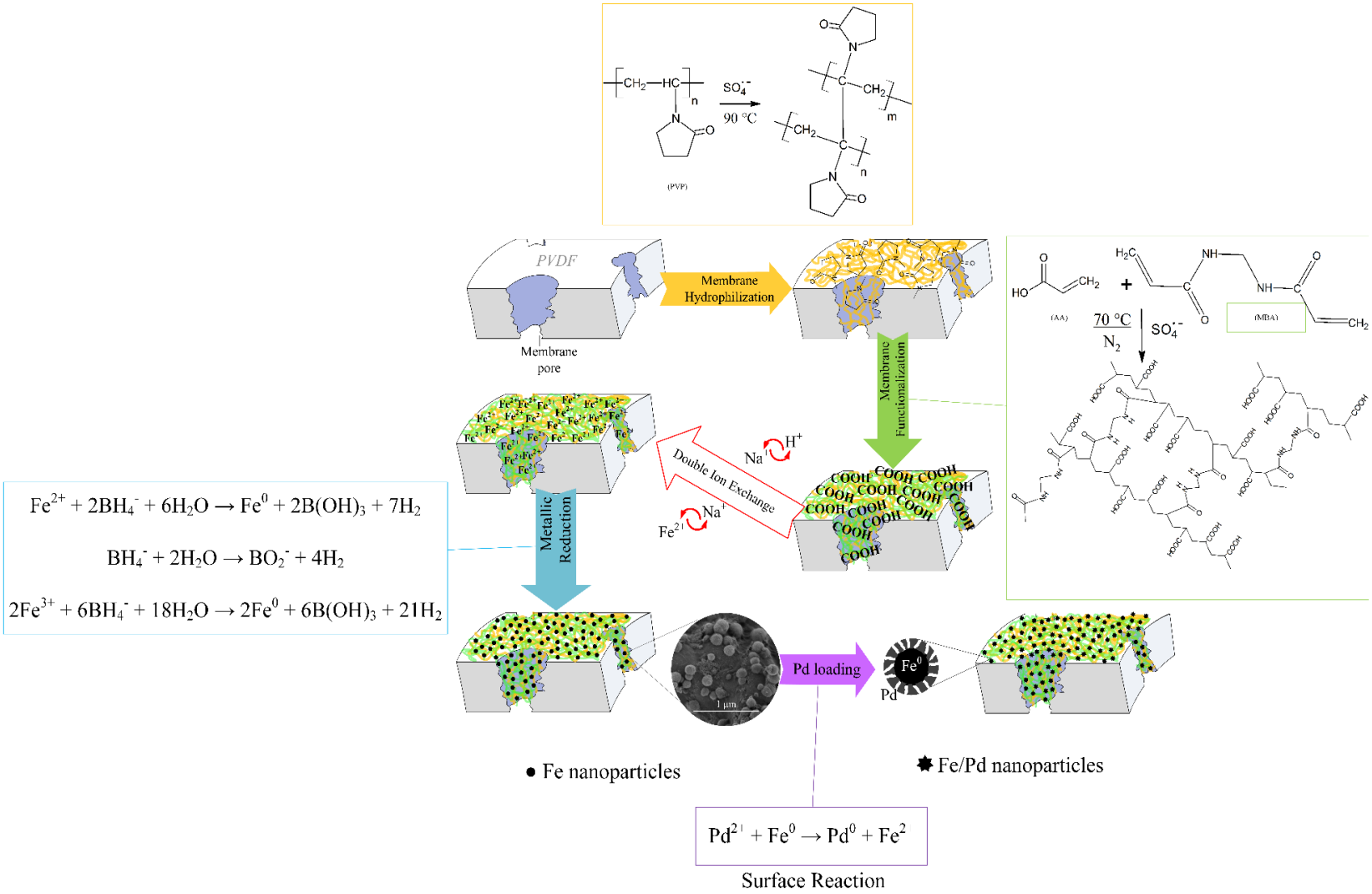

$$Fe^{2+} + 2BH_4^- + 6H_2O \rightarrow Fe^0 + 2B(OH)_3 + 7H_2$$

$$BH_4^- + 2H_2O \rightarrow BO_2^- + 4H_2$$

$$2Fe^{3+} + 6BH_4^- + 18H_2O \rightarrow 2Fe^0 + 6B(OH)_3 + 21H_2$$

$$Pd^{2+} + Fe^0 \rightarrow Pd^0 + Fe^2$$

Figure 3.1. Hydrophilization, functionalization and nanoparticle synthesis of PVDF hollow fiber and flat sheet membranes. Adapted from (Hernández, Saad, et al., 2016)

The next step is a double ion exchange as follows: the functionalized PVDF-PAA membranes were put in an alkaline solution (1 g/L of Na; pH ≈ 10.5; T ≈ 22 °C) to exchange the protons of the carboxylic groups from PAA by sodium ions. When the pH is constant and similar to the NaCl alkaline solution, the membrane samples are washed with DIUF and put in a solution of $FeCl_2 \cdot 4H_2O$ (200 mg/L of Fe; pH ≈ 4.6; T = 22 °C).

After the ion exchange with $FeCl_2 \cdot 4H_2O$, the membranes were put in a solution of $NaBH_4$ in excess (2.5:1 molar of $NaBH_4$ to Fe) to reduce the iron from Fe^{2+} to Fe^0, forming the NPs as showed in Figure 3.1 (Feng He & Zhao, 2008; J. Xu & Bhattacharyya, 2007). This procedure was also done in solution for comparison purposes. To increase faster reaction performance, post-coating with palladium, in concentrations between 1 to 5%, is applied using K_2PdCl_4 to form bimetallic Fe/Pd NPs (Smuleac et al., 2010b; Smuleac et al., 2011). Palladium is used to create a layer on the iron that increases the reactivity and reach a complete reduction of the model pollutant, avoiding intermediate products.

Fe/Pd NPs in solution phase were prepared in concentrations between 0.4 and 0.5 g/L in 20 mL of DIUF water with 0.5 wt. % of CMC. Fe^{2+} was reduced by adding $NaBH_4$ to the solution.

3.2.2 Hollow Fiber Fabrication and Hydrophilization

One of the main approaches for preparation of PVDF microporous membranes is TIPS. The homogeneous solution was formed by dissolving 30 wt. % PVDF polymer in DBP at 170 ºC. The polymer solution and DBP as inner coagulant were pumped into a spinneret by gear pump and syringe pump, respectively. The phase separation of homogeneous solution was induced by cooling down the exiting HF (HPVDF)

membranes in a 5 cm air gap followed by quenching in a water bath at 10 ºC. After the solidification of polymer-rich phase, the morphology of porous membrane structure can be created by extraction, evaporation or freeze-drying.

HPVDF membranes were fabricated without any addition of a hydrophilizing material. For this reason, the HPVDF had to be modified with PVP in order to use them in aqueous phase, see Figure 3.1. The membranes were treated in this study based on the results found elsewhere (Bi, Li, Tian, Lin, & Wang, 2013). The membranes were washed with IPA for 2 h, then washed with (DIUF) several times and finally put in an aqueous solution containing PVP (5 wt. %) and APS (0.4 wt. %) at 90 °C for 6 h with constant stirring.

3.2.3 Hydrogel Synthesis and Membrane Functionalization from Redox Polymerization

In this process, 5 g of AA was mixed maintaining constant stirring in 20 mL of DIUF with MBA (1.0%) and $(NH_4)_2S_2O_8$ (1.0%). $FeCl_2{\cdot}4H_2O$ (1.0%) and AH_2 (1.0%) were added in 20 mL of deoxygenated DIUF. The polymerization is performed through a redox reaction of ferrous ion and AH_2: accelerants and reductants, respectively, with persulfate ion (initiator/oxidant) (Misra & Bajpai, 1982; Sarac, 1999). This method started at room temperature (22-25 °C) and is exothermic, unlike the general method described previously. The pH is also a variable in the polymerization process, lower values (pH 2.0 to pH 6.0) are recommended using sulfuric acid or in this case, the monomer to control it. In this polymerization process the pH was 3.0. Figure 3.2 serves as explanation of the redox polymerization and the membrane functionalization.

The oxidant/reductants ratios of $S_2O_8^{2-}$: Fe^{2+}: AH_2 are 2:1:1 making the amount of iron selected suitable for polymerization (Fordham & Williams, 1951) and simultaneously, the concentration of iron has to be the highest possible for direct NPs synthesis. The reaction with AH_2 is well known in redox polymerization by itself or using different metals, including iron (Sarac, 1999). The combination of this two reducing agents increase the rate of polymerization making the AH_2 and the Fe^{3+} ion a redox pair, generating more initiating radicals. MPVDF membranes were soaked in the monomer solution while bubbling Nitrogen in it for about 30 min. Each membrane was put on a flat surface and sprayed with the initiator solution to begin the polymerization. For the hydrogel alone, the initiator solution was dripped on the monomer solution with constant stirring. Selected membranes and part of the hydrogel were washed with DIUF to eliminate the unreacted material of the product and dried for 12 h. or until having constant mass for posterior ion exchange. The temperature of the reaction in the membranes was not controlled assuming the values of the solution reaction.

The Fe/Pd NPs were synthesized in the PAA xerogel (dry hydrogel) and the MPVDF-PAA membranes from the redox polymerization by two methods: first, the same method described previously of double ion exchange and reduction by $NaBH_4$, followed by Pd coating. Second, the addition of $NaBH_4$ solution without ion exchange causing a direct NP synthesis from the iron added as accelerant in the polymerization.

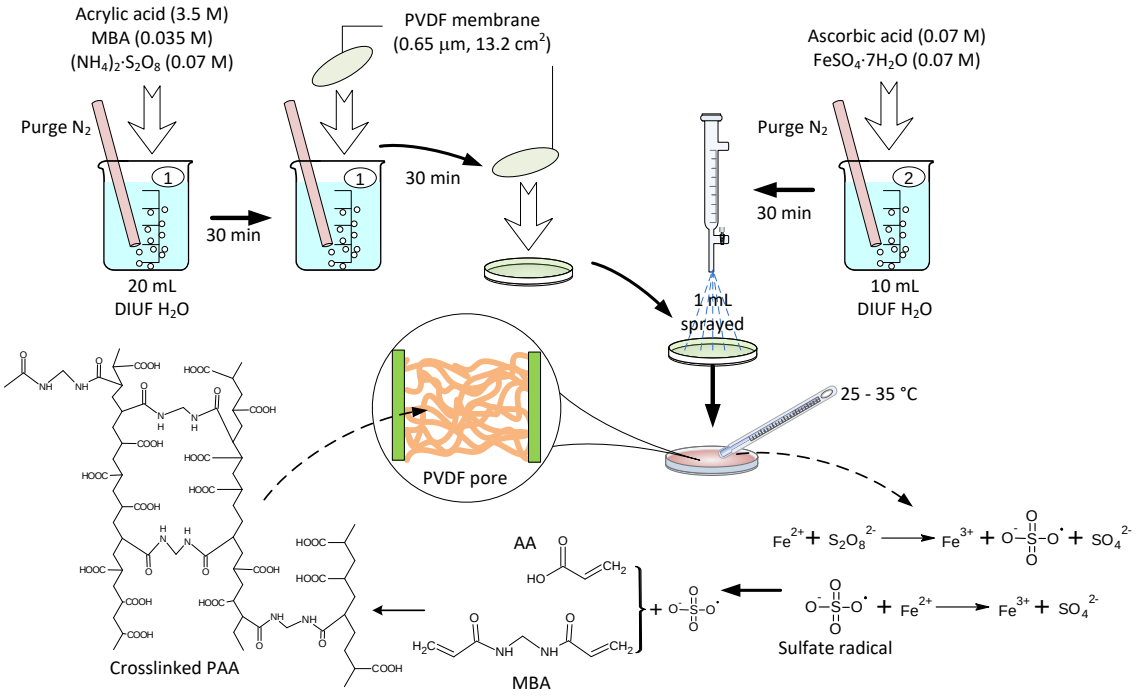

Figure 3.2. PAA-Hydrogel synthesis and functionalization of MPVDF membrane by a redox polymerization of AA and MBA. Adapted from (Hernandez et al., 2014).

3.2.4 Dechlorination Experiments

Fe/Pd NPs reactivity in hydrogel and membrane domain was determined by batch reaction with TCE. TCE solution is prepared by adding TCE liquid in deoxygenated DIUF water to make a solution of 30 mg/L of TCE.

Batch experiments were conducted at 22-25 °C and pH = 6.0 in 20 mL (24 without headspace), 40 mL (43 without headspace) and 120 mL vials, for membranes in the first two and hydrogel in last, in a shaker at 300 rpm. Functionalized membranes and a known weight of xerogel-NPs amount were soaked separately in the TCE solution and samples of liquid were collected at different time lapses with N_2 venting. The reason to make batch experiments is due to the high volatility of the TCE, which causes readings of erroneous (faster) reaction rates. The reaction was stopped by removal of the membranes. The membrane and aliquots of the solution were taken for TCE extraction with equal volume of pentane, containing EDB as internal standard to use in gas chromatography. This extraction takes about 2 h. Control experiments (no NPs) were also completed.

3.2.5 Layer-by-Layer Functionalization

Before OmpF were immobilized within the PVDF membranes, two layers were put within the PVDF membranes: the first layer was the previously described in situ free radical polymerization of PAA hydrogel. However, due to the tightness of the membrane (discussed in Chapter 4), the monomer: solvent (DIUF) ratio was changed to 1:10 by weight (1.26 M AA). The concentrations of KPS and MBA were not changed (1 mol % of AA, each). To prevent premature polymerization, KPS was separately dissolved in half of the DIUF used, then combined with the monomer solution right before soaking membranes

for 10 minutes. Figure 3.3 represents the entire LbL assembly to OmpF immobilization process.

The second layer was a solution of PAH. A 0.2 M NaCl solution was prepared with two-fold molar excess of PAH with respect to the immobilizaed PAA. The pH of the PAH solution was adjusted to ~9.0 using NaOH to deprotonate the PAA in order to bond the amine groups of PAH to the COO^- groups. The PAH solution was permeated twice for full polymer pickup.

For the OmpF immobilization, a frozen OmpF solution (2.3M valeric acid) containing 51.4 µg/mL of protein, was thawed to room temperature and filtered through a cellulose membrane syringe filter with average pore diameter of 200 nm to remove any remaining cell debris. Before diluting it with water, 5 mL of additional valeric acid were added to the purified OmpF solution to prevent excessive aggregation. For a total volume of 100 mL, 93 mL of DIUF water were added. pH was raised to 5.5 with the addition of NaOH to improve miscibility of valeric acid in water, observed through increased clarity of solution. OmpF solution was sonicated to reduce aggregation and permeated twice through the PVDF-PAA-PAH membrane at 6.8 bar for 5 hours and at 9.5 bar for 5.5 hours.

The final top layer of PSS was permeated through the membrane, one after the PAH layer and the other after OmpF immobilization for comparison. 25 mL of DIUF containing PSS repeating units equal to COOH groups was prepared. The PSS had a chain length of 721 repeat units long. The solution was passed twice, at 10.2 bar and pH = 6.0. A slightly acidic pH renders OmpF's extracellular loops to be overall positively charged, which will have affinity with the carboxylic groups in PSS.

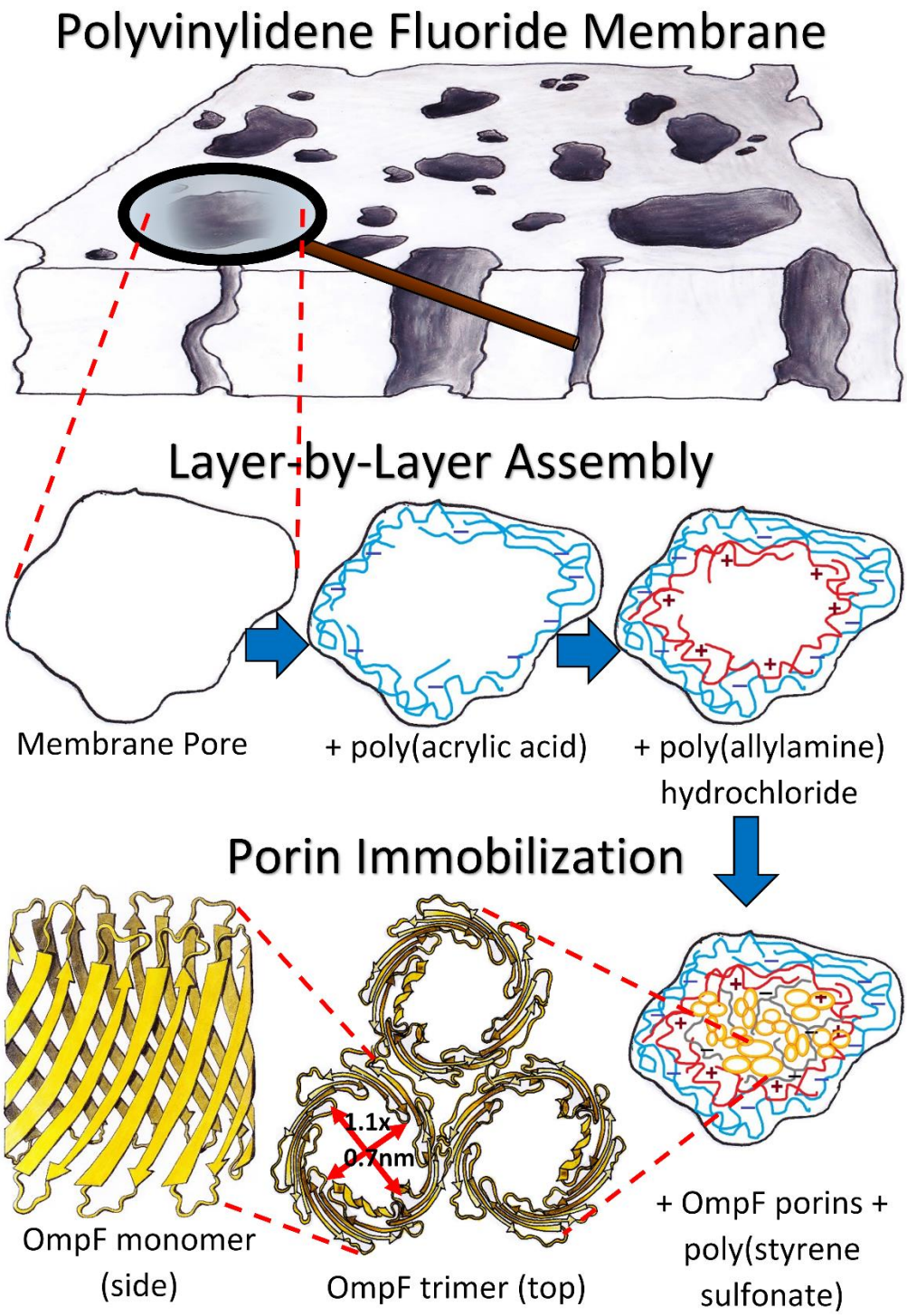

Figure 3.3. Schematic of layer-by-layer assembly process of polyionic polymers into a PVDF membrane and subsequent immobilization of OmpF. Reprinted from (Porter et al., 2017).

3.2.6 OmpF Solution Purification

Normally, membrane protein purification consists of various steps: culturing cells, cell lysis, protein extraction and purification through chromatography (Holzenburg et al., 1989; R. Taylor, Burgner, Clifton, & Cramer, 1998; Yoshimura, Zalman, & Nikaido, 1983). Studies have shown that porin trimers are stable in detergents and organic solvents due to the hydrogen-bonding, electrostatic, and hydrophobic interactions between each subunit (Garavito & Rosenbusch, 1986). Thus, to largely improve the efficiency of the purification process for OmpF, a method to rapidly extract membrane protein was developed. The procedure used was a modification from Arcidiacono et al. (Arcidiacono, Butler, & Mello, 2002). This method that uses a single step extraction is depicted in Figure 3.4. *E.coli* BL21 (DE3) were cultured in LB medium overnight. Harvested cells were centrifuged at 8000 rpm for 10 min, then frozen at -80 ℃ and lyophilized (Labconco Freezone 12). The lyophilized cells were ground to powder and 2 mL of valeric acid per gram of the powdered cell were added, followed by three fold of deionized water to get a concentration of 2.3 M valeric acid. The mixture was stirred at room temperature for 1 hour. Finally, the mixture was clarified by centrifugation at 20,000 g for 30 min. Through this method, the product contains OmpF as high as 76% of total protein (Arcidiacono et al., 2002).

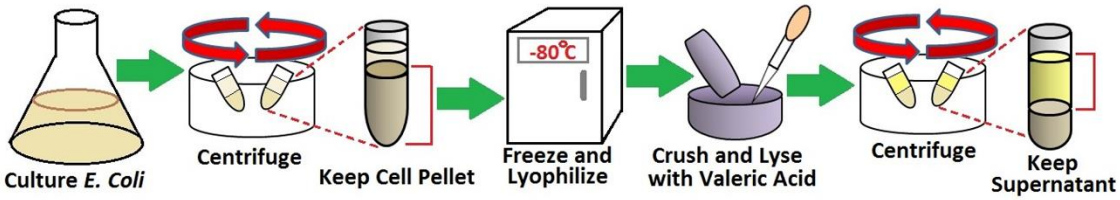

Figure 3.4. Schematic of the extraction process of OmpF from *E. coli*. Reprinted from (Porter et al., 2017).

3.2.7 Flux Rejection and Selectivity Studies

For each layer of assembly, permeability was measured in a dead-end batch cell (Sterlitech HP4750) at 3.4 bar with DIUF at pH = 7.0 to surpass the pKa of functional polymers, see Figure 3.5. Values of ζ potential (Anton-Paar Surpass Electrokinetic Analyzer) were used to quantify changes on surface charge. Depending on the functional groups present on the membrane surface, the ζ potential would significantly vary, rendering it as a method to verify proper functionalization of each layer. All runs started at a pH≈5.2 with a solution of 0.05 M KCl and target pressure of 300 mbar; the gap between mounting platforms was adjusted to reach this pressure. First, an acidic measurement for a given sample was taken using HCl to adjust the pH gradually lower than 5.2. The process was repeated for basic measurements using NaOH for gradual adjustment above the starting pH. Acidic pH's were tested separately from basic to avoid reaching large ionic strength of passing solution. Acidic and basic measurements were combined for each membrane type.

Other verification technique for layers was changing pH of water from 8 to 3 for both PVDF-PAA and PVDF-PAA-PAH. The different pH solutions were allowed to pass until flux reached a steady state. Between passes, the membrane was washed with DIUF water for approximately 30 min, ensuring ions are removed before the next pass at a different pH. Each pH sample was fluxed three times (cycles) to ensure stability of the layers.

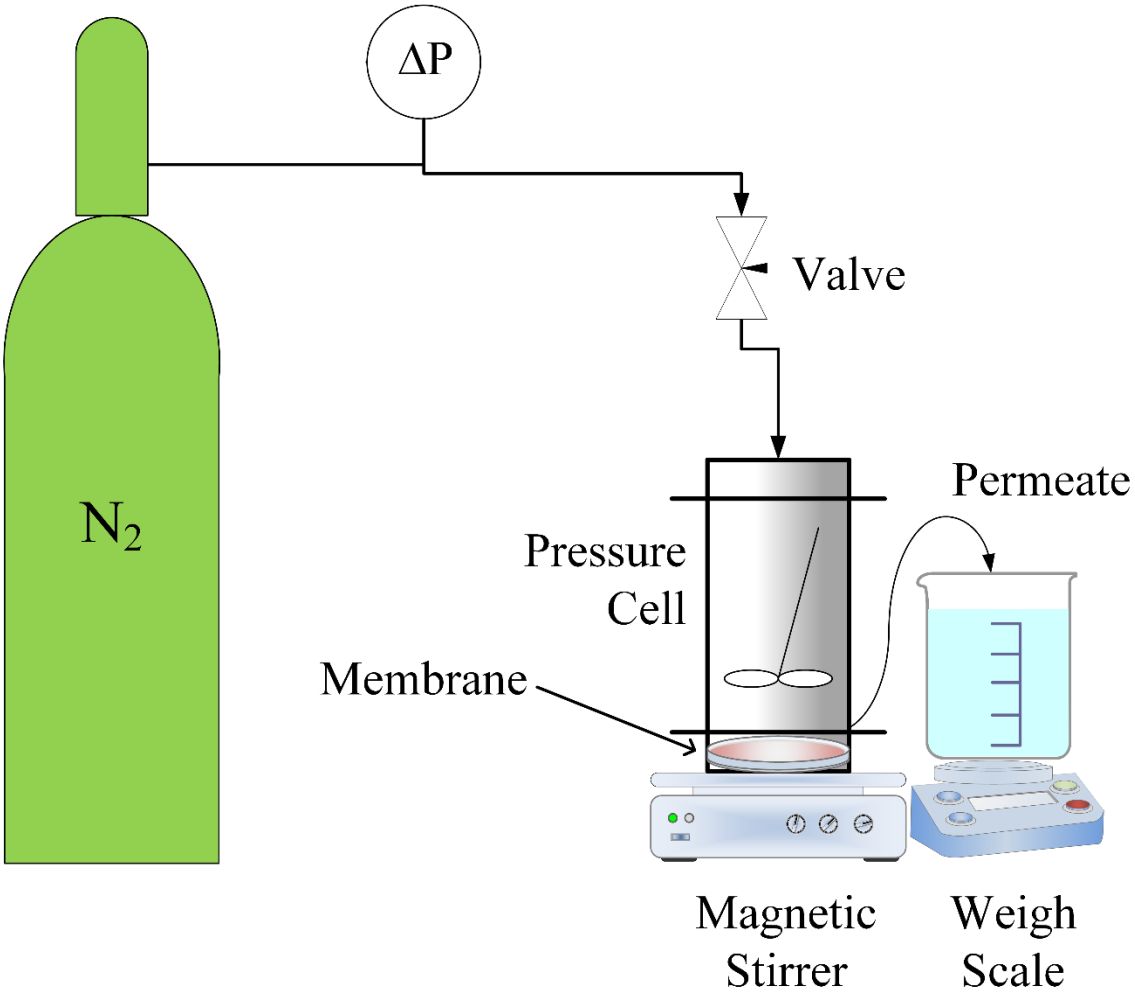

Figure 3.5. Set up of dead-end batch cell for LbL functionalization and selective separation tests.

The membrane throughout functionalization was tested for its rejection of salts and uncharged molecules (organic), as well as for pure water through each layer. Testing rejections of uncharged molecules gives an indication of the rejection capabilities based solely on size and thus indicates the size of pores. Testing rejections of uncharged molecules gives an indication of the rejection capabilities based solely on size and thus indicates the size of pores. At 3.4 bar, mixture solutions containing one uncharged molecule (glucose, sucrose, or polyethylene glycols) (PEG 400 and PEG 1000)) and one salt (NaCl or $CaCl_2$) were passed through the membrane after each layer of assembly to demonstrate selectivity. Passes were conducted at pH = 6 in pure DIUF water to avoid effects of additional ions.

Membranes containing OmpF should significantly reject molecules around the size of sucrose and larger while allowing the permeation of small ions. The aforementioned solutes plus Dextran Blue 5000 and Dextran 41000 mixture solutions were used in rejection cycles with the OmpF membrane. Here, one cycle consisted of passing all six model organic solutes, with DIUF permeation through the membrane between each cycle. Three cycles were performed to prove consistent results between rejection and stability. Due to reported functionality of OmpF at varying pH, rejection and flux were also measured at pH between 3 and 10 and compared to the non-OmpF membrane pH functionality.

3.2.8 Polycarbonate Membranes Studies

As a method of control, track-etched polycarbonate membranes (PC50) were used to investigate the necessity of LbL assembly for OmpF immobilization, and also see if aggregates break up into smaller sizes under shear stress. PC50 provides pores of consistent

size (75 ± 1 nm) and has effectively no surface charge to cause OmpF grafting. The OmpF aggregates used were 133 ± 3.1 nm in diameter after sonication in solution at a pH = 5.5 and 0.0352 M in valeric acid. This OmpF solution was permeated through PC50 at 3.4 bar, and samples of feed, permeate, and retentate were collected to calculate the OmpF loading.

3.3 MATERIAL CHARACTERIZATIONS

All the quantities are molar percent based on the amount of monomer, unless it is indicated. All measurements were done by triplicate (per cycle, when applicable), calculating the respective deviations and standard errors of the means.

3.3.1 Porosity of Hollow Fiber Membranes

The pore size and pore size distribution of the HPVDF membranes were measured by a capillary flow porometer (CFP) (Porous Materials, Inc. (PMI) CFP 1500A). The membrane samples were stabilized in the sample holder and wetted by a low surface tension liquid (Galwick). Then, nitrogen gas was allowed to pass through the saturated sample until the applied pressure exceeded the capillary attraction of the liquid in the membrane pores.

3.3.2 Polymer analysis by FTIR and ATR-FTIR

PAA xerogel samples were analyzed using a Fourier transform infrared spectroscopy (FTIR) (Thermo-Nicolet Nexus 470 FT-IR ESP). The hydrogel/membrane systems were analyzed with an Attenuated total reflectance FTIR (ATR-FTIR) (Varian 7000e) to validate qualitatively the presence of chemical functional groups from PVP hydrophilization and PAA functionalization. The spectrum was set between 500 and 4000

cm^{-1}. Membrane samples were vacuum-dried and put onto a flat surface with tape before any analysis.

3.3.3 Contact Angle

The hydrophilization of HPVDF membranes were determined from contact angle (CA) measurements, surface free energy calculations and infrared spectroscopy (IR). CA was measured using a NRL C. A. Goniometer (ramé-hart 100-00 115) at 20 ± 1 °C. The average CA was calculated from measurements on three sites of the surface, measuring the advancing and receding water CAs on both sides of the drop. The CA of the PVDF membrane varies depending on the solvents, chemical additives, manufacturing processes and conditions and other variables used in their fabrication.

3.3.4 Determination of swelling degree.

The produced hydrogel is washed with DIUF water until constant pH and then vacuum dried until constant weight. Then, the xerogel is immersed in different pH buffer solutions ($1.9 \leq pH \leq 9.3$) at constant temperature (22 °C) absorbing until the weight remains constant. Each sample of hydrogel was tested to calculate the changes in the diffusion characteristics due pH changes and thus, correlate them to the responsive behavior in the functionalized membranes.

3.3.5 Morphology of the Hydrogel, Membranes and Nanoparticles.

The morphology of the hydrogel (as xerogel), the bare and functionalized membranes and the immobilized NPs inside were observed and analyzed using a focus ion beam (FIB) (Helios NanoLab 660) coupled with a scanning electron microscope (SEM)

and energy dispersive X-ray spectrometer (EDS) detector (FEI Helios Nanolab 660), and with a SEM (Hitachi S-4300) operated between 3 and 20 kV of accelerating voltage. Samples were vacuum-freeze-dried in a LABCONCO FreeZone 2.5 Plus. Functionalized and control membrane samples were also analyzed with an EDS (Zeiss EVO MA) 10 with SE/VPSE (environmental)/BSE/EDX detectors to measure the elemental composition on the surface and cross-section of the membranes. Membrane samples were put in 20 mL EPA glass vials with DIUF water and sonicated at high output power (21 W) to determine NPs losses. Particle and pores size analysis and statistics were performed using Malvern, Image J and SAS software packages.

Detached NPs from membranes and NPs in solution phase were analyzed by dynamic light scattering (DLS) (Malvern Instruments Zetasizer Nano-ZS90 and Beckman Coulter Delsa^{TM} Nano C) after being strongly sonicated for two minutes (Fisher Scientific Sonic Dismembrator 100). To study the morphology of Fe NPs a Transmission Electron Microscope (TEM) (JEOL 2010F) (accelerating voltage: 200 kV) was utilized.

3.3.6 Determination of Metal Content

For the redox initiated functionalization the polymerization was made in solution putting the membranes on the bottom of the reactor in the monomer solution and then the persulfate (APS) solution was dripped into it (0.5 mL/min). To determine the ratio of Fe^{2+}/Fe^{3+} within the hydrogel and the membranes after the polymerization process, samples were put in a solution of HCl 0.2 M to prevent oxidation of ferrous ions for 12 h in 20 mL EPA glass vials and then spiked for analysis with Iron Standard solution. The concentration of ferrous ions was measured by the Ferrozine method (Gibbs, 1979; Stookey, 1970) in an

UV-Visible spectrophotometer (Varian Cary 300 Bio) setting the detection at 562.0 nm with analytical error of 1%.

Total iron was determined by digesting the solutions from the monomer solution and membranes in nitric acid. 20 mL EPA glass vials were used and the iron concentration was measured by atomic absorption spectrometer (Varian SpectrAA 220 Fast Sequential) with a Fe lamp detector at 386.0 nm and an analytical error of 2%. The amount of iron in the hydrogel was determined by material balance. The same procedure was performed for the determination of Pd (at 244.8 nm) content in the functionalized membranes and the hydrogel.

Sodium, iron and palladium ions from the ion exchange processes and nanoparticle synthesis were determined in an inductively coupled plasma optical emission spectrometer (ICP-OES) (Varian Vista-PRO ICP-OES) after digesting the membranes with a 20% nitric acid solution in 20 mL EPA glass vials overnight (300 rpm shaking)

3.3.7 Elemental composition of hydrogel and membranes.

To measure the elemental composition, samples were analyzed EDS in a SEM (Hitachi S-3200N). In addition, X-ray photoelectron spectroscopy scans were performed with (Thermo Scientific K-Alpha XPS System) to measure the elemental composition on the surface of the hydrogel and hydrogel/membrane systems. For the latter system, an additional etching was performed to elucidate the variation in composition through the membrane profile.

3.3.8 TCE reduction analysis

TCE content of each sample was extracted with an equal volume of pentane with 1, 2-dibromoethane (EDB) (0.116 mM) as internal standard for 2 h and analyzed by Gas Chromatography – Mass Spectrometry (GC-MS) (Hewlett-Packard Series II 5890 GC-MS) with helium as carrier gas. A calibration curve was created with different solution values varying from 10 mg/L to 40 mg/L with a linear $R^2 = 0.989$ and an error < 3%.

The extract was analyzed by gas chromatography – mass spectrometry (GC-MS) in a Hewlett-Packard 5890 Series II with a Hewlett-Packard 5971A detector. Aliquots were also analyzed for chloride concentration by ion chromatography with a conductivity detector (IC) (Dionex ICS 2500).

3.3.9 OmpF Solution Characterization

OmpF work as permeable barriers that transport small molecules through the cell membrane (Cowan et al., 1995). It has weak cation activity and can selective filter hydrophilic molecules smaller than 600 Da (Nikaido, 2003). Native OmpF is a trimer with each monomer forming a 16 stranded anti-parallel β-barrels (Cowan et al., 1992). The hydrophobic interaction between monomers stabilize the trimer conformation of OmpF, which is stable even in organic solvents, except phenol (Rosenbusch & Müller, 1977).

There are several methods to determine protein concentration. Aromatic amino acids like tyrosine and tryptophan absorb UV light at 280 nm. Therefore, protein concentration can be calculated through Beer's law. This method is easy and quick, however, it is only accurate when aromatic amino acids are exposed. The Bradford assay,

for example, is a colorimetric assay based on the interactions between Coomassie brilliant blue G-250 and the arginine and aromatic residues. The maximum absorption of Coomassie brilliant blue G-250 shifts from 470 to 595 nm when binding with these residues. Similarly, to measure absorbance at 280 nm, Bradford assay requires a decent number of aromatic and arginine residues. Besides, basic conditions or detergents such as SDS can inhibit the dye that binds to the protein. On the other hand, the BCA assay, is also a colorimetric assay based on the redox reaction between protein backbone and Cu^{2+}. When protein backbone reduces Cu^{2+} to Cu^{+}, bicinchoninic acid (BCA) binds with Cu^{+} to form a complex which absorbs at 562 nm. Reducing reagents are not involved during the OmpF purification steps described above. Also, BCA assay is not sensitive to detergents and denaturants, it involves with peptide backbone and is less sensitive to the amino acids present.

The purity of OmpF isolated by valeric acid was identified through sodium dodecyl sulfate polyacrylamide gel electrophoresis (SDS-PAGE). The sample was diluted 5 fold with 2% SDS and then boiled in a water bath for 5 min before loading into 20% polyacrylamide gel (20% polyacrylamide, 0.4 M Tris-HCl pH 8.8, 0.1% SDS, 0.1% ammonium persulfate, and 0.1% TEMED). The sample was run in the SDS running buffer (0.3% w/v Tris base, 1.44% w/v glycine, and 0.1% w/v SDS) at 200 V for one hour. Protein was stained with 0.1% Coomassie blue R-250 in 50% ethanol and 10% acetic acid for 15 min, and destained with 10% acetic acid and 20% ethanol for one hour. BCA assay was chosen to quantify OmpF concentration for each of the samples due to its non-destructive approach. Feed, permeate, and retentate was quantified through material balance in each of the membranes with the BCA method.

3.3.10 Charged and Non-charged molecules analysis

A total organic carbon analyzer (TOC) (TOC-5000A by Shimadzu) was used to measure feed, permeate, and retentate concentrations of the carbon-based molecules used. Inorganic salt rejection measurements were taken with a conductivity probe (Fisher Scientific Traceable Bench Conductivity Meter) and an ICP-OES (Varian Vista-PRO).

In order to gradually pass extracted OmpF through the functionalized membrane, the OmpF solution was diluted in water. To study size of aggregates, solutions with OmpF at pH values of 4.3 and 5.5 and from a range of 0.035 M to 1.32 M valeric acid were prepared and sonicated for five minutes. The lower bound of this concentration range and the pH = 5.5 match the parameters of the solution permeated through the membranes during LbL process. Aggregates were measured using dynamic light scattering (DLS) (Malvern Instruments Zetasizer Nano-ZS90). The significant peak, where > 90% of the counted particulates resided, was taken to be the aggregate size.

4 POLYELECTROLYTE FUNCTIONALIZATION

This chapter describes the polymerization processes, the poly(acrylic acid) (PAA) hydrogel synthesis, the poly(vinylidene fluoride) hollow fiber membrane (HPVDF) fabrication, and the functionalization and the Layer-by-Layer assembly of the different membranes used in this work. It also contains the characterization of these responsive materials, including swelling and flux studies. Parts of this chapter are published or submitted (Hernández, Lei, et al., 2016; Hernandez et al., 2014; Porter et al., 2017).

4.1 POLYMERIZATION OF ACRYLIC ACID

As described in Chapter 2, free radical polymerization in solution could use initiators to start the chain reaction. Such initiators include strong oxidants such as persulfates, perphosphates or peroxides, and can be degraded to generate the radicals.

4.1.1 Thermal Polymerization

The temperatures used in this degradation range from 50 to 90 °C or higher to initiate this process. In this work, ammonium or potassium persulfate (APS or KPS) are used as initiator and they required temperatures of about 70 °C or above to degrade (Z. S. Liu & Rempel, 1997), see Figure 4.1. The monomer solutions range from 10 to 23 wt. % of monomer, without changing the concentrations of cross-linker, N,N'-Methylenebisacrylamide (MBA), and initiator (1 mol % of AA each).

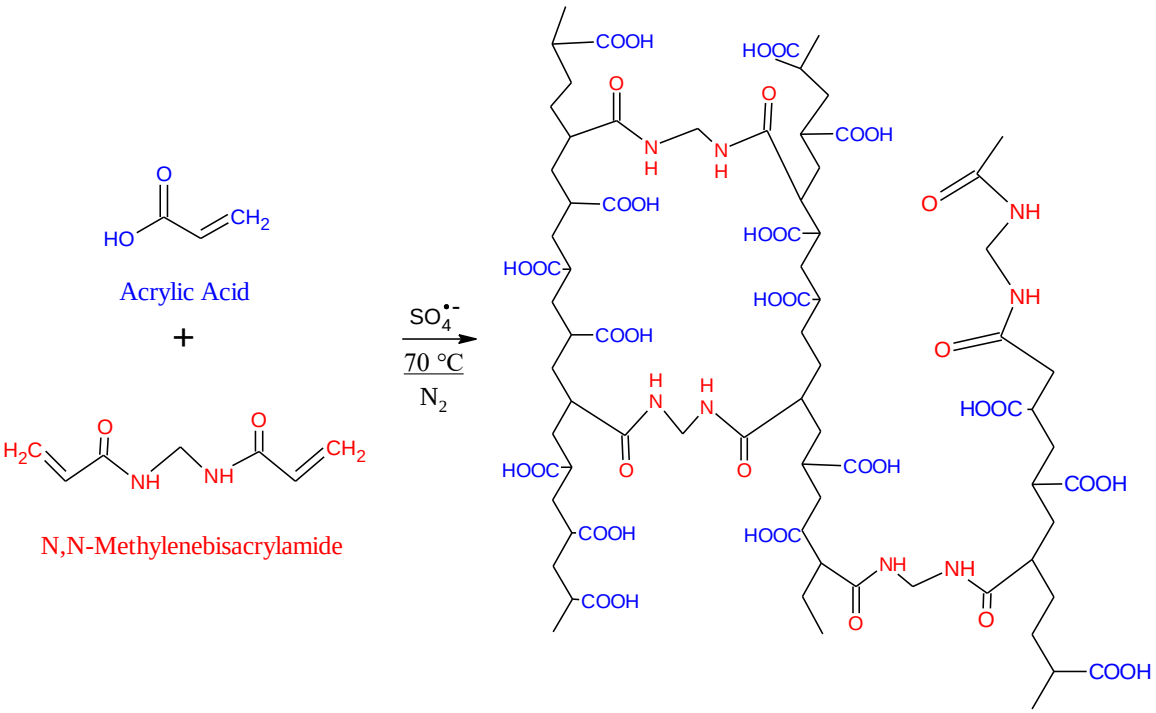

Figure 4.1. Scheme of thermal free radical polymerization in solution and cross-linking.

4.1.2 Redox Polymerization

The proposed process for hydrogel synthesis is a redox polymerization due to their high conversions (≥ 98%) and high molecular weight products. This polymerization is done in solution and/or using a bath to prevent overheating which gives a proper control of temperature, avoiding polymer gelation (Braun, 2005; Kricheldorf, 2004; Nagaraja, Demappa, & Mahadevaiah, 2011; Odian, 2004). This acid-redox polymerization includes the strong oxidants described and one or two reducing agents to initiate free radicals. The reducing agents or catalysts are inorganic salts from metals like Iron, Copper, Manganese, and sodium thiosulfate ($Na_2S_2O_3$) or ascorbic acid (AH_2) which have the purpose of preventing the rapid oxidation of the metal ions by reducing them and maintaining the production of free radicals (Braun, 2005; Hsieh & Hsieh, 1997; Khan & Martell, 1967; C. Liang, Bruell, Marley, & Sperry, 2004; Odian, 2004; Sarac, 1999).

The polymerization in this work is performed through a redox reaction of a metallic ion and a reducing agent (accelerants/reducers) with persulfate ion (initiator/oxidant) (Misra & Bajpai, 1982; Sarac, 1999). This method is started at room temperature (22-25 °C) and is exothermic. The pH is also a variable in the polymerization process and different values are recommended depending on the monomer (*M*) used. The reaction is heterogeneous and depends on the initiators and the monomer concentration with ½ and 3/2 power, respectively (Odian, 2004). Since this reaction has two initiators ($S_2O_8^-$, AH_2), the proposed mechanisms are the following:

$$SO_4^{-\bullet} + M \xrightarrow{k'_1} SO_4M^{\bullet} \tag{4.1}$$

$$SO_4M^{\bullet}_{x-1} + M \xrightarrow{k_{p1}} SO_4M^{\bullet}_{x} \tag{4.2}$$

$$SO_4M_x^{\bullet} + SO_4M_y^{\bullet} \xrightarrow{k_{t1}} Polymer \quad (4.3)$$

$$A^{\bullet}H + M \xrightarrow{k'_2} AHM^{\bullet} \quad (4.4)$$

$$AHM_{x-1}^{\bullet} + M \xrightarrow{k_{p2}} AHM_x^{\bullet} \quad (4.5)$$

$$AHM_x^{\bullet} + AHM_y^{\bullet} \xrightarrow{k_{t2}} Polymer \quad (4.6)$$

If the rates of each stage are the same (Equations (4.1) and (4.4); Equations (4.2) and (4.5); Equations (4.3) and (4.6)), the rate of initiation and polymerization become (Cutie, Smith, Henton, Staples, & Powell, 1997; Odian, 2004):

$$R_i = k_d[Reductant][Oxidant] \quad (4.7)$$

$$R_p = k_p\left[k'f\frac{k_d}{k_t}\right]^{1/2}[M]^{3/2}[I]^{1/2} \quad (4.8)$$

where *I*, is an average of the concentrations of AH_2 and $S_2O_8^-$. The polymerization of AA by redox couples of Fe^{2+} or AH_2 with $S_2O_8^-$ are discussed in different works with polymeric products with high molecular weight due to cross-linking. Reported data showed values of molecular weight of $M_n >> 5000$, only for acrylic acid polymerizations (Cutie et al., 1997). However, the utilization of this redox system was reported so far in one experimental work and is mentioned in polymerization reviews referenced (X. L. Sun, Sun, & Wang, 1998). The production of free radicals in this system is governed by 2 equations, adapted from (Sarac, 1999):

$$Fe^{2+} + S_2O_8^- \rightarrow Fe^{3+} + SO_4^{-\bullet} + SO_4^{2-} \quad (4.9)$$

$$AH_2 + S_2O_8^- \rightarrow A^{\bullet}H + 2H^+ + SO_4^{2-} \quad (4.10)$$

Ferrous ions start to oxidize creating sulfate radicals from persulfate and at the same time this compound starts to form ascorbate radicals (Equations (4.9) and (4.10)). The PAA starts to aggregate very fast forming a more dense material, which starts to absorb all the solution around it. The pH tends to be stable because of the ionization of the AA and AH_2. As explained, the reaction is heterogeneous and depends on the initiators and the monomer concentration (Cutie et al., 1997; Odian, 2004).

Some side reactions take place during the polymerization. The most important is the reduction of Fe^{3+} by AH_2 (Equation (4.11)). This reduction induces the generation of more sulfate radicals by production of Fe^{2+} ions, increasing the polymerization efficiency (high conversion) and leaving dehydroascorbic acid (*Ad*) as byproduct in a low pH environment. However, sulfate radical can be diminished by the Fe^{2+} formed (Equation (4.12)), it also can be created by chain transfer from the growing chain ($M_n^{\bullet}$) to persulfate (Equation (4.13)) or disappear by coupling (Equation (4.14)). Those two reactions give possibly short length chains of polymer.

$$2Fe^{3+} + AH_2 \rightarrow 2Fe^{2+} + 2H^+ + Ad \quad (4.11)$$

$$SO_4^{-\bullet} + Fe^{2+} \rightarrow Fe^{3+} + SO_4^{2-} \quad (4.12)$$

$$M_n^{\bullet} + S_2O_8^{2-} \rightarrow Polymer + SO_4^{-\bullet} \quad (4.13)$$

$$M_n^{\bullet} + SO_4^{-\bullet} \rightarrow Polymer \quad (4.14)$$

The increment in the temperature of the polymerization over time tends to a plateau as a result of the exothermic redox reaction. Temperatures around 50 °C for a reaction surrounded by water in an external vessel at 15 °C, and a faster reaction at ≈ 60 °C without water surroundings are reached. These temperatures are recognized by different studies in which the conversion reaches around 85% of the initial monomer concentration and were

heated at the same or higher temperature (Cutie et al., 1997; Kabanov, Topchiev, Karaputadze, & Mkrtchian, 1975; Manickam, Venkatarao, & Subbaratnam, 1979). By adding the initiators dropwise, it was suitable to control the temperature increment for hydrogel synthesis alone. The higher temperature reached was assumed for the membrane functionalization, since its control was not technically feasible.

4.2 HYDROGEL CHARACTERIZATION

Cross-linked PAA synthesis was conducted at known temperatures (70-80 °C) which give a very stable material under basic or acid conditions. These properties combined with the excellent chemical resistance of the PVDF in membranes to a numerous types of agents (acid, weak alkaline and oxidizing) generate a very versatile material.

4.2.1 Hydrogel Structural and Physicochemical Characterization

Based on the FTIR and ATR-FTIR spectra, the polymerization and functionalization can be confirmed. A comparison between commercial PAA powder and the hydrogel indicates the synthesis of the hydrogel, see Figure 4.2, showing a strong wide band in the region of 3300-2500 cm^{-1} and demonstrating presence of O-H groups. For PAA powder, at 1700 cm^{-1} the C=O group is defined (Figure 4.2a). Due to the washes after polymerization, the hydrogel can be ionized and show two defined peaks between 1750 and 1600 cm^{-1} related to C=O from the carboxylic acid, COOH, and carboxylate, COO^- groups, respectively (Figure 4.2b) (J. Chen et al., 1998; Cohen-Ofri, Weiner, Boaretto, Mintz, & Weiner, 2006).

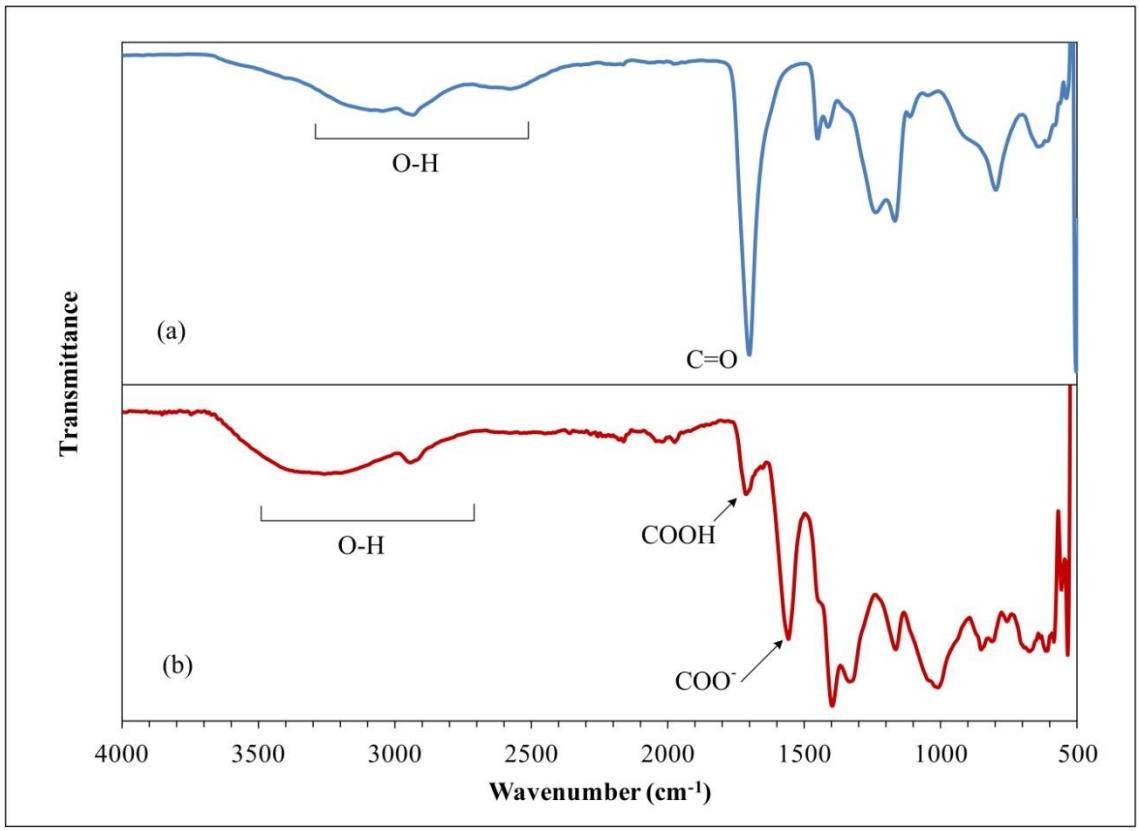

Figure 4.2. FTIR spectra of (a) PAA powder; (b) PAA cross-linked hydrogel. Reprinted from (Hernandez et al., 2014). Copyright (2014) American Chemical Society.

The morphology of the bare xerogel surface looks wrinkled, porous, and open in the Figure 4.3a-b. The lower voltage for the observations of the gel are because this material is not very stable at high voltages and can burn especially at low crosslinking degree. PAA as polyelectrolyte has a very good ion exchange capability at neutral to lower basic pH and its pKa ($4.3 \leq pKa \leq 4.9$) is similar to the monomer AA (pKa = 4.7) (A. Thakur, R. Wanchoo, & P. Singh, 2011a; Zhao, Nie, Tang, & Sun, 2011).

From a comparative survey done with the XPS to the xerogel from thermal and redox polymerization (Figure 4.4a, and Figure 4.4b, respectively) it is revealed the presence of oxygen and carbon in the former and a low amount of sulfur in the latter. Sulfur (from sulfate) as initiator in both reactions has higher concentration in the redox initiation, which is confirmed here. In the xerogel from redox initiation, the ratio between oxygen and carbon is near to the stoichiometric value (2:3) but is lower in the thermal sample due possibly to low ionization from the XPS equipment.

4.2.2 Hydrogel Swelling Characterization

The lattice size of a hydrogel is altered drastically with small pH changes. When the pH of cross-linked PAA is raised above its pKa, a charged repulsion of the carboxylic groups is created expanding the size of the hydrogel and increasing the swelling degree. When the pH is lowered, the charged repulsion phenomenon is the opposite and the swelling is lower. Since the membranes are modified with this material, swelling studies were done to demonstrate the relationship of pH response in the hydrogel to the change in the pore of functionalized membranes.

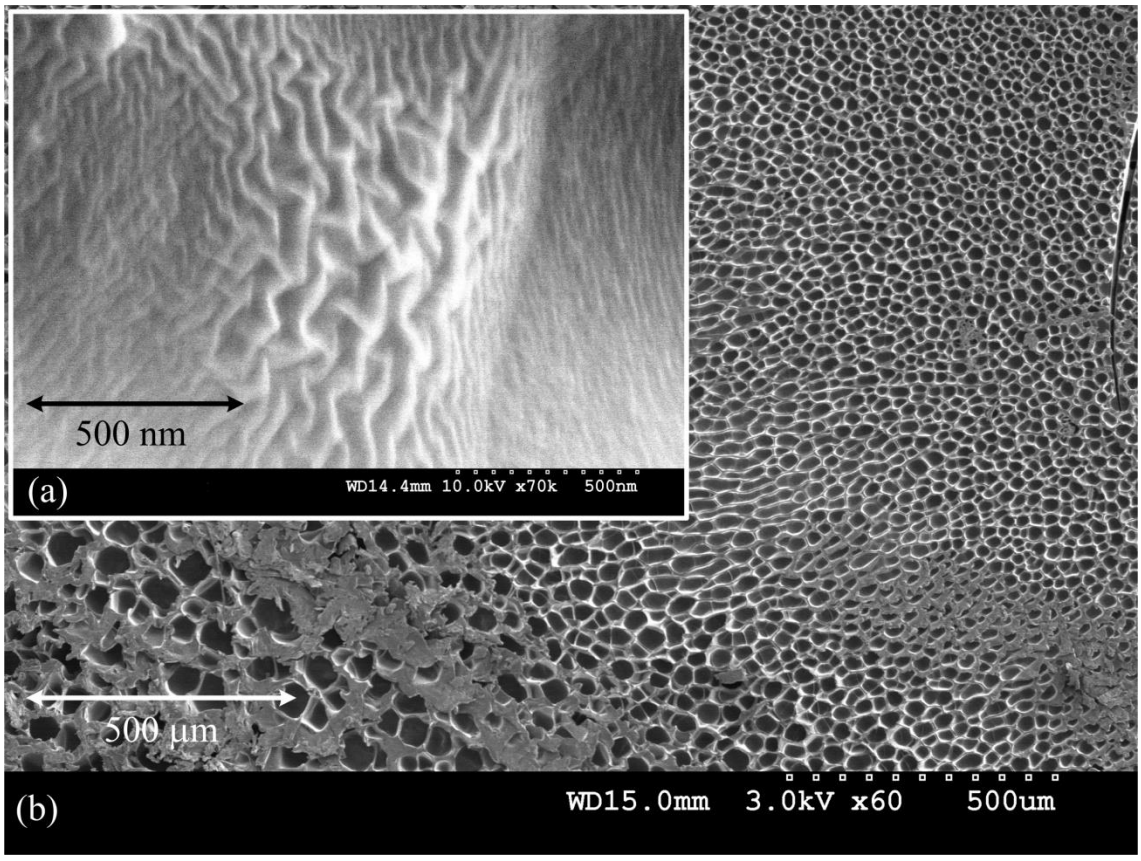

Figure 4.3. SEM images of the cross-linked PAA-MBA xerogel. (a) Wrinkled structure of the xerogel, (b) Porous surface of the xerogel. Reprinted from (Hernandez et al., 2014). Copyright (2014) American Chemical Society.

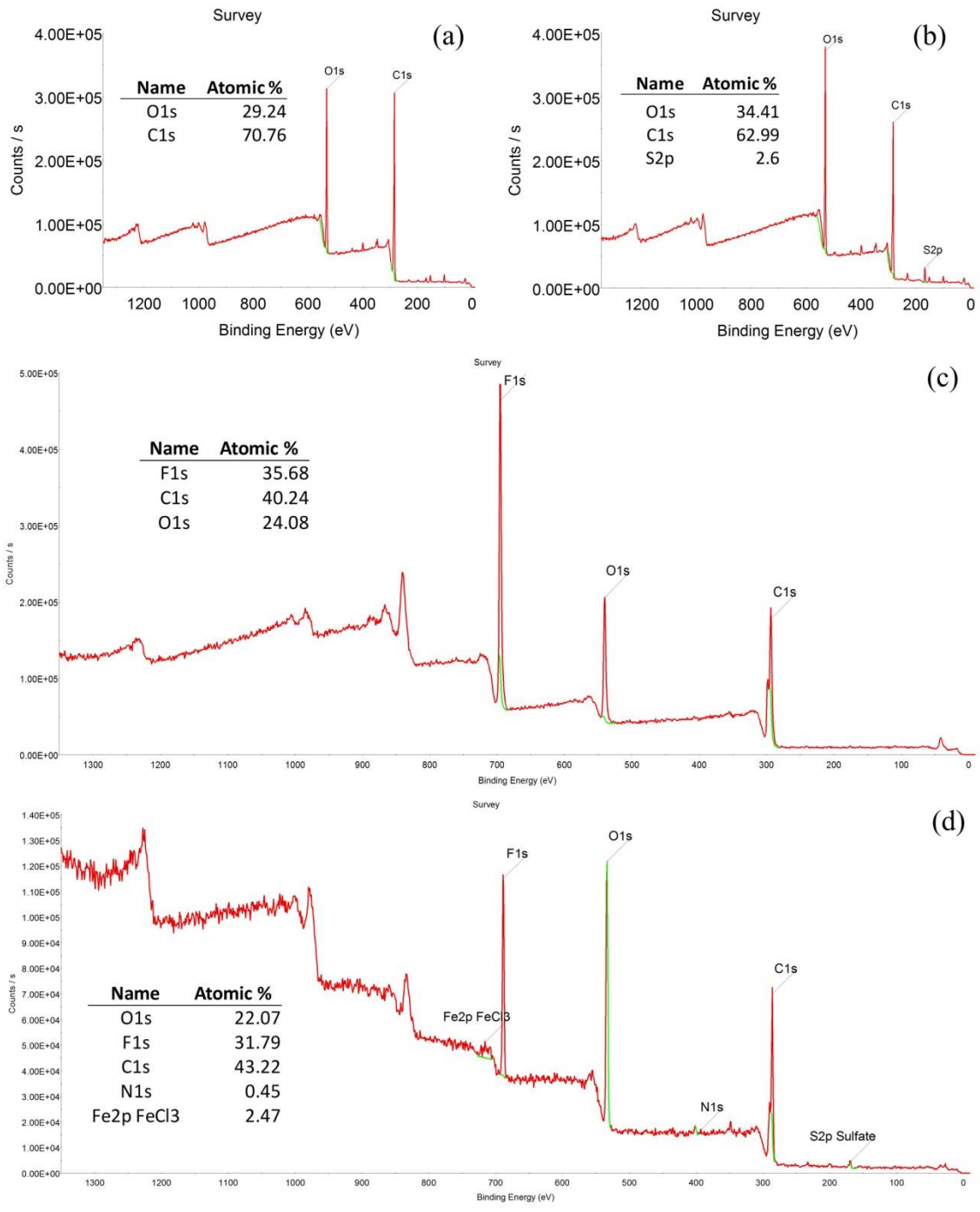

Figure 4.4. XPS spectra of the cross-linked PAA xerogel and PVDF-PAA membranes. (a) PAA Xerogel from thermal initiation, (b) PAA Xerogel from redox initiation, (c) PVDF-PAA from thermal initiation, (d) PVDF-PAA from redox initiation. Reprinted from (Hernandez et al., 2014). Copyright (2014) American Chemical Society.

The amount of water absorbed and retained by the hydrogel at constant temperature and pH can be expressed by:

$$W = \frac{water\ content\ in\ hydrogel}{total\ weight\ of\ hydrogel} = \frac{m - m_0}{m} \tag{4.15}$$

where m_0 and m are the weights of the xerogel and the hydrogel, respectively. Its behavior is asymptotic when W tends to the unit reaching the highest water uptake possible in equilibrium, W_{eq} (José, Nora, & Issa, 1999).

With the experimental data of water uptake by the hydrogel, the isothermal swelling degree calculated by the amount of water retained W is plotted as a function of time in Figure 4.5. All the samples showed similar behavior, increasing the water content drastically at the beginning, reaching a plateau after certain time. For the hydrogel fabricated by redox polymerization (Figure 4.5a), the plateau was reached in 15 min or less. Except for pH = 1.9, which plateau, was reached after approximately 50 min, due to the tight structure of no-repulsion between carboxylic groups. Then, the increment in water content was more slowly until equilibrium was reached (W_{eq}), showing higher amounts of buffer solution absorbed at higher pH values for both hydrogels. In the hydrogel made by thermal polymerization, the plateau was reached more slowly at almost 500 to 1000 min, see Figure 4.5b. The very high responsive behavior from the former hydrogel is a direct consequence of the electrolytes present within, due to the species involved in the synthesis. The absorption capacity of the hydrogels at equilibrium showed that the weight gain percentage with respect to the xerogel when swelling occurs goes from 213% at pH = 1.9 to 776% at pH = 9.3, in the one made by redox and from 194% to 1676% in the same range of pH.

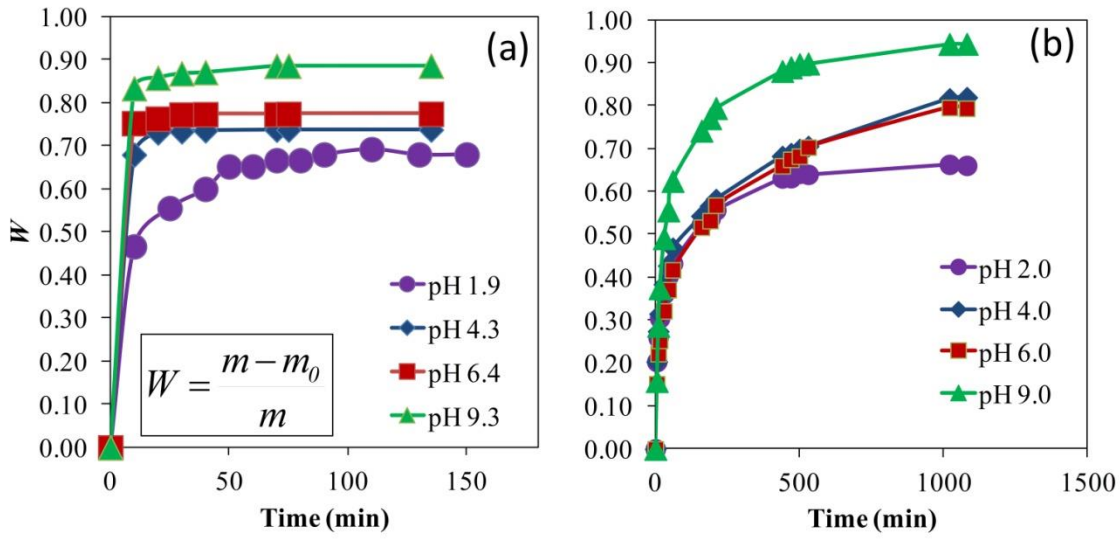

Figure 4.5. Swelling isotherms of cross-linked PAA hydrogel at different pH values. (a) Hydrogel by redox initiation, (b) hydrogel by thermal initiation. Crosslinking degree, X = 1% MBA. T = 22 °C. All measurements were done by triplicate, calculating the respective deviations and standard errors of the means. Error bars are negligible. Reprinted from (Hernandez et al., 2014). Copyright (2014) American Chemical Society.

The first results are low compared to literature and could be a consequence of the redox polymerization process and the presence of highly cross-linked sites in some parts of the material (Thakur et al., 2011a). In addition to that, these results agreed with different works that show lower capacities in the presence of more concentrated solutions (Fumio et al., 1990; Pa Achia & Florea, 2007).

To establish the swelling behavior, first-order and second-order swelling kinetics models were considered (Equations (4.16) and (4.18)). It is predictable that the first-order will not fit the experimental data due to the changes in the swelling and volume of the material with time (Katime et al., 1996). This is because the first-order swelling kinetics is similar to the obtained by Fick's law of diffusion in one-dimensional swelling of films for long times, which assumes the diffusion coefficient and the thickness of the hydrogel constant during the swelling process. After integration of each model (Equations (4.17) and (4.19)), only the second-order swelling model fits the experimental data. Shown in Figure 4.6 with R^2 between 0.999 and 1.000, the rate of swelling of the cross-linked PAA hydrogel is proportional to the quadratic of swelling capacity offered, making the swelling process faster at higher pH values.

$$\frac{dW}{dt} = K\left(W_{eq} - W\right) \tag{4.16}$$

$$\ln\left(\frac{W_{eq}}{W_{eq} - W}\right) = Kt \tag{4.17}$$

$$\frac{dW}{dt} = K\left(W_{eq} - W\right)^2 \tag{4.18}$$

$$\frac{t}{W} = \frac{1}{KW_{eq}^2} + \frac{1}{W_{eq}}t \tag{4.19}$$

The calculated constants adjusted to the second-order kinetics show higher values in intermediate pH values than in the extremes for the redox initiated hydrogel. At the extreme values of pH, the ionic hydrogels behave as non-ionic. In addition to that, the ion exchange rate seems to be higher when the hydrogel already has certain amount of electrolytes inside. For the thermal initiated hydrogel, the behavior is the opposite to the redox initiated due to the dissociation degree of the AA. This is based on the Henderson–Hasselbach relation (Table 4.1) on which below pH = 4.0, the potential of dissociation is higher compared with pH ≥ 5.0. The values of the constants for the redox initiated (Figure 4.6a) are two orders of magnitude higher than the thermal (Figure 4.6b), confirming the high responsive behavior of the redox initiated hydrogel.

The rate of swelling of a hydrogel is controlled by the mesh size (ξ) of the network. The mesh size can be theoretically determined based on the crosslinking density by calculating the distance of the swollen polymer chains between cross-linked points (based on (N. A. Peppas & S. L. Wright, 1996)):

$$\xi = l\left(v_{2eq}\right)^{-1/3} \cdot \sqrt{\frac{C_n}{X}} \tag{4.20}$$

where l, is the bond length along the backbone chain (1.54×10^{-10} m for carbon-carbon bonds), v_{2eq} is the volume fraction of swollen polymer assuming isotropic swelling (xerogel volume/ hydrogel volume in the case of PAA), C_n is the Flory characteristic ratio (for PAA, C_n = 6.7) and X is the degree of cross-linking (1% molar with respect to AA concentration) (Thakur et al., 2011a).

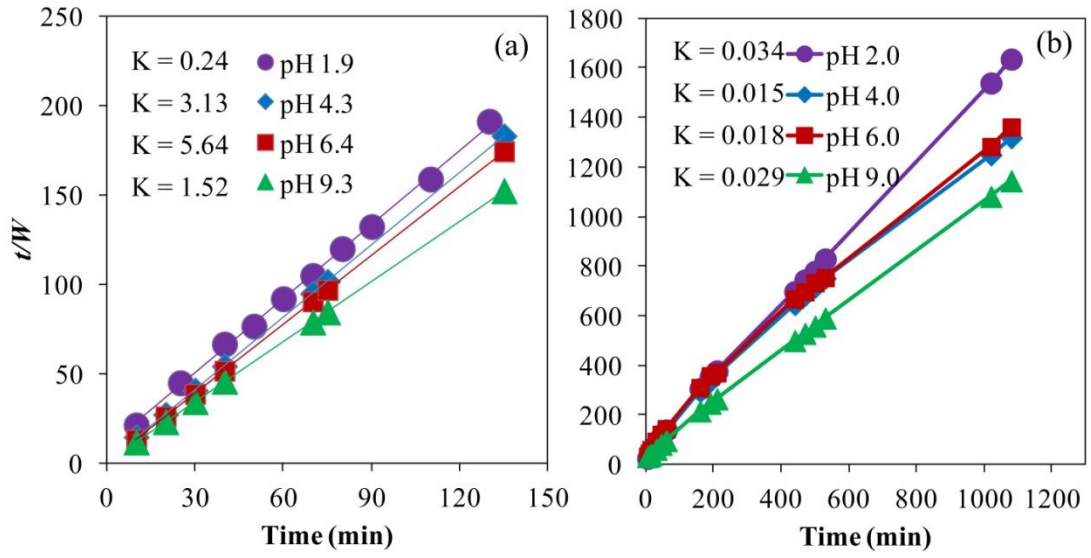

Figure 4.6. Second-order kinetics model for cross-linked PAA hydrogel at different pH values. (a) Hydrogel by redox initiation, (b) hydrogel by thermal initiation. Crosslinking degree, X = 1% NMBA. T = 22 °C. All measurements were done by triplicate, calculating the respective deviations and standard errors of the means. Error bars are negligible. Reprinted from (Hernandez et al., 2014). Copyright (2014) American Chemical Society.

Table 4.1. Determination of MPVDF-PAA membrane equivalent pore diameters d_p and permeability between high and low pressure conditions ($1.0 \leq \Delta P \leq 4.0$ bar; T = 22 °C) at different pH values. Area of membranes = 13.2 cm^2. Membrane thickness = 125 μm. Reprinted from (Hernandez et al., 2014). All measurements were done by triplicate, calculating the respective deviations and standard errors of the means. Copyright (2014) American Chemical Society.

pH	**Dissociation degree of AA (%)**	**Permeability ($L/(m^2 \cdot h \cdot bar)$)**	**Pore diameter d_p (nm)**
4.0	28.5	53.94 ± 7.59	222 ± 9
5.0	71.5	32.68 ± 3.39	198 ± 6
6.0	97.8	17.71 ± 1.28	171 ± 3
7. 0	99.6	7.44 ± 1.31	136 ± 7
9.0	99.9	3.39 ± 0.66	111 ± 7

Figure 4.7 shows that the mesh size increases at higher pH values, confirming the expansion in the volume of the hydrogel due to swelling and repulsion of carboxylic groups. For the redox initiated, the mesh size is small compared with other works giving the possibility of prevent aggregation of NPs which was discussed before (Pa Achia & Florea, 2007; N. A. Peppas & S. L. Wright, 1996). For the thermal initiated hydrogel, the mesh size varies more, correlating its behavior with the higher swelling capacity. However, in the intermediate pH values the swelling for this hydrogel is similar, showing no change in the mesh size due to the pKa values of the PAA lie between these pH values. In the redox initiated hydrogel, this change cannot be seen because the amount of electrolytes softens the transition. A change in the chain length of 2 nm between cross-links can generate a mass gain of 700% the weight of the xerogel for the redox initiated case. A change in 4 nm generates almost 1700% for the thermal initiated hydrogel, see Figure 4.7.

The calculated molecular weight of the polymer chains between cross-linked points M_c is 3603 g/mol using $M_c = M_0/2X$ with M_0 as the molecular weight of the repeating units. For these values, the polymer volume fraction v_{2eq} decreases at higher pH values, going from 0.31 to 0.11 for redox and from 0.33 to 0.05 for thermal initiated hydrogel. This confirms the increase in mesh size ξ and hence, the volume of the hydrogel. Due to the presence of electrolytes in the redox hydrogel, its v_{2eq} is higher, which represents lower swelling.

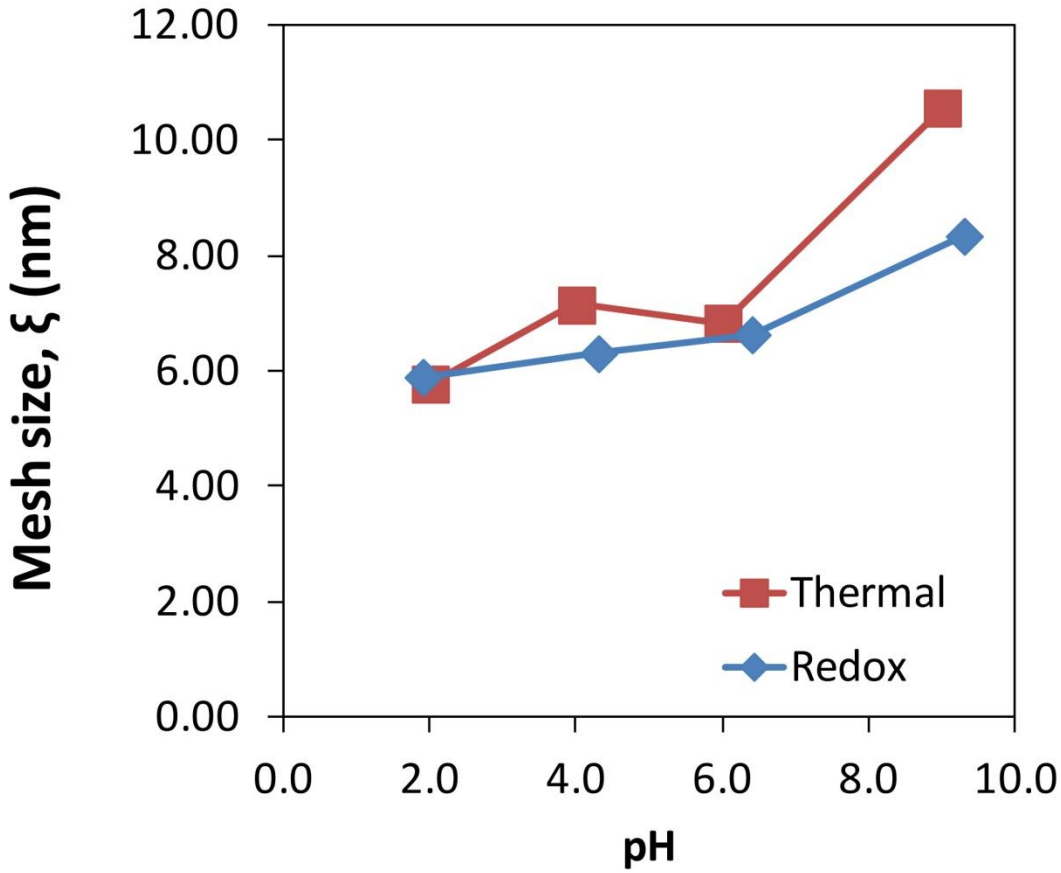

Figure 4.7. Calculated swollen polymer volume fraction and mesh size of the hydrogel as function of pH. Cross-linking degree, X = 1% MBA. T = 22°C. All measurements were done by triplicate, calculating the respective deviations and standard errors of the means. Error bars are negligible. Reprinted from (Hernandez et al., 2014). Copyright (2014) American Chemical Society.

4.3 MEMBRANE CHARACTERIZATION

As mentioned in Chapter 3, the functionalization of the PVDF membranes was done through a crosslinking polymerization of AA using different concentrations of monomer. This method is preferred since it can be used in already full-scale synthesized membranes, which represents an advantage in industry. In this method, the action of the cross-linking agent prevents the hydrogel from being removed from the membrane once it is synthesized (Stuart et al., 2010). Due to the polymerizations, including the hydrophilization with PVP for the HPVDF membranes, an increase in weight is expected. A membrane mass gain, Δm (g/m^2), was calculated as $\Delta m = (w_2 - w_1)/A$, were w_1 and w_2 are the weight (g) of the non-functionalized PVDF and the hydrophilized/functionalized membranes, respectively; A is the outer HF area or top FS surface area (m^2) of the membranes. In addition to this weight increase, the membrane composition and morphology change due to the presence of the polymer network, altering properties such as pore size, flux and wettability.

4.3.1 Swelling in Functionalized Membranes

The reason to choose 10 to 20 wt. % of AA concentration before the polymerization in membrane functionalization is because as the monomer concentration increases, the amount of water the hydrogel could absorb also increases, but its permeability and consequently the flux through the membrane decreases. Thus, the initial monomer concentration within this range will affect the flux, wettability, and structure of the membranes. In other PVDF membrane functionalization studies for heavy metal removal, this is confirmed, concluding that for the appropriate point for synthesizing PAA hydrogels, the ideal concentration of AA in the monomer solution is about 15-23 wt. % (M. Gui et al., 2015).

Using 3 concentrations of AA in the monomer solution, it was found the weight increase for xerogel, see Figure 4.8.The weight was measured once the membranes were washed with water and ethanol several times, and subsequently dried, for which this weight is due to the actual functionalization. This increase in weight is possible not only to more polymer produced, but also to an increase in its molecular weight. However, when these membranes were then put in different pH solutions to measure their swelling behavior, it was found that the lower monomer concentration (15 wt. %) was swelling more than the higher (23 wt. %). Although the cross-linker concentration was not varied, it was expected a higher swelling ratio, consequently this behavior can be attributed to higher molecular weights obtained and to membrane volume restrictions. Unlike a hydrogel alone, the hydrogel within the membrane pores does not have unlimited volume to swell because it is constrained by the available void volume in the membrane structure, which changes due to the same presence of the hydrogel and therefore the steric effect dominates caused by the available space on the swelling capacity.

The membrane synthesized with an initial monomer concentration of 20 wt. % had intermediate swelling properties between the properties of the other two membranes. In addition, it should be noted that because the support membrane is hydrophilic, the PVDF surface is more exposed for the case of the membrane with less hydrogel (15 wt. %) and this favors the water absorption.

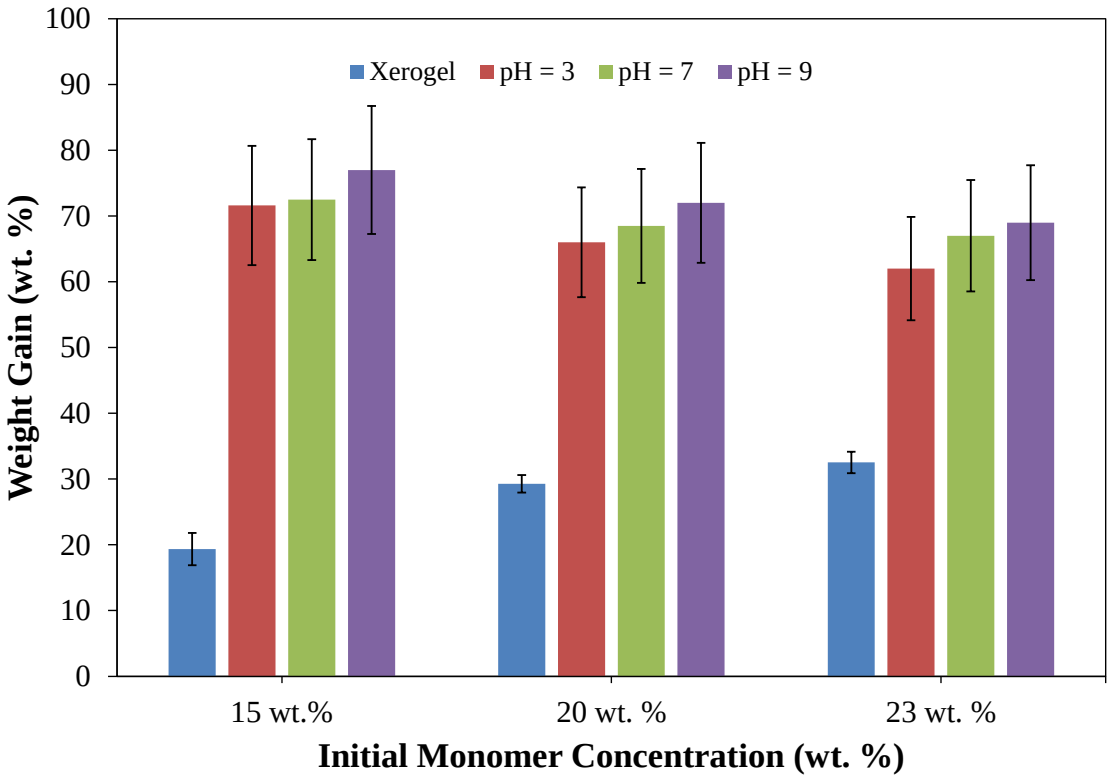

Figure 4.8. Weight gain of MPVDF-PAA membranes, dried (xerogel) and at different pH values (hydrogel). All measurements were done by triplicate, calculating the respective deviations and standard errors of the means.

4.3.2 Hollow Fiber and Sponge-like Flat Sheet Membranes

Non-functionalized HPVDF membranes were analyzed by SEM images, capillary flow and gravimetric methods in order to describe and compare their characteristics and to determine their physical properties, such as pore size, thickness and structure, among others. The HPVDF membrane fabricated, has 1.18 mm of outer diameter and 225 μm of thickness. Membrane porosity, ε_m, and pore size distribution were determined comparing the gas flow rates of wet and dry sample at the same pressures. The HPVDF membrane pore sizes obtained by CFP are 0.72 μm for the median, the average pore size is 0.89 μm and the maximum is 2.2 μm. In Figure 4.9, the pore size distribution shows that more than half of the pores are less than or equal to 0.8 μm (57.2%). The membrane porosity, ε_m, is defined as the volume of the pores divided by the total volume of the membrane. It was determined by gravimetric method, measuring the weight of IPA (here as wetting solvent) contained in the membrane pores:

$$\varepsilon_m = \frac{(\omega_1 - \omega_2)/\rho_I}{(\omega_1 - \omega_2)/\rho_I + \omega_2/\rho_P} \tag{4.21}$$

where ω_1 is the weight of the wet membrane, ω_2 is the weight of the dry membrane, ρ_I is the IPA density and ρ_P is the polymer density. Results for the HPVDF membrane show a porosity of 59.6 ± 1.3 %.

The HPVDF membrane in Figure 4.10a-b shows a thickness of about 250 μm, which is close to the value reported in its fabrication. The sponge-like morphology of cross-section in Figure 4.10b looks wrinkled, asymmetric and very porous. The outer surface showed in Figure 4.10c-d is porous structure with cracks sandwiched by crystalline sections (nonporous). Pores shown in Figure 4.10d are asymmetric with an apparent pore

size close to that obtained by CFP. The unique pore structure is originated from the polymer lean phase surrounded by the crystallizing polymer-rich phase during the TIPS process.

In the case of the non-functionalized SPVDF (sponge-like FS membranes), the thickness reported by Nanostone is 125 μm, to which the experimental value is very close (Figure 4.11a). In these SEM images, Figure 4.11a-b and Figure 4.11d, it is possible to see the very porous, sponge-like and also macro-void structure of the SPVDF membrane, unlike the HPVDF, which only has a sponge-like structure. The top surface has different pore shapes and sizes with an upper limit of around 400 nm (Figure 4.11c). The bottom surface in Figure 4.11d (without the backing material), was found to possess a very porous structure (around 500 nm pore size).

4.3.2.1 Contact Angle Characterization of Sponge-like Membranes

The surface free energy, γ_S^{TOT}, was evaluated from the contact angle hysteresis of water on the HF membrane surfaces in each step of the hydrophilization, including the functionalization with PAA, using the equation:

$$\gamma_S^{TOT} = \frac{\gamma_L(1 + cos\theta_A)}{2 + cos\theta_R + cos\theta_A} \tag{4.22}$$

were γ_L is the surface tension of water at the temperature of the CA measurements; θ_A and θ_R are the advancing CA and the receding CA, respectively. The CA measurements and the evaluation of γ_S^{TOT} are listed in Table 4.2 in each step of the treatment (Chibowski, 2003; Jurak & Chibowski, 2010; Pogorzelski, Berezowski, Rochowski, & Szurkowski, 2012)

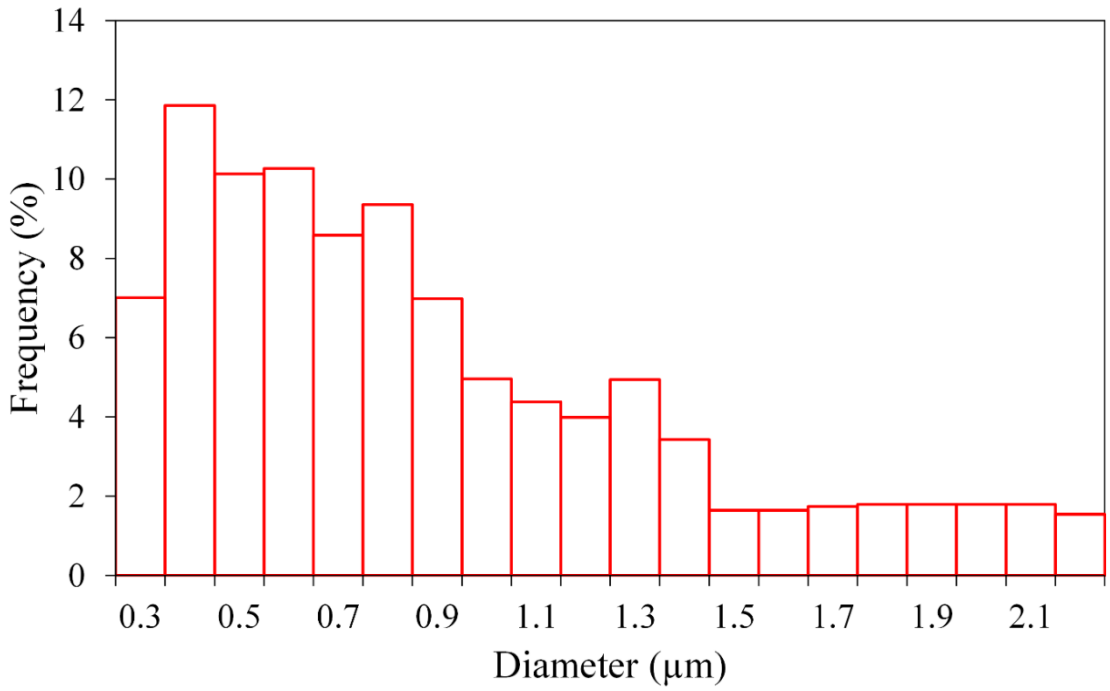

Figure 4.9. Histogram of pore size distribution of HPVDF membrane. Mean pore size: 0.89 µm. Reprinted from (Hernández, Lei, et al., 2016). Copyright (2016) American Chemical Society.

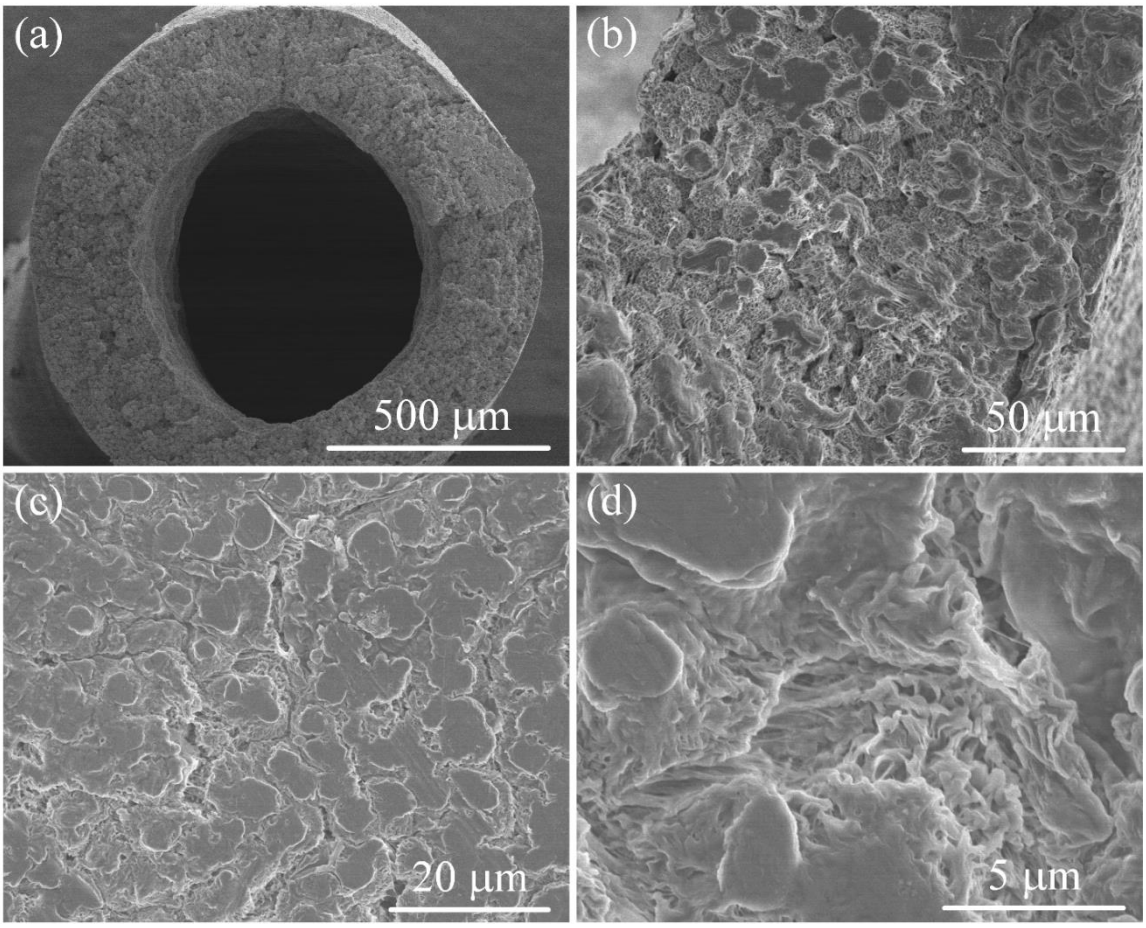

Figure 4.10. SEM images of HPVDF membranes at different magnitudes. (a) Cross-section, (b) zoom-in of cross-section, (c) outer surface, (d) outer surface zoom-in. Reprinted from (Hernández, Lei, et al., 2016). Copyright (2016) American Chemical Society.

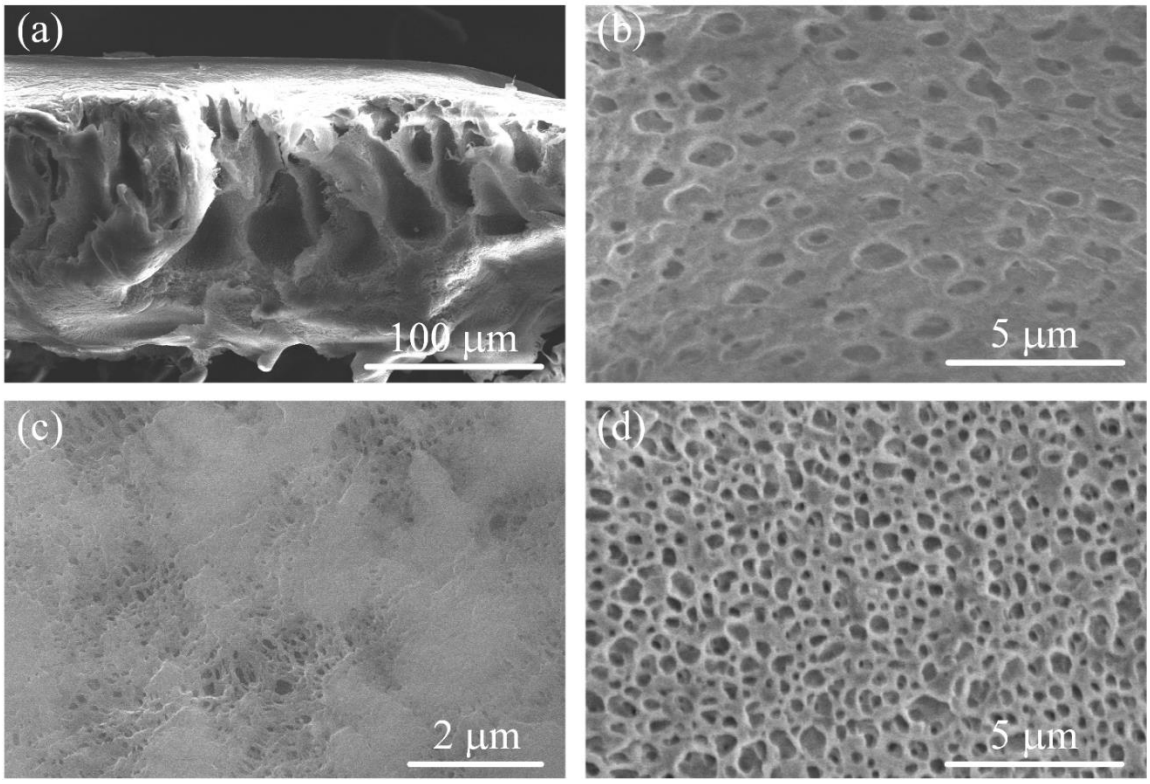

Figure 4.11. SEM images of SPVDF flat sheet membranes at different magnitudes. (a) Cross-section, (b) zoom-in of cross-section, (c) top surface, (d) bottom surface without backing. Reprinted from (Hernández, Lei, et al., 2016). Copyright (2016) American Chemical Society.

Membranes of PVDF can have CAs from around 75° (phase inversion with water) to 148° (phase inversion with alcohol) for hydrophobic applications (Duca, Plosceanu, & Pop, 1998; F. L. Huang et al., 2010; Kuo, Lin, Tsai, Wang, & Lai, 2008; T. Wu et al., 2015). The hydrophilization of PVDF membranes using PVP is well established in industry and academia as a part of the casting process. However, hydrophilization as post-process has been implemented in few research studies and they have been presented as a cross-linking procedure discussed by different authors. Diverse methods have been explained, such as ring-opening and self-cross-linking by ethanol-acetone (M. Sun, He, Ye, Yang, & Yin, 2014; M. Yin, Ye, Sun, Kang, & Yang, 2013), ring-opening using sodium hypochlorite in alkaline solution (I. M. Wienk, Meuleman, Borneman, van den Boomgaard, & Smolders, 1995), ether bonds with UV light (Lopérgolo, Lugão, & Catalani, 2003; Q. G. Zhang, Hu, Zhu, & Liu, 2013) or UV-H_2O_2 photo-initiation (Fechine, Barros, & Catalani, 2004; Kadłubowski et al., 2007).

The use of PVP using APS have also been discussed stating that the persulfate ion generates a free radical reaction on the carbon-carbon main chain to induce the cross-linking within the PVP molecules (Anderson, Rodriguez, & Thurston, 1979; Bi et al., 2013; Kang, Kim, & Lee, 2003; Ingrid Maria Wienk, 1993; W. Xu, Chen, Li, & Wang, 2005). After the HPVDF membranes were incorporated with PVP and PAA layers, the CA decreases and surface free energy increases simultaneously, as shown in Table 4.2. In this table, the calculated surface free energies are slightly higher than the references due to the porous outer surface of the membranes and the flattening caused in order to make the measurement.

4.3.2.2 Characterization of Functionalized Sponge-like Membranes

Infrared spectroscopy was used to characterize the hydrophilization and the functionalization of the membranes with PVP and PAA, respectively. First, the PVP cross-linking was established alone, since the concentrations used on the membranes were too low to describe the process by ATR-FTIR. On the Figure 4.12a, ATR-FTIR spectra show the PVP powder before and after the treatment with APS (PVP cross-linked). The empirical transmittance bands for the PVP are consistent with those previously reported in literature (Basha, 2010).

The two characteristic peaks at 2361 and 2338 cm^{-1} are distinctive of the PVP spectrum. A broad peak (3399 cm^{-1}) shows the higher presence of overlapping O-H and N-H groups in the hydrophilization process. The presence of free and numerous hydroxyl groups plus hydrogen bonds from residual water enhanced this band. There are also shifts in the symmetric CH_2 stretches (2920 to 2924 cm^{-1}), the carbonyl group stretches (C=O) (1651 to 1647 cm^{-1}), the amine group stretches (C-N) (1420 to 1424 cm^{-1}) and the CH bends (1273 to 1288 cm^{-1}). This behavior is characteristic to water absorption (L. S. Taylor, Langkilde, & Zografi, 2001). It is worth noting the addition of C-O stretches corresponding to ether group at 1045 and 1215 cm^{-1}. This implies that the persulfate not only initiates a free radical cross-linking of PVP, but could also intervene in the ring-opening and etherification of the molecules.

Table 4.2. Contact angle and Surface Free Energy for HF membranes of at different steps of hydrophilization. Reference values are from pure or coated materials. PAA, poly(acrylic acid); PVP, polyvinylpyrrolidone; HPVDF, PVDF hollow fiber membrane. All measurements were done by triplicate in different zones of the membrane. Reprinted from (Hernández, Lei, et al., 2016). Copyright (2016) American Chemical Society.

Treatment Steps of the HPVDF	**Advancing Contact Angle θ_A (°)**	**Receding Contact Angle θ_R (°)**	**Surface free energy* γ_S^{TOT} (mJ/m²)**	**Ref. Static Contact Angle θ (°)**	**Reference γ_S^{TOT} (mJ/m²)**
Hydrophobic HPVDF Membrane	76.3 ± 0.7	58.3 ± 1.2	40.26	72.5 (Duca et al., 1998)	33.2 (S. Wu, 1971)
Hydrophilization with PVP	60.3 ± 1.2	39.7 ± 1.3	49.79	50.0 - 60.0 (Hayama et al., 2004)	43.4 (DeMejo, Rimai, & Sharpe, 1999)
Functionalization with PAA	57.3 ± 2.0	30.3 ± 0.9	50.68	45.8 (O'neill, O'hare, & Goodwin, 2006)	No data

*Calculated surface free energy value for water: γ_L = 72.7 mJ/m^2 at 20 °C (Vargaftik, Volkov, & Voljak, 1983).

In the Figure 4.12b-c the polymer functionalization on the membrane surface is shown. The presence of little transmittance bands is because of small amounts of material applied to the membranes, as explained before. The average mass gain for PVP (Δm = 5.20 g/m^2) is slightly higher than the reported (Bi et al., 2013). For PAA, Δm = 5.04 g/m^2. Both Δm can contribute to the obstruction of the pores. All spectra show the characteristic peaks of the C-F and C-F_2 bonds in the range of 1100 and 1500 cm^{-1} (Figure 4.12b) without shifting, proving the chemical and thermal stability of the HPVDF under these processes. The HPVDF spectra before and after functionalization shows an addition at 1678 cm^{-1} from the ionized carbonyl group from the PAA polymerization. After the functionalization with PAA, the carbonyl band is shifted to 1674 cm^{-1} and a non-ionized band at 1732 cm^{-1} appears due to water absorption too. There are also shifting and small increases in the symmetric and asymmetric CH_2 bands (2924 and 2959 cm^{-1}) due to the extra chains from the PVP and PAA polymers.

4.3.3 Membranes Functionalized by Redox Polymerization

The ATR-FTIR spectra of the functionalized membranes compared to the bare MPVDF (C-F/C-F_2 groups between 1100 and 1500 cm^{-1}) in Figure 4.13 show the addition of the C=O at 1740 cm^{-1}, and broad peaks between 3000 and 2500 cm^{-1} demonstrating the presence of O-H from the hydrogel synthesized (Figure 4.13b). The presence of brown color due to the presence of hexaaquairon (III) diminishes the transmittance by an unclear signal, reflected in the noise of the spectra showed in the sole hydrogel and the functionalized membranes.

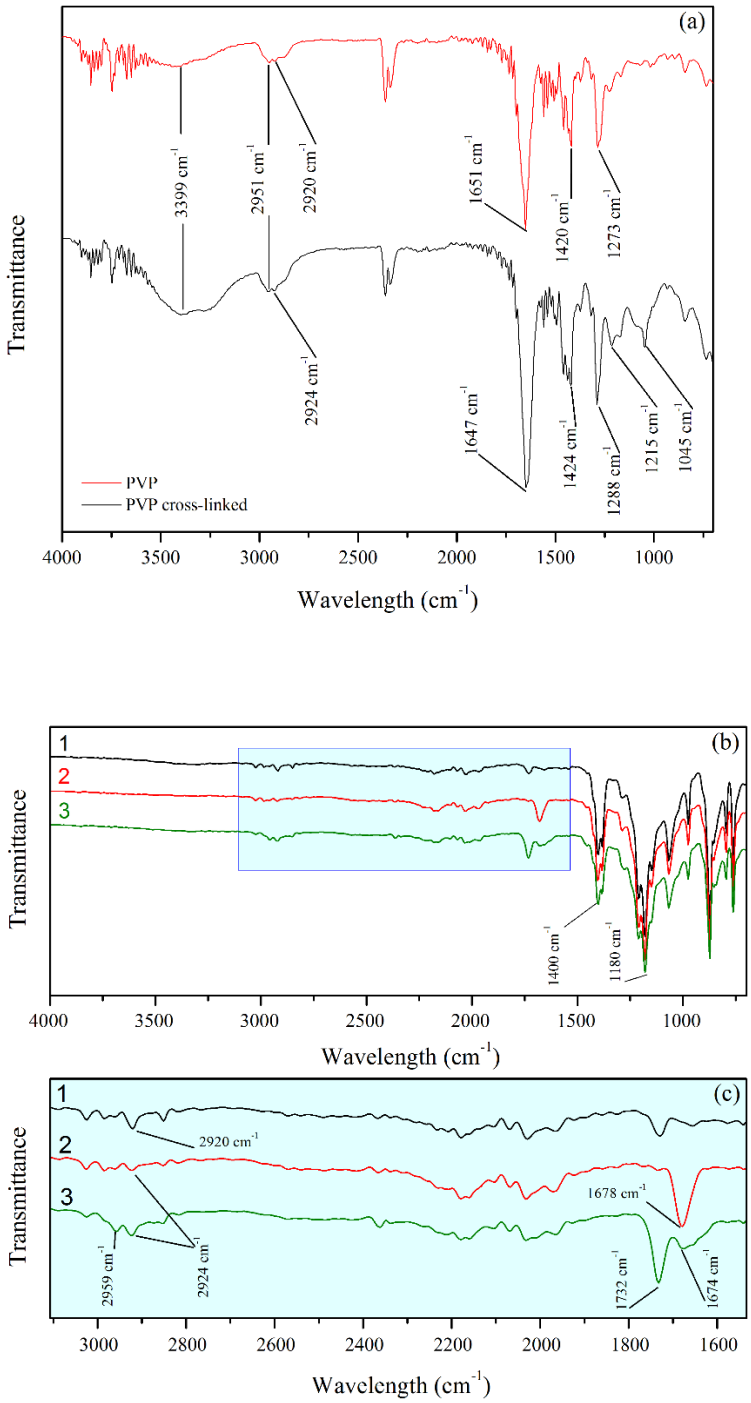

Figure 4.12. (a) ATR-FTIR spectra of PVP before and after treatment (PVP cross-linked) with APS on HPVDF membranes. (b) ATR-FTIR spectra of (1) hydrophobic HPVDF membranes, (2) HPVDF membranes after PVP hydrophilization and (3) HPVDF membranes after hydrophilization and subsequent functionalization with PAA. (c) Zoom-in of spectra showing the absorption bands of the PVP and PAA components. Reprinted from (Hernández, Lei, et al., 2016). Copyright (2016) American Chemical Society.

Bare MPVDF membrane (Figure 4.14a) shows a porous structure and the thickness is around 120 μm (125 μm from manufacturers data). After polymerization, the PAA spreads in the whole porous media of the membrane (Figure 4.14b), covering several areas at the interior of the membrane structure. On the surface, MPVDF membrane (Figure 4.14c) appears more open than the MPVDF-PAA (Figure 4.14d) that has a cover of polymer on the surface. MPVDF has a nominal diameter of 650 nm according to manufacturer's data. The MPVDF-PAA pore size was calculated from SEM images measuring the pore sizes in a defined area and generating an average value of 690 ± 58 nm. In addition, an analysis of the pores at higher magnification after polymerization (Figure 4.14e) and after reduction (Figure 4.14f) showed pore sizes near 600 nm. These are lower than the bare MPVDF membrane due to some polymer formed on the surface.

XPS comparative spectra of the membranes show that the fluorine/carbon ratio is near to the PVDF value (1:1) (from MPVDF membrane) with a decrease due to the presence of carboxylic groups (Figure 4.4c-d). In the Figure 4.4d, is also shown a presence of iron and a small amount of nitrogen on the surface of the membrane that is not perceived in the xerogel alone. The explanation for this phenomenon is that iron diffuses from the interior of the membrane to encounter the sulfate radical and the reaction initiates on the surface. Although this happens on the hydrogel system too, is more notorious in the membrane due to the mobility restriction within the pores. This also could explain the low amount of iron inside the membranes.

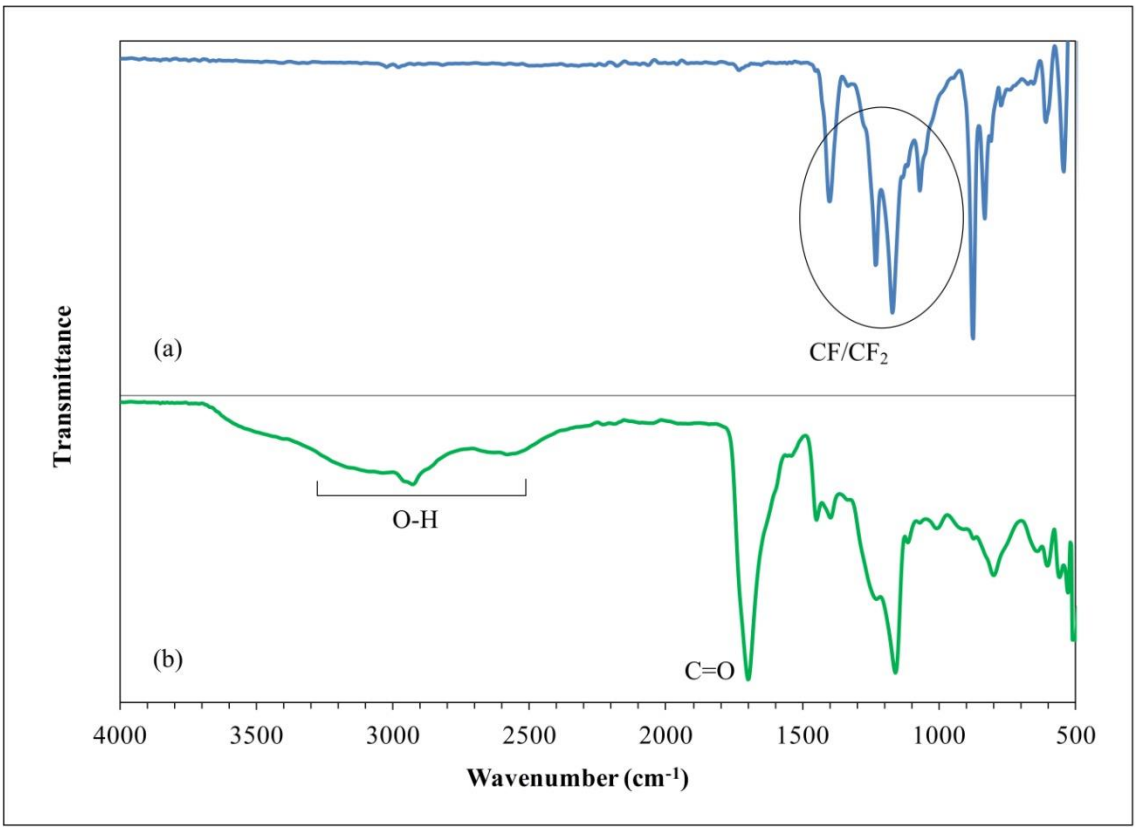

Figure 4.13 ATR-FTIR spectra of membranes. (a) MPVDF membrane; (b) MPVDF-PAA membrane. Reprinted from (Hernandez et al., 2014). Copyright (2014) American Chemical Society.

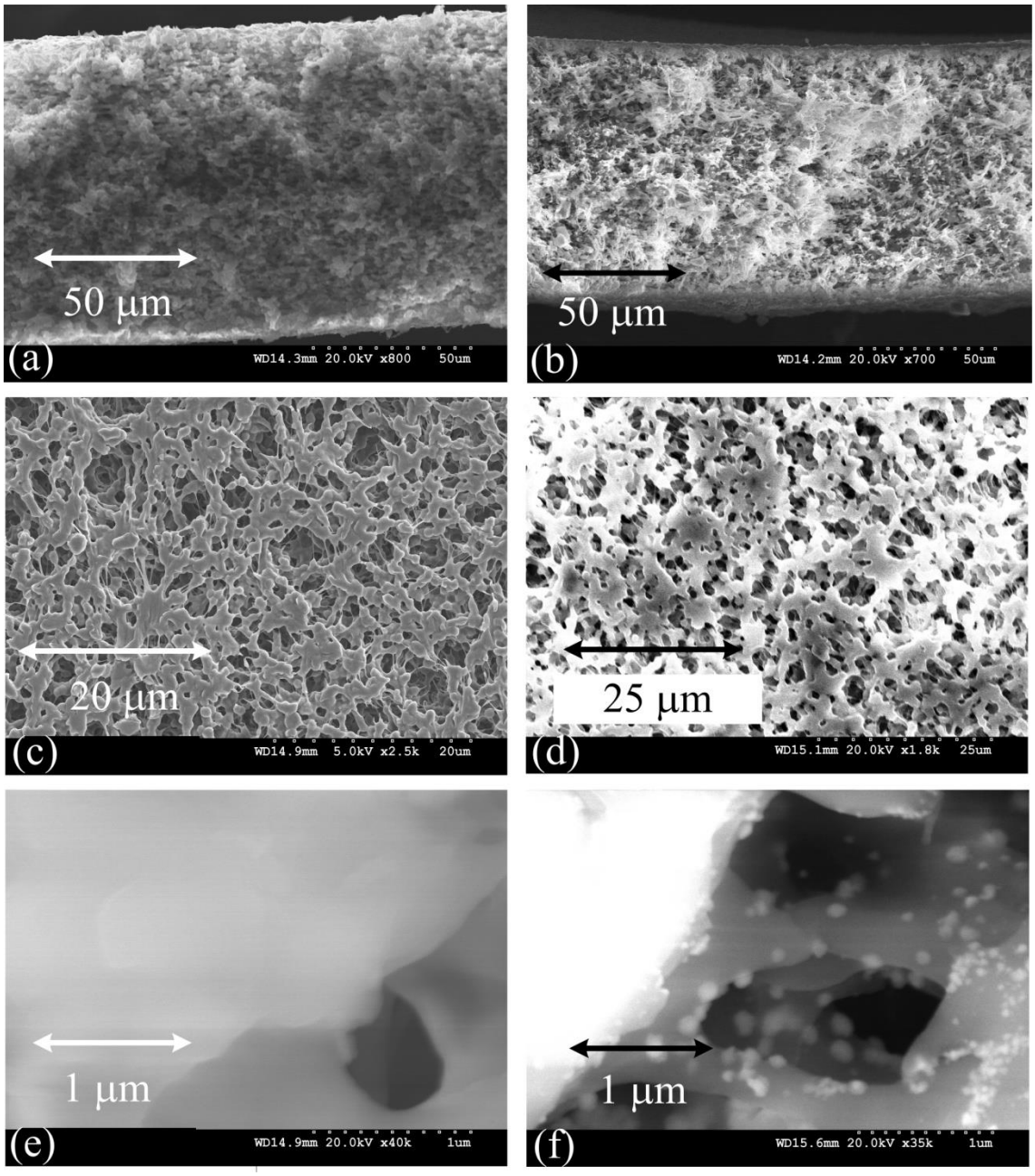

Figure 4.14. SEM images of bare MPVDF, MPVDF-PAA and MPVDF-PAA-Fe membranes (Millipore). (a) Cross section bare MPVDF; (b) Cross section MPVDF-PAA, (c) Porous surface MPVDF-PAA; (d) Porous surface MPVDF-PAA-Fe. Reprinted from (Hernandez et al., 2014). Copyright (2014) American Chemical Society.

Prior to the surface analysis, an etching procedure with an argon ion gun was performed. This procedure only analyzes the surface of the material and penetrates a few nm. However, it can show the trend of the elements composition through the material. The results of the XPS etching are shown in the Figure 4.15a. These show that the oxygen is more present on the surface of the membrane and decreases to a stable value of 13%. The amount of fluorine tends to be stable around 11%. Due to the presence of oxygen, the ratio of fluorine/carbon decreased from the theoretical 1:1 for PVDF to near 1:5 for the MPVDF-PAA (Figure 4.15b). The etching shows that, although the polymerization takes place in the surface level, it spreads into the membrane's interior. On the other hand, the amount of iron is stable lengthwise too with a value of 0.25%, which is lower than the one on the surface of 2.47 % (Figure 4.4d). This also confirms the diffusive behavior of iron to initiate polymerization.

Knowing that PAA is present in the interior and surface of the membrane, a pH effect on the water flux due this presence is shown in Figure 4.16. Due to high swelling at high pH values in the cross-linked PAA, hydrogel mesh size increases along with its total volume and in consequence, membrane pore size would decrease. The linear relationship between applied pressure (ΔP) from 1 to 4 bars and flux (J_v) illustrates a solid pore PAA functionalization and the change in the permeability of the membranes (slopes in the Figure 4.16).

The losses of PAA due to the low pressure applied are negligible due to the fact that these type of hydrogels has a certain degree of stickiness (W. Li, Zhao, Teasdale, John, & Zhang, 2002).

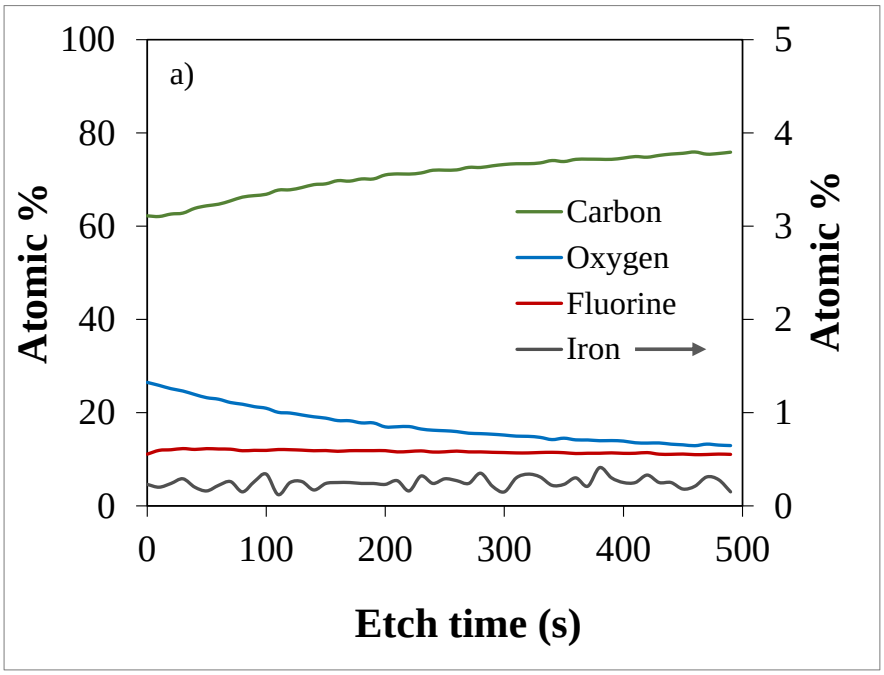

Figure 4.15. XPS etching in MPVDF-PAA membranes (Millipore) by redox polymerization. (a) Atomic percentage composition, (b) Atomic ratio based on carbon element. Reprinted from (Hernandez et al., 2014). Copyright (2014) American Chemical Society.

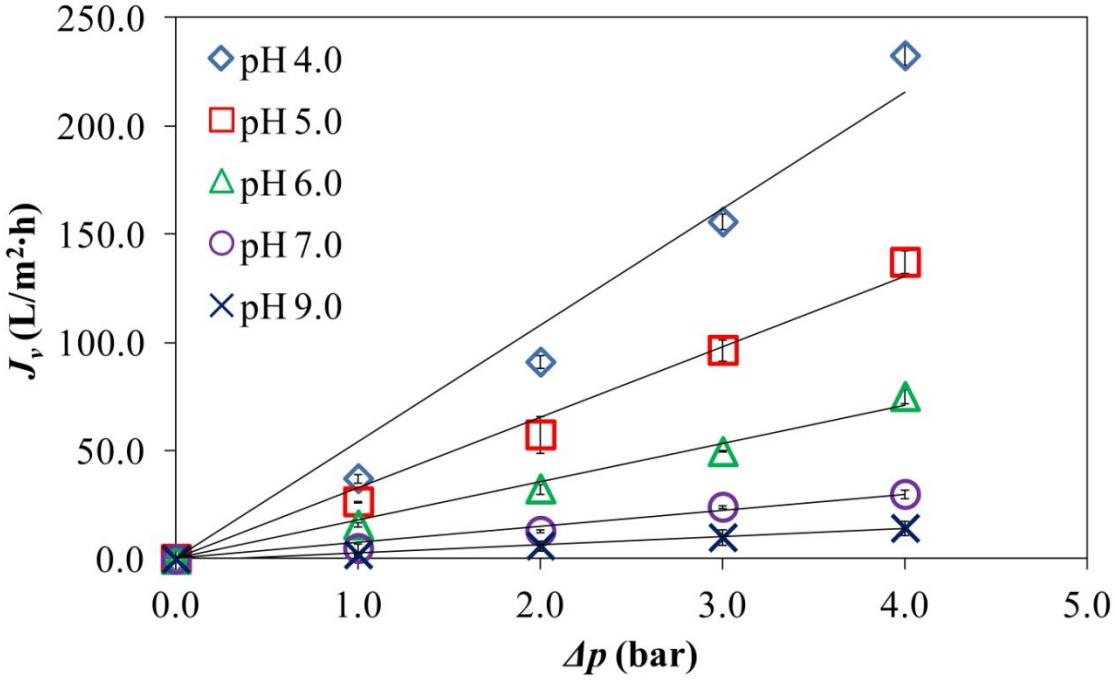

Figure 4.16. pH responsive flux in MPVDF-PAA membranes using convective cross-sectional flow. PAA content = 8.5 wt. %. Area MPVDF-PAA membrane = 13.2 cm^2. Cross-linking degree, *X* = 1% NMBA. T = 22 °C. All measurements were done by triplicate, calculating the respective deviations and standard errors of the means. Error bars are inside each symbol. Reprinted from (Hernandez et al., 2014). Copyright (2014) American Chemical Society.

In addition, some works report that fracture stresses are reached at 130 bar (Peak, Wilker, & Schmidt, 2013). Assuming cylindrical pores, no change in membrane thickness, and unchanged porosity in the MPVDF-PAA membranes (uniform cross-linked PAA distribution within pores), effective diameters can be estimated by applying Hagen-Poisseuille's modified equation (Smuleac et al., 2010b):

$$\frac{A_F}{A_0} = \left(\frac{d_p}{d_{p0}}\right)^4 \tag{4.23}$$

where A_F is the permeability at different pH values of MPVDF-PAA membrane, A_0 is the permeability of the bare MPVDF membrane to pure water, d_p is the equivalent pore diameter of the MPVDF-PAA at defined pH and d_{p0} the diameter of bare MPVDF membrane. Taking d_{p0} = 650 nm from manufacturer's data and a measured A_0 = 3800 L/ (m^2·h·bar) (LMH/bar), the calculated values of pore diameter at different pH values showed that pore size is more open at low pH values (Table 4.1). An approximated 50% decrease in pore size by shifting the pH from 3.0 to 9.0, with a simultaneous increase in the polymer mesh size is obtained.

The differences between these calculations and the observed by SEM (MPVDF-PAA = 690 ± 58 nm) are due possibly to that each membrane is dehydrated for sample preparation and thus, the polymer returns to its xerogel size opening the membrane pores. The mesh size values calculated in the hydrogel characterization (only 4 pH values were reported due to the loss of hydrogel material during swelling, increasing error of measurement) have an inverse relationship with permeability, as expected due swelling of the hydrogel, limiting the flux through the membrane's pores, see Figure 4.17. An increase from 5.89 to 8.33 nm for ξ represents great changes in the hydrogel macro-structure

creating almost a 93% of decrease in the permeability of MPVDF-PAA membranes from redox initiation (Table 4.1). This calculated mesh size is small compared with other works, giving the advantage of preventing NP aggregation (N. Peppas & S. Wright, 1996; Thakur et al., 2011a).

4.4 MEMBRANE FUNCTIONALIZATION FOR OmpF IMMOBILIZATION

The immobilization OmpF using LbL functionalization within the pores of polyvinylidene fluoride (PVDF) membranes is performed after two layers: PAA hydrogel, polymerized in situ, and poly(allylamine hydrochloride) (PAH) accumulated by convective flow. The exposed charged residues of OmpF were then crosslinked by a last layer of poly(styrene sulfonic acid) (PSS). The membranes were analyzed during each stage of the process including comparisons between LbL membranes with and without OmpF.

4.4.1 Membrane Selection

The microfiltration polyvinylidene fluoride (PVDF) membranes by Nanostone that were first considered in this study possessed different fluxes and pore size distributions. First, as shown in Table 4.3, a sponge-like membrane with a different concentration of AA was considered (SPVDF) but due to its thickness and low flux it was discarded expecting higher pore clogging once the other layers were placed onto it.

The next considered membrane was the PV700 due to its higher flux and functionalization values. Figure 4.18a shows the SEM image of PV700. Using ImageJ to measure pore perimeter and idealize pores into perfect cylinders to calculate an effective diameter, the average pore diameter of PV700 was 35 ± 20 nm.

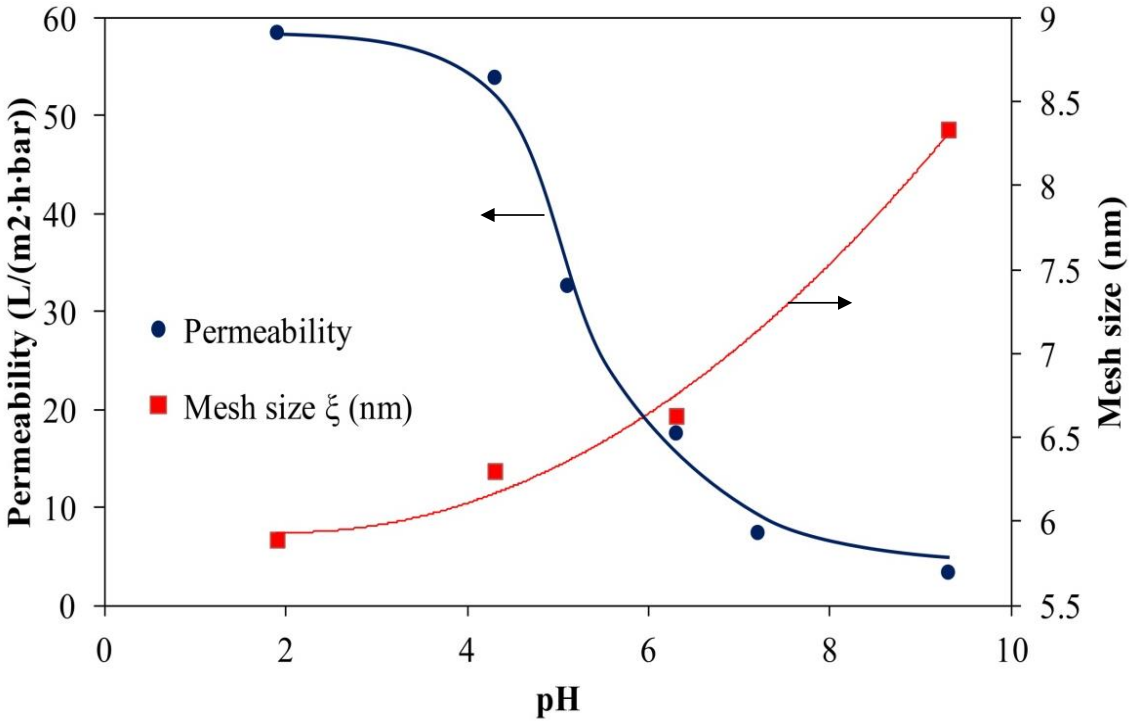

Figure 4.17. Permeability and mesh size in MPVDF-PAA membranes using convective cross-sectional flow. Continuous lines are regressions based on data. PAA content = 8.5 wt. %. Area MPVDF-PAA membrane = 13.2 cm^2. Cross-linking degree, *X* = 1% NMBA. T = 22 °C. All measurements were done by triplicate, calculating the respective deviations and standard errors of the means. Error bars are negligible. Adapted from (Hernandez et al., 2014).

Table 4.3. Flux, mass gain and carboxylic functionalization values of different Nanostone membranes. All measurements were done by triplicate, calculating the respective deviations and standard errors of the means. Errors are negligible. Reprinted from (Porter et al., 2017). PV200, Nanostone PVDF 50 kDa membrane; PV700, Nanostone PVDF 35 nm membrane; SPVDF, Nanostone PVDF sponge-like membrane.

Membrane	**Pure water Flux without PAA (LMH) at 2.04 bar**	**Mass without PAA (g)**	**Mass with PAA (g)**	**# of Carboxylic Groups (mmol)**
SPVDF	93.6	0.2654	0.2851	0.27
PV200	700.2	0.1817	0.2102	0.39
PV700	2182.3	0.1572	0.2007	0.60

The large standard deviations indicate that PV700 possesses pores of large variation. Figure 4.18b derived from the samples in the SEM images, depicts the histogram of PV700 pore sizes. PV700 has a distribution skewed toward lower values, with a significantly dominant population residing in 18.6-26.0 nm bin.

Although PV700's highly populated bins have lower values than the most populated size bins of PV200 (Figure 4.19a), its biggest pores are actually significantly larger. In the two samples taken, PV200's largest pore measured had a diameter of 149 nm while PV700's largest pore was 181 nm. The top largest 1% of measured pores from PV200 had an average diameter of 126 ± 16 nm while PV700's biggest 1% averaged 158 ± 17 nm. PV700's largest 1% exceeded that of PV200's by a whopping 25% while its average pore diameter was 27% lower. Such a large gap between pore size median and maximum made PV700's membrane initially less attractive for immobilizing biomolecules that come in definitive individual and aggregate sizes. For these reasons, it was selected the PV200 membrane. PV200 has a fairly porous, intricate surface of different pore shapes and sizes with an upper limit of 140 nm (Figure 4.19b).

On the other hand, the polycarbonate membrane of 50 nm pore size (PC50) has more uniform pores, as expected. Histograms of the size distributions for both PV200 and PC50 (Figure 4.19b, d) reveal an average pore diameter of 48 ± 1 nm and 75 ± 1 nm, respectively. For PV200, pore size distribution was well fitted with both lognormal and gamma distributions, with the latter being more adjusted. The Kolmogorov-Smirnov parameter was $D = 0.046$, with probability $p = 0.051$ for lognormal and $D = 0.038$, $p > 0.25$ for gamma functions.

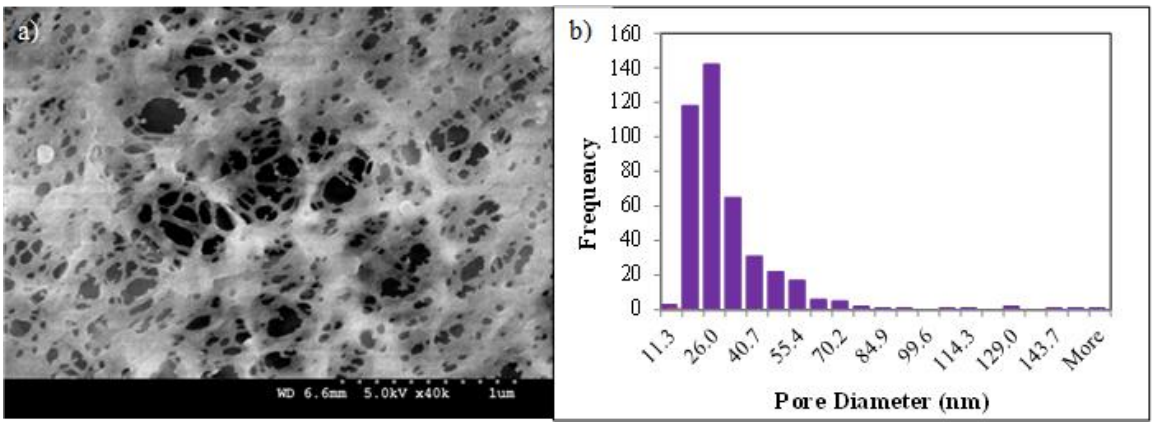

Figure 4.18. PVDF membrane characterization. (a) Top surface PV700, (b) Pore size distribution of PV700. Reprinted from (Porter et al., 2017).

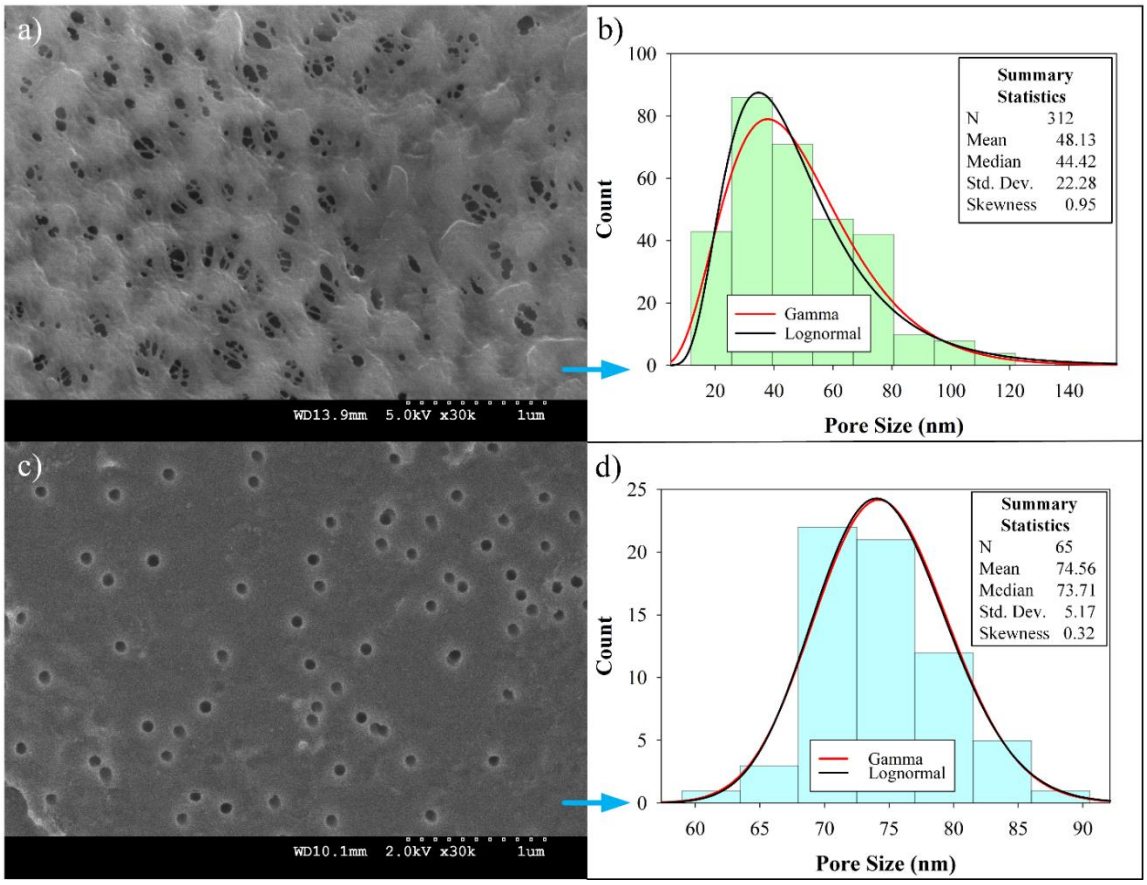

Figure 4.19. Bare membrane characterization. (a) Top surface PV200 microfiltration membrane; (b) Pore size distribution of PV200 membrane; (c) Top surface PC50 membrane; (d) Pore size distribution of PC50 membrane. Reprinted from (Porter et al., 2017).

PV200 provides pores that are large enough for LbL-assembled polyionic layers and the subsequent addition of OmpF aggregates without complete collapse. For PC50, the median pore diameter is 74 nm, closer to its mean value than PV200. Skewness is low for gamma and lognormal distribution models and standard deviation is low, suggesting highly consistent pores and more normal goodness-of-fit distribution parameters (D = 0.085, p = 0.170 for lognormal and D = 0.082, p = 0.209 for gamma).

4.4.2 Determination of Optimal First Layer

PAA was initially functionalized onto PV200 membranes at proportion of 1 gram acrylic acid (AA) to 5 grams water (2.31 M of AA) with KPS and MBA, respectively. However, this quantity of AA was shown to diminish water permeation at a pH ≈ 7 and 4.08 bar from 968 ± 63 (LMH/bar) in the non-functionalized PV200 membrane to only 7.7 ± 1.8 LMH/bar. Such low flux required at least ten hours for the subsequent second functionalization layer via convective flow of dissolved PAH. Pores were extremely tight with PAA-PAH functionalization, resulting in water permeation (pH ≈ 7 and 4.08 bar) of 0.45 LMH/bar. Such tight pores likely could not hold OmpF aggregates; at the proportions of water, acid, and NaOH used in the OmpF solution.

Trials with mass proportions of AA to water of 1:7.5, 1:10 and 1:20 revealed that 1:7.5 still produced a tight membrane, 1:10 allowed for observable functionalization of PV200, verified by using pH studies and mass-gain, and 1:20 showed no observable functionalization in PV200, see Figure 4.20. Functionalization is desirable to provide charges to help stabilize the immobilization of OmpF. Previous works shown that LbL assembly can increase immobilization of biomolecules by 25-fold (Smuleac et al., 2006). Average water flux through 1:10 promised a high likelihood that subsequent

functionalization with PAH would result in pore sizes that were fitting for immobilization of OmpF aggregates.

4.4.3 Verification of Ionic Polymer Layers and Functionality

Besides observing a mass gain, a PAA pH responsiveness was observed, represented in Figure 4.21. Three cycles demonstrate the pH responsiveness of PAA. Flux decreases at a higher pH, the extent to which is dependent on several factors like the quantity of PAA, initial size of pores, and degree of cross-linking. Consistent changes in permeability depending on pH also demonstrate the stability of this membrane. A particular ratio of DIUF permeability (A) at a pH = 3 compared to pH = 8 is observed. For this particular PV200-PAA membrane, A_{pH3}/A_{pH8} fluctuates between 17.8 ± 0.4 and 10.2 ± 0.6 LMH/bar for low and high pH's, respectively. In Figure 4.21, it is also shown that with the addition of PAH, this pH responsiveness is not observable. Although there is still a swelling within the polymeric layers of PAA at high pH, PAH contracts simultaneously, and vice versa, rendering any observable functionality null, with a balance of charged functional groups. For this PV200-PAA-PAH membrane, the permeability is in effect constant (6.3 ± 0.2 LMH/bar) at any pH.

Surface charge measurements verify the presence of each polymer layer. Each layer builds upon the next, with functional groups of the most recently added layer influencing the ζ potential. They show negative values when negatively charged ionization is present and positive for positively charged groups. Neutral surfaces change charge from positive to negative throughout the range of pH.

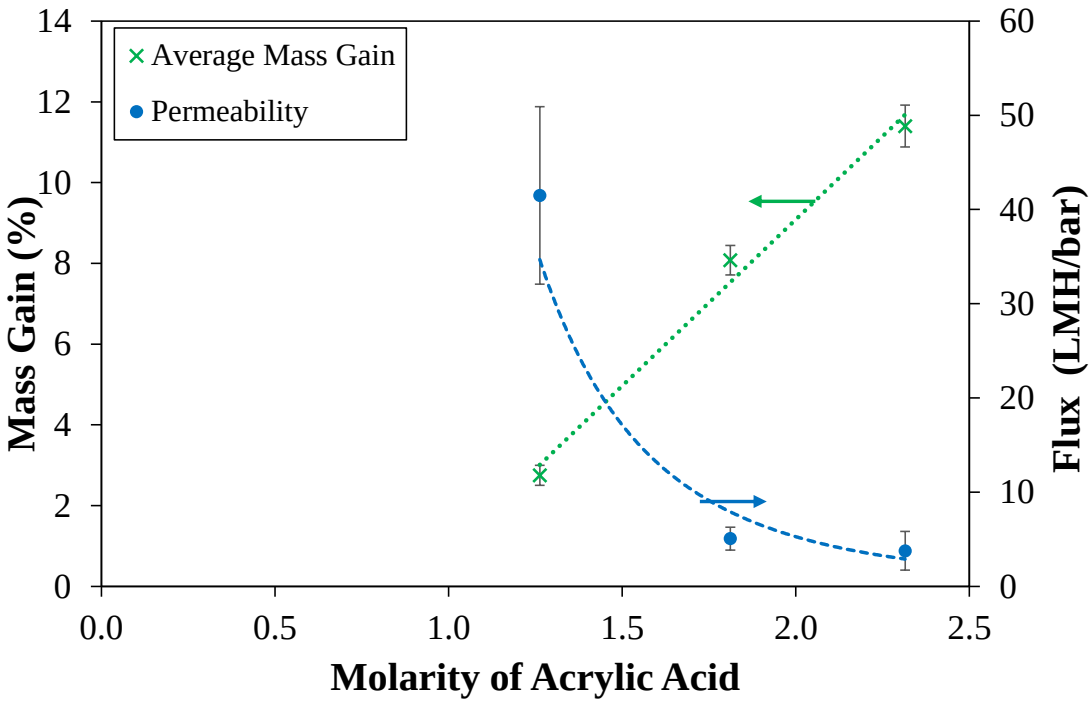

Figure 4.20. Concentrations of acrylic acid before polymerization as a function of polymer mass gain in PV200 membrane and respective flux. All measurements were done by triplicate, calculating the respective deviations and standard errors of the means. Reprinted from (Porter et al., 2017).

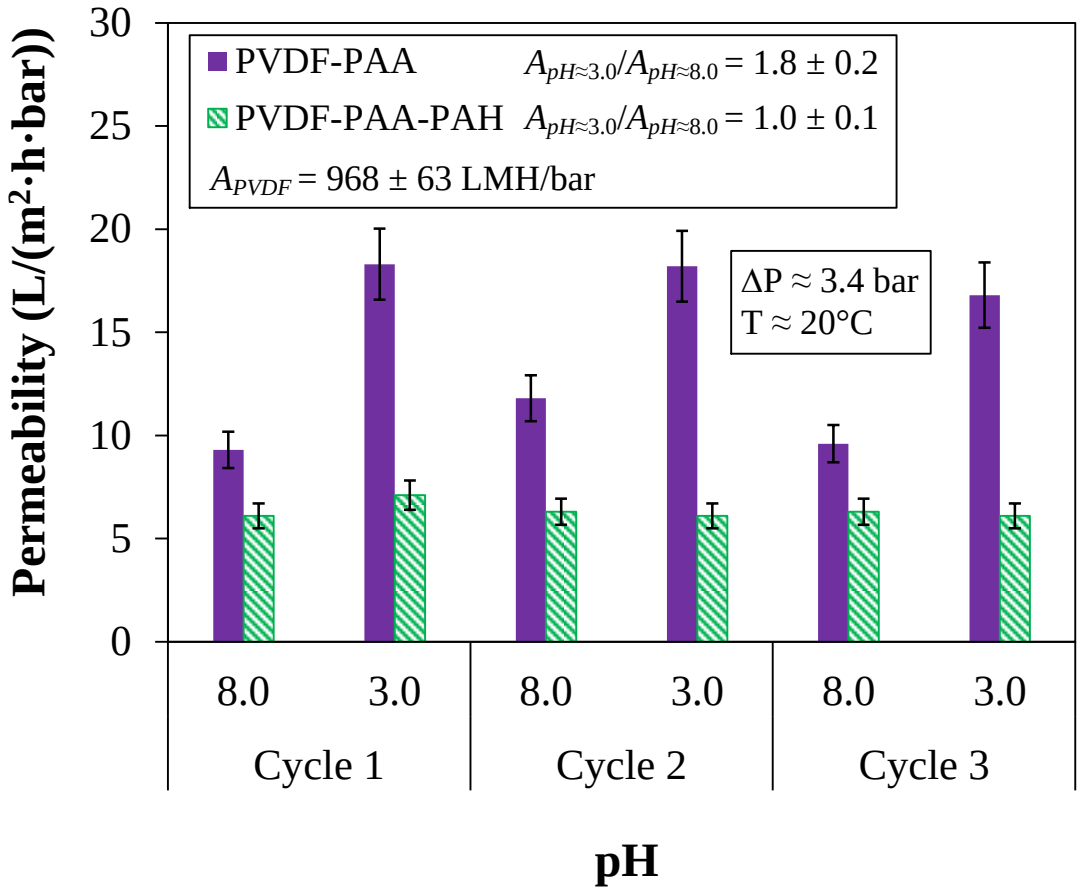

Figure 4.21. Water permeability and pH responsiveness in two layer-by-layer functionalization. Membrane used: PV200, original pore size of 48 ± 1 nm. Monomer concentration before polymerization = 1.26 M AA. A_{PVDF} is the permeability of the bare PV200 membrane to DIUF. All measurements were done by triplicate, calculating the respective deviations and standard errors of the means. Reprinted from (Porter et al., 2017).

As seen in Figure 4.22, the bare PV200 membrane has slightly acidic behavior, PV200-PAA shows negative behavior, and PV200-PAA-PAH is, positive as expected. PV200-PAA-PAH-OmpF-PSS in this case is neutral, likely because there is a balance of charges between OmpF exterior residues and the PSS layer.

4.4.4 Permeability throughout Each Layer

Additional layers within a channel reduce the diameter of the channel and thus also decrease the permeability of water, unless hydrophilicity is increased. Measurements of permeability of DIUF at pH 7.0 throughout functionalization are presented in Figure 4.23. Indeed, overall permeability decreases with each additional layer, from 968 ± 63 LMH/bar for the bare membrane to a final 2.6 ± 0.3 LMH/bar for PV200-PAA-PAH-OmpF-PSS. Also, a membrane is presented here with all polymeric layers including the same quantity of PSS permeated but excluding OmpF. A greater pickup of PSS in this membrane likely occurred due to the fact no OmpF are present and thus more positive charges from amine groups in PAH are available to bond to deprotonated, negative carboxylic groups in PSS. Unlike OmpF, this polymer layer does not inherently contain pores, so increased grafting of PSS decreased flux.

On the other hand, increased grafting of properly aligned OmpF within the pore could actually increase flux because OmpF contains positive and negative residues on opposite sides within the tightest midsection, rendering this area polar and highly hydrophilic at neutral pH (Aguilella, Queralt-Martin, Aguilella-Arzo, & Alcaraz, 2011). Thus, membranes without OmpF have, on average, a slightly smaller permeability (1.5 ± 0.5 LMH/bar) than with OmpF (2.6 ± 0.3 LMH/bar). From these results, an effective pore diameter was calculated using Equation (4.23). Note that the effective pore size based on

flow is larger for membranes with OmpF than for the non-OmpF membranes. Individual pores of OmpF are not that large, however, and properly aligned OmpF cannot be determined, but this value suggests a larger permeability due to presence of OmpF.

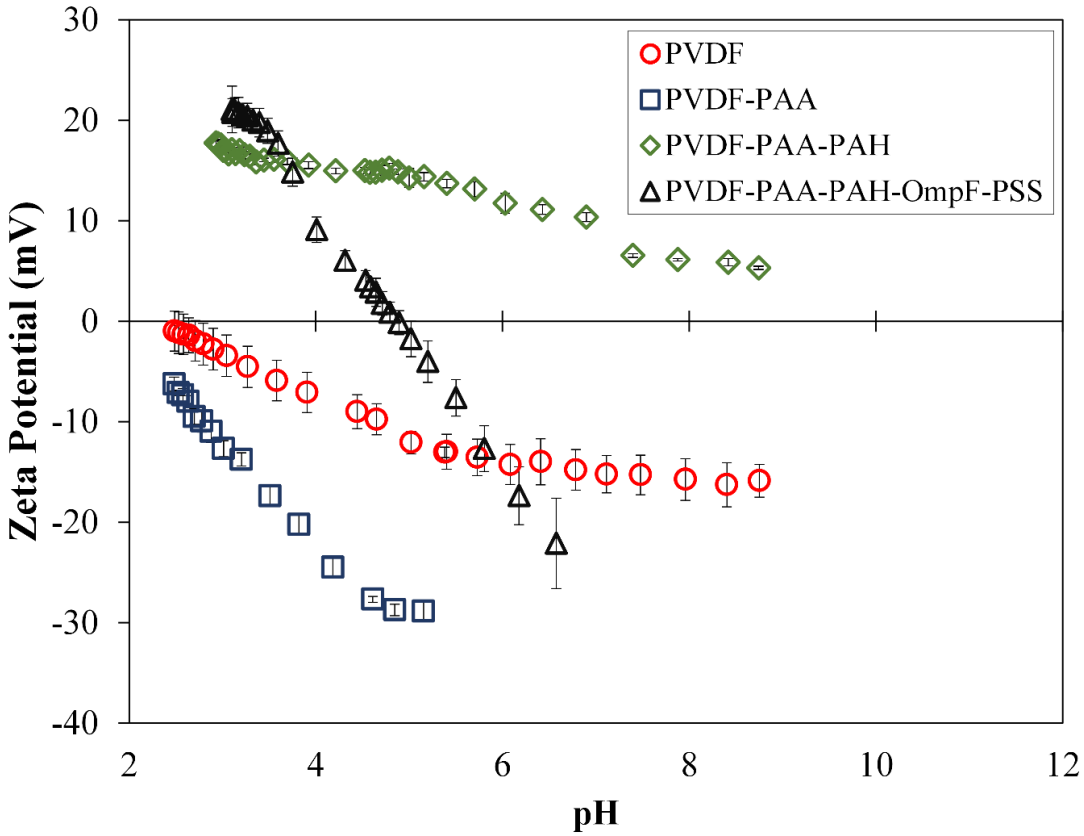

Figure 4.22. Zeta potential due to pH change in each step of layer-by-layer functionalization. Membrane used: PV200, original pore size of 48 ± 1 nm. PAA weight gain ≈ 3.0%. PAH:PAA = 2/1 molar, PSS:PAA = 1/1 molar; OmpF permeated: 1.74 g/m^2 of PV200 top surface. All measurements were done by triplicate, calculating the respective deviations and standard errors of the means. Some error bars are inside the symbols or are neglibible. Reprinted from (Porter et al., 2017).

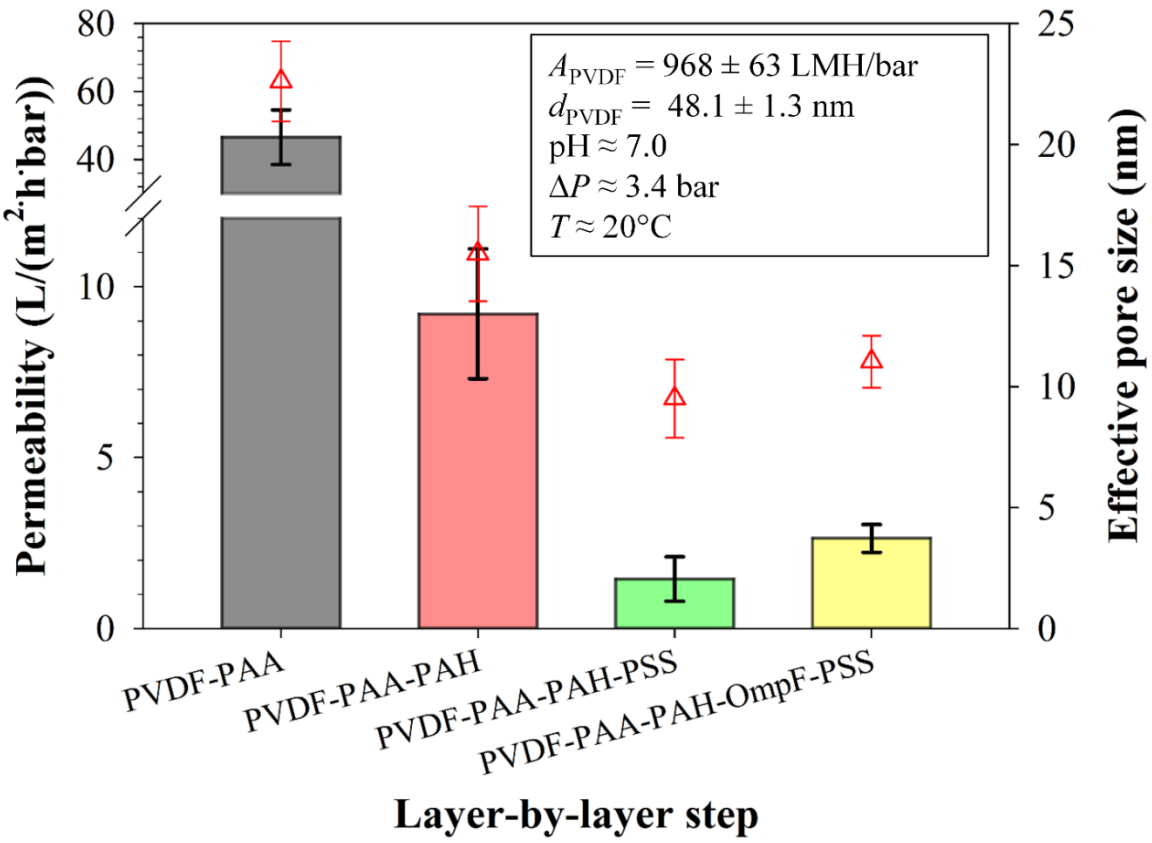

Figure 4.23. Permeability and pore size change of functionalized PV200 membrane per step of layer-by-layer functionalization. PAA weight gain ≈ 3.0%; PAH:PAA = 2/1 molar, PSS:PAA = 1/1 molar. A_{PVDF} and d_{PVDF} are the permeability and the effective pore diameter of the bare PV200 membrane, respectively to DIUF water. All measurements were done by triplicate, calculating the respective deviations and standard errors of the means. Reprinted from (Porter et al., 2017).

5 NANOPARTICLE SYNTHESIS

As described in Chapter 4, the PAA hydrogel synthesized in situ alone and within the PVDF membrane structure is used for iron and iron/palladium nanoparticle (NP) formations after ion exchange. This chapter describes the nanoparticle synthesis procedure and their characterization in solution and immobilized within the PAA alone or within the functionalized membranes. Parts of this chapter are published in (Hernández, Lei, et al., 2016; Hernandez et al., 2014).

5.1 IRON AND IRON/PALLADIUM NANOPARTICLE SYNTHESIS

The importance of synthesizing NPs for catalysis lies in the increment of the specific surface area and the edge effects of particle, which made it more effective in electrochemical interactions than the bulk material (X. Q. Li & Zhang, 2006; Noubactep, 2009; C.-B. Wang & Zhang, 1997). Better catalytic yields are not only related to higher specific surface areas but to the combination of these areas with the catalytic properties (oxidative or reductive) proportionated by atoms that are on the edges of the particle (X. Q. Li & Zhang, 2006; Lu et al., 2007; Ni & Wang, 2015).

5.1.1 Reactions for Nanoparticle Formation

Iron NPs can be formed by chemical reduction, tea phenols, vitamin B, and plant extracts (Nadagouda, Castle, Murdock, Hussain, & Varma, 2010; Nadagouda, Hoag, Collins, & Varma, 2009; Nadagouda, Polshettiwar, & Varma, 2009; Smuleac, Bachas, & Bhattacharyya, 2010a). Previous works showed that the tea extract, used as reducing agent, acts as capping agent, which makes some of the NPs surface less available for Pd deposition

in the post-coating (Smuleac et al., 2011). In this work, chemical reduction using only $NaBH_4$ was performed.

The reduction of iron to form zero-valent NPs (Fe^0) needs a $NaBH_4/Fe^{3+}$ ratio of about 2.1 to 2.5:1 (see Equations (5.1) to (5.3)) (Glavee, Klabunde, Sorensen, & Hadjipanayis, 1995; Feng He & Zhao, 2008; Y. P. Sun, Li, Cao, Zhang, & Wang, 2006). Depending on pH and temperature conditions, Fe^{2+} oxidizes to Fe^{3+} and be reduced by $NaBH_4$ which simultaneously can react with water producing hydrogen gas (Feng He & Zhao, 2008; Y. P. Sun et al., 2006; W.-x. Zhang, 2003).

$$Fe^{2+} + 2BH_4^- + 6H_2O \rightarrow Fe^0 + 2B(OH)_3 + 7H_2 \quad (5.1)$$

$$BH_4^- + 2H_2O \rightarrow BO_2^- + 4H_2 \quad (5.2)$$

$$Fe^{3+} + 3BH_4^- + 9H_2O \rightarrow Fe^0 + 3H_2BO_3^- + 12H^+ + 6H_2 \quad (5.3)$$

Once Fe^0 NPs are formed, a post-coating with palladium, in concentrations between 1 to 5 wt. %, is used to form bimetallic Fe/Pd NPs (Equation (5.4) (Smuleac et al., 2010b; Smuleac et al., 2011; C.-B. Wang & Zhang, 1997)). Pd is reduced on the Fe NP surface due to iron corrosion, see Equation (5.4).

$$Pd^{2+} + Fe^0 \rightarrow Fe^{2+} + Pd^0 \quad (5.4)$$

5.1.2 Nanoparticle Morphology

Different studies, most of them with NPs in solution, have shown that the composite structure of the constituent Fe^0 NPs consists of a core of zero-valent iron and a thin shell of iron oxide (J. H. Kim, Tratnyek, & Chang, 2008; Y. Liu et al., 2005; Nurmi et al., 2005; Ramos, Yan, Li, Koel, & Zhang, 2009). The core has shown a cubic crystal structure with

a Fe-Fe formation with bond distances of 2.25 Å and a coordination number of 9.66 for the body centered structure (Lin, Chang, & Chuang, 2008). It has been found that the fine oxide layer ranges from 2 to 20 nm (J. H. Kim et al., 2008; Nurmi et al., 2005; Ramos et al., 2009). The amorphous structure of the oxide layer, as seen in Figure 5.1, seemingly determines the spherical shape of the NPs by simultaneously passivating and covering the reactive core edges (Ramos et al., 2009). This spherical structure is formed instantaneously on the NPs surface and it has not found that the periodic lattice of the core penetrates into the oxide layer (Nurmi et al., 2005). Additionally, the amorphous characteristic of the oxide layer suggests the presence of defects on the surface, which can be seen in Figure 5.1, offering passages for electron transfer and preserving the reductive properties of the zero-valent iron (X. Q. Li & Zhang, 2006; Ramos et al., 2009).

Other considerations in the formation of Fe^0 NPs are that they can have magnetic properties due to the fine oxide shell that affect their formation and also promote aggregation. Surface effects and outer layers from the reducing agents (borates from $NaBH_4$) could also decrease these properties in comparison to bulk materials (Lu et al., 2007; Nurmi et al., 2005). Additionally, studies in solution have shown formation of Fe^0 spherical loose aggregates when the rate of addition of the reducing agent is slow, whereas non-spherical elongated structures were observed under faster reductant injection, and both structures when the injection rate is moderate. These differences affect nuclei formation and growth. The elongated ones are formed under unstable conditions of high reductant injection rate and high precursor concentration (Hwang, Kim, & Shin, 2011; C.-B. Wang & Zhang, 1997).

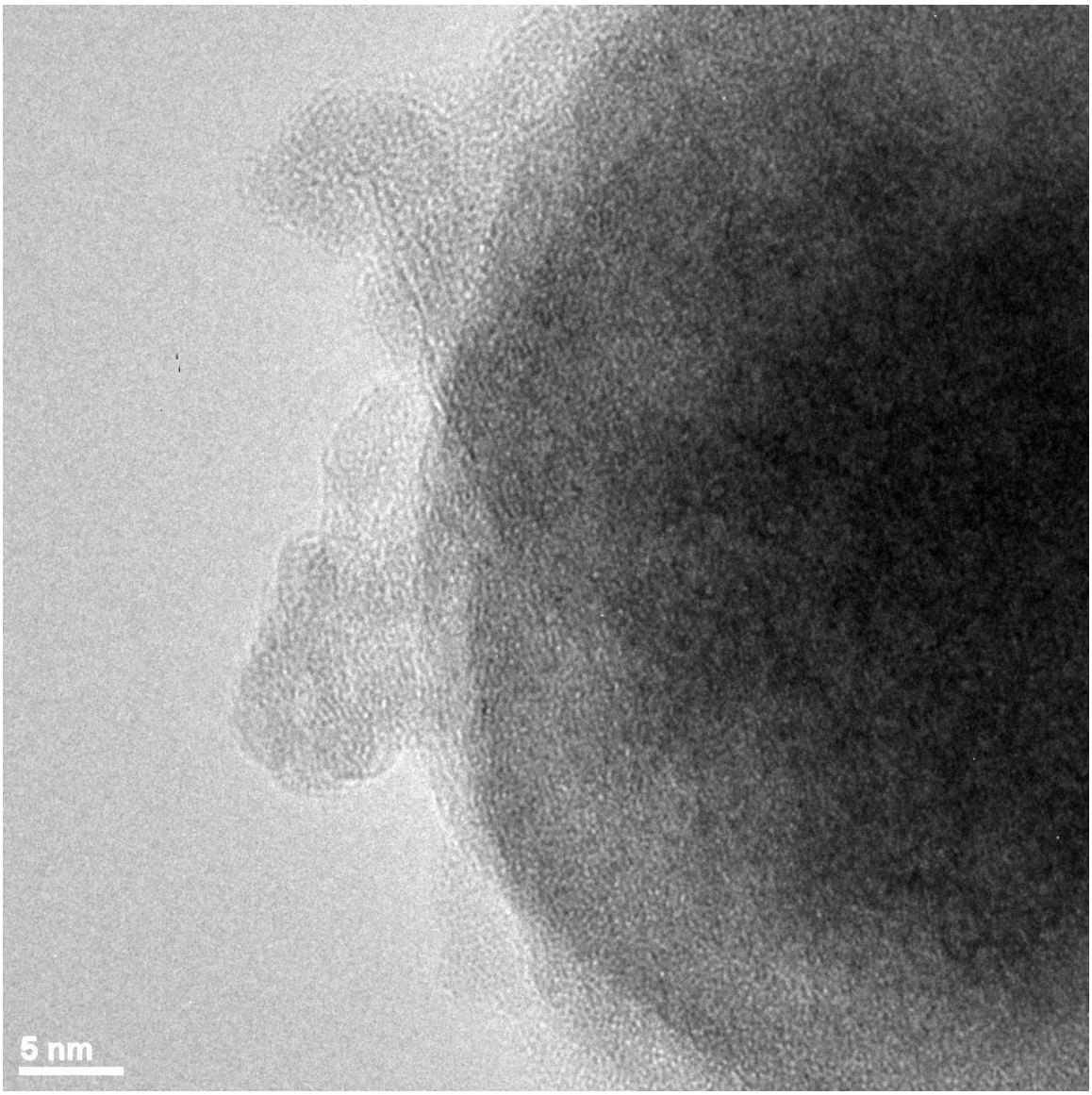

Figure 5.1. TEM of Fe^0 nanoparticles prepared in aqueous phase.

In contrast, palladium does not change the specific surface area of NPs, mostly because the low concentration used. However, Pd increases the oxide shell thickness (10 – 30 nm) due to Fe corrosion and is less uniform. This is advantageous because the non-uniform Pd reduction on the surface gives the defects needed in reductive reactions (J. H. Kim et al., 2008).

5.2 NANOPARTICLE CHARACTERIZATION FROM REDOX POLYMERIZATION PROCESS

The reduction of iron from the accelerant needed a higher $NaBH_4/Fe^{3+}$ ratio of 3:1 or 3:4 compared to the ion exchange. The pH of the reduction is around 9.0 and the hydrogel synthesized had anionic behavior, which could show presence of ferric and ferrous hydroxide (precipitated), see orange gel in Figure 5.2. The amounts of iron in each procedure are shown in Table 5.1. From the polymerization of the hydrogel alone, the iron obtained (9.2 mg Fe/g PAA) was higher to the calculated (7.75 mg/g PAA). After ion exchange, the amount of iron after ion exchange in the hydrogel (450 mg Fe/g PAA) was also higher (387.5 mg/g PAA) due to two different factors: first, the higher swelling capacity of the hydrogel which increases the iron adsorption and second, the possible residual iron from polymerization. On the other hand, the amount of iron after polymerization inside the membranes was lower. One of the reasons of this result is that the mass gain of the membranes by the polymerization was between 8.5 and 13.4% but this represents only about 1.0% of the total reactive solution.

The ratio of iron used for polymerization was 1:100 molar based on the monomer which is lower than the used in the ion exchange procedure, which is 1:2 to make NPs. The iron form is mostly ferric instead of ferrous (Table 5.1) due to the oxidation from the

initiation, this was confirmed by the Ferrozine method. Its characteristic brown color (See Figure 5.2) is due to the reaction of the hexaaquairon (III) ion formed with water. This reaction contributes to the decreasing in the pH by pulling off hydrogen atoms into water. In addition to this, the polymerization goes to a minimum pH = 2.0 as a result of the ionization of AH_2 and AA. The reduction of iron ions takes place immediately without wash, implying that ferrous and ferric ions stayed in solution before reduction.

Based on the quantities of iron and polymer used in the ion exchange, molar COOH/Fe^{2+} ratios were between 2.04 and 5.9 to 1. The first value is near the calculated ratio of 2 and demonstrates higher uptake of iron from ion exchange. The second value shows lower iron loading due possibly to transport phenomena and poor ion exchange with the sodium used. The amount of iron taken by ion exchange is higher than the one obtained only by polymerization itself, going from 9.2 to 457.5 mg Fe/g PAA (Table 5.1). However, the calculated amount of iron could be near 830 mg/g PAA based on the sodium exchanged which indicates higher capacity due to swelling rather than to ion exchange processes.

The percentage of PAA within the membrane MPVDF membrane (Millipore) showed less potential for iron loading compared to the hydrogel only. This is because most of the polymerization occurred on the membrane surface due to faster rates of redox reaction; this decreases the active area of the membranes and promotes losses of iron once the membrane is put in solution. The ion exchange process of Na^+ by Fe^{2+} ions is at lower pH than the exchange of H^+ by Na^+ which implies less swelling, influencing additional iron loading. The amount of iron inside MPVDF-PAA membranee ranged between 1.4 and 4.2 mg/13.2 cm^2 of membrane after ion exchange. This value is higher than the amount

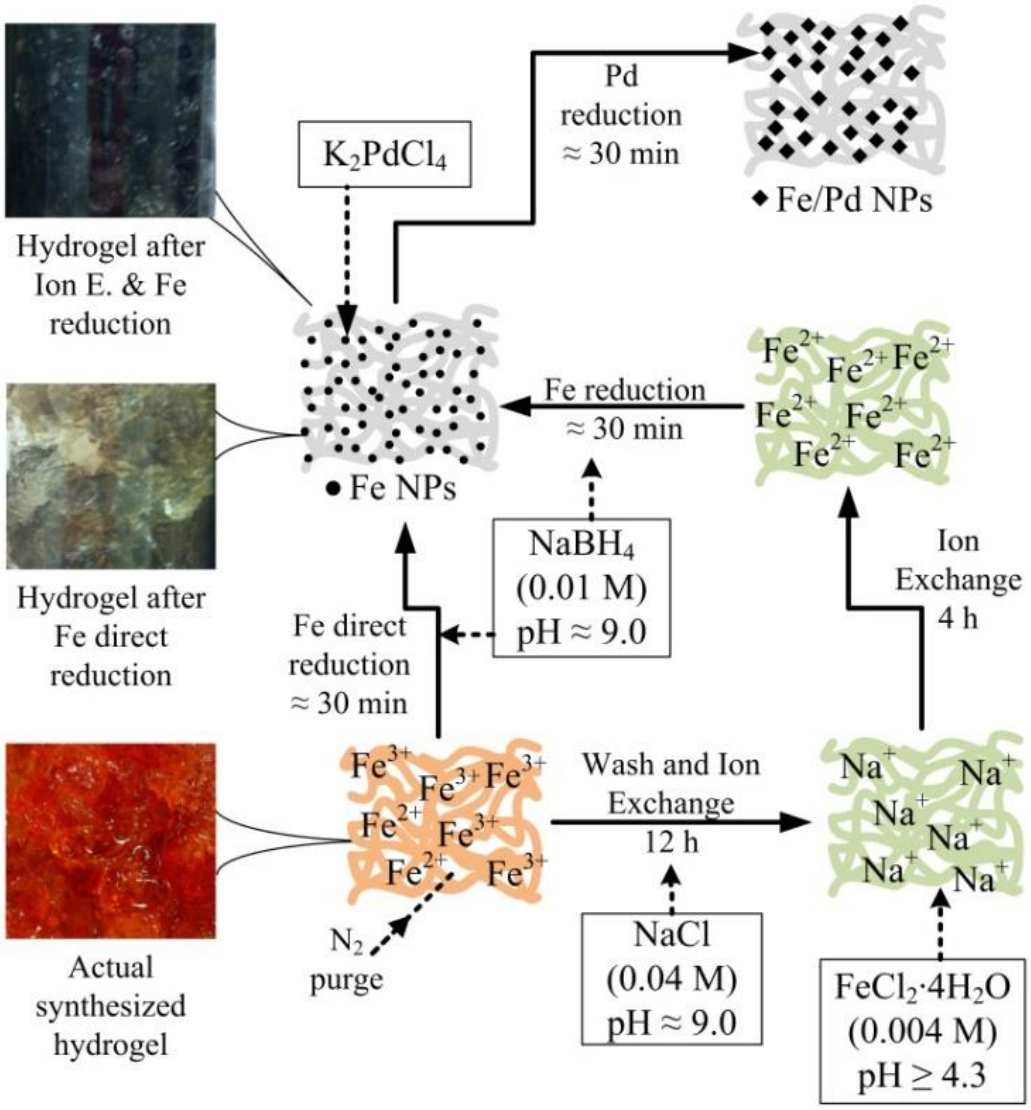

Figure 5.2. Nanoparticle synthesis of PAA-Hydrogel and PVDF-PAA functionalized membranes by redox polymerization. Adapted from (Hernandez et al., 2014). Copyright (2014) American Chemical Society.

obtained from direct hydrogel synthesis but less than the achieved by other studies (Smuleac et al., 2010b; Smuleac et al., 2011; J. Xu & Bhattacharyya, 2007). However, the iron loading obtained with respect to carboxylic groups is near the calculated of 1:2. This suggests the impossibility of higher iron loading due to space limitations within the pore. In addition to that, the chelating behavior of the ascorbic acid in the solution and the repulsion of the counter ions with the carboxylic groups could also influence the lower concentration of iron in the membrane.

Posterior to reduction, NPs were formed on the surface and the pores of the hydrogel and membranes. DLS analysis was also performed in the reductive solutions, to determine the loss of particles and their size. The particle loss was within the 1% and the mean and median particle sizes were 10.4 and 10.7 nm, respectively, possibly from iron excess on the hydrogel and membrane surfaces (see DLS report 1 in APPENDIX). In the hydrogel pores, NPs are more widely distributed (Figure 5.3a) and most of the aggregates are located on the surface (Figure 5.3b). In the membranes, ion exchange was performed before reduction. The structure of the membrane surface is less porous due to swelling stresses produced by pH changes during reduction. Hydrogel (Figure 5.3), membrane surface (Figure 5.4a) and membrane cross-section (Figure 5.4b) show that the size of the particles, not aggregates, are between 30 and 60 nm.

These figures demonstrate various facts: first, the immobilization prevents NPs aggregation. Second, the synthesis of NPs from the exhausted accelerant used in redox polymerization is possible. And finally, within the entangled structure of the hydrogel the NP formation was performed at slow reductant injection rates, which gives their spherical shape. This last feature was not controlled on purpose and it can be attributed to the

Table 5.1. Determination of iron species and total iron from polymerization in solution of AA (2.8 M at pH 3.0; T_0 = 22-25 °C) and Ion Exchange with $FeCl_2 \cdot 4H_2O$ (3.6 ± 0.04 mM; pH = 4.9); Area of membranes = 13.2 cm^2. All measurements were done by triplicate, calculating the respective deviations and standard errors of the means. Reprinted from (Hernandez et al., 2014). Copyright (2014) American Chemical Society.

Iron species	
Total Fe in hydrogel from polymerization	9.2 ± 1.1 mg/g PAA
Total Fe in membrane from polymerization	3.6 ± 0.3 mg/g PAA
Fe^{3+} in membrane from polymerization	91.7%
Fe^{2+} in membrane from polymerization	8.3%
Total Fe in hydrogel from ion exchange	457.5 ± 8.1 mg/g PAA
Total Fe in membrane from ion exchange	131.1 ± 3.1 to 428.3± 4.2 mg/g PAA

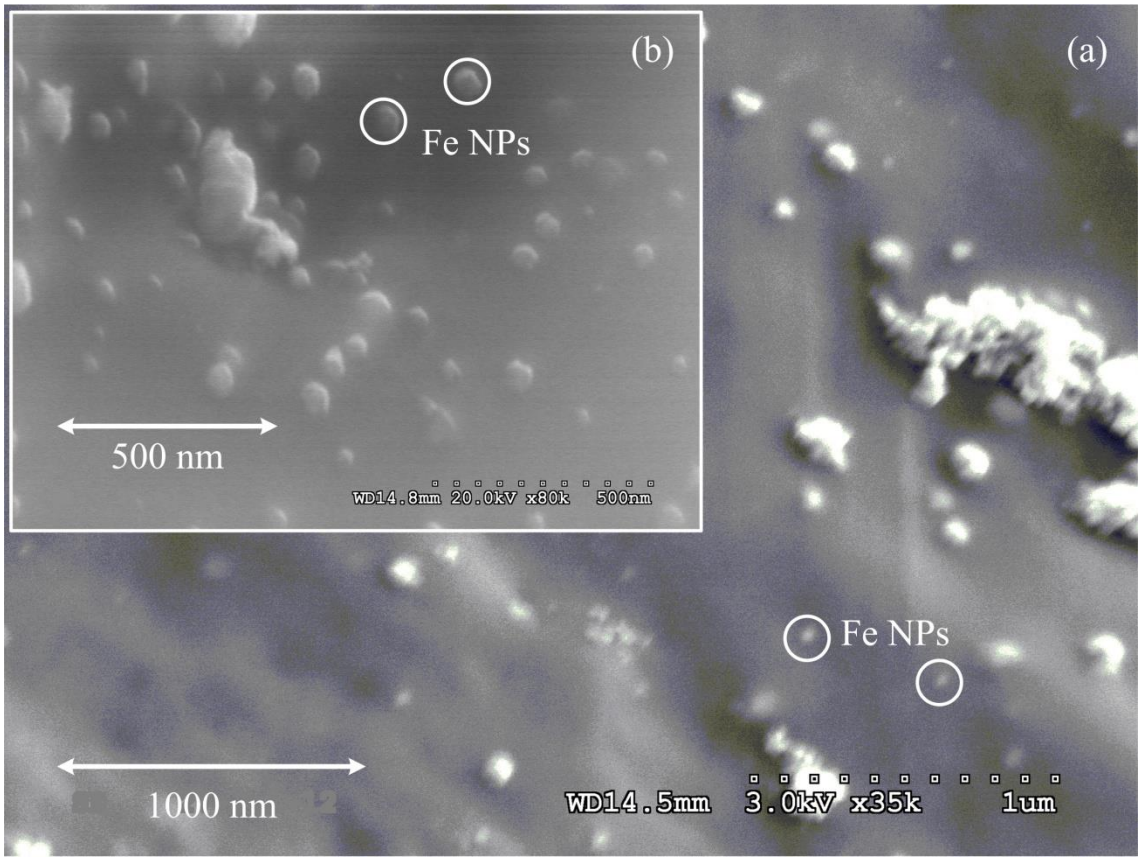

Figure 5.3. SEM images of the cross-linked PAA-Fe xerogel. (a) Pore surface of the xerogel, (b) Surface of the xerogel**.** Reprinted from (Hernandez et al., 2014). Copyright (2014) American Chemical Society.

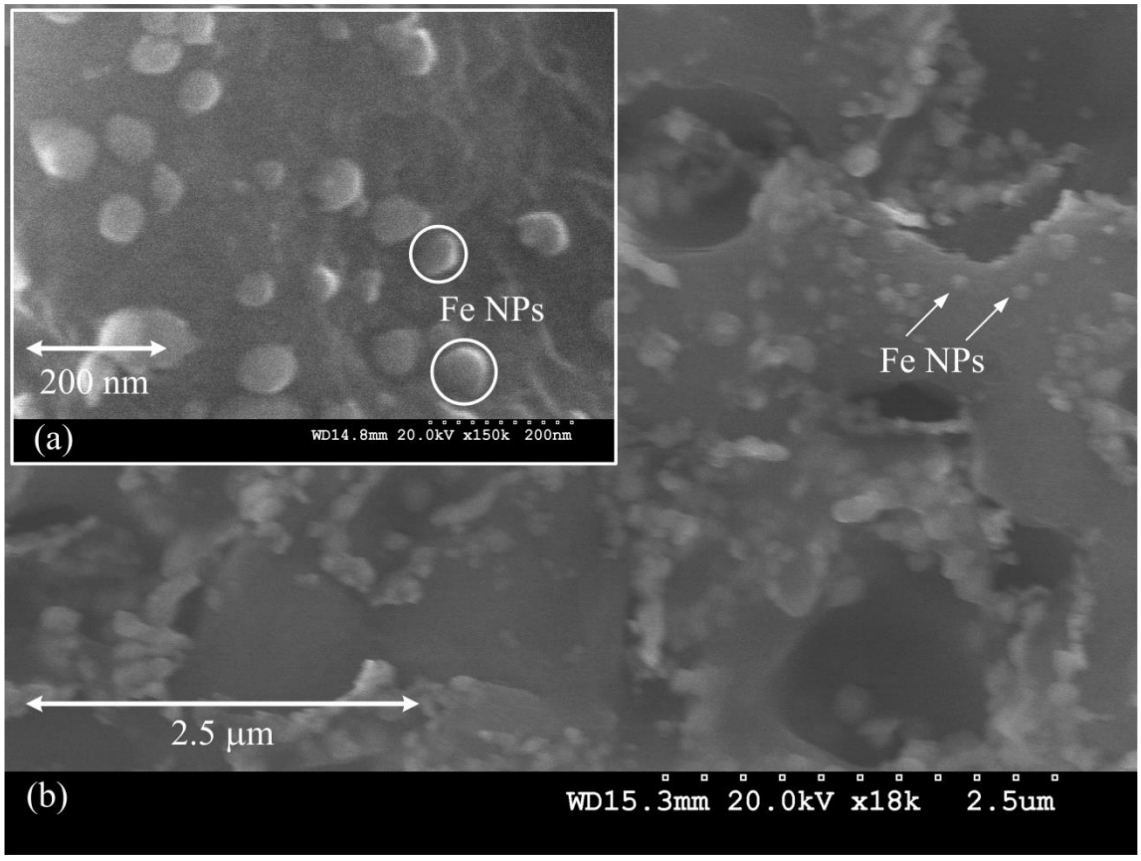

Figure 5.4. SEM images of MPVDF-PAA-Fe membranes (Millipore). (a) Membrane surface, (b) Cross section. Reprinted from (Hernandez et al., 2014). Copyright (2014) American Chemical Society.

swelling behavior of the hydrogel. The top surfaces of the membrane and hydrogel showed elongated aggregates, possibly due to the lack of hydrogel entanglements, exposing the Fe ions to a fast reduction.

The membrane and the gel verifies a decreasing in particle agglomeration and the presence of iron is confirmed by EDS analysis from Figure 5.5. The binding energy of iron is in the range of 7 keV, which confirm the presence of iron (Figure 5.5a). As it is shown in Figure 5.5b, some sodium is still in the membrane from the sodium borohydride and ion exchange processes (33% of Fe compared with 8% of Na). The mapping of the elements also accentuates the iron, carbon and fluorine on the surface of the membrane (Figure 5.5c) while oxygen is under-lapped.

5.3 NANOPARTICLE CHARACTERIZATION IN SPONGE-LIKE MEMBRANES

The HPVDF membranes after functionalization with PAA and subsequent in situ synthesis of Fe NPs show that the open structure of the HPVDF membrane between the polymer blocks as well as the porous surface of the SPVDF membrane are diminished (see Figure 5.6a and Figure 5.6c). Some aggregation of Fe NPs are seen on the surface of the HPVDF, but fewer aggregate on the SPVDF membrane, which shows a more separated and uniform distribution as is confirmed by the EDS mapping. Sodium presence is due to the reduction of iron by $NaBH_4$. Oxygen, fluorine and carbon served as reference compounds for the PVDF-PAA membrane.

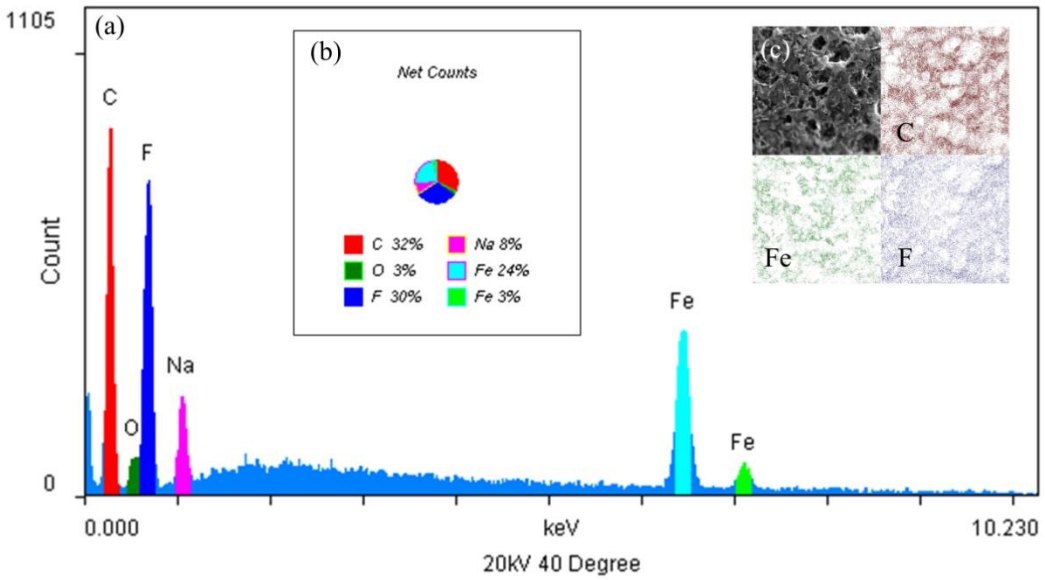

Figure 5.5. SEM-EDS spectrum and images of MPVDF-PAA-Fe membranes. (a) EDS spectrum, (b) Elemental net counts, (c) EDS mapping. Reprinted from (Hernandez et al., 2014). Copyright (2014) American Chemical Society.

In contrast, the internal structure of the membranes shows no changes (Figure 5.6b and Figure 5.6d). The densities of iron and sodium decrease with less agglomeration of Fe NPs. One explanation for this result is that due to the increase in the pH at the time of the iron reduction by $NaBH_4$, the pores of the membrane were closed and the transport of solvents through the membrane was low, preventing the aggregation of NPs due to more spaced carboxyl groups.

In the case of SPVDF membranes, it illustrates that the polymerization was done mostly on the surface, then the pores of the membrane were blocked, and the transport of solvents through the membrane was low, preventing the production of more Fe NPs. The average results of iron loading, as Δm, from the ICP-OES are 1.65 and 4.80 g/m^2 for HPVDF and SPVDF, respectively. After sonication in DIUF water, the membranes show almost no iron losses. DLS results showed a sample too polydisperse for cumulate analysis. Also the value of Δm for HPVDF was lower than 0.007 g/m^2. For SPVDF was 0.05 g/m^2, indicating strong nanoparticle adhesion on the membranes.

X-ray point-scans were performed on the surface and the cross-section of the HPVDF and SPVDF membranes to determine the metal loading in each membrane. These point-scans (green and red) and their spectra are shown in the Figure 5.7a-d. It can be seen that well-defined peaks of sodium occur around 1.0 keV, while peaks of iron (which is also overlapped with fluorine spectrum) occur around 0.6 and 6.4 keV. The atomic ratios (Fe/Na) on the outer and top surfaces of HPVDF and SPVDF are 1:2.2 and 3.8:1, respectively.

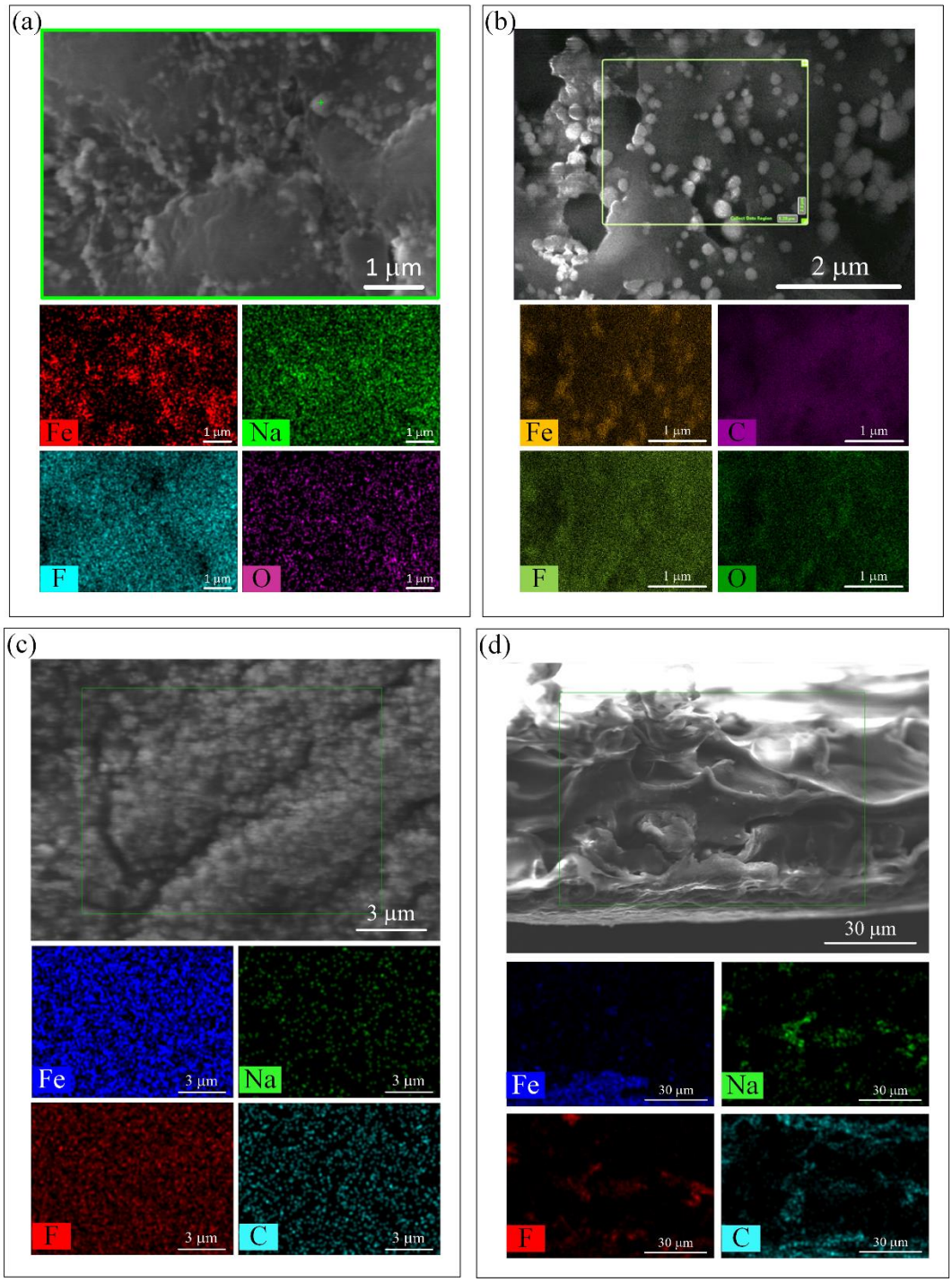

Figure 5.6. SEM-EDS imaging and mapping of PVDF-PAA-Fe hollow fiber and flat sheet membranes. (a) HPVDF outer surface, (b) FIB cut of HPVDF cross-section, (c) SPVDF top surface, (d) SPVDF cross-section. Reprinted from (Hernández, Lei, et al., 2016). Copyright (2016) American Chemical Society.

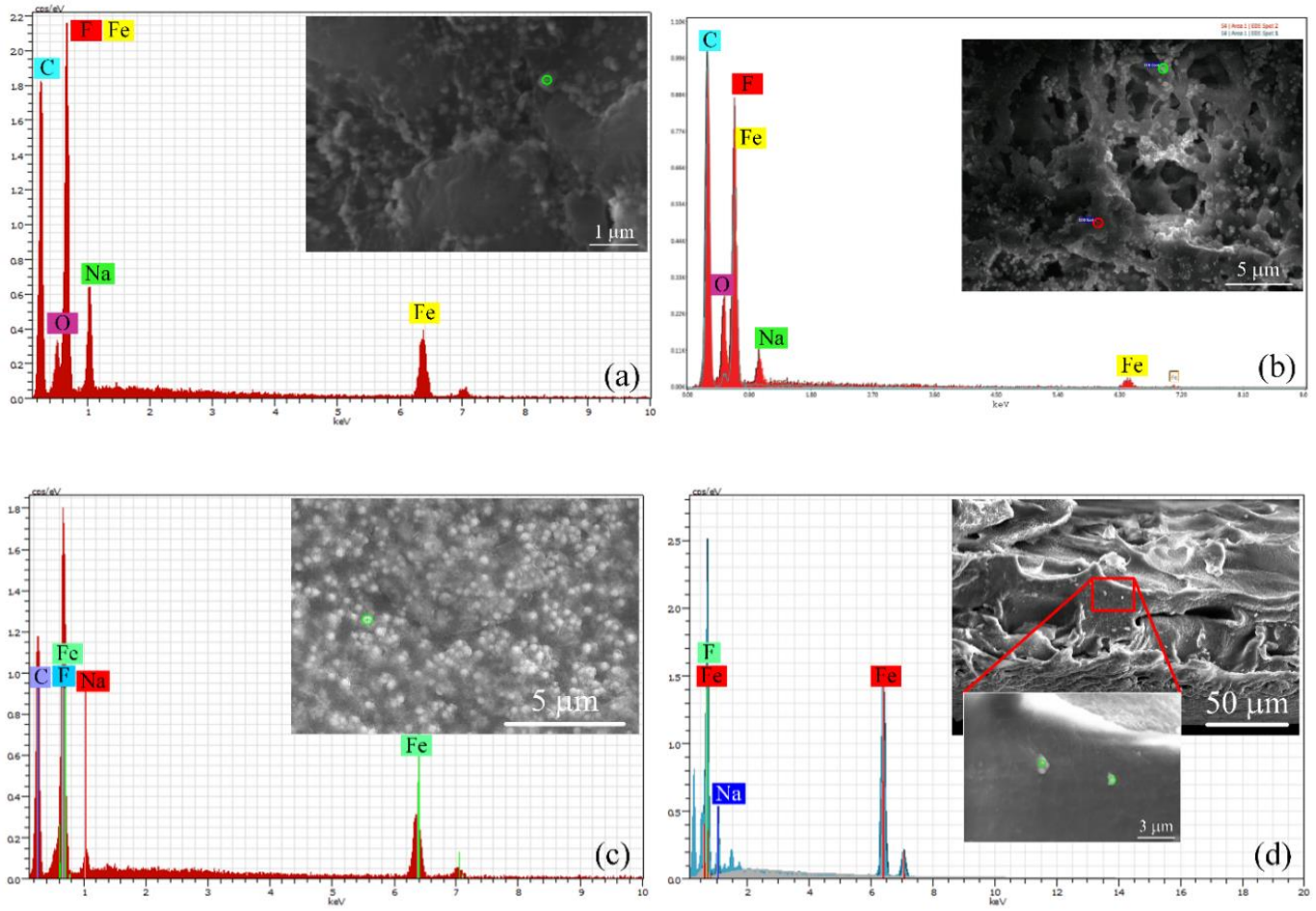

Figure 5.7 SEM images and EDS spectra of PVDF-PAA-Fe hollow fiber and flat sheet membranes. (a) HPVDF outer surface, (b) FIB cut of HPVDF cross-section, (c) SPVDF top surface, (d) SPVDF cross-section. Reprinted from (Hernández, Lei, et al., 2016). Copyright (2016) American Chemical Society.

Remarkably in the SPVDF membranes, the ratio Na/Fe is 8 times higher than the calculated value (2:1). This implies that not only did the ion exchange process occurred, but also that most of the iron present within the swollen structure of PAA was reduced to Fe NPs. In the cross-section of the SPVDF (Figure 5.7d), similar behavior of the top surface occurs but in lower proportions with a ratio of 1:1.57 (Na/Fe). For the cross-section part, the atomic ratio for the HPVDF is almost constant compared to the outer surface 2.15:1 (Na/Fe) and both metals counts are lower than the outer surface (Figure 5.7b).

5.4 PARTICLE SIZE ANALYSIS

Characterization of particle size is necessary to calculate the NP specific surface area, a_s, which is essential in the heterogeneous catalytic dechlorination, since bulk particles can only degrade about 10% of organic-chlorinated compounds (J. Xu & Bhattacharyya, 2007). Particle size has been discussed in a wide range of topics, such as geology, atmospheric sciences and engineering (Holdich, 2002; Petty & Huang, 2011; Rodriguez, Edeskär, & Knutsson, 2013).

5.4.1 Nanoparticle Sizes in Solution

As showed before for particle characterizations, most analyses are performed in solution using common methods such as DLS, transmission electron microscopy (TEM), atomic force microscopy (AFM), BET surface analysis or SEM picture analysis including works related to Fe, Fe/Ni and Fe/Pd NPs (Bueno, Catalani, Daghastanli, Cuccovia, & Chaimovich, 2010; M. Gui, V. Smuleac, L. Ormsbee, D. Sedlak, & D. Bhattacharyya, 2012a; Feng He, Zhao, Liu, & Roberts, 2007; Parshetti & Doong, 2009; Y. P. Sun et al., 2006; Thomas et al., 2007; Weibel, Bouchet, Boulc, & Knauth, 2005).

The results of the DLS analysis (see DLS report 2 in APPENDIX) indicate different NPs particle size depending upon the use of stabilizers. Note that the solutions were sonicated and therefore, the nanoparticles could have disaggregated; this aggregation does not occur in the membranes, giving them an operational advantage. However, the CMC-stabilized Fe/Pd NPs showed smaller particle size having a mean and a median size of 136.5 nm and 124.2 nm, respectively, with a standard deviation of 32.4 nm.

5.4.2 Image Analysis for Nanoparticle Size Characterization

For macro-particles in solid phase, many of these studies have used physical separation (sieve analysis) with 3D digital models based on laser scans (Hayakawa & Oguchi, 2005). But at nanoscale, supported NPs are analyzed by SEM/TEM pictures, calculating a_s values from the direct measuring of an average particle size, assuming the particle shape (spherical in most cases). It should be remembered that due to swelling control, most particles have a quasi-spherical shape in view, except when there are aggregates, mainly on the surface. For example, in section 5.2, NP sizes were manually measured, giving sizes between 30 and 60 nm and $a_s = 12.7\ m^2/g$ (Bell, Minelli, Tompkins, Stevens, & Shard, 2012).

Although the development of new microscopy technologies, such as the FIB - SEM, allow a better visual determination of the shape of the particles like the ones shown in Figure 5.8, it becomes more necessary to measure and analyze particle sizes due to its high influence on catalytic processes. Recent works have shown the potential of image analysis (2D metrics) for small particles, mostly TEM images in liquid phase (Bell et al., 2012; Fisker, Carstensen, Hansen, Bødker, & Mørup, 2000; Woehrle, Hutchison, Ozkar, & Finke, 2006). Here, this concept is applied on the SEM pictures from the nanocomposites to

quantify the shape descriptors of the Fe NPs in 2D. These novel results were extrapolated to the definition of the particle size through statistical distributions.

Using ImageJ on SEM pictures of the membranes (Figure 5.9a), the particles were surrounded, counted and highlighted (Figure 5.9b). The NP perimeter (P), projected area (A_p) from the image, minimum circumscribed and maximum inscribed circles (d_c and d_i, respectively) were calculated. 2D projection of each particle was used to quantify how close each shape was to a perfect circle, and hence, how it is related to a sphere. Based on the parameters measured, particle shape factors were calculated using the ImageJ program. The factors taken into account were roundness ($R = d_i \cdot d_c^{-1}$), its inverse (aspect ratio, AR) and circularity ($c = 4\pi A_p \cdot P^{-2}$) (Olson, 2011). Wadell's degree of sphericity was considered too ($\phi = d_{eq} \cdot d_c^{-1}$), where d_{eq} is the equivalent diameter of a circle with the same area as A_p, as it has been stated that ϕ accurately describes 3D particles (Cavarretta, O'Sullivan, Coop, Nakagawa, & Luding, 2009; Hayakawa & Oguchi, 2005). Based on circle and ellipse area formulas and emplacing A_p, d_{eq}, d_c and d_i, it was found that $\phi^2 = R$. Each quantity will be close to 1 when the projected area is close to a circle.

Comparing the shape descriptors distributions of ϕ and c in Figure 5.10, almost 95% of the NPs can be considered spheres/spheroids with values of ϕ and c higher than 0.7 (Holdich, 2002; Le Roux, 2004; Rodriguez et al., 2013). Hydrogel and MPVDF membrane have less uniform values due to the aggregates formed on the surface due to the lack of longer entanglements from the redox polymerization. With this confirmation, the particle size can be defined by the calculated equivalent diameter (d_{eq}) of a circle with area equal to the projected area A_p.

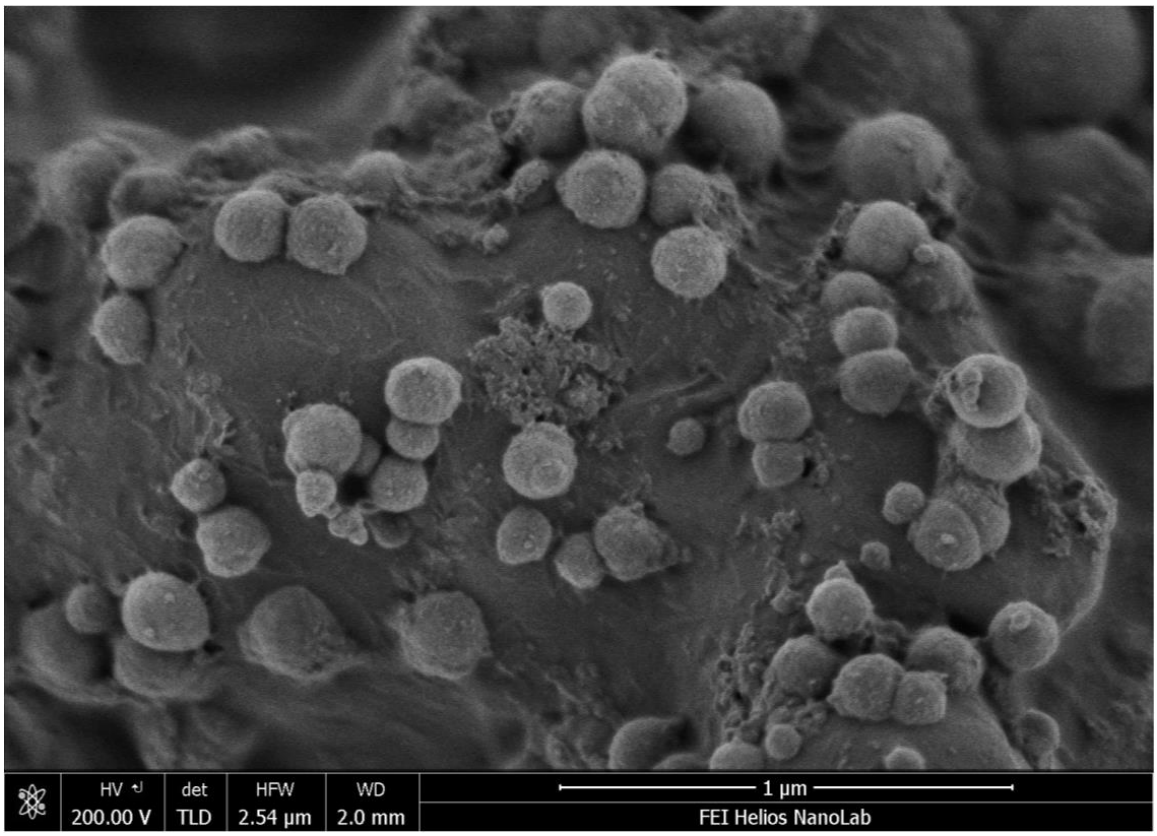

Figure 5.8. FIB-SEM Through-Lens-Detector (TLD) Backscattered Electron Mode imaging of Fe nanoparticles in HPVDF-PAA-Fe membrane. Courtesy of FEI.

The particle size distributions of Fe NPs inside the hydrogel and the membranes are shown in Figure 5.11. All the NP size distributions fit the lognormal and gamma functions with exception of the hydrogel that fits only the lognormal, see Table 5.2. The goodness-of-fit is determined by a significance level of a *p* value higher than the statistic test performed. Fitted lognormal and gamma distributions are frequently used to describe particle size, since they have multiplicative effects and the NPs grow randomly depending on their size (Fátima Vaz & Fortes, 1988). These distributions define the median instead of the mean as the characteristic value for the particle size (Fátima Vaz & Fortes, 1988; Olson, 2011).

The NP sizes are also shown in Figure 5.11 and are in the range of the arithmetic means, with 95% confidence. Based on the visual measurements made in section 5.2 it is worth to note that the NP size for MPVDF were larger than predicted (mean = 81 nm; median = 74 nm), but the hydrogel estimate were within the visual range (mean = 63 nm; median = 50 nm). This confirms the benefits of using image analysis. However, new developments in microscopy equipment and related software could improve and open new forms of image processing.

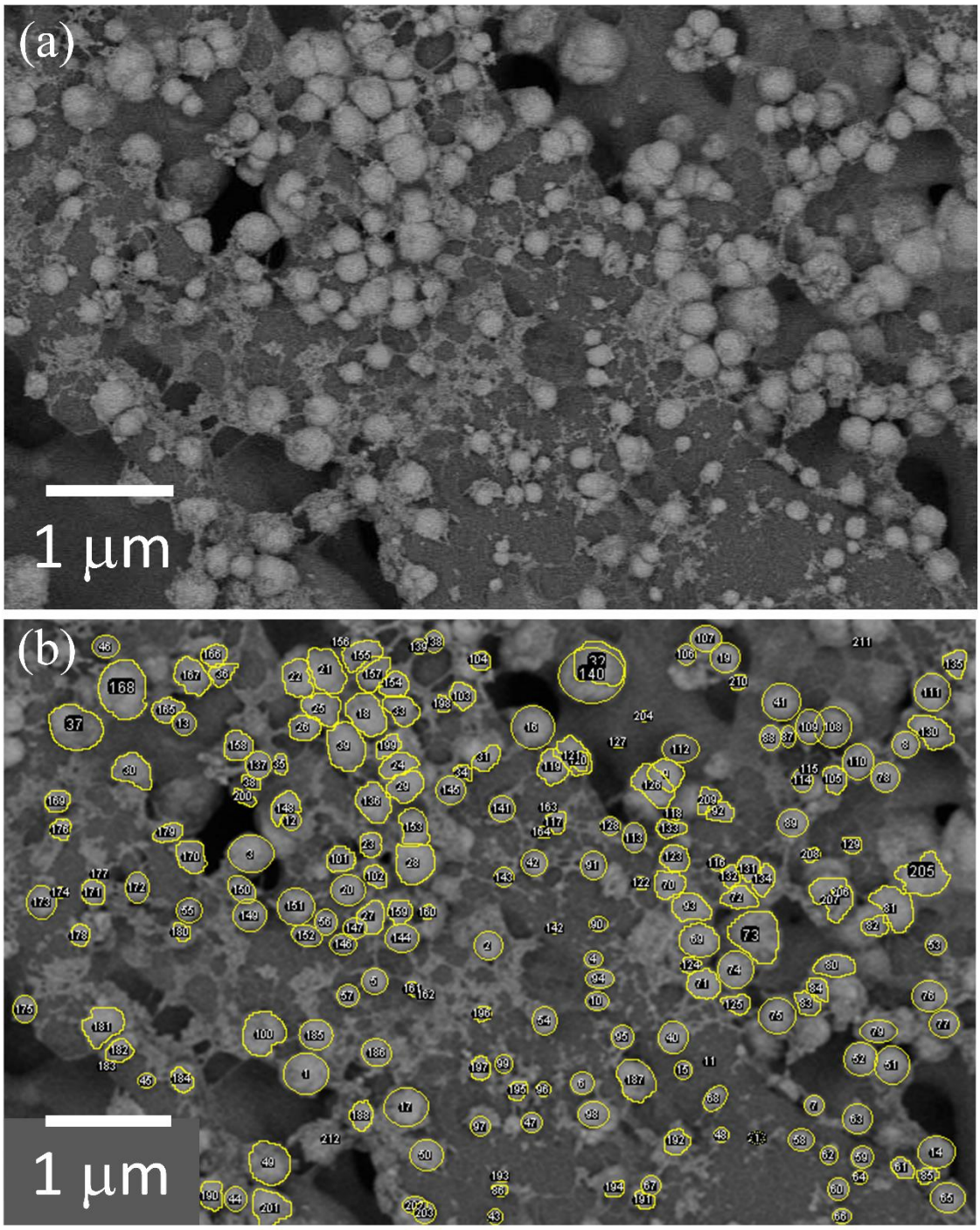

Figure 5.9. FIB-SEM imaging of Fe nanoparticles in HPVDF-PAA-Fe membrane. (a) Through-Lens-Detector (TLD) Backscattered Electron Mode of hollow fiber, (b) nanoparticle count and measurement. The fibers present are from the PAA hydrogel on top of the PVDF substrate.

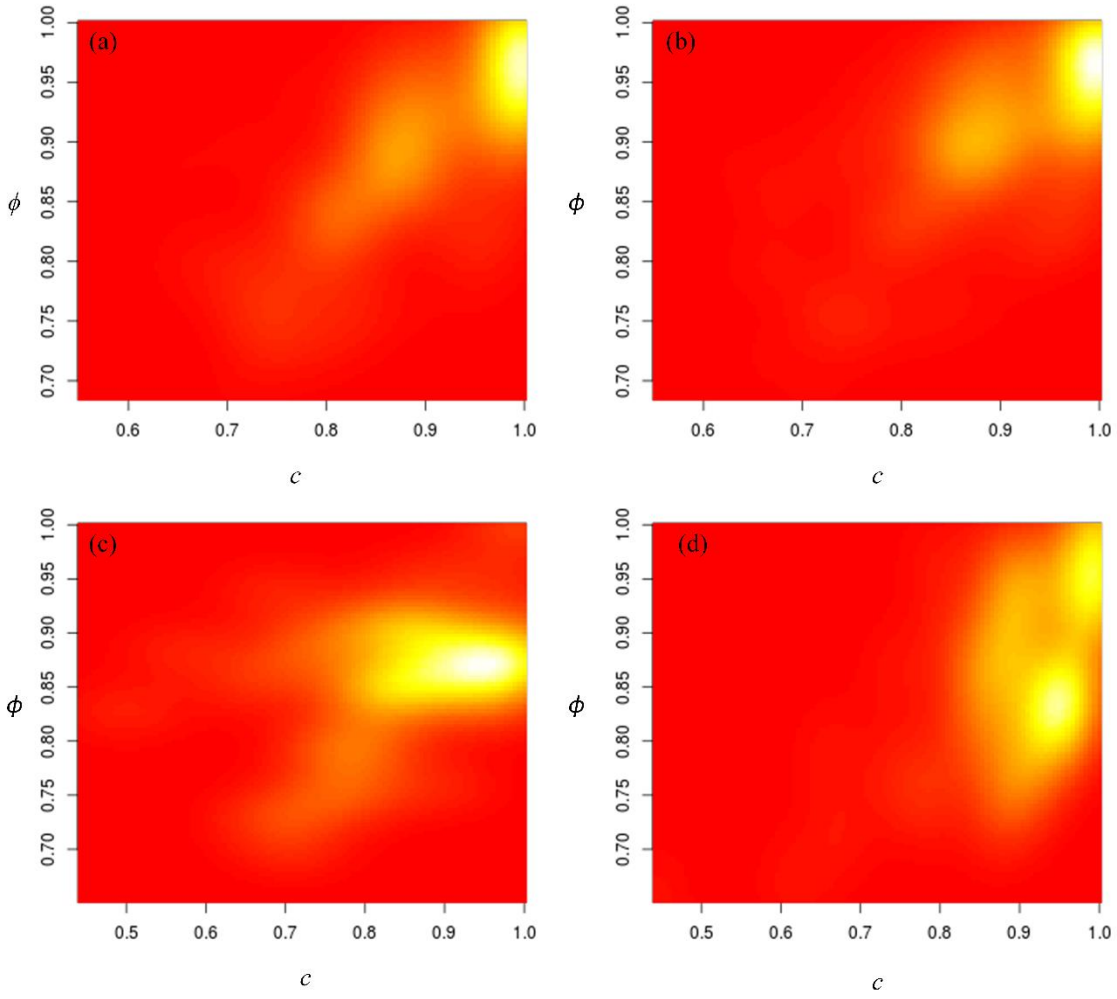

Figure 5.10. Bivariate distribution comparisons of nanoparticles' circularity and degree of sphericity in PVDF-PAA-Fe membrane. (a) HPVDF, (b) SPVDF, (c) MPVDF, (d) hydrogel.

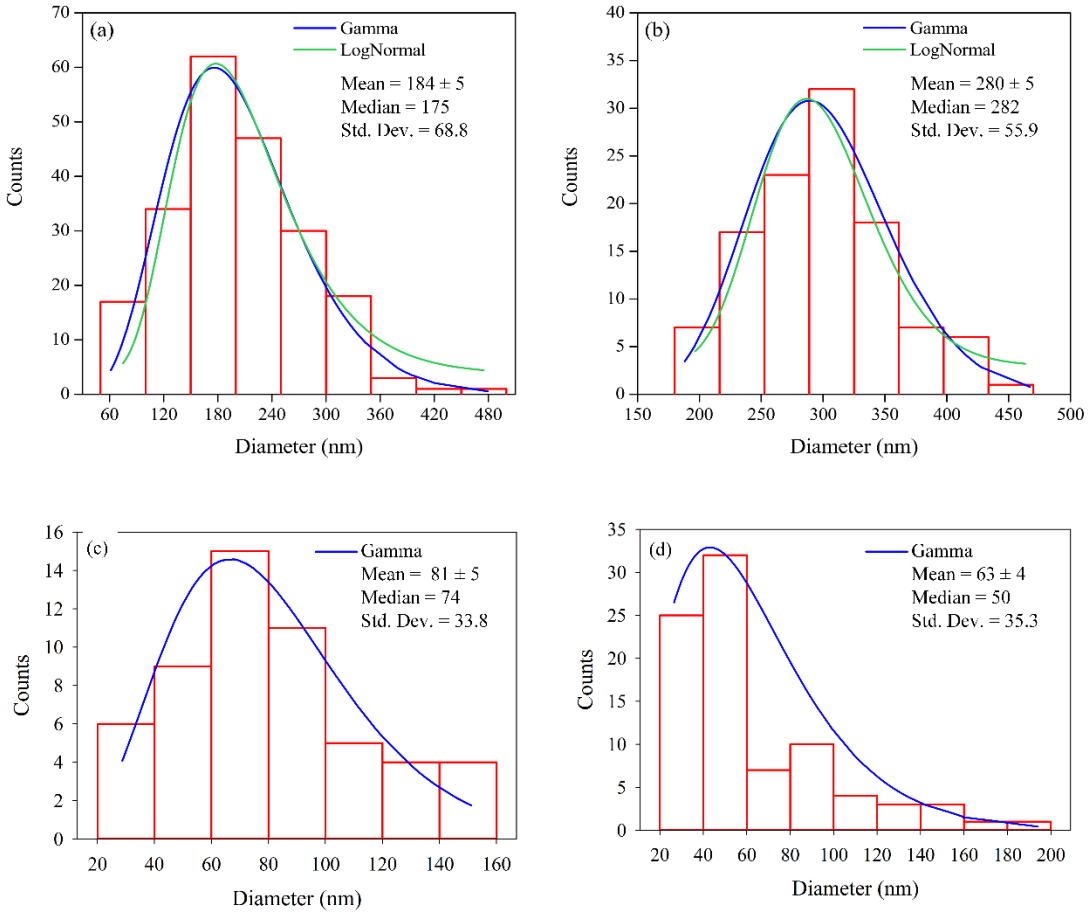

Figure 5.11. Nanoparticle size distribution. (a) HPVDF membrane, (b) SPVDF membrane, (c) MPVDF, (d) Hydrogel. Adapted from (Hernández, Lei, et al., 2016). Copyright (2016) American Chemical Society.

Table 5.2. Nanoparticle Size Goodness-of-fit for Lognormal and Gamma Distributions. D: Kolmogorov-Smirnov; W-Sq: Cramer-von Mises; A-Sq: Anderson-Darling

Support Material	d_{eq} (nm)	Lognormal		Gamma	
		Statistic	*p* Value	Statistic	*p* Value
HPVDF	175	D = 0.034 W-Sq = 0.041 A-Sq = 0.288	> 0.500 > 0.500 > 0.250	D = 0.034 W-Sq = 0.042 A-Sq = 0.285	> 0.500 > 0.500 > 0.500
SPVDF	282	D = 0.064 W-Sq = 0.069 A-Sq = 0.428	0.213 0.176 0.180	D = 0.059 W-Sq = 0.061 A-Sq = 0.397	> 0.250 0.247 0.232
MPVDF	74	D = 0.061 W-Sq = 0.028 A-Sq = 0.281	> 0.500 > 0.500 > 0.500	D = 0.060 W-Sq = 0.030 A-Sq = 0.293	> 0.500 > 0.500 > 0.250
Hydrogel	50	D = 0.061 W-Sq = 0.050 A-Sq = 0.308	> 0.500 > 0.250 > 0.250	D = 0.101 W-Sq = 0.129 A-Sq = 0.697	0.037 0.083 0.118

6 WATER REMEDIATION STUDIES

After the in situ synthesis of supported Fe/Pd NPs in membranes and hydrogels, the present Chapter describes their application towards water remediation of a toxic chlorinated organic compound, trichloroethylene (TCE). The high surface area of the hydrogel/membrane system and their open structure guarantee uniformly shaped and high loading of NPs in most of the structure. This allows the pollutant to access more freely to the NP active sites. Parts of this chapter are published in (Hernández, Lei, et al., 2016; Hernandez et al., 2014)

TCE was selected as a model compound because its low concentration in water demands costly ex situ treatments, without destroying it in most cases. Shifting to an in situ treatment offers lower costs and Fe NPs have thoroughly demonstrated their capability of reductive dechlorination in this field (Gotpagar, Grulke, Tsang, & Bhattacharyya, 1997; Feng He et al., 2007; E.-J. Kim, Murugesan, Kim, Tratnyek, & Chang, 2013; W.-x. Zhang, 2003). TCE has low biodegradability making it very persistent in nature, is heavier than water and small quantities of it go through leakages onto the soil to ground water, contaminating them. TCE then, is released very slowly with a half-life between months and decades. Due to these reasons, its treatment and elimination is necessary.

6.1 REDUCTIVE REACTIONS

The most important reaction in the reductive pathway for dechlorination and other processes is the corrosion of Fe^0 by water, usually at pH values from 5.5 to 7.0. This reaction is what starts the conditions that allow the subsequent reactions to proceed. The corrosion of Fe^0 can develop by anoxic and oxic ways. In order to achieve dechlorination of TCE, the anoxic pathway is needed. Besides, TCE presence is in groundwater which

generally have low concentrations of dissolved oxygen. The proposed reactions are as follows:

$$Fe^0 + 2H_2O \rightleftarrows Fe^{2+} + H_2 + 2OH^- \quad (6.1)$$

$$Fe^0 + H_2O + e^- \rightleftarrows FeH_{ads} + OH^- \quad (6.2)$$

$$FeH_{ads} + H_2O + e^- \rightleftarrows Fe^{2+} + H_2 + 2OH^- \quad (6.3)$$

These reactions are based in electron transfer, having H_2 as product which is in turn used in the following catalytic reactions. Matheson and Tratnyek show the evolution of H_2 directly (Equation (6.1)) but, Odziemkowski et al. propose the adsorption of hydrogen based on electrochemical findings (Equations (6.2) and (6.3)), which would make it more available for catalytic hydrogenation reactions (Matheson & Tratnyek, 1994; Odziemkowski, Gui, & Gillham, 2000). If oxygen is present, Fe^0 will be oxidized in the reaction shown in Equation (6.4), producing different forms of iron oxide. This reactions have to be avoided in lab-scale in order to obtain H_2 (Matheson & Tratnyek, 1994).

$$2Fe^0 + O_2 + 2H_2O \rightleftarrows 2Fe^{2+} + 4OH^- \quad (6.4)$$

When used in reductive dehalogenation, Fe^0, H_2 and Fe^{2+} act as reducing agents, although Fe^{2+} reactions are slow (Matheson & Tratnyek, 1994; Siantar, Schreier, Chou, & Reinhard, 1996):

$$mFe^0 + RCl_m + mH^+ \rightarrow mFe^{2+} + RH_m + mCl^- \quad (2.3)$$

$$mH_2 + RClm \longrightarrow RHm + mH^+ + mCl^- \quad (6.5)$$

$$2Fe^{2+} + RCl + H^+ \longrightarrow 2Fe^{3+} + RH + Cl^- \quad (6.6)$$

Note that the reaction in Equation (6.5) is similar to reaction in Equation (2.3), which implies that Fe^0 theoretically functions simultaneously as catalyst, forming H_2 (Equation (6.1)) and as reactant in the reductive process. However, for the reduction of TCE in specific, these reduction pathways (see Figure 6.1) form acetylene by β-elimination, and chlorinated byproducts including chloroacetylene, dichloroethenes, and vinyl chloride by hydrogenolysis (Y. Liu et al., 2005; Roberts, Totten, Arnold, Burris, & Campbell, 1996). These reactions are also are not desired and their reaction rates are quite slow (30 to 40 days) (Jeong, Kim, & Hayes, 2007; Y. Liu, S. Majetich, R. Tilton, D. Sholl, & G. Lowry, 2005). Other problem is the loss of reactivity due to formation of iron hydroxide on the NPs surface, inhibiting the reaction.

In addition to the aforementioned issues, H_2 without an effective catalyst could inhibit the corrosion and hence, the reduction. In this step, the production of H_2, is where other catalysts such as Pd or Ni are introduced to change the reaction pathway. These bimetallic systems will use the hydrogen from Fe corrosion to directly reduce TCE to ethylene/ethane (Y. Liu et al., 2005; J. Xu & Bhattacharyya, 2005). For these reasons, no dechlorination is feasible if all Fe is covered by the metal catalyst (Nutt, Hughes, & Michael, 2005). Pd, as explained in Chapter 5, is reduced onto the Fe^0 NPs (see Equation (5.4)). In this work TCE was treated by Pd-catalyzed hydrodechlorination only (see Figure 6.1).

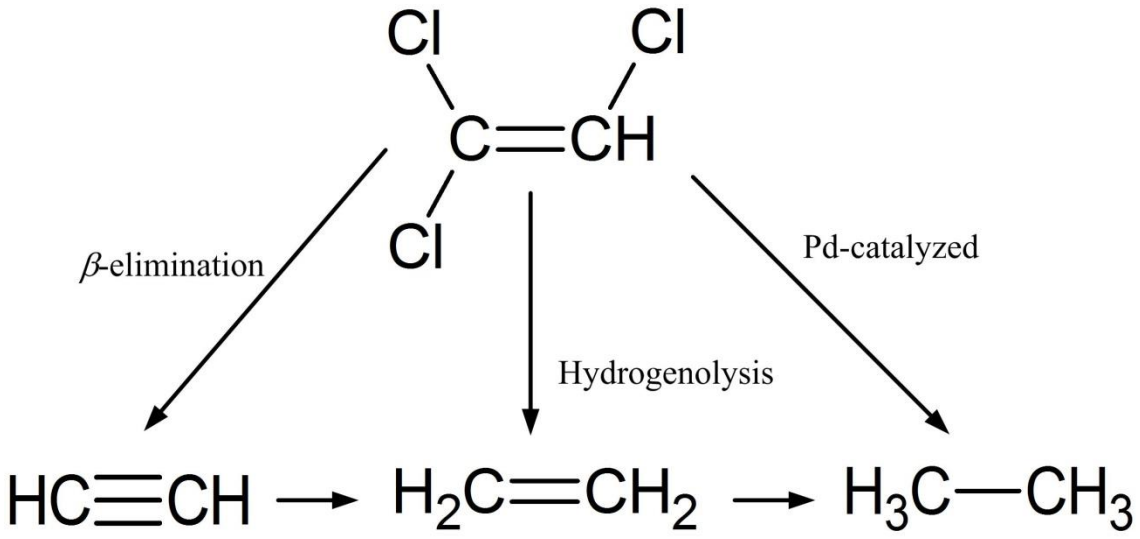

Figure 6.1 TCE abiotic dechlorination reaction pathways and reaction intermediates. Some intermediate compounds are not included. Adapted from (Y. Liu et al., 2005; Roberts et al., 1996).

In this bimetallic system, the catalyst (Pd^0) acts as cathode while the reductant Fe^0 is oxidized and acts as the anode. To promote Fe corrosion, Pd has to generate enough active sites on the NP surface (Smuleac et al., 2010b; C.-B. Wang & Zhang, 1997; X. Wang et al., 2008). The Pd coating can go from 0.8 to 3.4 monolayers, which could cover a large enough proportion of the particles, giving them less active sites and in consequence, a nonlinear dependence at higher Pd concentrations. Wei et al. explain that an active atomic hydrogen ($H^{\bullet}$) and also molecular hydrogen are formed on Pd surface due to reduction of protons from water, thanks to the corrosion of Fe (J. Wei et al., 2016). On the other hand, Wang et al. describe that the hydrogen gas is produced by the water corrosion (Equation (6.1)) and then $H^{\bullet}$ is formed on the Pd surface (Q. Wang, Jeong, & Choi, 2012). Then adsorbed TCE is reduced on the NP surface by $H^{\bullet}$, first to ethylene by hydrogenolysis and then to ethane by hydrogenation (J. Wei et al., 2016). The proposed reactions are:

$$C_2HCl_3 + 4Fe^0 + 5H_2O \xrightarrow{Pd} C_2H_6 + 4Fe^{2+} + 3Cl^- + 5OH^- \quad (6.7)$$

$$C_2HCl_3 + 3Fe^0 + 3H_2O \xrightarrow{Pd} C_2H_4 + 3Fe^{2+} + 3Cl^- + 3OH^- \quad (6.8)$$

It has been found that in supported Fe/Pd NPs, the production of ethane is greater than ethylene with 87% of the products, while with non-supported Fe/Pd NPs, only 59% of ethane is produced (J. Wei et al., 2016). One might think that the use of metallic Pd alone in an atmosphere rich in hydrogen gas could reduce TCE in the same way as Fe/Pd. However, a study have found that Pd/H_2 system produces 3 to 4% of chlorinated byproducts from TCE by hydrogenolysis (Lowry & Reinhard, 1999). In the same study, bimetallic Pd/Al catalyst show no intermediates, this is also true when the Pd NPs are capped with CMC (J. Liu, He, Durham, Zhao, & Roberts, 2008). Based on this, it is

important to highlight the role of Fe in the system as a constant electron donor in the galvanic cell process and possible co-reducing agent, as explained above.

In previous works of our research group, convective flow experiments for dechlorination of TCE were performed, resulting in low correlations in mass balances due to its high volatility. For these reasons, convective flow dechlorinations were not performed.

6.2 DECHLORINATION RESULTS

As specified in the introduction of this chapter, PAA hydrogel and different PVDF-PAA membranes (MPVDF, HPVDF and SPVDF) functionalized with Fe/Pd NPs were tested for dechlorination of TCE as a target chlorinated organic compound. The dechlorination results performed with different metal (Fe/Pd) loadings.

6.2.1 Fe/Pd Nanoparticle Dechlorination in Hydrogel and Membranes Functionalized by Redox Polymerization

Due to the low amount of iron found from the exhausted Fe-based accelerant in the polymerization, the dechlorination experiments in membranes were compared with and without the ion exchange procedure. During the reduction of Fe^{2+} to NPs, the carboxylic groups made a Na^{+} bond from the $NaBH_4$ used. As explained before, the addition of Pd to Fe NPs reduces the time for the same dechlorination yield using Fe NPs alone, because Pd catalyzes the production of hydrogen by Fe corrosion. As shown in Figure 6.2 (hydrogel alone) and Figure 6.3 (hydrogel in membrane), the reduction of TCE is confirmed by the reduction of its concentration.

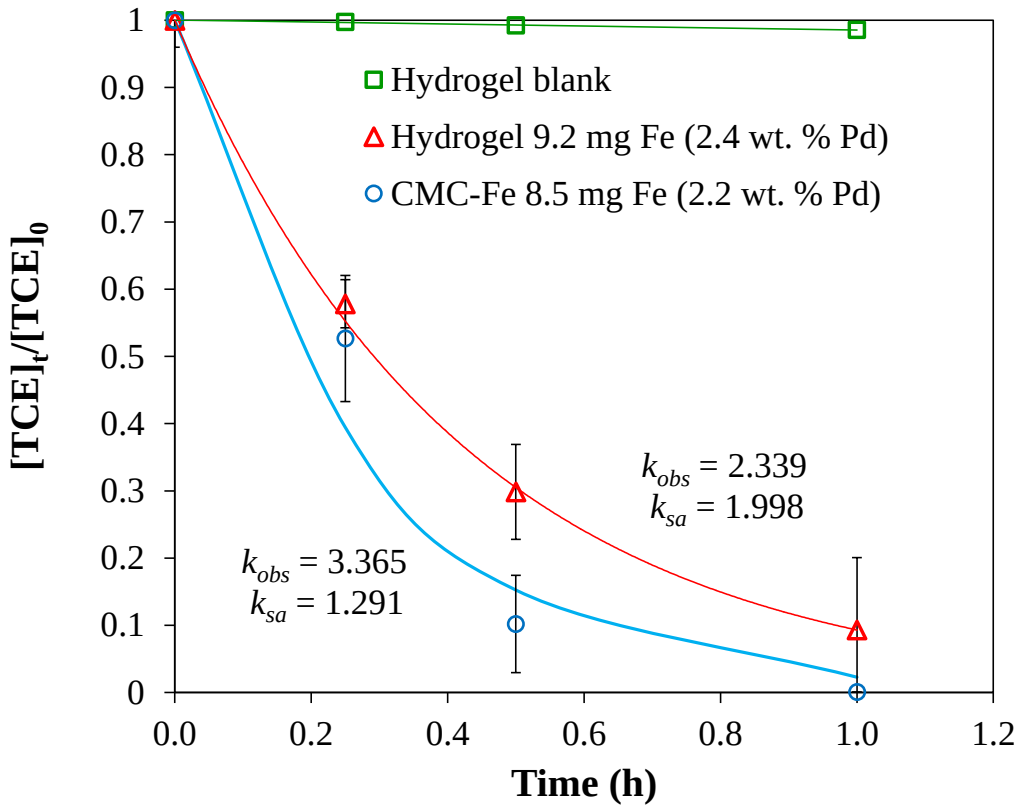

Figure 6.2. TCE batch reduction by Fe/Pd nanoparticles supported in PAA hydrogel and in solution phase stabilized with CMC (0.5 wt. %). TCE concentration = 0.21 mM. Volume = 0.12 L. pH ≈ 6.0. T = 22 °C. All measurements were done by triplicate, calculating the respective deviations and standard errors of the means. Some errors are negligible. Adapted from (Hernandez et al., 2014)

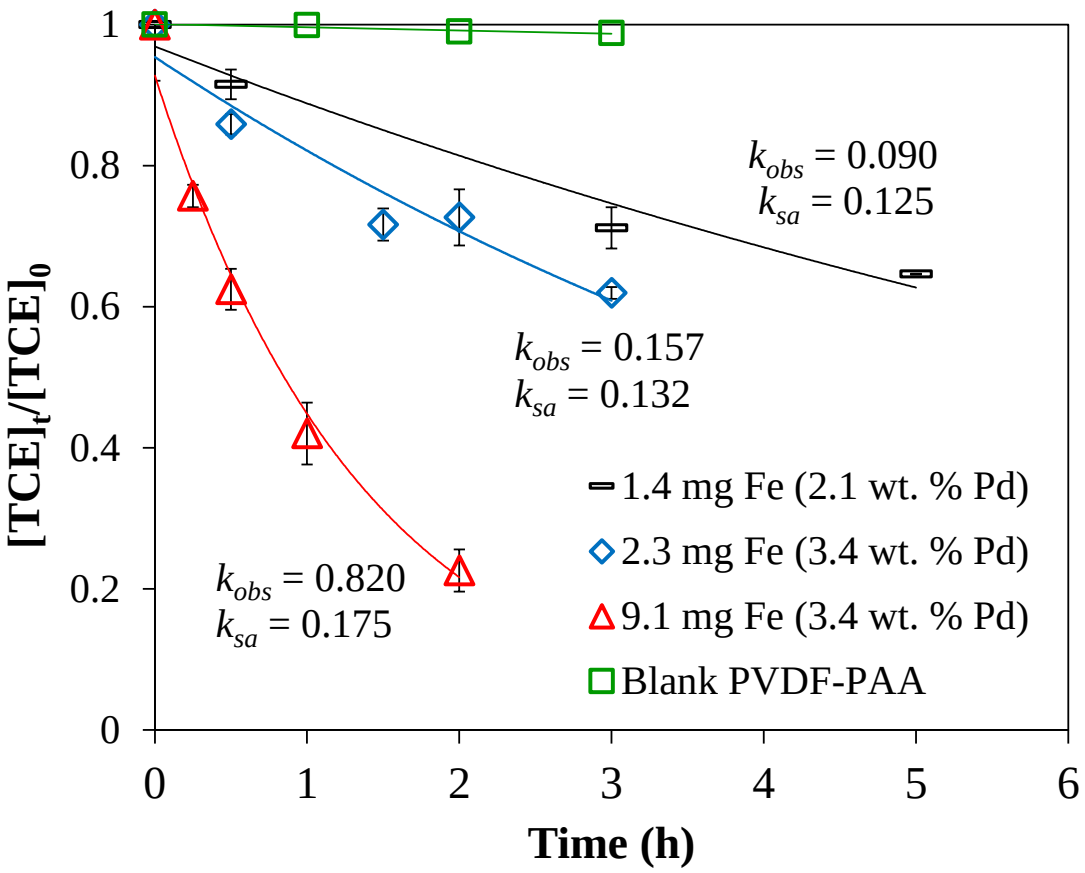

Figure 6.3. TCE batch reduction by Fe/Pd nanoparticles supported in MPVDF-PAA membranes. TCE concentration = 0.21 mM. Volume = 0.02L. pH ≈ 6.0. T = 22 °C. All measurements were done by triplicate, calculating the respective deviations and standard errors of the means. Some error bars are inside the symbols or are negligible. Adapted from (Hernandez et al., 2014).

Comparing to solution phase using CMC to prevent aggregation (Figure 6.2), it can be established that PAA-based immobilization systems also prevents NPs aggregation and provides high dechlorination rates (Feng He et al., 2007). In addition to that, hydrogel and membrane behaviors showed an increase in the reactivity by the increasing in Fe loading, which is confirmed by other studies (Smuleac et al., 2010b). The loss of iron for hydrogel/membrane systems was 0.1 wt. %, and for hydrogel, 0.5 wt. % during the reductive dechlorination experiments. The amount of Pd coating was not analyzed directly, but it affects the reaction rate depending on the extent of coverage of reactive by Pd layers on the Fe surface (J. Xu & Bhattacharyya, 2007).

In Figure 6.4, the molar ratio between chloride formation and TCE degradation is slightly lower (≈ 10%) than the stoichiometric 3:1 (dash line). This confirms the dechlorination of the pollutant without formation of byproducts, which is the main purpose of using Fe/Pd NPs. Although the maximum amount of iron in the membranes is near the calculated value, the reactivity in membrane domain is lower compared with the hydrogel alone. This is explained by the limitations in the diffusion and convective processes due to the performance of the batch experiment.

6.2.2 Fe/Pd Nanoparticle Dechlorination in Sponge-like Functionalized Membranes

An exponential dechlorination behavior (first order rate) at different times for each membrane is shown in Figure 6.5. The decline in TCE concentration is lower as time passes because of mass transfer limitations from the bulk solution to the NP core.

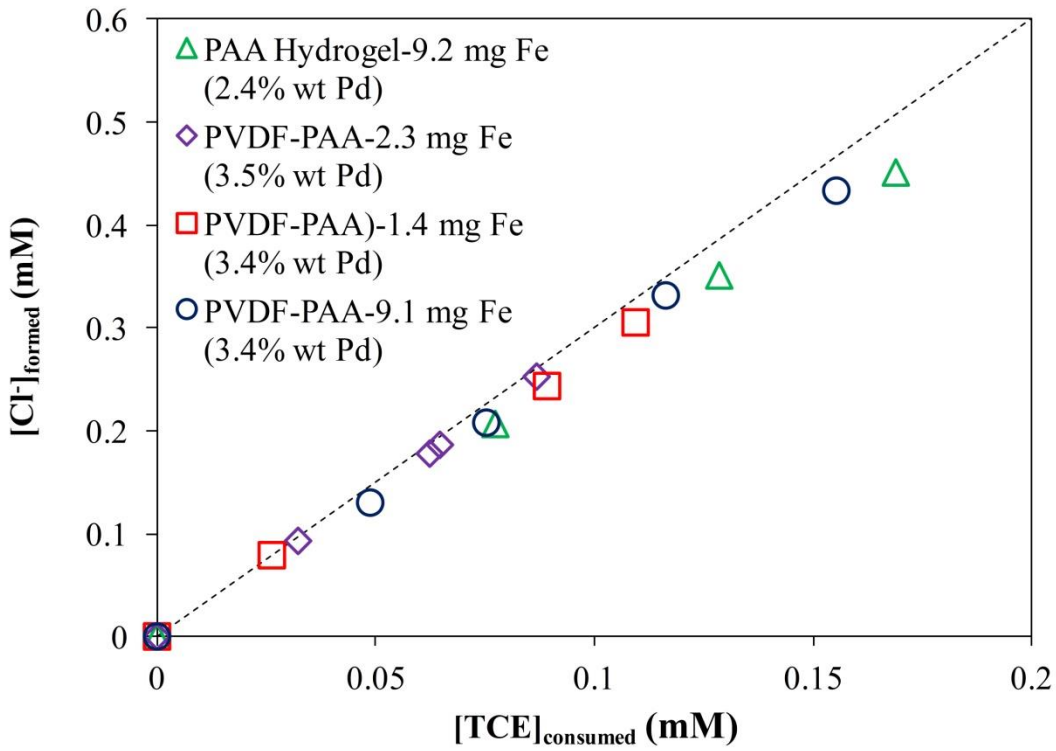

Figure 6.4. TCE consumed in batch reduction by immobilized Fe/Pd nanoparticles in PAA hydrogel and MPVDF membranes, and chloride formation. TCE concentration = 0.21 mM. Volume = 0.02L. pH ≈ 6.0. T = 22 °C. All measurements were done by triplicate, calculating the respective deviations and standard errors of the means. Error are negligible. Reprinted from (Hernandez et al., 2014).

The dechlorination in HF membranes corroborated the increase in the dechlorination rate when the NPs have higher Pd concentration (Figure 6.5a) (Smuleac et al., 2010b). The apparent dechlorination rate constant, k_{obs}, is higher when FS membranes were used with the same iron loading as one of the samples of HF membranes, in part to a slightly higher Pd loading (Figure 6.5b). Based on these results, it can be inferred that the Pd layer was defective at high concentrations or the sponge-like nature of both membranes provided a higher surface area, and hence, accessibility, which gave them more active sites for Fe corrosion, and subsequently higher dechlorination rates.

Chloride ion was also measured here (Figure 6.6) to corroborate the complete dechlorination. Theoretically, chloride concentrations could be lower in the beginning of the reaction or not appreciable due to chloride adsorption by corrosion (Gotpagar et al., 1997; Schrick, Blough, Jones, & Mallouk, 2002). A close correlation of the ratio Cl^- formed to TCE consumed to the stoichiometric value of 3/1 (Cl^-/TCE) was also obtained. This result also confirms that all TCE reacted with negligible presence of intermediates.

6.3 DECHLORINATION REACTION RATES

Johnson et al. developed an analysis of the degradation rates of halogenated hydrocarbons by elemental iron starting from a first-order rate reaction, see Equation (6.9) (Johnson, Scherer, & Tratnyek, 1996). This analysis showed that the dechlorination rate in a batch system can be described by a pseudo-first-order rate:

$$-\frac{dC}{dt} = k_{obs}C = k_{sa}a_s\rho_m C \tag{6.9}$$

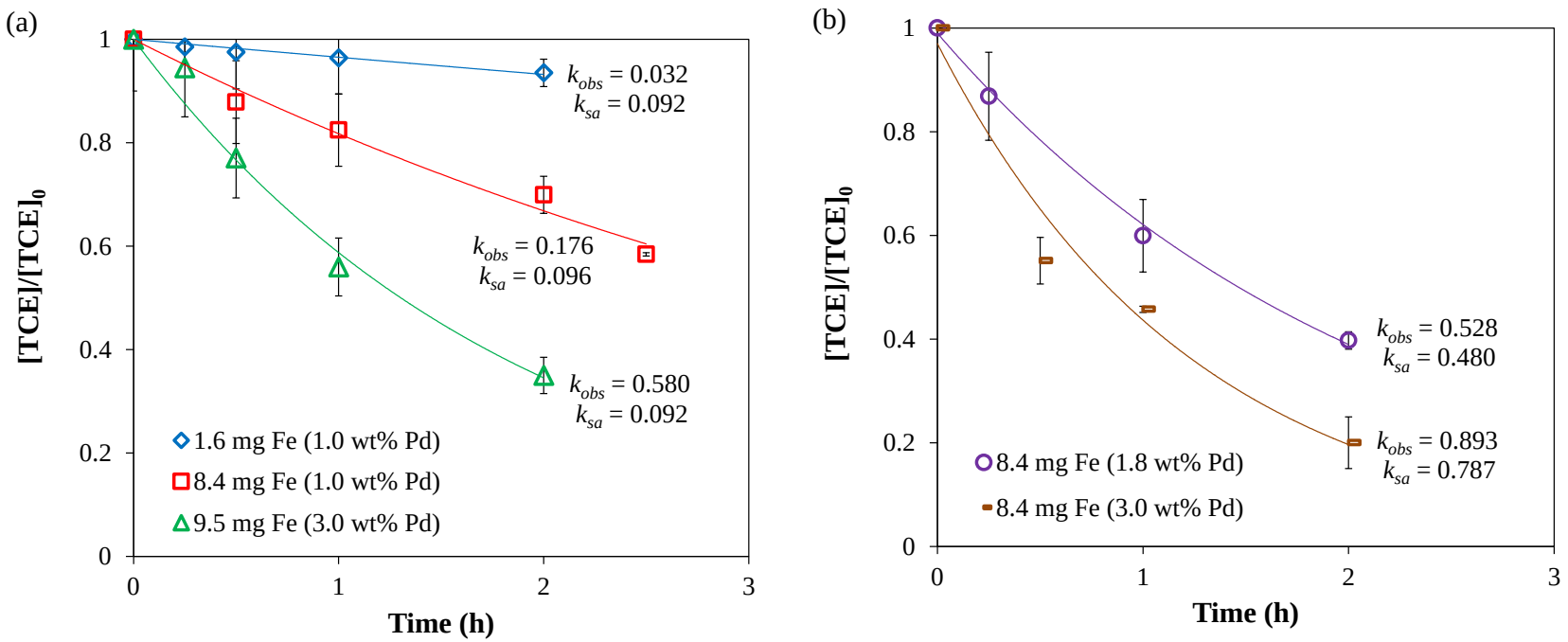

Figure 6.5. TCE reduction by Fe/Pd nanoparticles immobilized in PVDF-PAA membranes. TCE concentration = 0.29 mM. Volume = 0.02 L. pH ≈ 5.5. T = 22 °C. (a) HPVDF (outer surface area= 10.9 cm^2; membrane thickness = 225 µm), (b) SPVDF (Top surface area = 17.3 cm^2; membrane thickness = 125 µm). All measurements were done by triplicate, calculating the respective deviations and standard errors of the means. Some error bars are inside the symbols or are negligible. Adapted from (Hernández, Lei, et al., 2016)

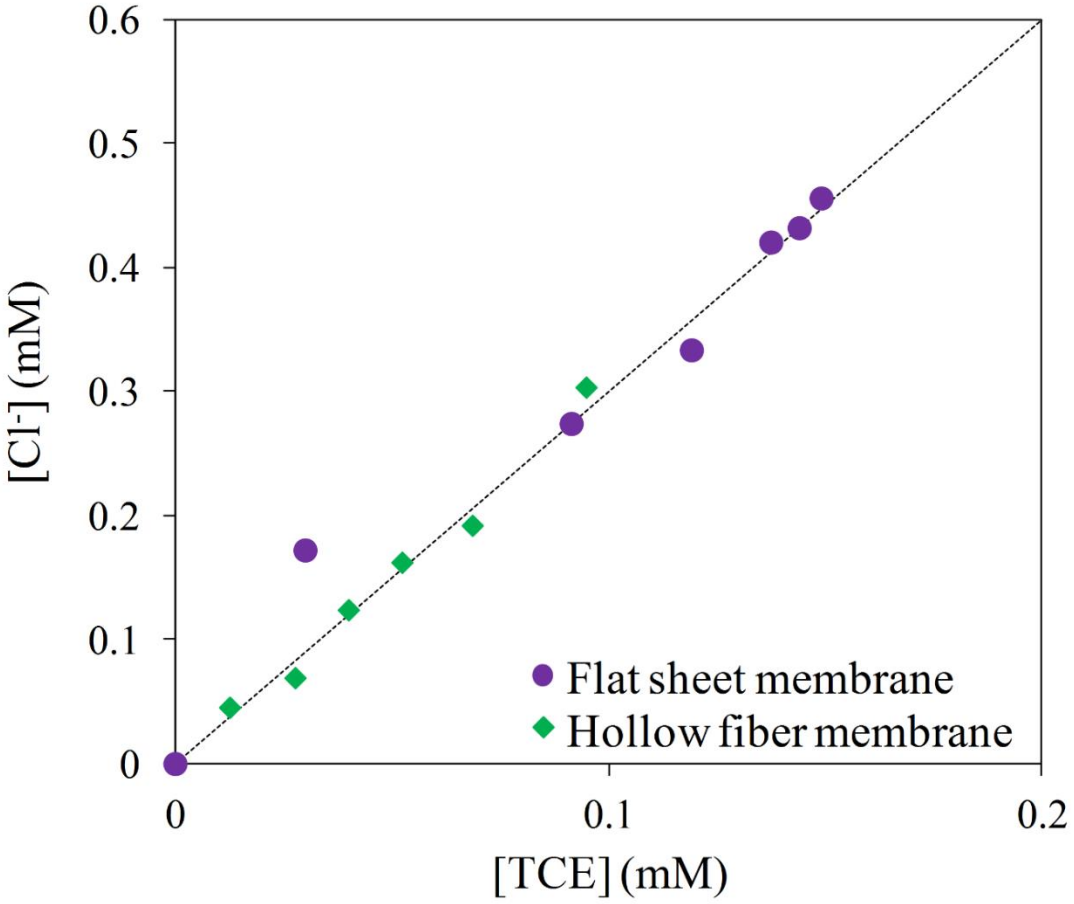

Figure 6.6. Relation of TCE consumed/Cl^- formed from TCE batch reduction by Fe/Pd nanoparticles in hollow fiber (HPVDF-PAA) and flat sheet (SPVDF-PAA) membranes. TCE concentration = 0.29 mM. Volume = 0.02 L. pH ≈ 5.5. T = 22 °C. All measurements were done by triplicate, calculating the respective deviations and standard errors of the means. Error are negligible. Reprinted from (Hernández, Lei, et al., 2016).

where k_{obs} is the observed pseudo-first order rate constant (h^{-1}), C is the TCE concentration (mg/L) at time t (h), k_{sa} is the surface-area rate constant related to the particle size ($L/m^2 \cdot h$), ρ_m is the NP loading (g/L) and a_s (m^2/g) is the specific surface area of the NPs determined from the particle size calculations in Chapter 5.

The k_{sa} values for each system are reported in Table 6.1 for hydrogel, membranes, and solution phase. The k_{sa} value for the hydrogel system is higher than for the membranes due to a more open area and larger volume for reaction. A comparison between the performance of the membranes from redox functionalization (MPVDF) and works from our group and others show similar k_{sa} values using $NaBH_4$ as reducing agent, see Table 6.1. These results demonstrate that the redox functionalization of the membrane give comparable results and can be used as an alternative in dechlorination processes. On the other hand, the membrane used directly from the redox polymerization avoiding ion exchange had very low iron concentration and this value is near to the error range reported from atomic absorption analysis. This result was not reported and implies that almost no reaction was achieved or there is a need of longer times to determine the rate constant. The k_{sa} values from HPVDF obtained are around twice the values of MPVDF and up to 3 times to some reported works with the same concentrations of Pd used (1 to 3 wt. % Pd). For SPVDF membranes these k_{sa} values go from four to almost eightfold previous works. Hydrogel is the support that has the highest results with up to 1.3 times the k_{sa} values of the solution phase Fe/Pd NPs. Comparing these results to Fe^0 NPs, the k_{sa} values are 1-2 orders of magnitude higher and to bulk Fe up to 5 orders of magnitude. Based on these results, it can be inferred that depending on the concentration of the dopant (Pd), the catalytic activity (established by the trichloroethylene (TCE) reduction), was enhanced.

Table 6.1. Fe loading, Pd concentration based on Fe, observed pseudo-first-order rate constants (k_{obs}) and surface-area-normalized rate constants (k_{sa}) for the reduction of TCE. CMC, carboxymethyl cellulose; HPVDF, PVDF hollow fiber membrane; MPVDF, Millipore PVDF membrane; PES, polyether sulfone membrane; SPVDF, Nanostone PVDF sponge-like membrane.

Support or stabilizing agent	**Fe[†] (g/L)**	**Pd[‡] (wt. %)**	k_{obs} **(h^{-1})**	d_{eq} **(nm)**	a_s **(m^2/g)**	k_{sa} **($L \cdot m^{-2} \cdot h^{-1}$)**	***Reference***
MPVDF	0.46	3.4	0.820	74	10.3	0.175	The present work (Hernandez et al., 2014)
	0.07	2.1	0.090	74	10.3	0.125	
	0.12	3.4	0.157	74	10.3	0.132	
HPVDF	0.08	1.0	0.032	175	4.3	0.092	The present work (Hernández, Lei, et al., 2016)
	0.42	1.0	0.176	175	4.3	0.096	
	0.46	3.0	0.580	175	4.3	0.281	
SPVDF	0.41	1.8	0.528	282	2.7	0.480	The present work (Hernández, Lei, et al., 2016)
	0.42	3.0	0.893	282	2.7	0.787	
Hydrogel	0.46	2.4	2.339	50	15.3	1.998	The present work (Hernandez et al., 2014)
CMC (0.5%)	0.43	2.2	3.365	124	6.1	1.291	
MPVDF	0.45	3.0	0.72	20 - 30	25	0.105	(Smuleac et al., 2011)
	0.45	None	0.12	20 - 30	25	0.016	
PES	1.0	11.1	n/a	30.5	25	0.948	(J. Xu, Dozier, & Bhattacharyya, 2005)
CMC (0.2%)	0.1	0.1	7.4	17.2	44	1.56	(Feng He et al., 2007)
None	1.0	0.42	4.2	n/a	30.7	0.140	(Meyer, Hampson, Ormsbee, & Bhattacharyya, 2009)*
	1.9	None	n/a	30 - 40	36.5	0.014	
	n/a	None	0.16	**0.3 - 3 cm**	n/a	6.7×10^{-5}	(Y. Liu et al., 2005)
							(Ebert et al., 2006)*

[†] Fe in membranes estimated on the vial used for reaction. [‡] Percentage based on Fe loading. * Use of Fe in packed columns

7 EXTENSION OF THE MEMBRANE FUNCTIONALIZATION APPLICATION ON A LAYER-BY-LAYER ASSEMBLY FOR THE IMMOBILIZATION OF PORINS

Synthesizing and functionalizing membranes that hold separation aids or reactive species so they selectively separate diverse compounds and simultaneously are responsive to various stimuli promises new and advanced opportunities. The integration of bio-based channels is one of these advancements in membrane technologies and is the motivation of doing this extension of the application. By an LbL assembly of polyelectrolytes, OmpF from *Escherichia coli* with ~2 nm diameter at its opening and ~0.7 × 1.1 nm at its constricted region are immobilized within the pores of PVDF membranes. These biomimetic LbL membranes are studied for rejection of various organic compounds (0.37-4.60 nm radius) and compared to a traditional LbL membranes. The salt rejection depending on pH is also studied in membranes with presence of OmpF. The membrane's stability and consistency in its performance opens up a new field for biomimetic membranes.

This chapter describes the immobilization of OmpF using LbL functionalization, within the pores of previously selected poly(vinylidene fluoride) (PVDF) membranes. OmpF were immobilized after two layers: one of poly(acrylic acid) PAA hydrogel, polymerized in situ, and other of poly(allylamine hydrochloride) (PAH), accumulated by convective flow. The exposed charged residues of OmpF were then crosslinked by a last layer of poly(styrene sulfonic acid) (PSS). The membranes were analyzed during each stage of the process including comparisons between LbL membranes with and without OmpF. Characterizations include Zeta (ζ) potential, pH responsiveness, and changes in

permeability, and rejection of various small organic solutes with salts in the same solution. The characterizations of OmpF purified solutions for immobilization include aggregate size, feed and permeate concentrations, and ζ potential. The effects of pH on permeability and salt rejection were also studied. Parts of this chapter are submitted for publication (Porter et al., 2017).

7.1 CHARACTERIZATION OF OmpF

As indicated by the single band shown in Figure 7.1a, from the SDS-PAGE test, where Lane 1 is the protein marker and Lane 2 is the purified OmpF, the major band between 35 and 40 kDa indicates the presence of OmpF monomer, which has a molecular weight of 38900 Da. OmpF aggregates measured via DLS at varying pH and/or valeric acid concentration present into different sizes (Figure 7.1b). A similar skewed parabolic trend was observed for both pH's, which differs from the negative linear trend observed without pH control, where lower values tend to aggregate more OmpF. With uncontrolled pH, the aggregates tend to be smaller with higher concentrations of valeric acid (from 32 nm in 0.29 M to 16 nm in 2.3 M). It is possible that the addition of sodium hydroxide, which is higher with increased valeric acid to maintain pH, affected the OmpF-solvent interactions. The conditions during the membrane functionalization lie at a pH = 5.5 and 0.035M valeric acid. The pH = 5.5 was chosen because aggregates were significantly smaller than with lower pH, valeric acid is miscible in water at this pH, and the slightly acidic pH achieves the desired charge of residues on the OmpF extracellular loops. Still, 133 nm of aggregate size is much larger than even the non-functionalized membrane pores. However, results from the study with the PC50 membrane suggest shear stress can breakup these aggregates.

7.1.1 OmpF Aggregation Studies

Ideally, the OmpF were to be immobilized within the pores of the functionalized membrane. However, if the aggregates are too large, this might not be possible. In the initial aggregation study, unfiltered solutions exhibited large particulate sizes at a higher concentration of valeric acid, with no observable trend (Figure 7.1b). A negative linear trend of aggregation diameter from 46 nm to 39 nm at valeric acid concentrations of 0.29 M to 0.58 M was observed. However, a significant jump in size occurred between the data points at 0.58 M to 1.15 M valeric acid, from 39 nm to 192 nm. This large aggregation size was maintained up through 2.3 M valeric acid. This behavior of data did not match the observed trends in the filtered in solutions, which exhibited linearly decreasing aggregation diameters from 32 nm to 16 nm for the range of 0.29 M to 2.3 M valeric acid concentrations. Because the higher valeric acid molarity contained a higher concentration of the original OmpF solution, it was assumed that there was a higher concentrations of cell debris in the unfiltered solutions; these larger debris potentially significantly blocked the scattering of light on the smaller OmpF biomolecules. Due to the preliminary studies, filtration of extracted OmpF solution was added to the procedure for the synthesis of the membrane. Another difference between what is observed here and the sizes of the aggregates in the main study is the overall smaller aggregate sizes.

7.1.2 Material Balance during OmpF Membrane Immobilization

From BCA assay, the OmpF material balance in Figure 7.2 presents the feed and the subsequent permeates. A permeate of one pass becomes the feed of the next; for instance, Permeate 1 = Feed 2. As can be seen, by the third pass, no decrease in

concentration between feed (Permeate 2) and Permeate 3 is observed, suggesting for subsequent membrane preparation only two passes of OmpF solution.

For the first and second passes of OmpF solution, protein loaded was 1.74 g/m^2 after two passes. The total number of OmpF's loaded can be determined from their molecular weight (2.69×10^{19} porins/m^2). The permeation of 50 mL DIUF water at pH 6 and 6.8 bar contained 0 μg/mL of OmpF, suggesting secure immobilization of the protein. OmpF feed used was 51-53 μg/mL for all membranes produced. As discussed, a pH = 5.5 was used for the OmpF solution because it theoretically helps to align OmpF within the LbL polymer matrix. The charges of OmpF's outer, exposed residues, or those in the extracellular loops at the top and bottom of the β-barrel are mainly positive at low pH and negative at high pH (Aguilella et al., 2011). Thus, with the final layer of polyelectrolytes being PAH, extracellular loops would orientate away from the layer when permeated at relative acidic pH but are forced into pores by pressure. Consequently, the OmpF pores can be orientated parallel to the flux through the membrane.

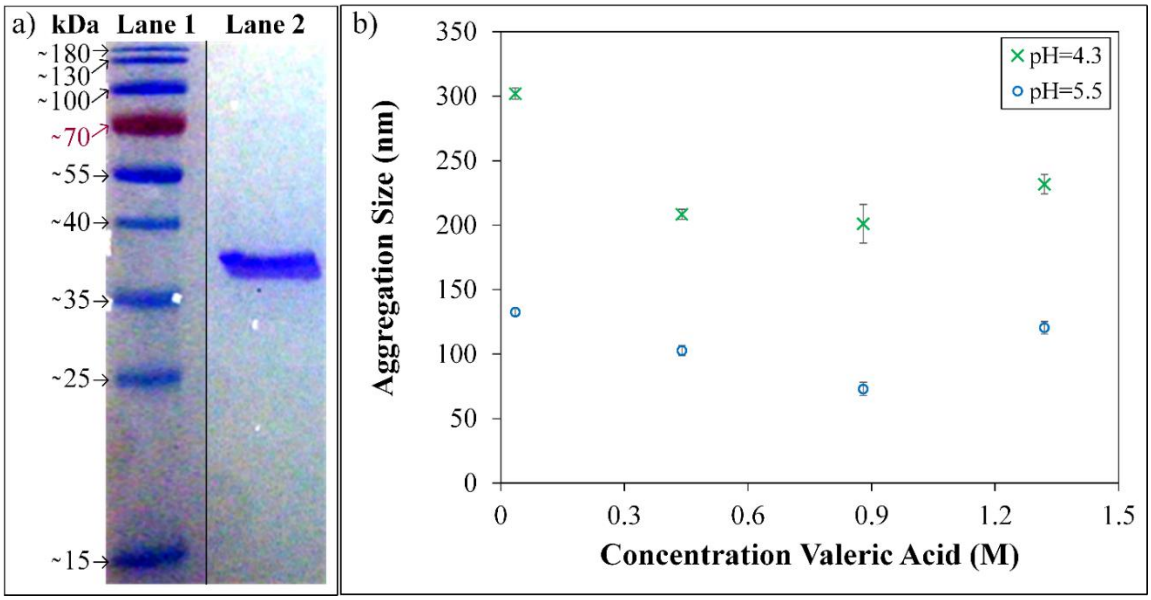

Figure 7.1. (a) SDS-PAGE of OmpF extracted from valeric acid. Lane 1 is the protein marker, and lane 2 is the purified OmpF obtained. (b) DLS aggregation sizes of OmpF solutions at different pH values and valeric acid concentrations. All measurements were done by triplicate, calculating the respective deviations and standard errors of the means. Some error bars are inside the symbols or are negligible. Reprinted from (Porter et al., 2017).

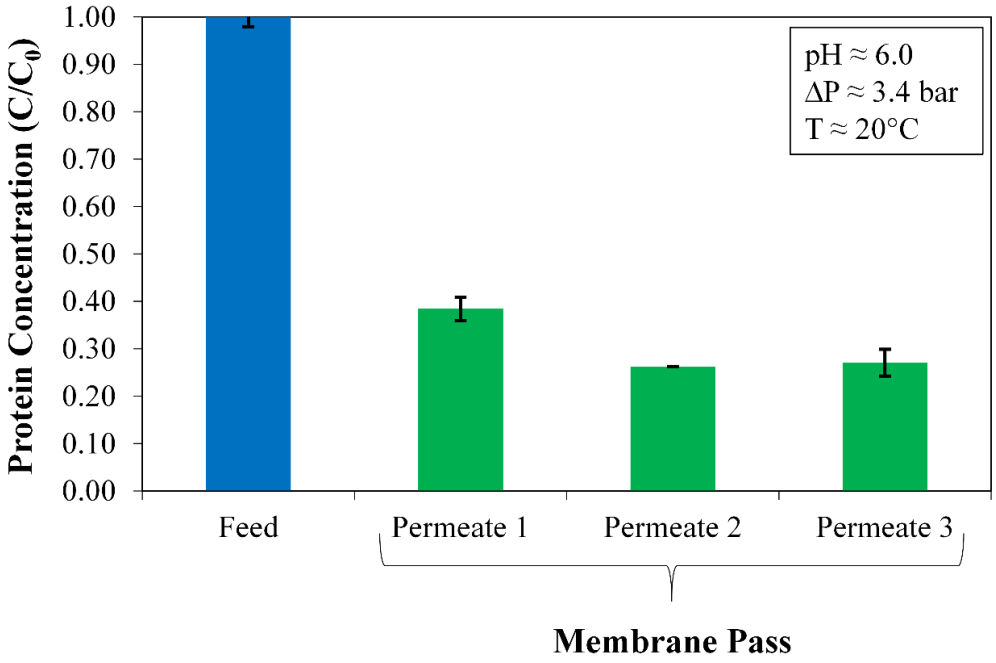

Figure 7.2. OmpF concentration of feed and permeate streams during layer-by-layer functionalization in PVDF-PAA-PAH membrane. Original PVDF: Nanostone PV200 with pore size of 48 ± 1 nm. All measurements were done by triplicate, calculating the respective deviations and standard errors of the means. Reprinted from (Porter et al., 2017).

7.2 REJECTION OF SOLUTIONS

Glucose, sucrose, and different molecular weights of PEG and Dextran were mixed separately with salts (NaCl or $CaCl_2$) in each solution. Table 7.1 shows the hydrodynamic radii (r_H), the hydrated radii and the molecular weight of the solutes used from different references (Baron-Epel, Gharyal, & Schindler, 1988; Choi, Wang, Tung, Morrison, & Konofagou, 2010; Dove & Nix, 1997; Ghandehari, Smith, Ellens, Yeh, & Kopecek, 1997; Kasianowicz, Kellermayer, & Deamer, 2012; Lebrun & Junter, 1993; Ling, Jiang, & Zhang, 2013; Nightingale, 1959; Pappenheimer, 1953; Pluen, Netti, Jain, & Berk, 1999; Ramm, Whitlow, & Mayer, 1982; Ribeiro et al., 2006; Sabek et al., 2013; Schultz & Solomon, 1961). The different values of molecular weights and their corresponding hydrodynamic radius r_H, were correlated for Dextran and poly(ethylene glycol) (PEG) molecules, while mean values were used for glucose and sucrose. From these correlations, the calculated values where used in the rejections studies for each of the species, see Figure A 3 and Figure A 4 in APPENDIX.

It is important to note that the two largest molecules have merely an average r_H of a normally-distributed range of sizes. PEG and Dextran molecules show polydispersity because the length of their chains is not controllable during synthesis. Also, the exact way the chain coils is not consistent and depends on the solvent. Long polymer chains of the same degree of polymerization don't “balled-up” in the same way (Masuelli, 2013; Pluen et al., 1999). Thus, although it seems like 100% rejection should be observed for these molecules with number-average sizes well above the dimensions of OmpF’s constriction zone, the membrane could be defective or there could be polymer chains possessing lengths, and consequently radii, significantly smaller than the average.

Table 7.1. Molecular weight, hydrodynamic and ionic radii of ions and model organic molecules used in rejection studies. †Mean of r_H referenced values. ‡Calculated r_H by curve fitting of referenced values. *Hydrated radii. Reprinted from (Porter et al., 2017)

Molecule	Molecular Weight (Da)	r_H (nm)	Ionic Radii (nm)	Reference
Na^+	23.0	0.36*	0.095	(Dove & Nix, 1997; Nightingale, 1959)
Ca^{2+}	40.1	0.41*	0.099	
Cl^-	35.5	0.33*	0.181	(Nightingale, 1959)
Glucose†	180.2	0.37	-	(Kasianowicz et al., 2012; Pappenheimer, 1953; Ramm et al., 1982; Ribeiro et al., 2006; Sabek et al., 2013; Schultz & Solomon, 1961)
Sucrose†	342.3	0.46	-	(Kasianowicz et al., 2012; Lebrun & Junter, 1993; Pappenheimer, 1953; Ramm et al., 1982; Ribeiro et al., 2006; Schultz & Solomon, 1961)
PEG 400‡	400	0.65	-	(Ghandehari et al., 1997; Kasianowicz et al., 2012; Ling et al., 2013)
PEG 1000‡	1000	0.93	-	
Dextran Blue 5000‡	5000	1.87	-	(Baron-Epel et al., 1988; Choi et al., 2010; Lebrun & Junter, 1993; Pluen et al., 1999)
Dextran 41000‡	41000	4.60	-	

In the case of the ions, large differences are depicted between the Stokes and the hydrated radius in Table 7.1. However, reported values show high variation and only few are depicted here. This phenomena was initially discussed by Nightingale and later by Tansel et al. (Nightingale, 1959; Tansel et al., 2006). Briefly, the Stokes radius in some ions, like Cl^-, is dependent on temperature change and therefore chloride becomes more hydrated at higher temperatures but also, Cl^- is able to lose its hydration water during permeation. The Stokes radius of Na^+ varies slightly with temperature and for Ca^{2+} on the other hand, both Stokes and hydrated radii are independent of temperature. Both, Na^+ and mostly Ca^{2+} are not large enough compared with the water molecule to satisfy the Stokes law. Na^+ has very low charge dispersion, then the hydration water is held more strongly. Ca^{2+} retains less its hydration water than other divalent ions, like Mg^{2+}, making Ca^{2+} more suitable for adsorption on the membrane surface, but also, its rejection is higher than Na^+ because Ca^{2+} hydration radius is larger than Na^+.

7.2.1 Control Studies with OmpF in Track-etched Polycarbonate Membranes

The OmpF immobilization within the track-etched PC50 membrane shows that the permeability of water at 3.4 bar and pH 6.0 went from 204 ± 2 LMH/bar to 20 ± 0.54 LMH/bar, implying OmpF immobilization. No protein was rejected into the retentate and a rinse on the surface did not remove any protein either. A material balance revealed an immobilization of 1.01 g/m^2 of OmpF. However, subsequent rejection tests of the salt/organic mixtures revealed that the PC50-OmpF membrane rejected nothing significantly (all rejections were < 9%) and over the duration of the rejections, permeability increased up to 54 LMH/bar, indicating some OmpF loss. This result confirms that

immobilization of aggregates by simple mechanical wedging is temporary, inconsistent between pores, unstable, and does not improve selectivity and rejection.

7.2.2 Rejection of Organic and Inorganic Solutes during Functionalization

Each additional layer of functionalization increases the rejection of all solutes, as seen in Figure 7.3. The rejections were measured in each of the mixtures salt-organic. Here, rejections are calculated from $R = 1 - C_P/C$, where C_P is the cumulative concentration of permeate and C is the concentration of retentate, per salt and per model organic solute. These trends, are horizontally asymptotic as the size of the model organic solutes increases as they approach 100% rejection, with almost the same recovery V_P/V, where V_P is the cumulative permeate volume and V the feed or retentate volume.

The most important comparison can be made between the fully functionalized membrane with and without OmpF. Rejections of the model organic solutes are slightly different between these two membranes with higher rejections for the non-OmpF membranes, except for glucose, which has a negligible difference between the non-OmpF and the OmpF membranes. Sucrose on the other hand have larger difference in rejections (83 to 62%). It is possible that OmpF's elliptical opening (1.1 × 0.7 nm) allows for sucrose to orientate in such a way that it can passes through more easily than through a rounded pore of the same diameter. OmpF have shown to open larger at high and low pH, and although pH values were around neutral (pH = 6.0), this phenomenon could have been replicated by interactions with individual ions and molecules. This makes OmpF's midsection open and close due to ionization, with the above constriction zone measurements only true for the non-hydrated channel (Jap & Walian, 1996; Todt & McGroarty, 1992).

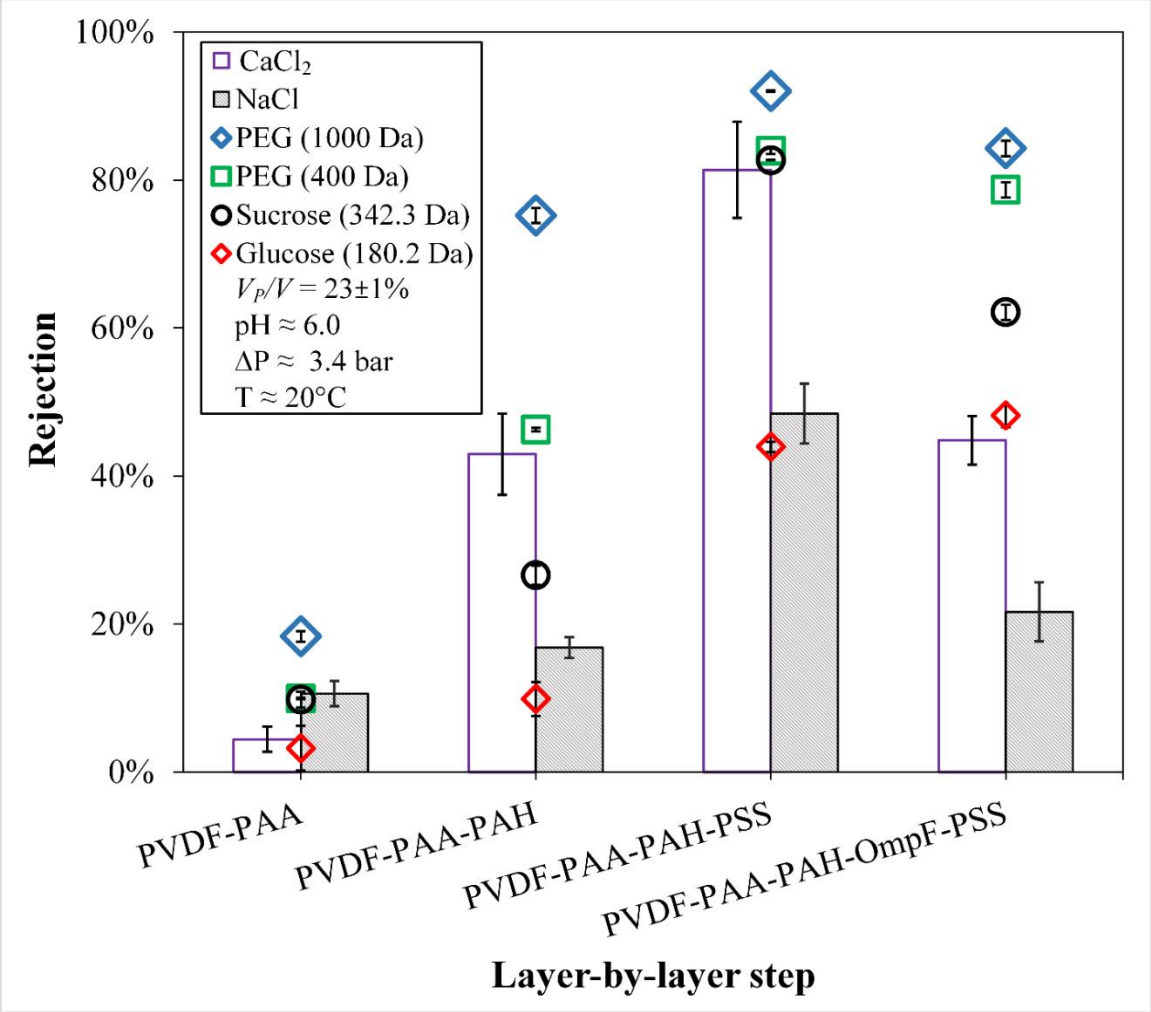

Figure 7.3. Rejection of different organic molecular sizes and inorganic salts for each layer of the layer-by-layer functionalization. Membrane used: PVDF (Nanostone PV200). All measurements were done by triplicate, calculating the respective deviations and standard errors of the means. Some error bars are inside the symbols or are negligible. Reprinted from (Porter et al., 2017).

These rejections for OmpF membranes do not expound what OmpF fully and partially rejects. It is possible that there are pores in the membrane that do not contain OmpF or are only partially horizontally filled, allowing solutes to pass.

OmpF-membranes significantly reject uncharged molecules higher than 1 nm while allowing small ions to pass through. Although the membranes in this study are for microfiltration, due to their functionalization they may behave as UF and nanofiltration membranes, and in these processes, the aim is the removal of small solutes, such as small ions and some organics, from larger compounds. However, it can be observed that the type of these organic compounds did not affect the rejection of the small ions (no larger ions, such as phosphates, nitrates or organics such as carboxylates were studied), feature conventional UF membranes do not present. Even more, with almost similar r_H, OmpF membranes selectively filtrate more small ions, especially NaCl, than the model organics from the mixtures. Sodium chloride rejection is 22% and calcium chloride is 45%, compared to 48 and 62% of glucose and sucrose, respectively.

Therefore, the membrane containing OmpF demonstrates superior selectivity over membranes containing various polymeric layers. Although fully-functionalized non-OmpF membranes reject organics slightly higher than OmpF membranes, with similar permeability, they better separate small ions from uncharged molecules. In fact, non-OmpF membranes reject $CaCl_2$ (Figure 7.3) as well as it rejects larger organics; the exposed charges of the polymeric layers likely are improving ionic rejection and sacrificing selectivity. To estimate this ion/organic selectivity (α), one could calculate a ratio of the sieving coefficients of each of the species ($\alpha = 1 - R_{salt}/1 - R_{org}$), in other words, the ratio of concentration ratios in permeate over retentate (Mehta & Zydney, 2005; Umpuch,

Galier, Kanchanatawee, & Balmann, 2010). Values of α higher than 1 mean that small ions are being filtrated, increasing permeate specific concentrations during the process. In contrast, α values lower than 1 correspond to an increase in ionic concentration in the retentate. Observing the Figure 7.3 for OmpF membranes for example, the ratio of rejections R_{org}/R_{salt} for PEG 1000 go from 1.8 to 3.9 times, depending on the salt used. This represents higher filtration selectivity for small ions, with α values from 3.5 to 5.0.

For the OmpF membrane, more significant values are achieved with NaCl than $CaCl_2$, likely owing to the slightly higher hydrated radius of the calcium salt. These rejections were calculated as an average from multiple passes of salts and model organic solute combinations for each membrane type, taking in account the error propagation for calculations. For all tests, permeability was consistent and not affected by the presence of the solutes, which is confirmed by the recovery. In order to observe the effects of osmotic pressure on permeability over time in the case of significant rejections (those in non-OmpF membranes), much larger initial salt concentration and much more time is needed.

7.2.3 Effect of pH on Inorganic Salt Rejection and Permeability

The functional behavior based on pH between OmpF and non-OmpF membranes shows that the membrane lacking OmpF having a much more drastic increase in rejection from low to a neutral-range pH than from neutral to high (salt solutions with pH 6 were not adjusted). Change in permeability is similar between the two membranes, with lower flux for low pH and higher flux for high pH. The behavior with $CaCl_2$ could be attributed to a simply calcium-polyelectrolyte interaction that could possibly be binding two negative charges, resulting in pseudo-crosslinking of the polymers by chelation, where the

membrane without OmpF exhibits higher degrees of change due to higher number of charges.

However, the rejection of NaCl is different. NaCl of OmpF membranes presents a slightly negative, linear trend. Sodium's slightly smaller r_H represents that the protein's pore residues have dominating rejection factor in the OmpF membrane as opposed to the PSS that crosslinks together the OmpF. This means that more sodium can bypass outer surface charges and make its way into the OmpF pore.

7.3 STABILITY OF OmpF MEMBRANES AND MATERIAL BALANCE EVALUATION DURING SEPARATION PROCESS

The stability and consistency of the rejections for OmpF membranes was tested in three cycles for all organic solutes shown in Table 7.1. In Figure 7.4, the solutions permeated through the membrane for an average of 8 h/day in three weeks, demonstrating the resiliency of the membrane with extremely consistent values with an estimated error of 3.3%. The logarithmic pattern (dash lines in Figure 7.4) again correlates rejection with organics molecular weight (R^2 = 0.90) and thus, with r_H values of the solutes used. The mean recovery, 24 ± 1%, for these cycles is also constant and similar to the previous results. It is worth noting that there is an increase in the recovery (up to 9%) after the first cycle due to adsorption, mainly for solutes with lower molecular weights. These absorptions and measurement errors were up to absolute 8% in all experiments performed and have to be taken into account as imbalances in the material balances, see Material Imbalance Minimization in APPENDIX. At this point, it is confirmed again that OmpF membranes selectively separate the model organic solutes with sizes similar to those of the salts starting from rejections of over 40%.

A material balance calculation for a batch process was done using a model solution of sucrose and NaCl, taking samples of retentate and cumulative permeate over time. Assuming that density does not change due to low solute concentration, the total and the solute mass balances can be calculated by $JA = -\rho\, dV/dt$ and $JAC_p = -\rho\, d(VC)/dt$, respectively, where *J* is the flux of the solution through the membrane, *A* is the area normal to the direction of flux, and *V* is the volume of the feed-retentate through time *t*, and *C* and C_p are the concentrations of feed/retentate and permeate at any given time, respectively.

To calculate the batch operation, analytical integration gives the retentate volume *V* as a function of its concentration in every step of the integration, leaving only one numerical integration for *t* using the functions of the experimental data (*J* and C_p vs. *C*), between the initial and final concentrations, C_0 and *C*. The experimental and the integration values in Figure 7.5 show an expected increase of the retentate *C* as well of α values of NaCl, and an almost constant behavior of the cumulative permeate, C_P. This confirms that OmpF membranes increase the selective filtration of small ions over non-charged organics through time. Comparing the two data sets by a two tails *t*-test shows that there is no evidence of a difference between experimental and calculated values ($|t| = 1.046 < 2.023$ with 5.0% error).

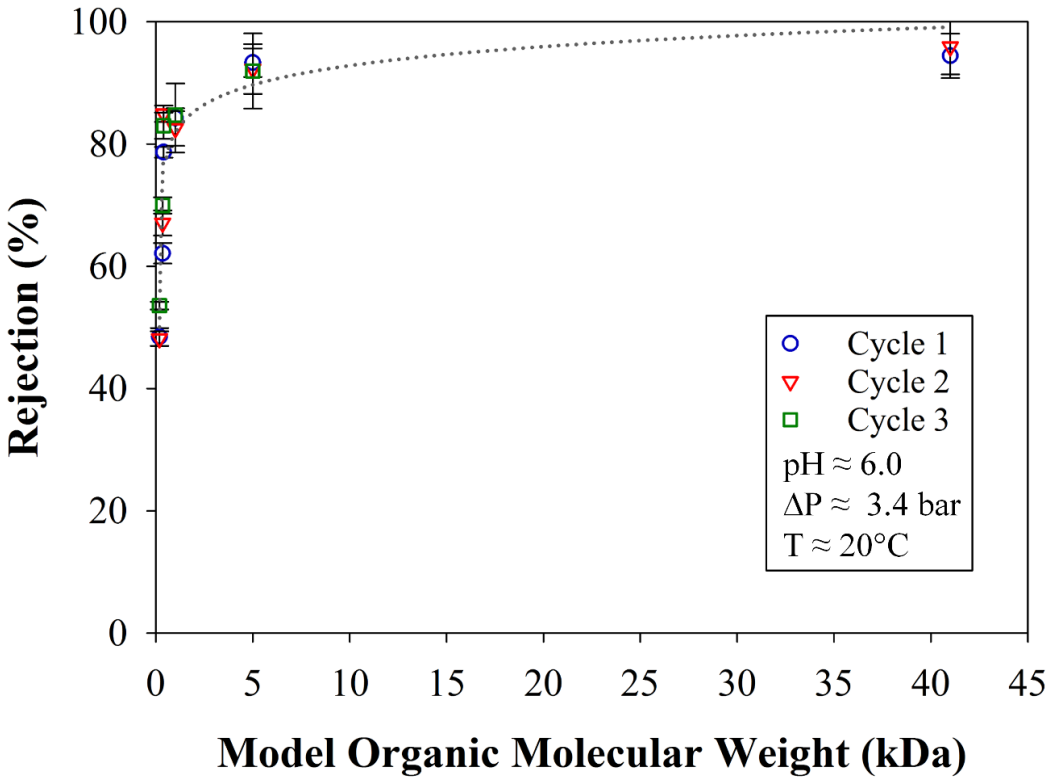

Figure 7.4. Rejections of solutions with different molecular weights of organic solutes over the course of three cycles. Membrane used: PVDF (Nanostone PV200) with a layer-by-layer functionalization of PAA-PAH-OmpF-PSS. All measurements were done by triplicate, calculating the respective deviations and standard errors of the means. Some error bars are inside the symbols or are negligible. Reprinted from (Porter et al., 2017).

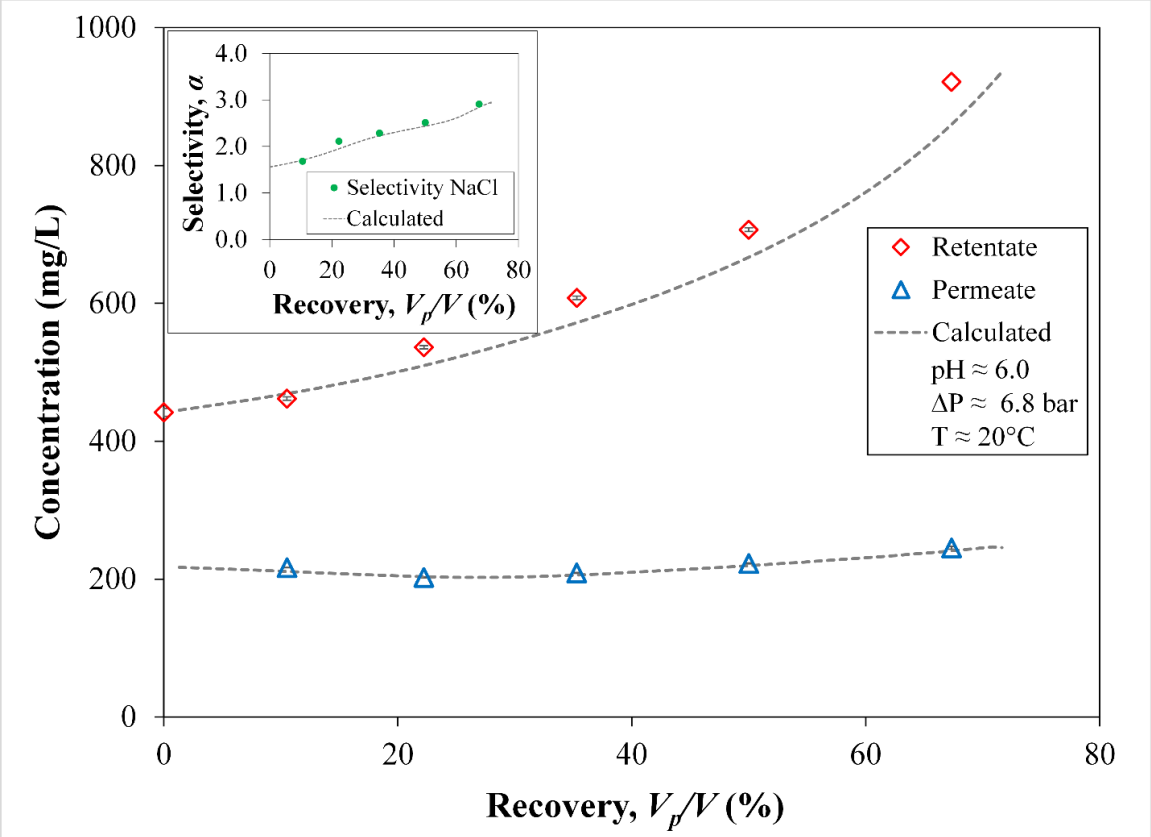

Figure 7.5. Measured and calculated concentrations over time for a solution of sucrose and NaCl. Insert: Selectivity of NaCl from sucrose. Membrane used: PVDF (Nanostone PV200) with layer-by-layer functionalization of PAA-PAH-OmpF-PSS. Sucrose initial concentration, C_0 = 442.05±0.85 mg/L. Initial volume, V_0 = 0.190 L. All measurements were done by triplicate, calculating the respective deviations and standard errors of the means. Error bars are inside the symbols or are negligible. Reprinted from (Porter et al., 2017)

8 CONCLUSIONS

The purpose of the present work was to improve the functionalization aspects of polymeric membranes using a polyelectrolyte hydrogel of acrylic acid and reactive bimetallic nanoparticles (NPs) of Fe/Pd. The performance of these responsive and nanocomposite materials was evaluated in the elimination of chlorinated organics in water, specifically, trichloroethylene (TCE). The polyelectrolyte functionalization was applied throughout layer-by-layer (LbL) polyelectrolyte assembly to immobilize OmpF porins in order to perform selective separation of non-charged molecules.

This work has demonstrated an effective improvement in this reductive treatment by the variation of the supporting membrane types and the functionalization (polymerization and nanoparticle synthesis) processes. The TCE normalized dechlorination rate by membrane supported Fe/Pd nanoparticles is similar to previous works in redox polymerization functionalized membranes, but it goes up to 3 times for hollow fiber and up to 8 times for sponge-like flat sheet membranes. Hydrogel is the support that has the highest results with 1.3 times the k_{sa} values of the solution phase Fe/Pd NPs. This means more than 10 times the k_{sa} values of the membranes.

The extension of membrane functionalization applications through the immobilization of OmpF by polyelectrolyte LbL assembly, in opposition to micellar methods, guarantees better selectivity of charged solutes (small ions) over uncharged (organic species) and consistency of the membranes. This methodology could be applied for immobilizing other biomolecules, such as aquaporins which have the potential to reject 100% of ions.

8.1 KEY ADVANCEMENTS TO SCIENCE AND ENGINEERING

- A significant advancement was developed towards the degradation of chlorinated organics in various types of supports, such as sponge-like membranes (hollow fiber and large scale flat sheet), and hydrogels.

- The growth and the spherical core-shell shape of Fe^0 nanoparticles within the hydrogel is due to the controlled diffusion of the reducing agent caused by the swelling and the degree of entanglement of the hydrogel.

- The development of a methodology for nanoparticle size characterization on a solid support through image analysis (2D metrics) and statistical distributions with specialized software.

- The successful immobilization of OmpF through LbL assembly resulted in higher selectivity values up to 4 times selectivity of charged molecules (small ions) over non-charged (organic species) and the consistency of the membranes for over 3 cycles of filtration process.

8.2 SPECIFIC ACCOMPLISHMENTS

The following accomplishments are described below: methods of membrane functionalization; use of different membrane supports; image analysis technique; and extension of the polyion functionalization through layer-by-layer assembly of OmpF porins.

8.2.1 Membrane Functionalization by Redox Polymerization

- This study demonstrates that the synthesis of Fe/Pd NPs in poly(acrylic acid) PAA hydrogel and membranes using the exhausted metal accelerant from the PAA hydrogel redox polymerization is feasible. NPs formed in the macro-structure of the hydrogel showed low aggregation demonstrating their immobilization in hydrogel/membrane platforms.

- The PAA hydrogel formed by redox polymerization can be used alone directly in catalytic processes after polymerization, avoiding ion exchange processes. However, iron loadings depend on the accelerant concentration required for redox polymerization, which made it a limiting factor for the NP synthesis.

- After ion exchange, the PAA hydrogel showed a large iron loading capacity, allowing less polymer material in the reaction system. This feature could be applied in direct injection for underground water treatment.

- It was demonstrated a relationship between the mesh size of the hydrogel and the pore size of the membrane due to pH changes by swelling and permeability measurements. Mesh size dependence of pH variations in the hydrogel is an important factor in the ion exchange processes towards higher Fe loading.

- The dechlorination of TCE was performed by Fe/Pd NPs in both hydrogel/membrane and single hydrogel systems, showing direct dependence on the Fe amount (and Pd coating).

- The produced chloride using bimetallic Fe/Pd NPs in dechlorination experiments is close to the stoichiometric value, indicating negligible production of intermediates.

- Rate constants of dechlorination have similar values than previous works demonstrating the effectiveness of the functionalization based on redox polymerization.

8.2.2 Sponge-like Membrane Functionalization

- The fabrication of a poly(vinylidene fluoride) (PVDF) hollow fiber membrane by thermal induced phase separation with a porosity of nearly 60%, a pore size distribution with 69% of pores smaller than 1.0 µm and an average size of 0.72 µm.

- The hollow fiber membranes were successfully hydrophilized by crosslinking of polyvinylpyrrolidone (PVP) on top of the porous structure. This was corroborated by the increase of the hydrophilicity and surface free energy of the membranes (40.26 to 50.68 mJ/m^2).

- The cross-linking of PVP on the surface, not only suggests free radical reaction, but also ring-opening and etherification due to the presence of ether bonds in the FTIR spectra.

- The functionalization of PVDF sponge-like membranes, hollow fiber and flat sheet, with a poly(acrylic acid) hydrogel and a subsequent in situ synthesis of bimetallic Fe/Pd NPs. Flat sheet membranes showed a constant iron loading capacity (4.7 ± 0.3 g/m^2). In contrast, hollow fiber membranes showed a variable iron loading (1.6

to 8.7 g/m^2) possibly due to loss of the PVP coating during the functionalization with PAA.

- Particle (NP) size characterization within a solid domain using image analyses of the SEM pictures was applied. This was a method previously not used in this field.

- Image analyses show a close correlation between the degree of sphericity and the circularity of the particles in functionalized membranes, stating that 95% of the particles can be considered spherical.

- The sponge-like structure of the hollow fiber and flat sheet membranes could increase the accessibility to the NP domain and hence, the reactivity of the species.

- The surface-area-normalized dechlorination rate constants are almost four times higher with similar iron loadings to previous studies. Flat sheet membranes have larger surface areas due to their spongy nature.

- The hollow fiber membrane functionalization is highly variable and can present hydrophobic patches or complete inaccessible zones due to hydrogel covering, which makes hollow fibers partially inaccessible. These results represented lower iron loadings than the flat sheet membranes. This behavior explains the inability of Na/Fe ion exchange due to a transport limiting processes through the hydrogel.

8.2.3 OmpF Functionalized Membranes

- Various methods of verifying the grafting of different layers of PAA, poly(allylamine hydrochloride) (PAH), OmpF and poly(styrene sulfonic acid)

(PSS) onto a PVDF microfiltration membrane were accomplished, including pH responsiveness, changes in flux, and Zeta potential values.

- Organic solute rejection studies reveal that a membranes functionalized with OmpF reject these compounds at a comparable amount and flux than the membrane without OmpF.

- Inorganic salt rejections (small ions) through an OmpF LbL membrane are much lower than that of the polymeric membrane without OmpF. LbL membranes with OmpF have higher selectivity for small ions over non-charged molecules than membranes without OmpF.

- For $CaCl_2$, selectivity values are up to 3.5 times higher than a non-OmpF membrane, while NaCl could go up to 6.5 times higher than the non-OmpF one.

- The LbL membrane with OmpF is stable and consistent up to three cycles. Solutions flow through both properly aligned OmpF pores and the spaces between unaligned yet immobilized OmpF.

- A unique pH responsiveness of the LbL membrane with OmpF was observed as it changes in permeability and small ion rejection. This is an indicator that solution is passing mostly through OmpF.

- A study with a polycarbonate membrane proved that OmpF aggregates break up under shear stress. After OmpF immobilization, the decrease of flux and lack of protein in the retentate suggested OmpF went into the pores.

- The insignificant rejection of small ions and model organic solutes and a merely temporary decrease flux of polycarbonate membranes proves that LbL assembly stabilizes OmpF within the membranes and improves their performance.

- The unique behavior of the functionalized PVDF membranes with immobilized OmpF is a promising result, suggesting porins are immobilized, aligned, and functioning.

- The membrane potentially provides more mechanical stability than bioinspired membranes with traditional ruptured lipid bilayer or vesicles contain biomolecular channels.

NOMENCLATURE

Chapter 1

AA, acrylic acid

FS, flat sheet membrane

HF, hollow fiber

LbL, layer-by-layer

MF, microfiltration

NF, nanofiltration

NP, nanoparticle

OmpF, outer membrane protein F or porin

PAA, poly(acrylic acid)

PVDF, poly(vinylidene fluoride)

PVP, polyvinylpyrrolidone

RO, reverse osmosis

TIPS, thermal induced phase separation

TCE, trichloroethylene

UF, ultrafiltration

UV, ultraviolet

Chapter 2

a_s, specific surface area, m^2/g

A_m, area of the membrane, m^2 or cm^2

AA, acrylic acid

C_n, Flory characteristic ratio

CA, cellulose acetate

CNTs, carbon-based nanotubes

COD, chemical oxygen demand

DMF, *N*, *N*-dimethyl-formamide

d, thickness of the membrane excluding the supporting material

EG, ethylene glycol

FO, forward osmosis

GO, graphene and graphene oxide

J_w, flux of water

K, swelling constant

k_{sa}, surface area normalized rate constant

k_{obs}, observed rate constant

l, bond length along the backbone chain for molecules

LbL, layer-by-layer

LCST, lower critical solution temperature

LMH, L/(m^2·h)

m_{Fe}, mass of loaded NPs in the membrane

MBA or NMBA, N,N'-Methylenebisacrylamide

MF, microfiltration

NF, nanofiltration

NIPAm, N-isopropylacrylamide

NP, nanoparticle

NIPS, non-solvent induced phase separation

OMC, ordered mesoporous carbon

OmpF, outer membrane protein F or porin

PA, polyamide

PAA, poly(acrylic acid)

PAN, poly(acrylonitrile)

PAN-*co*-PAA, poly(acrylonitrile-*co*-acrylic acid)

PCB, polychlorinated biphenyl

PDMAEMA, poly(N-N'-dimethylaminoethyl methacrylate)

PES, polyether sulfone

PI, phase inversion

PLA, poly(lactic acid)

PMMA-*b*-P4VP, poly(methyl methacrylate)-block-poly(4-vinylpyridine)

PNIPAm, poly(N-isopropylacrylamide)

polyHEMA, poly(2-hydrocyethyl methacrylate)

PPEGMA, poly(ethylene glycol) methyl ether methacrylate

PS, polysulfone

PVDF, poly(vinylidene fluoride)

PVP, polyvinylpyrrolidone

Q, water flow rate

RO, reverse osmosis

TAP, 2, 4, 6-triaminopyrimidine

TCE, trichloroethylene

TESPN, 3-(Triethoxysilyl) propionitrile

TFC's, thin-film membranes created by interfacial polymerization

TFN, thin film nanocomposites

TIPS, thermal induced phase separation

T_g, glass transition temperature

TOC, total organic carbon

UCST, upper critical solution temperature

UF, ultrafiltration

W_0, weights of the membrane before functionalization with hydrogel

W, weights of the membrane after functionalization with hydrogel

ε_s, membrane porosity

ρ_m, density of loaded NPs in the membrane or hydrogel

ρ_{gel}, hydrogel density

hydrogel density

τ, residence time

Φ, gel volume fraction of the functionalized membrane

Chapter 3

AA, acrylic acid

AH_2, ascorbic acid

APS, ammonium persulfate ($(NH_4)_2S_2O_8$)

ATR-FTIR, Attenuated total reflectance – Fourier transform infrared spectrum

CA, contact angle

CFP, capillary flow porometer

CMC, carboxymethyl cellulose

DBP, dibutyl phthalate

DIUF, deionized ultra-filtered water

DLS, dynamic light scattering

EDB, 1, 2 dibromoethane

EDS, energy dispersive X-ray spectrometer

FIB, focus ion beam

FS, flat sheet membrane(s)

FTIR, Fourier transform infra-red

GC-MS, gas chromatography – mass spectrometry

HF, hollow fiber membrane(s)

HPVDF, PVDF hollow fiber membrane

IC, ion chromatography

ICP, inductively coupled plasma optical emission spectrometer

IPA, isopropanol

IR, infrared spectroscopy

KPS, potassium persulfate

LbL, layer-by-layer

MBA or NMBA, N,N'-Methylenebisacrylamide

MPVDF, Millipore PVDF membrane

NP, nanoparticle

OmpF, outer membrane protein F or porin

PAA, poly(acrylic acid)

PAH, poly(allylamine hydrochloride)

PC50, polycarbonate membrane of 50 nm pore size

PEG, polyethylene glycol

PSS, poly(styrene sulfonic acid)

PV200, Nanostone PVDF 50 kDa membrane

PV700, Nanostone PVDF 35 nm membrane

PVDF, poly(vinylidene fluoride)

PVP, polyvinylpyrrolidone

SEM, scanning electron microscope

SDS, sodium dodecyl sulfate

SDS-PAGE, sodium dodecyl sulfate polyacrylamide gel electrophoresis

SPVDF, Nanostone PVDF sponge-like membrane

TCE, trichloroethylene

TEM, transmission electron microscopy

TEMED, N,N,N′,N′-Tetramethylethylenediamine

TIPS, thermal induced phase separation

TOC, total organic carbon

UV, ultraviolet spectroscopy

XPS, X-ray photoelectron spectroscopy scan

ζ, zeta potential

Chapter 4

A, area of the membrane, m^2 or cm^2

A_0, or A_{PVDF}, permeability of the bare membrane, L/ (m^2·h·bar)

AA, acrylic acid

Ad, dehydroascorbic acid

A_F, permeability of the functionalized membrane, L/ (m^2·h·bar) = LMH/ bar

AH_2, ascorbic acid

APS, ammonium persulfate ($(NH_4)_2S_2O_8$)

ATR-FTIR, Attenuated total reflectance – Fourier transform infrared spectrum

C_n, Flory characteristic ratio

CA, contact angle

CFP, capillary flow porometer

DIUF, deionized ultra-filtered water

d_p, equivalent pore diameter

d_{p0} or d_{PVDF}, equivalent (effective) pore diameter of the bare membrane

FS, flat sheet membrane

FTIR, Fourier transform infrared spectrum

HF, hollow fiber membrane

HPVDF, PVDF hollow fiber membrane

I, initiator

IPA, isopropanol

J_v, flux solution through the membrane

K, swelling constant

k', initiation constant in polymerization

k_d, dissociation constant in polymerization

k_p, propagation constant in polymerization

k_t, termination constant in polymerization

KPS, potassium persulfate

l, bond length along the backbone chain for molecules

LbL, layer-by-layer

LMH, L/(m^2·h)

M, monomer

m_0 and *m*, weights of xerogel and hydrogel, respectively

M_0, molecular weight of the repeating units

MBA or NMBA, N,N'-Methylenebisacrylamide

M_c, molecular weight of the polymer chains between cross-linked points

MPVDF, Millipore PVDF membrane

M_n, molecular weight by number

NP, nanoparticle

OmpF, outer membrane protein F or porin

PAA, poly(acrylic acid)

PAH, poly(allylamine hydrochloride)

PSS, poly(styrene sulfonic acid)

PV200, Nanostone PVDF 50 kDa membrane

PV700, Nanostone PVDF 35 nm membrane

PVDF, poly(vinylidene fluoride)

PVP, polyvinylpyrrolidone

R_i, rate of initiation (polymerization)

R_p, rate of propagation (polymerization)

SEM, scanning electron microscope

SPVDF, Nanostone PVDF sponge-like membrane

t, time, s or h

T, temperature, °C

TIPS, thermal induced phase separation

v_{2eq}, volume fraction of the swollen polymer

w, weight of the non-functionalized PVDF membranes, g

W, water absorbed

W_{eq}, water absorbed in equilibrium

X, degree of cross-linking

XPS, X-ray photoelectron spectroscopy scan

Δm, average mass gain

ΔP, applied pressure

γ_S^{TOT}, surface free energy

γ_L, surface tension of water

ε_m, membrane porosity

ζ, zeta potential

θ_A, advancing contact angle, °

θ_R, receding contact angle, °

ξ, mesh size

ρ_I, IPA density

ρ_P, polymer density

ω, weight of membrane in porosity calculations

Chapter 5

a_s, specific surface area, m^2/g

A_p, projected area of nanoparticle

AA, acrylic acid

AFM, atomic force microscopy

AH_2, ascorbic acid

AR, aspect ratio

BET, Brunauer–Emmett–Teller surface analysis

c, circularity

d_c, minimum circumscribed circle

d_{eq}, equivalent diameter

d_i, maximum inscribed circle

DIUF, deionized ultra-filtered water

DLS, dynamic light scattering

EDS, energy dispersive X-ray spectrometer

FIB, focus ion beam

HPVDF, PVDF hollow fiber membrane

ICP, inductively coupled plasma optical emission spectrometer

MPVDF, Millipore PVDF membrane

NP, nanoparticle

P, perimeter

PAA, poly(acrylic acid)

PVDF, poly(vinylidene fluoride)

R, roundness

SPVDF, Nanostone PVDF sponge-like membrane

SEM, scanning electron microscope

TEM, transmission electron microscopy

Δm, average mass gain

ϕ, Wadell's degree of sphericity

Chapter 6

a_s, specific surface area, m2/g

C, concentration of TCE

CMC, carboxymethyl cellulose

d_{eq}, equivalent diameter

FS, flat sheet membrane(s)

HF, hollow fiber membrane(s)

HPVDF, PVDF hollow fiber membrane

k_{obs}, apparent dechlorination rate constant

k_{sa}, surface area normalized rate constant

MPVDF, Millipore PVDF membrane

NP, nanoparticle

PAA, poly(acrylic acid)

PES, polyether sulfone

PVDF, poly(vinylidene fluoride)

SPVDF, Nanostone PVDF sponge-like membrane

TCE, trichloroethylene

ρ_m, density of loaded NPs in the membrane or hydrogel

Chapter 7

A, area of the membrane, m^2 or cm^2

BCA, bicinchoninic acid

C or C_0 concentration of retentate

C_P, cumulative concentration of permeate

DIUF, deionized ultra-filtered water

DLS, dynamic light scattering

J, flux solution through the membrane

LbL, layer-by-layer

LMH, L/(m^2·h)

OmpF, outer membrane protein F or porin

PAA, poly(acrylic acid)

PAH, poly(allylamine hydrochloride)

PC50, polycarbonate membrane of 50 nm pore size

PEG, polyethylene glycol

PSS, poly(styrene sulfonic acid)

PV200, Nanostone PVDF 50 kDa membrane

PV700, Nanostone PVDF 35 nm membrane

PVDF, poly(vinylidene fluoride)

R, rejection

R_{salt}, rejection of inorganic solute

R_{org}, rejection of organic solute

r_H, hydrodynamic radius

SDS, sodium dodecyl sulfate

SDS-PAGE, sodium dodecyl sulfate polyacrylamide gel electrophoresis

SPVDF, Nanostone PVDF sponge-like membrane

t, time, s or h

V_P, cumulative permeate volume

V, feed/retentate volume

α, selectivity.

ρ, water density

Chapter 8

LbL, layer-by-layer

NP, nanoparticle

OmpF, outer membrane protein F or porin

PAA, poly(acrylic acid)

PAH, poly(allylamine hydrochloride)

PSS, poly(styrene sulfonic acid)

PVDF, poly(vinylidene fluoride)

PVP, polyvinylpyrrolidone

TCE, trichloroethylene

APPENDIX

Chapter 5.

DLS Nanoparticle Characterization

BECKMAN COULTER

Delsa™ Nano
igertdls

Number Distribution S/N : 103207

User	: igertdls	Group	:	Repetition	: 2/3
Date	: 6/22/2012	File Name	: SEB_062212_FIL_20120622_130958		
Time	: 13:09:58	Sample Information	: 1		
SOP Name	: DB Lab 06222012			Security	: Security

Version 2.31 / 2.00

Number Distribution

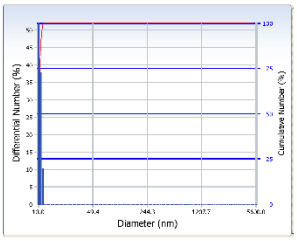

ACF

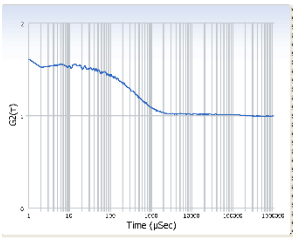

Distribution Results (Contin)

Peak	Diameter (nm)	Std. Dev.
1	10.4	0.5
2	209.2	28.7
3	5,234.5	251.2
4	0.0	0.0
5	0.0	0.0
Average	10.4	0.8

Residual : 4.323e-002 (N.G)

Cumulants Results

Diameter	(d)	: 376.4	(nm)
Polydispersity Index	(P.I.)	: 0.166	
Diffusion Const.	(D)	: 1.307e-008	(cm^2/sec)

Measurement Condition

Temperature	: 25.0	(°C)
Diluent Name	: WATER	
Refractive Index	: 1.3328	
Viscosity	: 0.8878	(cP)
Scattering Intensity	: 6965	(cps)

Number Distribution Table

d (nm)	f(%)	f(cum.%)	d (nm)	f(%)	f(cum.%)	d (nm)	f(%)	f(cum.%)	d (nm)	f(%)	f(cum.%)
10.0	52.0	52.0	49.4	0.0	100.0	244.3	0.0	100.0	1207.7	0.0	100.0
10.7	37.8	89.8	52.7	0.0	100.0	260.5	0.0	100.0	1287.4	0.0	100.0
11.4	10.2	100.0	56.2	0.0	100.0	277.6	0.0	100.0	1372.4	0.0	100.0
12.1	0.0	100.0	59.9	0.0	100.0	296.0	0.0	100.0	1463.0	0.0	100.0
12.9	0.0	100.0	63.8	0.0	100.0	315.5	0.0	100.0	1559.5	0.0	100.0
13.8	0.0	100.0	68.0	0.0	100.0	336.3	0.0	100.0	1662.5	0.0	100.0
14.7	0.0	100.0	72.5	0.0	100.0	358.5	0.0	100.0	1772.2	0.0	100.0
15.6	0.0	100.0	77.3	0.0	100.0	382.2	0.0	100.0	1889.2	0.0	100.0
16.7	0.0	100.0	82.4	0.0	100.0	407.4	0.0	100.0	2013.9	0.0	100.0
17.8	0.0	100.0	87.9	0.0	100.0	434.3	0.0	100.0	2146.8	0.0	100.0
18.9	0.0	100.0	93.7	0.0	100.0	463.0	0.0	100.0	2288.5	0.0	100.0
20.2	0.0	100.0	99.8	0.0	100.0	493.5	0.0	100.0	2439.6	0.0	100.0
21.5	0.0	100.0	106.4	0.0	100.0	526.1	0.0	100.0	2600.6	0.0	100.0
23.0	0.0	100.0	113.5	0.0	100.0	560.9	0.0	100.0	2772.3	0.0	100.0
24.5	0.0	100.0	121.0	0.0	100.0	597.9	0.0	100.0	2955.2	0.0	100.0
26.1	0.0	100.0	128.9	0.0	100.0	637.3	0.0	100.0	3150.3	0.0	100.0
27.8	0.0	100.0	137.4	0.0	100.0	679.4	0.0	100.0	3358.2	0.0	100.0
29.6	0.0	100.0	146.5	0.0	100.0	724.2	0.0	100.0	3579.9	0.0	100.0
31.6	0.0	100.0	156.2	0.0	100.0	772.0	0.0	100.0	3816.2	0.0	100.0
33.7	0.0	100.0	166.5	0.0	100.0	823.0	0.0	100.0	4068.1	0.0	100.0

D (10%) : 10.70 (nm) D (50%) : 10.70 (nm) D (90%) : 10.70 (nm)

Figure A 1. DLS report 1

BECKMAN COULTER

Delsa™ Nano
igertdls

Number Distribution S/N : 103207

User	: igertdls	Group	:	Repetition	: 2/3
Date	: 6/22/2012	File Name	: SEB_062212_FIL_20120622_130958		
Time	: 13:09:58	Sample Information	: 1		
SOP Name	: DB Lab 06222012			Security	: Security

Version 2.31 / 2.00

Number Distribution

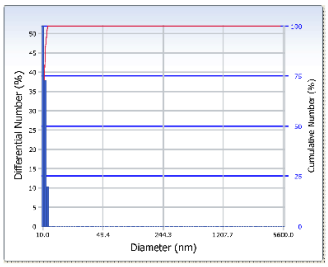

ACF

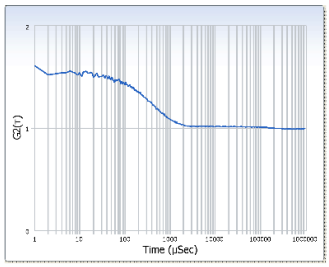

Distribution Results (Contin)

Peak	Diameter (nm)	Std. Dev.
1	10.4	0.5
2	209.2	28.7
3	5,234.5	251.2
4	0.0	0.0
5	0.0	0.0
Average	10.4	0.8

Residual : 4.323e-002 (N.G)

Cumulants Results

Diameter	(d)	: 376.4	(nm)
Polydispersity Index	(P.I.)	: 0.166	
Diffusion Const.	(D)	: 1.307e-008	(cm²/sec)

Measurement Condition

Temperature	: 25.0	(°C)
Diluent Name	: WATER	
Refractive Index	: 1.3328	
Viscosity	: 0.8878	(cP)
Scattering Intensity	: 6965	(cps)

Number Distribution Table

d (nm)	f(%)	f(cum.%)	d (nm)	f(%)	f(cum.%)	d (nm)	f(%)	f(cum.%)	d (nm)	f(%)	f(cum.%)
10.0	52.0	52.0	49.4	0.0	100.0	244.3	0.0	100.0	1207.7	0.0	100.0
10.7	37.8	89.8	52.7	0.0	100.0	260.5	0.0	100.0	1287.4	0.0	100.0
11.4	10.2	100.0	56.2	0.0	100.0	277.6	0.0	100.0	1372.4	0.0	100.0
12.1	0.0	100.0	59.9	0.0	100.0	296.0	0.0	100.0	1463.0	0.0	100.0
12.9	0.0	100.0	63.8	0.0	100.0	315.5	0.0	100.0	1559.5	0.0	100.0
13.8	0.0	100.0	68.0	0.0	100.0	336.3	0.0	100.0	1662.5	0.0	100.0
14.7	0.0	100.0	72.5	0.0	100.0	358.5	0.0	100.0	1772.2	0.0	100.0
15.6	0.0	100.0	77.3	0.0	100.0	382.2	0.0	100.0	1889.2	0.0	100.0
16.7	0.0	100.0	82.4	0.0	100.0	407.4	0.0	100.0	2013.9	0.0	100.0
17.8	0.0	100.0	87.9	0.0	100.0	434.3	0.0	100.0	2146.8	0.0	100.0
18.9	0.0	100.0	93.7	0.0	100.0	463.0	0.0	100.0	2288.5	0.0	100.0
20.2	0.0	100.0	99.8	0.0	100.0	493.5	0.0	100.0	2439.6	0.0	100.0
21.5	0.0	100.0	106.4	0.0	100.0	526.1	0.0	100.0	2600.6	0.0	100.0
23.0	0.0	100.0	113.5	0.0	100.0	560.9	0.0	100.0	2772.3	0.0	100.0
24.5	0.0	100.0	121.0	0.0	100.0	597.9	0.0	100.0	2955.2	0.0	100.0
26.1	0.0	100.0	128.9	0.0	100.0	637.3	0.0	100.0	3150.3	0.0	100.0
27.8	0.0	100.0	137.4	0.0	100.0	679.4	0.0	100.0	3358.2	0.0	100.0
29.6	0.0	100.0	146.5	0.0	100.0	724.2	0.0	100.0	3579.9	0.0	100.0
31.6	0.0	100.0	156.2	0.0	100.0	772.0	0.0	100.0	3816.2	0.0	100.0
33.7	0.0	100.0	166.5	0.0	100.0	823.0	0.0	100.0	4068.1	0.0	100.0

D (10%) : 10.70 (nm) D (50%) : 10.70 (nm) D (90%) : 10.70 (nm)

Figure A 2. DLS report 2

Nanoparticle Distributions SAS Code

```
data NP;
        label size = 'Diameter (nm)';
        input size @@;
        datalines;
        "insert values";
        run;
        title 'Distribution of Nanoparticle Size';
        proc univariate data=NP;
          var size;
          histogram / lognormal(THETA=EST)
                gamma(THETA=EST)
                      normal
                      vaxis   = axis1;
          inset n mean(5.3) mode(5.3) median(5.3) std='Std Dev'(5.3)
                / pos = ne  header = 'Summary Statistics';
          axis1 label=(a=90 r=0);
run;
```

Chapter 7.

Rejection of Solutions

The different values of molecular weights and their corresponding hydrodynamic radius r_H, were correlated for Dextran and poly(ethylene glycol) (PEG) molecules. From these correlations, the calculated values where used in the rejections studies for each of the species. See Figure A 3and Figure A 4.

Material Imbalance Minimization

Although the deviation from the mass conservation due to measurements and/or absorption of the species within the membranes are somewhat low (absolute 8%), it is important to minimize these results in order to calculate batch operation processes. The mass conservation equations including imbalances are:

$$V_0 - V_P - V = I_V \tag{A1}$$

$$V_0 C_0 - V_P C_P - VC = I_C \tag{A2}$$

Where V_0, V_P and V are the volumes of feed, permeate and retentate, respectively, and C_0, C_P and C, the respective concentrations of the species. I_V and I_C are the imbalances due to absorption or errors for volume and species, respectively. Adapting the process from Wills with only one process unit and one species per minimization, the function to minimize is (Wills, Napier-Munn, & Julius Kruttschnitt Mineral Research, 2006):

$$S = \sum (I_V)^2 + \sum_i (I_{Ci})^2 \tag{A3}$$

Where i stands for each component in solution to be evaluated. However, in this research, only one compound was evaluated at the time. Deriving (A3) for V_P and V,

equating them to zero and combining the two derivatives, the following ratio can be obtained:

$$\frac{V_P}{V_0} = \frac{C - C_0}{C - C_P} \tag{A4}$$

Which gives new estimated values for V_0, V_P and V using the original mass conservation equations with negligible or zero imbalance.

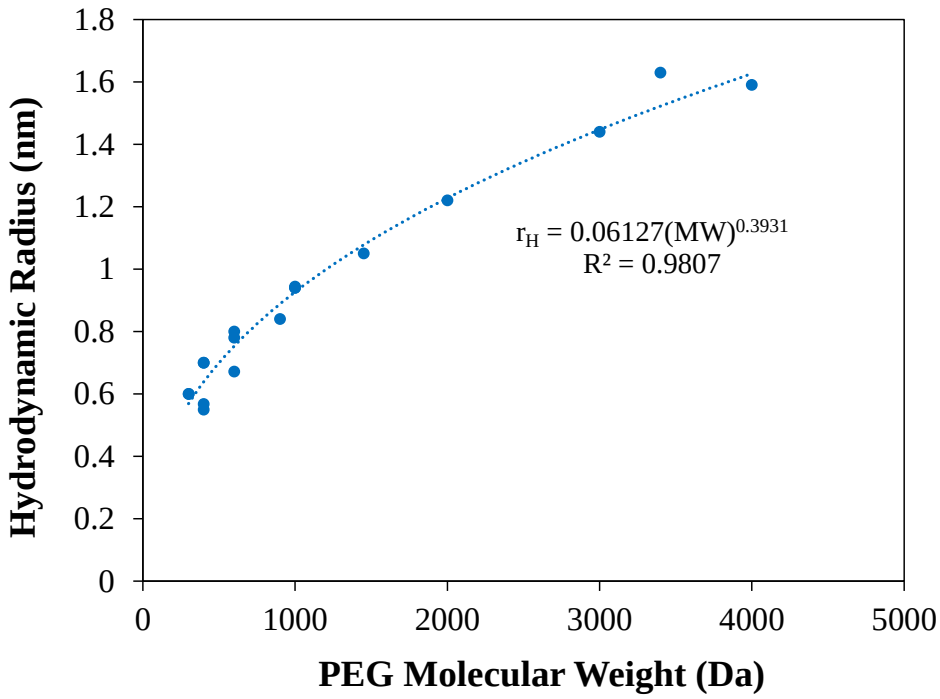

Figure A 3. Regression of molecular weights vs. hydrodynamic radius of PEG (Ghandehari et al., 1997; Kasianowicz et al., 2012; Ling et al., 2013; Thein, 2009).

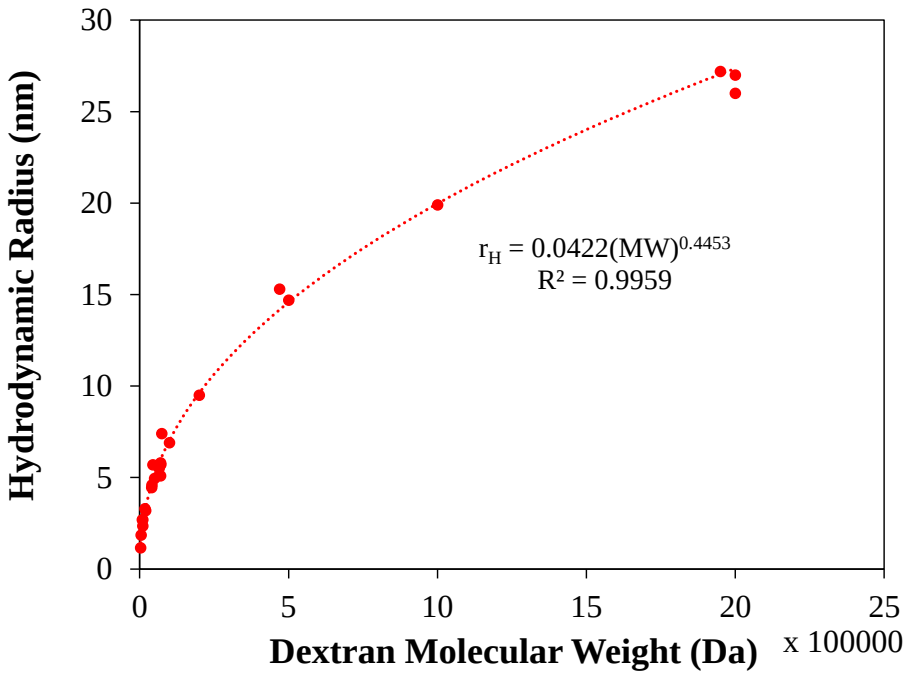

Figure A 4. Regression of molecular weights vs. hydrodynamic radius of Dextran (Baron-Epel et al., 1988; Choi et al., 2010; Lebrun & Junter, 1993; Pluen et al., 1999; Theodore, Robin, Gaudio, & Acevedo, 1975).

REFERENCES

Adrus, N., & Ulbricht, M. (2012). Novel hydrogel pore-filled composite membranes with tunable and temperature-responsive size-selectivity. *Journal of Materials Chemistry, 22*(7), 3088. doi:10.1039/c2jm15022k

Aguilella, V. M., Queralt-Martin, M., Aguilella-Arzo, M., & Alcaraz, A. (2011). Insights on the permeability of wide protein channels: measurement and interpretation of ion selectivity. *Integr Biol (Camb), 3*(3), 159-172. doi:10.1039/c0ib00048e

Akar, N., Asar, B., Dizge, N., & Koyuncu, I. (2013). Investigation of characterization and biofouling properties of PES membrane containing selenium and copper nanoparticles. *Journal of Membrane Science, 437*, 216-226. doi:10.1016/j.memsci.2013.02.012

Al-Hobaib, A., AL-Sheetan, K., Shaik, M., Al-Andis, N., & Al-Suhybani, M. (2015). Characterization and Evaluation of Reverse Osmosis Membranes Modified with Ag 2 O Nanoparticles to Improve Performance. *Nanoscale Research Letters, 10*(1), 379.

Alam, J., Dass, L. A., Ghasemi, M., & Alhoshan, M. (2013). Synthesis and optimization of PES-Fe3O4mixed matrix nanocomposite membrane: Application studies in water purification. *Polymer Composites, 34*(11), 1870-1877. doi:10.1002/pc.22593

Alhoshan, M., Alam, J., Dass, L. A., & Al-Homaidi, N. (2013). Fabrication of Polysulfone/ZnO Membrane: Influence of ZnO Nanoparticles on Membrane Characteristics. *Advances in Polymer Technology, 32*(4), n/a-n/a. doi:10.1002/adv.21369

Anderson, C. C., Rodriguez, F., & Thurston, D. A. (1979). Crosslinking aqueous poly(vinyl pyrrolidone) solutions by persulfate. *Journal of Applied Polymer Science, 23*(8), 2453-2462. doi:10.1002/app.1979.070230823

Arcidiacono, S., Butler, M. M., & Mello, C. M. (2002). A rapid selective extraction procedure for the outer membrane protein (OmpF) from Escherichia coli. *Protein Expr Purif, 25*(1), 134-137. doi:10.1006/prep.2002.1619

Arthanareeswaran, G., & Thanikaivelan, P. (2010). Fabrication of cellulose acetate–zirconia hybrid membranes for ultrafiltration applications: Performance, structure and fouling analysis. *Separation and Purification Technology, 74*(2), 230-235. doi:10.1016/j.seppur.2010.06.010

Azzaroni, O., Brown, A. A., & Huck, W. T. S. (2007). Tunable Wettability by Clicking Counterions Into Polyelectrolyte Brushes. *Advanced Materials, 19*(1), 151-154. doi:10.1002/adma.200601257

Baron-Epel, O., Gharyal, P. K., & Schindler, M. (1988). Pectins as mediators of wall porosity in soybean cells. *Planta, 175*(3), 389-395. doi:10.1007/BF00396345

Basha, M. A.-F. (2010). Magnetic and optical studies on polyvinylpyrrolidone thin films doped with rare earth metal salts. *Polymer Journal, 42*(9), 728-734. doi:10.1038/pj.2010.60

Basri, H., Ismail, A. F., & Aziz, M. (2011). Polyethersulfone (PES)–silver composite UF membrane: Effect of silver loading and PVP molecular weight on membrane morphology and antibacterial activity. *Desalination, 273*(1), 72-80. doi:10.1016/j.desal.2010.11.010

Basri, H., Ismail, A. F., Aziz, M., Nagai, K., Matsuura, T., Abdullah, M. S., & Ng, B. C. (2010). Silver-filled polyethersulfone membranes for antibacterial applications - Effect of PVP and TAP addition on silver dispersion. *Desalination, 261*(3), 264-271. doi:10.1016/j.desa1.2010.05.009

Bell, N. C., Minelli, C., Tompkins, J., Stevens, M. M., & Shard, A. G. (2012). Emerging techniques for submicrometer particle sizing applied to Stober silica. *Langmuir, 28*(29), 10860-10872. doi:10.1021/la301351k

Benz, R., Janko, K., & Lauger, P. (1979). Ionic selectivity of pores formed by the matrix protein (porin) of Escherichia coli. *Biochim Biophys Acta, 551*(2), 238-247. doi:http://dx.doi.org/10.1016/0005-2736(89)90002-3

Bhattacharyya, D., Schäfer, T., Wickramasinghe, S. R., & Daunert, S. (2013). *Responsive Membranes and Materials*: John Wiley & Sons.

Bi, Q., Li, Q., Tian, Y., Lin, Y., & Wang, X. (2013). Hydrophilic modification of poly(vinylidene fluoride) membrane with poly(vinyl pyrrolidone) via a cross-linking reaction. *Journal of Applied Polymer Science, 127*(1), 394-401. doi:10.1002/app.37629

Braun, D. (2005). *Polymer synthesis : theory and practice : fundamentals, methods, experiments*. Berlin; New York: Springer.

Buehler, L. K., & Rosenbusch, J. P. (1993). Single channel behavior of matrix porin of Escherichia coli. *Biochem Biophys Res Commun, 190*(2), 624-629. doi:10.1006/bbrc.1993.1094

Bueno, V. B., Catalani, L. H., Daghastanli, K. R. P., Cuccovia, I. M., & Chaimovich, H. (2010). Preparation of PVP hydrogel nanoparticles using lecithin vesicles. *Química Nova, 33*(10), 2083-2087. doi:10.1590/s0100-40422010001000015

Butterfield, D. A., Bhattacharyya, D., Daunert, S., & Bachas, L. (2001). Catalytic biofunctional membranes containing site-specifically immobilized enzyme arrays: a review. *Journal of Membrane Science, 181*(1), 29-37. doi:10.1016/s0376-7388(00)00342-2

Cao, X., Ma, J., Shi, X., & Ren, Z. (2006). Effect of TiO2 nanoparticle size on the performance of PVDF membrane. *Applied Surface Science, 253*(4), 2003-2010. doi:10.1016/j.apsusc.2006.03.090

Cavarretta, I., O'Sullivan, C., Coop, M. R., Nakagawa, M., & Luding, S. (2009). Applying 2D shape analysis techniques to granular materials with 3D particle geometries. *AIP Conference Proceedings, 1145*(1), 833-836. doi:10.1063/1.3180057

Chen, J., Hamon, M. A., Hu, H., Chen, Y., Rao, A. M., Eklund, P. C., & Haddon, R. C. (1998). Solution properties of single-walled carbon nanotubes. *Science, 282*(5386), 95-98.

Chen, W., Su, Y., Zhang, L., Shi, Q., Peng, J., & Jiang, Z. (2010). In situ generated silica nanoparticles as pore-forming agent for enhanced permeability of cellulose acetate membranes. *Journal of Membrane Science, 348*(1-2), 75-83. doi:10.1016/j.memsci.2009.10.042

Chibowski, E. (2003). Surface free energy of a solid from contact angle hysteresis. *Adv Colloid Interface Sci, 103*(2), 149-172. doi:10.1016/S0001-8686(02)00093-3

Choi, J. J., Wang, S., Tung, Y. S., Morrison, B., 3rd, & Konofagou, E. E. (2010). Molecules of various pharmacologically-relevant sizes can cross the ultrasound-induced blood-brain barrier opening in vivo. *Ultrasound Med Biol, 36*(1), 58-67. doi:10.1016/j.ultrasmedbio.2009.08.006

Chou, W.-L., Yu, D.-G., & Yang, M.-C. (2005). The preparation and characterization of silver-loading cellulose acetate hollow fiber membrane for water treatment. *Polymers for Advanced Technologies, 16*(8), 600-607. doi:10.1002/pat.630

Chun, C. L., Baer, D. R., Matson, D. W., Amonette, J. E., & Penn, R. L. (2010). Characterization and reactivity of iron nanoparticles prepared with added Cu, Pd, and Ni. *Environmental Science & Technology, 44*(13), 5079-5085. doi:10.1021/es903278e

Cohen-Ofri, I., Weiner, L., Boaretto, E., Mintz, G., & Weiner, S. (2006). Modern and fossil charcoal: aspects of structure and diagenesis. *Journal of Archaeological Science, 33*(3), 428-439. doi:10.1016/j.jas.2005.08.008

Cowan, S. W., Garavito, R. M., Jansonius, J. N., Jenkins, J. A., Karlsson, R., Konig, N., . . . et al. (1995). The structure of OmpF porin in a tetragonal crystal form. *Structure, 3*(10), 1041-1050.

Cowan, S. W., Schirmer, T., Rummel, G., Steiert, M., Ghosh, R., Pauptit, R. A., . . . Rosenbusch, J. P. (1992). Crystal structures explain functional properties of two E. coli porins. *Nature, 358*(6389), 727-733. doi:10.1038/358727a0

Crane, R. A., & Scott, T. B. (2012). Nanoscale zero-valent iron: future prospects for an emerging water treatment technology. *Journal of Hazardous Materials, 211-212*(0), 112-125. doi:10.1016/j.jhazmat.2011.11.073

Csetneki, I., Filipcsei, G., & Zrínyi, M. (2006). Smart Nanocomposite Polymer Membranes with On/Off Switching Control. *Macromolecules, 39*(5), 1939-1942. doi:10.1021/ma052189a

Cutie, S. S., Smith, P. B., Henton, D. E., Staples, T. L., & Powell, C. (1997). Acrylic acid polymerization kinetics. *Journal of Polymer Science Part B-Polymer Physics, 35*(13), 2029-2047. doi:Doi 10.1002/(Sici)1099-0488(19970930)35:13<2029::Aid-Polb4>3.0.Co;2-R

Daraei, P., Madaeni, S. S., Ghaemi, N., Khadivi, M. A., Astinchap, B., & Moradian, R. (2013). Fouling resistant mixed matrix polyethersulfone membranes blended with magnetic nanoparticles: Study of magnetic field induced casting. *Separation and Purification Technology, 109*, 111-121. doi:10.1016/j.seppur.2013.02.035

Daraei, P., Madaeni, S. S., Ghaemi, N., Salehi, E., Khadivi, M. A., Moradian, R., & Astinchap, B. (2012). Novel polyethersulfone nanocomposite membrane prepared by PANI/Fe3O4 nanoparticles with enhanced performance for Cu(II) removal from water. *Journal of Membrane Science, 415-416*, 250-259. doi:10.1016/j.memsci.2012.05.007

Darvishmanesh, S., Qian, X., & Wickramasinghe, S. R. (2015). Responsive membranes for advanced separations. *Current Opinion in Chemical Engineering, 8*, 98-104. doi:10.1016/j.coche.2015.04.002

Das, R., Ali, M. E., Hamid, S. B. A., Ramakrishna, S., & Chowdhury, Z. Z. (2014). Carbon nanotube membranes for water purification: A bright future in water desalination. *Desalination, 336*, 97-109. doi:10.1016/j.desal.2013.12.026

Dasari, A., Quirós, J., Herrero, B., Boltes, K., García-Calvo, E., & Rosal, R. (2012). Antifouling membranes prepared by electrospinning polylactic acid containing biocidal nanoparticles. *Journal of Membrane Science, 405-406*, 134-140. doi:10.1016/j.memsci.2012.02.060

DeMejo, L. P., Rimai, D., & Sharpe, L. H. (1999). *Fundamentals of adhesion and interfaces*. Australia: Gordon and Breach Science Publishers.

Dong, H., & Lo, I. M. (2013). Influence of humic acid on the colloidal stability of surface-modified nano zero-valent iron. *Water Research, 47*(1), 419-427. doi:10.1016/j.watres.2012.10.013

Dove, P. M., & Nix, C. J. (1997). The influence of the alkaline earth cations, magnesium, calcium, and barium on the dissolution kinetics of quartz. *Geochimica et Cosmochimica Acta, 61*(16), 3329-3340. doi:10.1016/s0016-7037(97)00217-2

Duca, M. D., Plosceanu, C. L., & Pop, T. (1998). Surface modifications of polyvinylidene fluoride (PVDF) under rf Ar plasma. *Polymer Degradation and Stability, 61*(1), 65-72. doi:10.1016/s0141-3910(97)00130-4

Dussan Garzón, J., Vives-Florez, M. J., Sarria, V. M., Sánchez Medina, O. F., Delgado, L. F., González Barrios, A. F., & Hernández Sierra, S. (2010). *Aproximaciones Biológicas y Fisicoquímicas en el tratamiento de contaminantes: un resumen del aporte de la Universidad de los Andes*.

Ebert, M., Köber, R., Parbs, A., Plagentz, V., Schäfer, D., & Dahmke, A. (2006). Assessing Degradation Rates of Chlorinated Ethylenes in Column Experiments with Commercial Iron Materials Used in Permeable Reactive Barriers. *Environmental Science & Technology, 40*(6), 2004-2010. doi:10.1021/es051720e

Fátima Vaz, M., & Fortes, M. A. (1988). Grain size distribution: The lognormal and the gamma distribution functions. *Scripta Metallurgica, 22*(1), 35-40. doi:10.1016/s0036-9748(88)80302-8

Fechine, G. J. M., Barros, J. A. G., & Catalani, L. H. (2004). Poly(N-vinyl-2-pyrrolidone) hydrogel production by ultraviolet radiation: new methodologies to accelerate crosslinking. *Polymer, 45*(14), 4705-4709. doi:10.1016/j.polymer.2004.05.006

Fisker, R., Carstensen, J. M., Hansen, M. F., Bødker, F., & Mørup, S. (2000). Estimation of nanoparticle size distributions by image analysis. *Journal of Nanoparticle Research, 2*(3), 267-277. doi:10.1023/a:1010023316775

Flesch, C., Unterfinger, Y., Bourgeat-Lami, E., Duguet, E., Delaite, C., & Dumas, P. (2005). Poly(ethylene glycol) Surface Coated Magnetic Particles. *Macromolecular Rapid Communications, 26*(18), 1494-1498. doi:10.1002/marc.200500402

Fordham, J. W. L., & Williams, H. L. (1951). The Persulfate-Iron(II) Initiator System for Free Radical Polymerizations1. *Journal of the American Chemical Society, 73*(10), 4855-4859. doi:10.1021/ja01154a114

Fumio, U., Hiroshi, Y., Kumiko, N., Sachihiko, N., Kenji, S., & Yasunori, M. (1990). Swelling and mechanical properties of poly(vinyl alcohol) hydrogels. *International Journal of Pharmaceutics, 58*(2), 135-142. doi:10.1016/0378-5173(90)90251-x

Garavito, R. M., & Rosenbusch, J. P. (1986). [25] Isolation and crystallization of bacterial porin. *Methods in enzymology, 125*, 309-328.

Geise, G. M., Lee, H.-S., Miller, D. J., Freeman, B. D., McGrath, J. E., & Paul, D. R. (2010). Water purification by membranes: The role of polymer science. *Journal of Polymer Science Part B: Polymer Physics, 48*(15), 1685-1718. doi:10.1002/polb.22037

Ghandehari, H., Smith, P. L., Ellens, H., Yeh, P. Y., & Kopecek, J. (1997). Size-dependent permeability of hydrophilic probes across rabbit colonic epithelium. *Journal of Pharmacology and Experimental Therapeutics, 280*(2), 747-753.

Gholami, A., Moghadassi, A. R., Hosseini, S. M., Shabani, S., & Gholami, F. (2014). Preparation and characterization of polyvinyl chloride based nanocomposite nanofiltration-membrane modified by iron oxide nanoparticles for lead removal from water. *Journal of Industrial and Engineering Chemistry, 20*(4), 1517-1522. doi:10.1016/j.jiec.2013.07.041

Gibbs, M. (1979). A simple method for the rapid determination of iron in natural waters. *Water Research, 13*(3), 295-297. doi:10.1016/0043-1354(79)90209-4

Glavee, G. N., Klabunde, K. J., Sorensen, C. M., & Hadjipanayis, G. C. (1995). Chemistry of Borohydride Reduction of Iron(II) and Iron(III) Ions in Aqueous and Nonaqueous Media. Formation of Nanoscale Fe, FeB, and Fe2B Powders. *Inorganic Chemistry, 34*(1), 28-35. doi:10.1021/ic00105a009

Goh, P. S., Ng, B. C., Lau, W. J., & Ismail, A. F. (2014). Inorganic Nanomaterials in Polymeric Ultrafiltration Membranes for Water Treatment. *Separation & Purification Reviews, 44*(3), 216-249. doi:10.1080/15422119.2014.926274

Gotpagar, J., Grulke, E., Tsang, T., & Bhattacharyya, D. (1997). Reductive dehalogenation of trichloroethylene using zero-valent iron. *Environmental Progress, 16*(2), 137-143. doi:10.1002/ep.3300160221

Gui, M., Ormsbee, L. E., & Bhattacharyya, D. (2013). Reactive Functionalized Membranes for Polychlorinated Biphenyl Degradation. *Industrial & Engineering Chemistry Research, 52*(31), 10430-10440. doi:10.1021/ie400507c

Gui, M., Papp, J. K., Colburn, A. S., Meeks, N. D., Weaver, B., Wilf, I., & Bhattacharyya, D. (2015). Engineered Iron/Iron Oxide Functionalized Membranes for Selenium and Other Toxic Metal Removal from Power Plant Scrubber Water. *J Memb Sci, 488*, 79-91. doi:10.1016/j.memsci.2015.03.089

Gui, M., Smuleac, V., Ormsbee, L., Sedlak, D., & Bhattacharyya, D. (2012a). Iron oxide nanoparticle synthesis in aqueous and membrane systems for oxidative degradation of trichloroethylene from water. *Journal of Nanoparticle Research, 14*(5), 1-16. doi:10.1007/s11051-012-0861-1

Gui, M., Smuleac, V., Ormsbee, L. E., Sedlak, D. L., & Bhattacharyya, D. (2012b). Iron oxide nanoparticle synthesis in aqueous and membrane systems for oxidative degradation of trichloroethylene from water. *Journal of Nanoparticle Research, 14*(5), 1-16. doi:10.1007/s11051-012-0861-1

Han, X., Gai, L., Jiang, H., Zhao, L., Liu, H., & Zhang, W. (2013). Core–shell structured Fe3O4/PANI microspheres and their Cr(VI) ion removal properties. *Synthetic Metals, 171*, 1-6. doi:10.1016/j.synthmet.2013.02.025

Hanemann, T., & Szabó, D. V. (2010). Polymer-Nanoparticle Composites: From Synthesis to Modern Applications. *Materials, 3*(6), 3468-3517. doi:10.3390/ma3063468

Hayakawa, Y., & Oguchi, T. (2005). Evaluation of gravel sphericity and roundness based on surface-area measurement with a laser scanner. *Computers & Geosciences, 31*(6), 735-741. doi:10.1016/j.cageo.2005.01.004

Hayama, M., Yamamoto, K., Kohori, F., Uesaka, T., Ueno, Y., Sugaya, H., . . . Sakai, K. (2004). Nanoscopic behavior of polyvinylpyrrolidone particles on polysulfone/polyvinylpyrrolidone film. *Biomaterials, 25*(6), 1019-1028. doi:10.1016/S0142-9612(03)00629-X

He, F., & Zhao, D. (2008). Hydrodechlorination of trichloroethene using stabilized Fe-Pd nanoparticles: Reaction mechanism and effects of stabilizers, catalysts and reaction conditions. *Applied Catalysis B: Environmental, 84*(3-4), 533-540. doi:10.1016/j.apcatb.2008.05.008

He, F., Zhao, D., Liu, J., & Roberts, C. B. (2007). Stabilization of Fe−Pd Nanoparticles with Sodium Carboxymethyl Cellulose for Enhanced Transport and Dechlorination of Trichloroethylene in Soil and Groundwater. *Industrial & Engineering Chemistry Research, 46*(1), 29-34. doi:10.1021/ie0610896

He, F., Zhao, D., & Paul, C. (2010). Field assessment of carboxymethyl cellulose stabilized iron nanoparticles for in situ destruction of chlorinated solvents in source zones. *Water Research, 44*(7), 2360-2370. doi:10.1016/j.watres.2009.12.041

Hernández, S., Lei, S., Rong, W., Ormsbee, L., & Bhattacharyya, D. (2016). Functionalization of Flat Sheet and Hollow Fiber Microfiltration Membranes for Water Applications. *ACS Sustainable Chemistry & Engineering, 4*(3), 907-918. doi:10.1021/acssuschemeng.5b01005

Hernandez, S., Papp, J. K., & Bhattacharyya, D. (2014). Iron-Based Redox Polymerization of Acrylic Acid for Direct Synthesis of Hydrogel/Membranes, and Metal Nanoparticles for Water Treatment. *Industrial & Engineering Chemistry Research, 53*(3), 1130-1142. doi:10.1021/ie403353g

Hernández, S., Saad, A., Ormsbee, L., & Bhattacharyya, D. (2016). Chapter 16 - Nanocomposite and Responsive Membranes for Water Treatment A2 - Hankins, Nicholas P. In R. Singh (Ed.), *Emerging Membrane Technology for Sustainable Water Treatment* (pp. 389-431). Boston: Elsevier.

Himstedt, H. H., Yang, Q., Qian, X., Ranil Wickramasinghe, S., & Ulbricht, M. (2012). Toward remote-controlled valve functions via magnetically responsive capillary pore membranes. *Journal of Membrane Science, 423-424*, 257-266. doi:10.1016/j.memsci.2012.08.015

Hinds, B. (2012). Carbon Nanotube Membranes as an Idealized Platform for Protein Channel Mimetic Pumps *Responsive Membranes and Materials* (pp. 51-71): John Wiley & Sons, Ltd.

Hoek, E. M. V., Ghosh, A. K., Huang, X., Liong, M., & Zink, J. I. (2011). Physical–chemical properties, separation performance, and fouling resistance of mixed-matrix ultrafiltration membranes. *Desalination, 283*, 89-99. doi:10.1016/j.desal.2011.04.008

Holdich, R. G. (2002). *Fundamentals of particle technology*. Shepshed: Midland Information Technology and Pub.

Holzenburg, A., Engel, A., Kessler, R., Manz, H. J., Lustig, A., & Aebi, U. (1989). Rapid isolation of OmpF porin-LPS complexes suitable for structure-function studies. *Biochemistry, 28*(10), 4187-4193.

Hsieh, Y. H. P., & Hsieh, Y. P. (1997). Valence State of Iron in the Presence of Ascorbic Acid and Ethylenediaminetetraacetic Acid. *Journal of Agricultural and Food Chemistry, 45*(4), 1126-1129. doi:10.1021/jf960684n

Huang, C.-C., Lo, S.-L., & Lien, H.-L. (2012). Zero-valent copper nanoparticles for effective dechlorination of dichloromethane using sodium borohydride as a reductant. *Chemical Engineering Journal, 203*(0), 95-100. doi:10.1016/j.cej.2012.07.002

Huang, F. L., Wang, Q. Q., Wei, Q. F., Gao, W. D., Shou, H. Y., & Jiang, S. D. (2010). Dynamic wettability and contact angles of poly(vinylidene fluoride) nanofiber membranes grafted with acrylic acid. *Express Polymer Letters, 4*(9), 551-558. doi:10.3144/expresspolymlett.2010.69

Huang, X., Zhang, J., Wang, W., Liu, Y., Zhang, Z., Li, L., & Fan, W. (2015). Effects of PVDF/SiO2hybrid ultrafiltration membranes by sol–gel method for the concentration of fennel oil in herbal water extract. *RSC Adv., 5*(24), 18258-18266. doi:10.1039/c4ra15448g

Huang, Z.-Q., Chen, K., Li, S.-N., Yin, X.-T., Zhang, Z., & Xu, H.-T. (2008). Effect of ferrosoferric oxide content on the performances of polysulfone–ferrosoferric oxide ultrafiltration membranes. *Journal of Membrane Science, 315*(1-2), 164-171. doi:10.1016/j.memsci.2008.02.028

Husson, S. M. (2012). Synthesis Aspects in the Design of Responsive Membranes *Responsive Membranes and Materials* (pp. 73-96): John Wiley & Sons, Ltd.

Hwang, Y.-H., Kim, D.-G., & Shin, H.-S. (2011). Effects of synthesis conditions on the characteristics and reactivity of nano scale zero valent iron. *Applied Catalysis B: Environmental, 105*(1-2), 144-150. doi:10.1016/j.apcatb.2011.04.005

Jadav, G. L., & Singh, P. S. (2009). Synthesis of novel silica-polyamide nanocomposite membrane with enhanced properties. *Journal of Membrane Science, 328*(1-2), 257-267. doi:10.1016/j.memsci.2008.12.014

Jamshidi Gohari, R., Halakoo, E., Nazri, N. A. M., Lau, W. J., Matsuura, T., & Ismail, A. F. (2014). Improving performance and antifouling capability of PES UF membranes via blending with highly hydrophilic hydrous manganese dioxide nanoparticles. *Desalination, 335*(1), 87-95. doi:10.1016/j.desal.2013.12.011

Jamshidi Gohari, R., Lau, W. J., Matsuura, T., Halakoo, E., & Ismail, A. F. (2013). Adsorptive removal of Pb(II) from aqueous solution by novel PES/HMO ultrafiltration mixed matrix membrane. *Separation and Purification Technology, 120*, 59-68. doi:10.1016/j.seppur.2013.09.024

Jap, B. K., & Walian, P. J. (1996). Structure and functional mechanism of porins. *Physiol Rev, 76*(4), 1073-1088.

Jeong, H., Kim, H., & Hayes, K. (2007). Reductive dechlorination pathways of tetrachloroethylene and trichloroethylene and subsequent transformation of their dechlorination products by mackinawite (FeS) in the presence of metals. *Environmental Science & Technology, 41*(22), 7736-7743. doi:10.1021/es0708518

Jewrajka, S. K., & Haldar, S. (2011). Amphiphilic poly(acrylonitrile-co-acrylic acid)/silver nanocomposite additives for the preparation of antibiofouling membranes with improved properties. *Polymer Composites, 32*(11), 1851-1861. doi:10.1002/pc.21218

Jian, P., Yahui, H., Yang, W., & Linlin, L. (2006). Preparation of polysulfone–Fe3O4 composite ultrafiltration membrane and its behavior in magnetic field. *Journal of Membrane Science, 284*(1-2), 9-16. doi:10.1016/j.memsci.2006.07.052

Jiang, Y., Wang, W. N., Liu, D., Nie, Y., Li, W., Wu, J., . . . Fortner, J. D. (2015). Engineered crumpled graphene oxide nanocomposite membrane assemblies for advanced water treatment processes. *Environmental Science & Technology, 49*(11), 6846-6854. doi:10.1021/acs.est.5b00904

Johnson, T. L., Scherer, M. M., & Tratnyek, P. G. (1996). Kinetics of Halogenated Organic Compound Degradation by Iron Metal. *Environmental Science & Technology, 30*(8), 2634-2640. doi:10.1021/es9600901

José, R. Q., Nora, E. V., & Issa, K. (1999). Synthesis and Swelling Kinetics of Poly(Dimethylaminoethyl acrylate methyl chloride quaternary- co -itaconic acid) Hydrogels. *Langmuir, 15*. doi:10.1021/la980982

Jurak, M., & Chibowski, E. (2010). Surface free energy and topography of mixed lipid layers on mica. *Colloids Surf B Biointerfaces, 75*(1), 165-174. doi:10.1016/j.colsurfb.2009.08.034

Kabanov, V. A., Topchiev, D. A., Karaputadze, T. M., & Mkrtchian, L. A. (1975). Kinetics and mechanism of radical polymerization of weak unsaturated acids in aqueous solutions. *European Polymer Journal, 11*(2), 153-159. doi:10.1016/0014-3057(75)90140-8

Kadłubowski, S., Henke, A., Ulański, P., Rosiak, J. M., Bromberg, L., & Hatton, T. A. (2007). Hydrogels of polyvinylpyrrolidone (PVP) and poly(acrylic acid) (PAA) synthesized by photoinduced crosslinking of homopolymers. *Polymer, 48*(17), 4974-4981. doi:10.1016/j.polymer.2007.06.033

Kang, J. S., Kim, K. Y., & Lee, Y. M. (2003). Preparation of PVP immobilized microporous chlorinated polyvinyl chloride membranes on fabric and their hydraulic

permeation behavior. *Journal of Membrane Science, 214*(2), 311-321. doi:10.1016/s0376-7388(02)00597-5

Kasianowicz, J. J., Kellermayer, M., & Deamer, D. (2012). *Structure and Dynamics of Confined Polymers: Proceedings of the NATO Advanced Research Workshop on Biological, Biophysical & Theoretical Aspects of Polymer Structure and Transport Bikal, Hungary 20–25 June 1999*: Springer Netherlands.

Kastantin, M., & Tirrell, M. (2011). Helix formation in the polymer brush. *Macromolecules, 44*(12), 4977-4987. doi:10.1021/ma200782e

Katime, I., Velada, J. L., Novoa, R., Díaz de Apodaca, E., Puig, J., & Mendizabal, E. (1996). Swelling Kinetics of Poly(acrylamide)/Poly(mono-n-alkyl itaconates) Hydrogels. *Polymer International, 40*(4), 281-286. doi:10.1002/(sici)1097-0126(199608)40:4<281::aid-pi555>3.0.co;2-h

Keenan, C. R., & Sedlak, D. L. (2008). Factors affecting the yield of oxidants from the reaction of nanoparticulate zero-valent iron and oxygen. *Environmental Science & Technology, 42*(4), 1262-1267. doi:10.1021/es7025664

Khan, M. M. T., & Martell, A. E. (1967). Metal ion and metal chelate catalyzed oxidation of ascorbic acid by molecular oxygen. I. Cupric and ferric ion catalyzed oxidation. *Journal of the American Chemical Society, 89*(16), 4176-4185. doi:10.1021/ja00992a036

Kim, E.-J., Murugesan, K., Kim, J.-H., Tratnyek, P. G., & Chang, Y.-S. (2013). Remediation of Trichloroethylene by FeS-Coated Iron Nanoparticles in Simulated and Real Groundwater: Effects of Water Chemistry. *Industrial & Engineering Chemistry Research, 52*(27), 9343-9350. doi:10.1021/ie400165a

Kim, E.-S., & Deng, B. (2011). Fabrication of polyamide thin-film nano-composite (PA-TFN) membrane with hydrophilized ordered mesoporous carbon (H-OMC) for water purifications. *Journal of Membrane Science, 375*(1-2), 46-54. doi:10.1016/j.memsci.2011.01.041

Kim, E.-S., Hwang, G., Gamal El-Din, M., & Liu, Y. (2012). Development of nanosilver and multi-walled carbon nanotubes thin-film nanocomposite membrane for enhanced water treatment. *Journal of Membrane Science, 394-395*, 37-48. doi:10.1016/j.memsci.2011.11.041

Kim, J. H., Tratnyek, P. G., & Chang, Y. S. (2008). Rapid dechlorination of polychlorinated dibenzo-p-dioxins by bimetallic and nanosized zerovalent iron. *Environmental Science & Technology, 42*(11), 4106-4112. doi:10.1021/es702560k

Klara, S. S., Saboe, P. O., Sines, I. T., Babaei, M., Chiu, P. L., DeZorzi, R., . . . Mauter, M. S. (2016). Magnetically Directed Two-Dimensional Crystallization of OmpF Membrane Proteins in Block Copolymers. *Journal of the American Chemical Society, 138*(1), 28-31. doi:10.1021/jacs.5b03320

Kojima, S., & Nikaido, H. (2013). Permeation rates of penicillins indicate that Escherichia coli porins function principally as nonspecific channels. *Proc Natl Acad Sci U S A, 110*(28), E2629-2634. doi:10.1073/pnas.1310333110

Kricheldorf, H. R. (2004). *Handbook of polymer synthesis*. New York: Marcel Dekker.

Kumar, M., Grzelakowski, M., Zilles, J., Clark, M., & Meier, W. (2007). Highly permeable polymeric membranes based on the incorporation of the functional water channel protein Aquaporin Z. *Proc Natl Acad Sci U S A, 104*(52), 20719-20724. doi:10.1073/pnas.0708762104

Kuo, C.-Y., Lin, H.-N., Tsai, H.-A., Wang, D.-M., & Lai, J.-Y. (2008). Fabrication of a high hydrophobic PVDF membrane via nonsolvent induced phase separation. *Desalination, 233*(1-3), 40-47. doi:10.1016/j.desal.2007.09.025

Kurth, C. J., Burk, R. L., & Green, J. (2013). Improving Seawater Desalination with Nanocomposite Membranes. *IDA Journal of Desalination and Water Reuse, 2*(3), 26-31. doi:10.1179/ida.2010.2.3.26

Kwak, S. Y., Kim, S. H., & Kim, S. S. (2001). Hybrid organic/inorganic reverse osmosis (RO) membrane for bactericidal anti-fouling. 1. Preparation and characterization of TiO2 nanoparticle self-assembled aromatic polyamide thin-film-composite (TFC) membrane. *Environmental Science & Technology, 35*(11), 2388-2394. doi:10.1021/es0017099

Ladhe, A. R., Frailie, P., Hua, D., Darsillo, M., & Bhattacharyya, D. (2009). Thiol Functionalized Silica-Mixed Matrix Membranes for Silver Capture from Aqueous Solutions: Experimental Results and Modeling. *J Memb Sci, 326*(2), 460-471. doi:10.1016/j.memsci.2008.10.025

Lai, C. Y., Groth, A., Gray, S., & Duke, M. (2014). Nanocomposites for Improved Physical Durability of Porous PVDF Membranes. *Membranes (Basel), 4*(1), 55-78. doi:10.3390/membranes4010055

Le Roux, J. P. (2004). A Hydrodynamic Classification of Grain Shapes. *Journal of Sedimentary Research, 74*(1), 135-143. doi:10.1306/060603740135

Lebrun, L., & Junter, G. A. (1993). Diffusion of sucrose and dextran through agar gel membranes. *Enzyme and Microbial Technology, 15*(12), 1057-1062. doi:10.1016/0141-0229(93)90054-6

Lee, J. Y., Tang, C. Y., & Huo, F. (2014). Fabrication of porous matrix membrane (PMM) using metal-organic framework as green template for water treatment. *Sci Rep, 4*, 3740. doi:10.1038/srep03740

Lee, S. Y., Kim, H. J., Patel, R., Im, S. J., Kim, J. H., & Min, B. R. (2007). Silver nanoparticles immobilized on thin film composite polyamide membrane: characterization, nanofiltration, antifouling properties. *Polymers for Advanced Technologies, 18*(7), 562-568. doi:10.1002/pat.918

Leng, Y., Sato, K., Li, J.-G., Ishigaki, T., Iijima, M., Kamiya, H., & Yoshida, T. (2009). Iron nanoparticles dispersible in both ethanol and water for direct silica coating. *Powder Technology, 196*(1), 80-84. doi:10.1016/j.powtec.2009.07.012

Lewis, S. R., Smuleac, V., Xiao, L., & Bhattacharyya, D. (2012). Tunable Separations, Reactions, and Nanoparticle Synthesis in Functionalized Membranes *Responsive Membranes and Materials* (pp. 97-142): John Wiley & Sons, Ltd.

Li, J.-H., Shao, X.-S., Zhou, Q., Li, M.-Z., & Zhang, Q.-Q. (2013). The double effects of silver nanoparticles on the PVDF membrane: Surface hydrophilicity and antifouling performance. *Applied Surface Science, 265*, 663-670. doi:10.1016/j.apsusc.2012.11.072

Li, J. J., Zhou, Y. N., & Luo, Z. H. (2015). Smart Fiber Membrane for pH-Induced Oil/Water Separation. *ACS Appl Mater Interfaces, 7*(35), 19643-19650. doi:10.1021/acsami.5b04146

Li, W., Zhao, H., Teasdale, P. R., John, R., & Zhang, S. (2002). Synthesis and characterisation of a polyacrylamide–polyacrylic acid copolymer hydrogel for environmental analysis of Cu and Cd. *Reactive and Functional Polymers, 52*(1), 31-41. doi:10.1016/s1381-5148(02)00055-x

Li, X., Sotto, A., Li, J., & Van der Bruggen, B. (2017). Progress and perspectives for synthesis of sustainable antifouling composite membranes containing in situ generated nanoparticles. *Journal of Membrane Science, 524*, 502-528. doi:10.1016/j.memsci.2016.11.040

Li, X. Q., & Zhang, W. X. (2006). Iron nanoparticles: the core-shell structure and unique properties for Ni(II) sequestration. *Langmuir, 22*(10), 4638-4642. doi:10.1021/la060057k

Li, Y., Su, Y., Zhao, X., Zhang, R., Zhao, J., Fan, X., & Jiang, Z. (2014). Surface fluorination of polyamide nanofiltration membrane for enhanced antifouling property. *Journal of Membrane Science, 455*, 15-23. doi:10.1016/j.memsci.2013.12.060

Liang, C., Bruell, C. J., Marley, M. C., & Sperry, K. L. (2004). Persulfate oxidation for in situ remediation of TCE. II. Activated by chelated ferrous ion. *Chemosphere, 55*(9), 1225-1233. doi:10.1016/j.chemosphere.2004.01.030

Liang, S., Xiao, K., Mo, Y., & Huang, X. (2012). A novel ZnO nanoparticle blended polyvinylidene fluoride membrane for anti-irreversible fouling. *Journal of Membrane Science, 394-395*, 184-192. doi:10.1016/j.memsci.2011.12.040

Liao, C., Yu, P., Zhao, J., Wang, L., & Luo, Y. (2011). Preparation and characterization of NaY/PVDF hybrid ultrafiltration membranes containing silver ions as antibacterial materials. *Desalination, 272*(1-3), 59-65. doi:10.1016/j.desal.2010.12.048

Lien, H.-L., & Zhang, W.-X. (2007). Nanoscale Pd/Fe bimetallic particles: Catalytic effects of palladium on hydrodechlorination. *Applied Catalysis B: Environmental, 77*(1-2), 110-116. doi:10.1016/j.apcatb.2007.07.014

Lin, K. S., Chang, N. B., & Chuang, T. D. (2008). Fine structure characterization of zero-valent iron nanoparticles for decontamination of nitrites and nitrates in wastewater and groundwater. *Sci Technol Adv Mater, 9*(2), 025015. doi:10.1088/1468-6996/9/2/025015

Ling, K., Jiang, H., & Zhang, Q. (2013). A colorimetric method for the molecular weight determination of polyethylene glycol using gold nanoparticles. *Nanoscale Research Letters, 8*(1), 538. doi:10.1186/1556-276X-8-538

Liu, F., & Urban, M. W. (2010). Recent advances and challenges in designing stimuli-responsive polymers. *Progress in Polymer Science, 35*(1-2), 3-23. doi:10.1016/j.progpolymsci.2009.10.002

Liu, H., Wang, Q., Wang, C., & Li, X.-z. (2013). Electron efficiency of zero-valent iron for groundwater remediation and wastewater treatment. *Chemical Engineering Journal, 215-216*(0), 90-95. doi:10.1016/j.cej.2012.11.010

Liu, J., He, F., Durham, E., Zhao, D., & Roberts, C. B. (2008). Polysugar-stabilized Pd nanoparticles exhibiting high catalytic activities for hydrodechlorination of environmentally deleterious trichloroethylene. *Langmuir, 24*(1), 328-336. doi:10.1021/la702731h

Liu, X., Qi, S., Li, Y., Yang, L., Cao, B., & Tang, C. Y. (2013). Synthesis and characterization of novel antibacterial silver nanocomposite nanofiltration and forward

osmosis membranes based on layer-by-layer assembly. *Water Research, 47*(9), 3081-3092. doi:10.1016/j.watres.2013.03.018

Liu, Y., & Lowry, G. V. (2006). Effect of particle age (Fe0 content) and solution pH on NZVI reactivity: H2 evolution and TCE dechlorination. *Environmental Science & Technology, 40*(19), 6085-6090. doi:Doi 10.1021/Es060685o

Liu, Y., Majetich, S., Tilton, R., Sholl, D., & Lowry, G. (2005). TCE dechlorination rates, pathways, and efficiency of nanoscale iron particles with different properties. *Environmental Science & Technology, 39*(5), 1338-1345. doi:10.1021/es049195r

Liu, Y., Majetich, S. A., Tilton, R. D., Sholl, D. S., & Lowry, G. V. (2005). TCE dechlorination rates, pathways, and efficiency of nanoscale iron particles with different properties. *Environmental Science & Technology, 39*(5), 1338-1345. doi:Doi 10.1021/Es049195r

Liu, Y., Rosenfield, E., Hu, M., & Mi, B. (2013). Direct observation of bacterial deposition on and detachment from nanocomposite membranes embedded with silver nanoparticles. *Water Research, 47*(9), 2949-2958. doi:10.1016/j.watres.2013.03.005

Liu, Z. S., & Rempel, G. L. (1997). Preparation of superabsorbent polymers by crosslinking acrylic acid and acrylamide copolymers. *Journal of Applied Polymer Science, 64*(7), 1345-1353. doi:10.1002/(sici)1097-4628(19970516)64:7<1345::aid-app14>3.0.co;2-w

Lopérgolo, L. C., Lugão, A. B., & Catalani, L. H. (2003). Direct UV photocrosslinking of poly(N-vinyl-2-pyrrolidone) (PVP) to produce hydrogels. *Polymer, 44*(20), 6217-6222. doi:10.1016/s0032-3861(03)00686-4

Low, Z. X., Liu, Q., Shamsaei, E., Zhang, X., & Wang, H. (2015). Preparation and characterization of thin-film composite membrane with nanowire-modified support for forward osmosis process. *Membranes (Basel), 5*(1), 136-149. doi:10.3390/membranes5010136

Lowry, G. V., & Reinhard, M. (1999). Hydrodehalogenation of 1- to 3-Carbon Halogenated Organic Compounds in Water Using a Palladium Catalyst and Hydrogen Gas. *Environmental Science & Technology, 33*(11), 1905-1910. doi:10.1021/es980963m

Lu, A. H., Salabas, E. L., & Schuth, F. (2007). Magnetic nanoparticles: synthesis, protection, functionalization, and application. *Angew Chem Int Ed Engl, 46*(8), 1222-1244. doi:10.1002/anie.200602866

Ma, N., Wei, J., Liao, R., & Tang, C. Y. (2012). Zeolite-polyamide thin film nanocomposite membranes: Towards enhanced performance for forward osmosis. *Journal of Membrane Science, 405-406*, 149-157. doi:10.1016/j.memsci.2012.03.002

Mahajan, R., Burns, R., Schaeffer, M., & Koros, W. J. (2002). Challenges in forming successful mixed matrix membranes with rigid polymeric materials. *Journal of Applied Polymer Science, 86*(4), 881-890. doi:10.1002/app.10998

Manickam, S. P., Venkatarao, K., & Subbaratnam, N. R. (1979). Peroxo salts as initiators of vinyl polymerization—2. Kinetics of polymerization of acrylic acid and sodium-acrylate by peroxodisulphate in aqueous solution—effect of pH and Ag+ catalysis. *European Polymer Journal, 15*(5), 483-487. doi:10.1016/0014-3057(79)90063-6

María Arsuaga, J., Sotto, A., del Rosario, G., Martínez, A., Molina, S., Teli, S. B., & de Abajo, J. (2013). Influence of the type, size, and distribution of metal oxide particles on the properties of nanocomposite ultrafiltration membranes. *Journal of Membrane Science, 428*, 131-141. doi:10.1016/j.memsci.2012.11.008

Masuelli, M. A. (2013). Dextrans in Aqueous Solution. Experimental Review on Intrinsic Viscosity Measurements and Temperature Effect. *Journal of Polymer and Biopolymer Physics Chemistry, 1*(1), 13-21.

Matheson, L. J., & Tratnyek, P. G. (1994). Reductive dehalogenation of chlorinated methanes by iron metal. *Environmental Science & Technology, 28*(12), 2045-2053. doi:10.1021/es00061a012

Maximous, N., Nakhla, G., Wan, W., & Wong, K. (2010). Effect of the metal oxide particle distributions on modified PES membranes characteristics and performance. *Journal of Membrane Science, 361*(1-2), 213-222. doi:10.1016/j.memsci.2010.05.051

Meeks, N. D., Davis, E., Jain, M., Skandan, G., & Bhattacharyya, D. (2013). Mercury removal by thiol-functionalized metal oxide-carbon black sorbent and mixed-matrix membranes. *Environmental Progress & Sustainable Energy, 32*(3), 705-714. doi:10.1002/ep.11690

Meeks, N. D., Smuleac, V., Stevens, C., & Bhattacharyya, D. (2012). Iron-Based Nanoparticles for Toxic Organic Degradation: Silica Platform and Green Synthesis. *Industrial & Engineering Chemistry Research, 51*(28), 9581-9590. doi:10.1021/ie301031u

Mehta, A., & Zydney, A. L. (2005). Permeability and selectivity analysis for ultrafiltration membranes. *Journal of Membrane Science, 249*(1-2), 245-249. doi:10.1016/j.memsci.2004.09.040

Mendes, P. M. (2008). Stimuli-responsive surfaces for bio-applications. *Chem Soc Rev, 37*(11), 2512-2529. doi:10.1039/b714635n

Merkel, T. C., Freeman, B. D., Spontak, R. J., He, Z., Pinnau, I., Meakin, P., & Hill, A. J. (2002). Ultrapermeable, reverse-selective nanocomposite membranes. *Science, 296*(5567), 519-522. doi:10.1126/science.1069580

Meyer, D. E., Hampson, S., Ormsbee, L., & Bhattacharyya, D. (2009). A Study of Groundwater Matrix Effects for the Destruction of Trichloroethylene Using Fe/Pd Nanoaggregates. *Environ Prog Sustain Energy, 28*(4), 507-518. doi:10.1002/ep.10334

Misra, G. S., & Bajpai, U. D. N. (1982). Redox polymerization. *Progress in Polymer Science, 8*(1-2), 61-131. doi:10.1016/0079-6700(82)90008-9

Mollahosseini, A., Rahimpour, A., Jahamshahi, M., Peyravi, M., & Khavarpour, M. (2012). The effect of silver nanoparticle size on performance and antibacteriality of polysulfone ultrafiltration membrane. *Desalination, 306*, 41-50. doi:10.1016/j.desal.2012.08.035

Nadagouda, M. N., Castle, A. B., Murdock, R. C., Hussain, S. M., & Varma, R. S. (2010). In vitro biocompatibility of nanoscale zerovalent iron particles (NZVI) synthesized using tea polyphenols. *Green Chemistry, 12*(1), 114-122. doi:10.1039/b921203p

Nadagouda, M. N., Hoag, G., Collins, J., & Varma, R. S. (2009). Green Synthesis of Au Nanostructures at Room Temperature Using Biodegradable Plant Surfactants. *Crystal Growth & Design, 9*(11), 4979-4983. doi:10.1021/cg9007685

Nadagouda, M. N., Polshettiwar, V., & Varma, R. S. (2009). Self-assembly of palladium nanoparticles: synthesis of nanobelts, nanoplates and nanotrees using vitamin B-1, and their application in carbon-carbon coupling reactions. *Journal of Materials Chemistry, 19*(14), 2026-2031. doi:10.1039/b817112b

Nagaraja, G. K., Demappa, T., & Mahadevaiah. (2011). Polymerization kinetics of acrylonitrile by oxidation: Reduction system using potassium persulfate/ascorbic acid in an aqueous medium. *Journal of Applied Polymer Science, 121*(3), 1299-1303. doi:10.1002/app.33365

Nagpal, V., Bokare, A. D., Chikate, R. C., Rode, C. V., & Paknikar, K. M. (2010). Reductive dechlorination of gamma-hexachlorocyclohexane using Fe-Pd bimetallic nanoparticles. *Journal of Hazardous Materials, 175*(1-3), 680-687. doi:10.1016/j.jhazmat.2009.10.063

Ngang, H. P., Ooi, B. S., Ahmad, A. L., & Lai, S. O. (2012). Preparation of PVDF–TiO2 mixed-matrix membrane and its evaluation on dye adsorption and UV-cleaning properties. *Chemical Engineering Journal, 197*, 359-367. doi:10.1016/j.cej.2012.05.050

Ni, B., & Wang, X. (2015). Face the Edges: Catalytic Active Sites of Nanomaterials. *Adv Sci (Weinh), 2*(7), 1500085. doi:10.1002/advs.201500085

Nightingale, E. R. (1959). Phenomenological Theory of Ion Solvation. Effective Radii of Hydrated Ions. *The Journal of Physical Chemistry, 63*(9), 1381-1387. doi:10.1021/j150579a011

Nigmatullin, R., Gao, F., & Konovalova, V. (2008). Polymer-layered silicate nanocomposites in the design of antimicrobial materials. *Journal of Materials Science, 43*(17), 5728-5733. doi:10.1007/s10853-008-2879-4

Nikaido, H. (1981). Effect on solute size on diffusion rates through the transmembrane pores of the outer membrane of Escherichia coli. *The Journal of General Physiology, 77*(2), 121-135. doi:10.1085/jgp.77.2.121

Nikaido, H. (2003). Molecular basis of bacterial outer membrane permeability revisited. *Microbiol Mol Biol Rev, 67*(4), 593-656.

Nikaido, H., & Rosenberg, E. Y. (1983). Porin channels in Escherichia coli: studies with liposomes reconstituted from purified proteins. *Journal of Bacteriology, 153*(1), 241-252.

Nikaido, H., Rosenberg, E. Y., & Foulds, J. (1983). Porin channels in Escherichia coli: studies with beta-lactams in intact cells. *Journal of Bacteriology, 153*(1), 232-240.

Nikaido, H., & Vaara, M. (1985). Molecular basis of bacterial outer membrane permeability. *Microbiol Rev, 49*(1), 1-32.

Noubactep, C. (2009). On the operating mode of bimetallic systems for environmental remediation. *Journal of Hazardous Materials, 164*(1), 394-395. doi:10.1016/j.jhazmat.2008.08.004

Nurmi, J. T., Tratnyek, P. G., Sarathy, V., Baer, D. R., Amonette, J. E., Pecher, K., . . . Driessen, M. D. (2005). Characterization and properties of metallic iron nanoparticles: spectroscopy, electrochemistry, and kinetics. *Environmental Science & Technology, 39*(5), 1221-1230. doi:10.1021/es049190u

Nutt, M. O., Hughes, J. B., & Michael, S. W. (2005). Designing Pd-on-Au bimetallic nanoparticle catalysts for trichloroethene hydrodechlorination. *Environmental Science & Technology, 39*(5), 1346-1353. doi:10.1021/es048560b

O'neill, L., O'hare, L. A., & Goodwin, A. J. (2006). Method for coating a substrate using plasma: Google Patents.

O'Carroll, D., Sleep, B., Krol, M., Boparai, H., & Kocur, C. (2013). Nanoscale zero valent iron and bimetallic particles for contaminated site remediation. *Advances in Water Resources, 51*(0), 104-122. doi:10.1016/j.advwatres.2012.02.005

Odian, G. (2004). *Principles of polymerization*. New York; Chichester: Wiley.

Odziemkowski, M. S., Gui, L., & Gillham, R. W. (2000). Reduction ofN-Nitrosodimethylamine with Granular Iron and Nickel-Enhanced Iron. 2. Mechanistic Studies. *Environmental Science & Technology, 34*(16), 3495-3500. doi:10.1021/es9909780

Oh, S. J., Kim, N., & Lee, Y. T. (2009). Preparation and characterization of PVDF/TiO2 organic–inorganic composite membranes for fouling resistance improvement. *Journal of Membrane Science, 345*(1-2), 13-20. doi:10.1016/j.memsci.2009.08.003

Olson, E. (2011). Particle Shape Factors and Their Use in Image Analysis Part 1: Theory. *JOURNAL OF GXP COMPLIANCE, 15*(3), 85-96.

Pa Achia, S., & Florea, C. B. (2007). POLY (VINYL ALCOHOL) HYDROGELS INTERACTIONS WITH ELECTROLYTES IN AQUEOUS SOLUTION. *Revue Roumaine de Chimie, 52*(12), 1145-1149.

Pappenheimer, J. R. (1953). Passage of Molecules Through Capillary Walls. *Physiological Reviews, 33*(3), 387-423.

Parshetti, G. K., & Doong, R. A. (2009). Dechlorination of trichloroethylene by Ni/Fe nanoparticles immobilized in PEG/PVDF and PEG/nylon 66 membranes. *Water Research, 43*(12), 3086-3094. doi:10.1016/j.watres.2009.04.037

Paul, D. R., & Robeson, L. M. (2008). Polymer nanotechnology: Nanocomposites. *Polymer, 49*(15), 3187-3204. doi:10.1016/j.polymer.2008.04.017

Peak, C. W., Wilker, J. J., & Schmidt, G. (2013). A review on tough and sticky hydrogels. *Colloid and Polymer Science, 291*(9), 2031-2047. doi:10.1007/s00396-013-3021-y

Pendergast, M. M., & Hoek, E. M. V. (2011). A review of water treatment membrane nanotechnologies. *Energy & Environmental Science, 4*(6), 1946. doi:10.1039/c0ee00541j

Pendergast, M. T. M., Nygaard, J. M., Ghosh, A. K., & Hoek, E. M. V. (2010). Using nanocomposite materials technology to understand and control reverse osmosis membrane compaction. *Desalination, 261*(3), 255-263. doi:10.1016/j.desa1.2010.06.008

Peppas, N., & Wright, S. (1996). Solute Diffusion in Poly(vinyl alcohol)/Poly(acrylic acid) Interpenetrating Networks. *Macromolecules*. doi:10.1021/ma9613392

Peppas, N. A., & Wright, S. L. (1996). Solute Diffusion in Poly(vinyl alcohol)/Poly(acrylic acid) Interpenetrating Networks. *Macromolecules, 29*(27), 8798-8804. doi:10.1021/ma9613392

Petty, G. W., & Huang, W. (2011). The Modified Gamma Size Distribution Applied to Inhomogeneous and Nonspherical Particles: Key Relationships and Conversions. *Journal of the Atmospheric Sciences, 68*(7), 1460-1473. doi:10.1175/2011jas3645.1

Pluen, A., Netti, P. A., Jain, R. K., & Berk, D. A. (1999). Diffusion of macromolecules in agarose gels: comparison of linear and globular configurations. *Biophysical Journal, 77*(1), 542-552. doi:10.1016/S0006-3495(99)76911-0

Pogorzelski, S. J., Berezowski, Z., Rochowski, P., & Szurkowski, J. (2012). A novel methodology based on contact angle hysteresis approach for surface changes monitoring in model PMMA-Corega Tabs system. *Applied Surface Science, 258*(8), 3652-3658. doi:10.1016/j.apsusc.2011.11.132

Porter, C., Hernández, S., Zhang, X., Wei, Y., & Bhattacharyya, D. (2017). *Bioinspired membranes through incorporation of layer-by-layer and "porin" functionalization*.

Qin, Z., Ren, X., Shan, L., Guo, H., Geng, C., Zhang, G., . . . Liang, Y. (2016). Nacrelike-structured multilayered polyelectrolyte/calcium carbonate nanocomposite membrane via Ca-incorporated layer-by-layer-assembly and CO2-induced biomineralization. *Journal of Membrane Science, 498*, 180-191. doi:10.1016/j.memsci.2015.09.016

Rackaitis, M., Strawhecker, K., & Manias, E. (2002). Water-soluble polymers with tunable temperature sensitivity: Solution behavior. *Journal of Polymer Science Part B: Polymer Physics, 40*(19), 2339-2342. doi:10.1002/polb.10284

Rahimpour, A., Madaeni, S. S., Taheri, A. H., & Mansourpanah, Y. (2008). Coupling TiO2 nanoparticles with UV irradiation for modification of polyethersulfone ultrafiltration membranes. *Journal of Membrane Science, 313*(1-2), 158-169. doi:10.1016/j.memsei.2007.12.075

Ramm, L. E., Whitlow, M. B., & Mayer, M. M. (1982). Transmembrane channel formation by complement: functional analysis of the number of C5b6, C7, C8, and C9 molecules required for a single channel. *Proc Natl Acad Sci U S A, 79*(15), 4751-4755.

Ramos, M. A. V., Yan, W., Li, X.-q., Koel, B. E., & Zhang, W.-x. (2009). Simultaneous Oxidation and Reduction of Arsenic by Zero-Valent Iron Nanoparticles: Understanding the Significance of the Core−Shell Structure. *The Journal of Physical Chemistry C, 113*(33), 14591-14594. doi:10.1021/jp9051837

Ribeiro, A. C. F., Ortona, O., Simões, S. M. N., Santos, C. I. A. V., Prazeres, P. M. R. A., Valente, A. J. M., . . . Burrows, H. D. (2006). Binary Mutual Diffusion Coefficients of Aqueous Solutions of Sucrose, Lactose, Glucose, and Fructose in the Temperature Range from (298.15 to 328.15) K. *Journal of Chemical & Engineering Data, 51*(5), 1836-1840. doi:10.1021/je0602061

Ritchie, S. M. C., & Bhattacharyya, D. (2001). Polymeric ligand-based functionalized materials and membranes for ion exchange. *Ion Exch. Solvent Extr., 14*, 81-118.

Roberts, A. L., Totten, L. A., Arnold, W. A., Burris, D. R., & Campbell, T. J. (1996). Reductive Elimination of Chlorinated Ethylenes by Zero-Valent Metals. *Environmental Science & Technology, 30*(8), 2654-2659. doi:10.1021/es9509644

Rodriguez, J. M., Edeskär, T., & Knutsson, S. (2013). Particle shape quantities and measurement Techniques–A review. *Electronic Journal of Geotechnical Engineering, 18*, 169-198.

Rosenbusch, J., & Müller, R. (1977). Solubilization of a major bacterial envelope protein. *Solubilization of Lipoprotein Complexes. H. Peeters and JP MaSSUC, editors. European Press. Ghent, Belgium*, 59-68.

Roy, D., Cambre, J. N., & Sumerlin, B. S. (2010). Future perspectives and recent advances in stimuli-responsive materials. *Progress in Polymer Science, 35*(1-2), 278-301. doi:10.1016/j.progpolymsci.2009.10.008

Rudick, J. G., & Percec, V. (2007). Helical chirality in dendronized polyarylacetylenes. *New Journal of Chemistry, 31*(7), 1083. doi:10.1039/b616449h

Sabek, O. M., Ferrati, S., Fraga, D. W., Sih, J., Zabre, E. V., Fine, D. H., . . . Grattoni, A. (2013). Characterization of a nanogland for the autotransplantation of human pancreatic islets. *Lab on a Chip, 13*(18), 3675-3688. doi:10.1039/c3lc50601k

Sagle, A. C., Van Wagner, E. M., Ju, H., McCloskey, B. D., Freeman, B. D., & Sharma, M. M. (2009). PEG-coated reverse osmosis membranes: Desalination properties and

fouling resistance. *Journal of Membrane Science, 340*(1-2), 92-108. doi:10.1016/j.memsci.2009.05.013

Sahiner, N., Butun, S., Ozay, O., & Dibek, B. (2012). Utilization of smart hydrogel-metal composites as catalysis media. *J Colloid Interface Sci, 373*(1), 122-128. doi:10.1016/j.jcis.2011.08.080

Saint, N., Lou, K. L., Widmer, C., Luckey, M., Schirmer, T., & Rosenbusch, J. P. (1996). Structural and functional characterization of OmpF porin mutants selected for larger pore size. II. Functional characterization. *Journal of Biological Chemistry, 271*(34), 20676-20680. doi:10.1074/jbc.271.34.20676

Sarac, A. S. (1999). Redox polymerization. *Progress in Polymer Science, 24*(8), 1149-1204. doi:10.1016/s0079-6700(99)00026-x

Sarkar, S., Guibal, E., Quignard, F., & SenGupta, A. K. (2012). Polymer-supported metals and metal oxide nanoparticles: synthesis, characterization, and applications. *Journal of Nanoparticle Research, 14*(2), 1-24. doi:10.1007/s11051-011-0715-2

Savage, N., & Diallo, M. S. (2005). Nanomaterials and Water Purification: Opportunities and Challenges. *Journal of Nanoparticle Research, 7*(4-5), 331-342. doi:10.1007/s11051-005-7523-5

Sawada, I., Fachrul, R., Ito, T., Ohmukai, Y., Maruyama, T., & Matsuyama, H. (2012). Development of a hydrophilic polymer membrane containing silver nanoparticles with both organic antifouling and antibacterial properties. *Journal of Membrane Science, 387-388*, 1-6. doi:10.1016/j.memsci.2011.06.020

Schacher, F., Rudolph, T., Wieberger, F., Ulbricht, M., & Muller, A. H. (2009). Double stimuli-responsive ultrafiltration membranes from polystyrene-block-poly(N,N-dimethylaminoethyl methacrylate) diblock copolymers. *ACS Appl Mater Interfaces, 1*(7), 1492-1503. doi:10.1021/am900175u

Schindler, H., & Rosenbusch, J. P. (1978). Matrix protein from Escherichia coli outer membranes forms voltage-controlled channels in lipid bilayers. *Proc Natl Acad Sci U S A, 75*(8), 3751-3755.

Schirmer, T., & Phale, P. S. (1999). Brownian dynamics simulation of ion flow through porin channels. *Journal of Molecular Biology, 294*(5), 1159-1167. doi:10.1006/jmbi.1999.3326

Schlüter, A. D., & Rabe, J. P. (2000). Dendronized Polymers: Synthesis, Characterization, Assembly at Interfaces, and Manipulation. *Angewandte Chemie*

International Edition, 39(5), 864-883. doi:10.1002/(sici)1521-3773(20000303)39:5<864::aid-anie864>3.0.co;2-e

Schrick, B., Blough, J. L., Jones, A. D., & Mallouk, T. E. (2002). Hydrodechlorination of Trichloroethylene to Hydrocarbons Using Bimetallic Nickel−Iron Nanoparticles. *Chemistry of Materials, 14*(12), 5140-5147. doi:10.1021/cm020737i

Schultz, S. G., & Solomon, A. K. (1961). Determination of the effective hydrodynamic radii of small molecules by viscometry. *J Gen Physiol, 44*(6), 1189-1199. doi:10.1085/jgp.44.6.1189

Sergiy, M. (2007). Smart Responsive Coatings from Mixed Polymer Brushes *Smart Coatings* (Vol. 957, pp. 79-93): American Chemical Society.

Seteni, B., Ngila, J. C., Sikhwivhilu, K., Moutloali, R. M., & Mamba, B. (2013). Dechlorination of 3,3′,4,4′-tetrachlorobiphenyl (PCB77) in water, by nickel/iron nanoparticles immobilized on L-lysine/PAA/PVDF membrane. *Physics and Chemistry of the Earth, Parts A/B/C, 66*, 60-67. doi:10.1016/j.pce.2013.08.010

Shen, Y.-x., Saboe, P. O., Sines, I. T., Erbakan, M., & Kumar, M. (2014). Biomimetic membranes: A review. *Journal of Membrane Science, 454*, 359-381. doi:10.1016/j.memsci.2013.12.019

Shen, Y. X., Si, W., Erbakan, M., Decker, K., De Zorzi, R., Saboe, P. O., . . . Kumar, M. (2015). Highly permeable artificial water channels that can self-assemble into two-dimensional arrays. *Proc Natl Acad Sci U S A, 112*(32), 9810-9815. doi:10.1073/pnas.1508575112

Siantar, D. P., Schreier, C. G., Chou, C.-S., & Reinhard, M. (1996). Treatment of 1,2-dibromo-3-chloropropane and nitrate-contaminated water with zero-valent iron or hydrogen/palladium catalysts. *Water Research, 30*(10), 2315-2322. doi:10.1016/0043-1354(96)00120-0

Sinha Ray, S., & Okamoto, M. (2003). Polymer/layered silicate nanocomposites: a review from preparation to processing. *Progress in Polymer Science, 28*(11), 1539-1641. doi:10.1016/j.progpolymsci.2003.08.002

Smuleac, V., Bachas, L., & Bhattacharyya, D. (2010a). Aqueous-phase synthesis of PAA in PVDF membrane pores for nanoparticle synthesis and dichlorobiphenyl degradation. *Journal of Membrane Science, 346*(2), 310-317. doi:DOI 10.1016/j.memsci.2009.09.052

Smuleac, V., Bachas, L., & Bhattacharyya, D. (2010b). Aqueous - Phase Synthesis of PAA in PVDF Membrane Pores for Nanoparticle Synthesis and Dichlorobiphenyl Degradation. *J Memb Sci, 346*(2), 310-317. doi:10.1016/j.memsci.2009.09.052

Smuleac, V., Butterfield, D. A., & Bhattacharyya, D. (2006). Layer-by-layer-assembled microfiltration membranes for biomolecule immobilization and enzymatic catalysis. *Langmuir, 22*(24), 10118-10124. doi:10.1021/la061124d

Smuleac, V., Varma, R., Sikdar, S., & Bhattacharyya, D. (2011). Green Synthesis of Fe and Fe/Pd Bimetallic Nanoparticles in Membranes for Reductive Degradation of Chlorinated Organics. *J Memb Sci, 379*(1-2), 131-137. doi:10.1016/j.memsci.2011.05.054

Smuleac, V., Xiao, L., & Bhattacharyya, D. (2013). Greener and Other Approaches To Synthesize Fe and Pd Nanoparticles in Functionalized Membranes and Hydrogel *Sustainable Nanotechnology and the Environment: Advances and Achievements* (Vol. 1124, pp. 41-58): American Chemical Society.

Sorribas, S., Gorgojo, P., Tellez, C., Coronas, J., & Livingston, A. G. (2013). High flux thin film nanocomposite membranes based on metal-organic frameworks for organic solvent nanofiltration. *Journal of the American Chemical Society, 135*(40), 15201-15208. doi:10.1021/ja407665w

Stoimenov, P. K., Klinger, R. L., Marchin, G. L., & Klabunde, K. J. (2002). Metal Oxide Nanoparticles as Bactericidal Agents. *Langmuir, 18*(17), 6679-6686. doi:10.1021/la0202374

Stookey, L. L. (1970). Ferrozine - a New Spectrophotometric Reagent for Iron. *Analytical Chemistry, 42*(7), 779-&.

Stuart, M. A., Huck, W. T., Genzer, J., Muller, M., Ober, C., Stamm, M., . . . Minko, S. (2010). Emerging applications of stimuli-responsive polymer materials. *Nat Mater, 9*(2), 101-113. doi:10.1038/nmat2614

Sun, M., He, Y., Ye, Y., Yang, W., & Yin, M. (2014). Nucleophilic Substitution of Tetrachloroperylene Diimide in Fluorescent Polyvinylpyrrolidone Film. *Macromolecular Chemistry and Physics, 215*(6), 493-498. doi:10.1002/macp.201300688

Sun, X. L., Sun, H. H., & Wang, Y. A. (1998). Polyacrylamide Gel Polymerization: Ascorbic Acid-ferrous Sulfate-ammonium Persulfate Initiator for Acid System. *Sheng Wu Hua Xue Yu Sheng Wu Wu Li Xue Bao (Shanghai), 30*(4), 407-410.

Sun, Y. P., Li, X. Q., Cao, J., Zhang, W. X., & Wang, H. P. (2006). Characterization of zero-valent iron nanoparticles. *Adv Colloid Interface Sci, 120*(1-3), 47-56. doi:10.1016/j.cis.2006.03.001

Tansel, B., Sager, J., Rector, T., Garland, J., Strayer, R. F., Levine, L., . . . Bauer, J. (2006). Significance of hydrated radius and hydration shells on ionic permeability during nanofiltration in dead end and cross flow modes. *Separation and Purification Technology, 51*(1), 40-47. doi:10.1016/j.seppur.2005.12.020

Tauer, K., Gau, D., Schulze, S., Völkel, A., & Dimova, R. (2009). Thermal property changes of poly(N-isopropylacrylamide) microgel particles and block copolymers. *Colloid and Polymer Science, 287*(3), 299-312. doi:10.1007/s00396-008-1984-x

Taurozzi, J. S., Arul, H., Bosak, V. Z., Burban, A. F., Voice, T. C., Bruening, M. L., & Tarabara, V. V. (2008). Effect of filler incorporation route on the properties of polysulfone–silver nanocomposite membranes of different porosities. *Journal of Membrane Science, 325*(1), 58-68. doi:10.1016/j.memsci.2008.07.010

Taylor, L. S., Langkilde, F. W., & Zografi, G. (2001). Fourier transform Raman spectroscopic study of the interaction of water vapor with amorphous polymers. *J Pharm Sci, 90*(7), 888-901. doi:10.1002/jps.1041

Taylor, R., Burgner, J. W., Clifton, J., & Cramer, W. A. (1998). Purification and characterization of monomeric Escherichia coli vitamin B12 receptor with high affinity for colicin E3. *Journal of Biological Chemistry, 273*(47), 31113-31118. doi:10.1074/jbc.273.47.31113

Tee, Y. H., Bachas, L., & Bhattacharyya, D. (2009). Degradation of Trichloroethylene and Dichlorobiphenyls by Iron-Based Bimetallic Nanoparticles. *J Phys Chem C Nanomater Interfaces, 113*(22), 9454-9464. doi:10.1021/jp809098z

Thakur, A., Wanchoo, R., & Singh, P. (2011a). Structural parameters and swelling behavior of pH sensitive poly (acrylamide-co-acrylic acid) hydrogels. *Chemical and Biochemical Engineering Quarterly, 25*(2), 181-194.

Thakur, A., Wanchoo, R. K., & Singh, P. (2011b). Structural Parameters and Swelling Behavior of pH Sensitive Poly(acrylamide-co-acrylic acid) Hydrogels. *Chemical and Biochemical Engineering Quarterly, 25*(2), 181-194.

Thein, M. (2009). *Porins of Lyme Disease and Relapsing Fever Spirochetes.* (Copyright (C) 2016 American Chemical Society (ACS). All Rights Reserved.). Retrieved from http://www.meind.de/search.py?recid=391579

Theodore, J., Robin, E. D., Gaudio, R., & Acevedo, J. (1975). Transalveolar transport of large polar solutes (sucrose, inulin, and dextran). *American Journal of Physiology, 229*(4), 989-996.

Thomas, V., Namdeo, M., Murali Mohan, Y., Bajpai, S. K., & Bajpai, M. (2007). Review on Polymer, Hydrogel and Microgel Metal Nanocomposites: A Facile Nanotechnological Approach. *Journal of Macromolecular Science, Part A, 45*(1), 107-119. doi:10.1080/10601320701683470

Thompson, J. M., Chisholm, B. J., & Bezbaruah, A. N. (2010). Reductive Dechlorination of Chloroacetanilide Herbicide (Alachlor) Using Zero-Valent Iron Nanoparticles. *Environmental Engineering Science, 27*(3), 227-232. doi:10.1089/ees.2009.0147

Tjong, S. C. (2006). Structural and mechanical properties of polymer nanocomposites. *Materials Science and Engineering: R: Reports, 53*(3-4), 73-197. doi:10.1016/j.mser.2006.06.001

Todt, J. C., & McGroarty, E. J. (1992). Acid pH decreases OmpF and OmpC channel size in vivo. *Biochem Biophys Res Commun, 189*(3), 1498-1502. doi:http://dx.doi.org/10.1016/0006-291X(92)90244-F

Todt, J. C., Rocque, W. J., & McGroarty, E. J. (1992). Effects of pH on bacterial porin function. *Biochemistry, 31*(43), 10471-10478. doi:10.1021/bi00158a009

Ulbricht, M. (2006). Advanced functional polymer membranes. *Polymer, 47*(7), 2217-2262. doi:10.1016/j.polymer.2006.01.084

Umpuch, C., Galier, S., Kanchanatawee, S., & Balmann, H. R.-d. (2010). Nanofiltration as a purification step in production process of organic acids: Selectivity improvement by addition of an inorganic salt. *Process Biochemistry, 45*(11), 1763-1768. doi:10.1016/j.procbio.2010.01.015

Varanasi, P., Fullana, A., & Sidhu, S. (2007). Remediation of PCB contaminated soils using iron nano-particles. *Chemosphere, 66*(6), 1031-1038. doi:10.1016/j.chemosphere.2006.07.036

Vargaftik, N. B., Volkov, B. N., & Voljak, L. D. (1983). International Tables of the Surface Tension of Water. *Journal of Physical and Chemical Reference Data, 12*(3), 817-820. doi:10.1063/1.555688

Vatanpour, V., Madaeni, S. S., Moradian, R., Zinadini, S., & Astinchap, B. (2012). Novel antibifouling nanofiltration polyethersulfone membrane fabricated from embedding TiO2

coated multiwalled carbon nanotubes. *Separation and Purification Technology, 90*, 69-82. doi:10.1016/j.seppur.2012.02.014

Vijay, Y. K., Kulshrestha, V., Awasthi, K., Acharya, N. K., Jain, A., Singh, M., . . . Avasthi, D. K. (2006). Characterization of Nanocomposite Polymeric Membrane. *Journal of Polymer Research, 13*(5), 357-360. doi:10.1007/s10965-006-9051-0

Wandera, D., Himstedt, H. H., Marroquin, M., Wickramasinghe, S. R., & Husson, S. M. (2012). Modification of ultrafiltration membranes with block copolymer nanolayers for produced water treatment: The roles of polymer chain density and polymerization time on performance. *Journal of Membrane Science, 403-404*, 250-260. doi:10.1016/j.memsci.2012.02.061

Wang, C.-B., & Zhang, W.-x. (1997). Synthesizing Nanoscale Iron Particles for Rapid and Complete Dechlorination of TCE and PCBs. *Environmental Science & Technology, 31*(7), 2154-2156. doi:10.1021/es970039c

Wang, H., Chung, T. S., Tong, Y. W., Jeyaseelan, K., Armugam, A., Chen, Z., . . . Meier, W. (2012). Highly permeable and selective pore-spanning biomimetic membrane embedded with aquaporin Z. *Small, 8*(8), 1185-1190, 1125. doi:10.1002/smll.201102120

Wang, M., Wang, Z., Wang, X., Wang, S., Ding, W., & Gao, C. (2015). Layer-by-layer assembly of aquaporin Z-incorporated biomimetic membranes for water purification. *Environmental Science & Technology, 49*(6), 3761-3768. doi:10.1021/es5056337

Wang, Q., Jeong, S. W., & Choi, H. (2012). Removal of trichloroethylene DNAPL trapped in porous media using nanoscale zerovalent iron and bimetallic nanoparticles: direct observation and quantification. *Journal of Hazardous Materials, 213-214*, 299-310. doi:10.1016/j.jhazmat.2012.02.002

Wang, W., Zhou, M., Jin, Z., & Li, T. (2010). Reactivity characteristics of poly(methyl methacrylate) coated nanoscale iron particles for trichloroethylene remediation. *Journal of Hazardous Materials, 173*(1-3), 724-730. doi:10.1016/j.jhazmat.2009.08.145

Wang, X., Chen, C., Liu, H., & Ma, J. (2008). Preparation and characterization of PAA/PVDF membrane-immobilized Pd/Fe nanoparticles for dechlorination of trichloroacetic acid. *Water Research, 42*(18), 4656-4664. doi:10.1016/j.watres.2008.08.005

Wei, J., Qian, Y., Wang, L., Ge, Y., Su, L., Zhai, D., . . . Yu, J. (2016). Enhancement of Degradation and Dechlorination of Trichloroethylene via Supporting Palladium/Iron Bimetallic Nanoparticles onto Mesoporous Silica. *Catalysts, 6*(7), 105.

Wei, Y. T., Wu, S. C., Yang, S. W., Che, C. H., Lien, H. L., & Huang, D. H. (2012). Biodegradable surfactant stabilized nanoscale zero-valent iron for in situ treatment of vinyl chloride and 1,2-dichloroethane. *Journal of Hazardous Materials, 211-212*(0), 373-380. doi:10.1016/j.jhazmat.2011.11.018

Weibel, A., Bouchet, R., Boulc, F., & Knauth, P. (2005). The Big Problem of Small Particles: A Comparison of Methods for Determination of Particle Size in Nanocrystalline Anatase Powders. *Chemistry of Materials, 17*(9), 2378-2385. doi:10.1021/cm0403762

Werber, J. R., Osuji, C. O., & Elimelech, M. (2016). Materials for next-generation desalination and water purification membranes. *Nature Reviews Materials, 1*(5), 16018. doi:10.1038/natrevmats.2016.18

Wienk, I. M. (1993). *Ultrafiltration membranes from a polymer blend : hollow fiber preparation and characterization*. [S.l.]: [s.n.].

Wienk, I. M., Meuleman, E. E. B., Borneman, Z., van den Boomgaard, T., & Smolders, C. A. (1995). Chemical treatment of membranes of a polymer blend: Mechanism of the reaction of hypochlorite with poly(vinyl pyrrolidone). *Journal of Polymer Science Part A: Polymer Chemistry, 33*(1), 49-54. doi:10.1002/pola.1995.080330105

Wilke, C. R., & Chang, P. (1955). Correlation of diffusion coefficients in dilute solutions. *Aiche Journal, 1*(2), 264-270. doi:10.1002/aic.690010222

Wills, B. A., Napier-Munn, T., & Julius Kruttschnitt Mineral Research, C. (2006). Wills' mineral processing technology : an introduction to the practical aspects of ore treatment and mineral recovery. 73-75.

Woehrle, G. H., Hutchison, J. E., Ozkar, S., & Finke, R. G. (2006). Analysis of nanoparticle Transmission Electron Microscopy data using a public-domain image-processing program, Image. *Turkish Journal of Chemistry, 30*(1), 1-13.

Wu, H., Mansouri, J., & Chen, V. (2013). Silica nanoparticles as carriers of antifouling ligands for PVDF ultrafiltration membranes. *Journal of Membrane Science, 433*, 135-151. doi:10.1016/j.memsci.2013.01.029

Wu, H., Tang, B., & Wu, P. (2014). Development of novel SiO2–GO nanohybrid/polysulfone membrane with enhanced performance. *Journal of Membrane Science, 451*, 94-102. doi:10.1016/j.memsci.2013.09.018

Wu, S. (1971). Calculation of interfacial tension in polymer systems. *Journal of Polymer Science Part C: Polymer Symposia, 34*(1), 19-30. doi:10.1002/polc.5070340105

Wu, T., Zhou, B., Zhu, T., Shi, J., Xu, Z., Hu, C., & Wang, J. (2015). Facile and low-cost approach towards a PVDF ultrafiltration membrane with enhanced hydrophilicity and antifouling performance via graphene oxide/water-bath coagulation. *RSC Adv., 5*(11), 7880-7889. doi:10.1039/c4ra13476a

Xiao, L., Davenport, D. M., Ormsbee, L., & Bhattacharyya, D. (2015). Polymerization and Functionalization of Membrane Pores for Water Related Applications. *Industrial & Engineering Chemistry Research, 54*(16), 4174-4182. doi:10.1021/ie504149t

Xiao, L., Isner, A., Waldrop, K., Saad, A., Takigawa, D., & Bhattacharyya, D. (2014). Development of Bench and Full-Scale Temperature and pH Responsive Functionalized PVDF Membranes with Tunable Properties. *J Memb Sci, 457*, 39-49. doi:10.1016/j.memsci.2014.01.033

Xiao, L., Isner, A. B., Hilt, J. Z., & Bhattacharyya, D. (2012). Temperature responsive hydrogel with reactive nanoparticles. *Journal of Applied Polymer Science, 128*(3), n/a-n/a. doi:10.1002/app.38335

Xiao, S., Wu, S., Shen, M., Guo, R., Huang, Q., Wang, S., & Shi, X. (2009). Polyelectrolyte multilayer-assisted immobilization of zero-valent iron nanoparticles onto polymer nanofibers for potential environmental applications. *ACS Appl Mater Interfaces, 1*(12), 2848-2855. doi:10.1021/am900590j

Xu, J., & Bhattacharyya, D. (2005). Membrane-based bimetallic nanoparticles for environmental remediation: Synthesis and reactive properties. *Environmental Progress, 24*(4), 358-366. doi:10.1002/ep.10106

Xu, J., & Bhattacharyya, D. (2007). Fe/Pd Nanoparticle Immobilization in Microfiltration Membrane Pores: Synthesis, Characterization, and Application in the Dechlorination of Polychlorinated Biphenyls. *Industrial & Engineering Chemistry Research, 46*(8), 2348-2359. doi:10.1021/ie0611498

Xu, J., & Bhattacharyya, D. (2008). Modeling of Fe/Pd Nanoparticle-Based Functionalized Membrane Reactor for PCB Dechlorination at Room Temperature. *The Journal of Physical Chemistry C, 112*(25), 9133-9144. doi:10.1021/jp7097262

Xu, J., Dozier, A., & Bhattacharyya, D. (2005). Synthesis of Nanoscale Bimetallic Particles in Polyelectrolyte Membrane Matrix for Reductive Transformation of Halogenated Organic Compounds. *Journal of Nanoparticle Research, 7*(4-5), 449-467. doi:10.1007/s11051-005-4273-3

Xu, Q., Xu, H., Chen, J., Lv, Y., Dong, C., & Sreeprasad, T. S. (2015). Graphene and graphene oxide: advanced membranes for gas separation and water purification. *Inorg. Chem. Front., 2*(5), 417-424. doi:10.1039/c4qi00230j

Xu, T., & Xie, C. S. (2003). Tetrapod-like nano-particle ZnO/acrylic resin composite and its multi-function property. *Progress in Organic Coatings, 46*(4), 297-301. doi:10.1016/s0300-9440(03)00016-x

Xu, W., Chen, H., Li, H., & Wang, M. (2005). Fabrication of carbon black/crosslinked poly(vinyl pyrrolidone) core-shell nanoparticles stable in water. *Colloids and Surfaces A: Physicochemical and Engineering Aspects, 266*(1-3), 68-72. doi:10.1016/j.colsurfa.2005.05.072

Xu, Z.-l., Yu, L.-y., & Han, L.-f. (2009). Polymer-nanoinorganic particles composite membranes: a brief overview. *Frontiers of Chemical Engineering in China, 3*(3), 318-329. doi:10.1007/s11705-009-0199-0

Yan, L., Hong, S., Li, M. L., & Li, Y. S. (2009). Application of the Al2O3–PVDF nanocomposite tubular ultrafiltration (UF) membrane for oily wastewater treatment and its antifouling research. *Separation and Purification Technology, 66*(2), 347-352. doi:10.1016/j.seppur.2008.12.015

Yan, W., Herzing, A. A., Li, X. Q., Kiely, C. J., & Zhang, W. X. (2010). Structural evolution of Pd-doped nanoscale zero-valent iron (nZVI) in aqueous media and implications for particle aging and reactivity. *Environmental Science & Technology, 44*(11), 4288-4294. doi:10.1021/es100051q

Yang, H. L., Lin, J. C., & Huang, C. (2009). Application of nanosilver surface modification to RO membrane and spacer for mitigating biofouling in seawater desalination. *Water Research, 43*(15), 3777-3786. doi:10.1016/j.watres.2009.06.002

Yang, Q., Himstedt, H. H., Ulbricht, M., Qian, X., & Ranil Wickramasinghe, S. (2013). Designing magnetic field responsive nanofiltration membranes. *Journal of Membrane Science, 430*, 70-78. doi:10.1016/j.memsci.2012.11.068

Yang, Q., & Wickramasinghe, S. R. (2012). Responsive Membranes for Water Treatment *Responsive Membranes and Materials* (pp. 143-162): John Wiley & Sons, Ltd.

Yim, H., Kent, M. S., Mendez, S., Balamurugan, S. S., Balamurugan, S., Lopez, G. P., & Satija, S. (2004). Temperature-Dependent Conformational Change of PNIPAM Grafted Chains at High Surface Density in Water. *Macromolecules, 37*(5), 1994-1997. doi:10.1021/ma0354290

Yin, J., & Deng, B. (2015). Polymer-matrix nanocomposite membranes for water treatment. *Journal of Membrane Science, 479*, 256-275. doi:10.1016/j.memsci.2014.11.019

Yin, J., Kim, E.-S., Yang, J., & Deng, B. (2012). Fabrication of a novel thin-film nanocomposite (TFN) membrane containing MCM-41 silica nanoparticles (NPs) for water purification. *Journal of Membrane Science, 423-424*, 238-246. doi:10.1016/j.memsci.2012.08.020

Yin, K., Lo, I. M., Dong, H., Rao, P., & Mak, M. S. (2012). Lab-scale simulation of the fate and transport of nano zero-valent iron in subsurface environments: aggregation, sedimentation, and contaminant desorption. *Journal of Hazardous Materials, 227-228*(0), 118-125. doi:10.1016/j.jhazmat.2012.05.019

Yin, M., Ye, Y., Sun, M., Kang, N., & Yang, W. (2013). Facile one-pot synthesis of a polyvinylpyrrolidone-based self-crosslinked fluorescent film. *Macromol Rapid Commun, 34*(7), 616-620. doi:10.1002/marc.201200750

Yoshimura, F., Zalman, L. S., & Nikaido, H. (1983). Purification and properties of Pseudomonas aeruginosa porin. *Journal of Biological Chemistry, 258*(4), 2308-2314.

Zahran, E. M., Prodromidis, M. I., Bhattacharyya, D., & Bachas, L. G. (2012). Palladium nanoparticle-decorated iron nanotubes hosted in a polycarbonate porous membrane: development, characterization, and performance as electrocatalysts of ascorbic acid. *Analytical and Bioanalytical Chemistry, 404*(6-7), 1637-1642. doi:10.1007/s00216-012-6291-1

Zehm, D., Laschewsky, A., Heunemann, P., Gradzielski, M., Prévost, S., Liang, H., . . . Lutz, J.-F. (2011). Synthesis and self-assembly of amphiphilic semi-brush and dual brush block copolymers in solution and on surfaces. *Polym. Chem., 2*(1), 137-147. doi:10.1039/c0py00200c

Zhang, G., Lu, S., Zhang, L., Meng, Q., Shen, C., & Zhang, J. (2013). Novel polysulfone hybrid ultrafiltration membrane prepared with TiO2-g-HEMA and its antifouling characteristics. *Journal of Membrane Science, 436*, 163-173. doi:10.1016/j.memsci.2013.02.009

Zhang, H., Qu, C., & He, J. (2015). Cylindrical polymer brushes with dendritic side chains by iterative anionic reactions. *Polymer, 64*, 240-248. doi:10.1016/j.polymer.2015.02.004

Zhang, J., Xu, S., & Kumacheva, E. (2004). Polymer microgels: reactors for semiconductor, metal, and magnetic nanoparticles. *Journal of the American Chemical Society, 126*(25), 7908-7914. doi:10.1021/ja031523k

Zhang, M., He, F., Zhao, D., & Hao, X. (2011). Degradation of soil-sorbed trichloroethylene by stabilized zero valent iron nanoparticles: effects of sorption,

surfactants, and natural organic matter. *Water Research, 45*(7), 2401-2414. doi:10.1016/j.watres.2011.01.028

Zhang, M., Zhang, K., De Gusseme, B., & Verstraete, W. (2012). Biogenic silver nanoparticles (bio-Ag 0) decrease biofouling of bio-Ag 0/PES nanocomposite membranes. *Water Research, 46*(7), 2077-2087. doi:10.1016/j.watres.2012.01.015

Zhang, Q., Xia, F., Sun, T., Song, W., Zhao, T., Liu, M., & Jiang, L. (2008). Wettability switching between high hydrophilicity at low pH and high hydrophobicity at high pH on surface based on pH-responsive polymer. *Chem Commun (Camb)*(10), 1199-1201. doi:10.1039/b716681h

Zhang, Q. G., Hu, W. W., Zhu, A. M., & Liu, Q. L. (2013). UV-crosslinked chitosan/polyvinylpyrrolidone blended membranes for pervaporation. *RSC Adv., 3*(6), 1855-1861. doi:10.1039/c2ra21827e

Zhang, W.-x. (2003). Nanoscale iron particles for environmental remediation: An overview. *Journal of Nanoparticle Research, 5*(3/4), 323-332. doi:10.1023/a:1025520116015

Zhao, C., Nie, S., Tang, M., & Sun, S. (2011). Polymeric pH-sensitive membranes—A review. *Progress in Polymer Science, 36*(11), 1499-1520. doi:10.1016/j.progpolymsci.2011.05.004

Zhu, B. W., & Lim, T. T. (2007). Catalytic reduction of chlorobenzenes with Pd/Fe nanoparticles: reactive sites, catalyst stability, particle aging, and regeneration. *Environmental Science & Technology, 41*(21), 7523-7529. doi:Doi 10.1021/Es0712625

Zhu, B. W., Lim, T. T., & Feng, J. (2008). Influences of amphiphiles on dechlorination of a trichlorobenzene by nanoscale Pd/Fe: adsorption, reaction kinetics, and interfacial Interactions. *Environmental Science & Technology, 42*(12), 4513-4519. doi:Doi 10.1021/Es800227r

Zhu, N., Luan, H., Yuan, S., Chen, J., Wu, X., & Wang, L. (2010). Effective dechlorination of HCB by nanoscale Cu/Fe particles. *Journal of Hazardous Materials, 176*(1-3), 1101-1105. doi:10.1016/j.jhazmat.2009.11.092

Zodrow, K., Brunet, L., Mahendra, S., Li, D., Zhang, A., Li, Q., & Alvarez, P. J. (2009). Polysulfone ultrafiltration membranes impregnated with silver nanoparticles show improved biofouling resistance and virus removal. *Water Research, 43*(3), 715-723. doi:10.1016/j.watres.2008.11.014

VITA

Sebastián Hernández was born in Medellín, Colombia. He was raised in Medellín until he was 11 years old and moved to Bogotá D. C. where he graduated from Gimnasio del Norte HS in 1993. He received his B.S. degree in Chemical Engineering from the Universidad Nacional de Colombia, Bogotá D.C., Colombia in 2002 and received a Meritorious Mention for his graduation project. He worked as teacher in middle to high school education, and an industry sales representative as application specialist for water and filtration technologies. He received his master degree in Civil Engineering with emphasis in environmental engineering in Universidad de los Andes, Bogotá D. C., Colombia in 2008 and worked as adjunct professor in the Chemical Engineering Department of the same university. In August 2011, he began his Ph.D. in Chemical Engineering under the guidance of Professor Dibakar Bhattacharyya at the University of Kentucky.

Awards and Honors

- **Outstanding Graduate Student Award**, Chemical and Materials Engineering Department of the University of Kentucky (May, 2016)
- **Second Place Poster Award**, RE^3 Workshop - Renewable Energy & Energy Efficiency (March, 2015)
- **Runners Up Poster Award**, Advanced Membrane Technology VI: Water, Energy, and New Frontiers (February, 2015)
- **Best Presentation Award**, Separations Division at 2014 AIChE Annual Meeting (November, 2014)
- **Meritorious Mention Award**, BS degree project "*Design and Construction of an Equipment to Determine Liquid-Vapor Equilibrium Conditions with Pressures Up to 5 bar*" (March, 2002)

Publications

- Sebastián Hernández, Anthony Saad, Lindell Ormsbee and Dibakar Bhattacharyya: *Nanocomposite and Responsive Membranes for Water Treatment*, In Emerging Membrane Technology for Sustainable Water Treatment, edited by Nicholas Hankins and Rajindar Singh, Elsevier, Boston, 2016, pages 389-431, ISBN 9780444633125. DOI:10.1016/B978-0-444-63312-5.00016-4

- Sebastián Hernández, Shi Lei, Wang Rong, Lindell Ormsbee and Dibakar Bhattacharyya: *Functionalization of Flat Sheet and Hollow Fiber Microfiltration Membranes for Water Applications*. ACS Sustainable Chemistry & Engineering. 2016; 4 (3): 907-918. DOI: 10.1021/acssuschemeng.5b01005

- Sebastián Hernández, Joseph K. Papp and Dibakar Bhattacharyya: *Iron-Based Redox Polymerization of Acrylic Acid for Direct Synthesis of Hydrogel/Membranes and Metal Nanoparticles for Water Treatment*. Industrial & Engineering Chemistry Research 2014; 53(3):1130-1142. DOI: 10.1021/ie403353g

- Sebastián Hernández Sierra, Maryhan Paola Villamil Rodríguez and Lady Liliana Miranda Gómez: *Agua Potable*. Evaluación de Tecnologías para Dotación de Servicios Vitales en Alojamientos Institucionales, edited by Universidad de Los Andes, Alcaldía Mayor de Bogotá D.C., 07/2010

- Jenny Dussan Garzón, Martha Josefina Vives-Florez, Víctor Manuel Sarria, Oscar Fernando Sánchez Medina, Luis Fernando Delgado, Andrés Fernando González Barrios and Sebastián Hernández Sierra: *Aproximaciones Biológicas y Fisicoquímicas en el tratamiento de contaminantes: un resumen del aporte de la Universidad de Los Andes*. 2009; DOI: 10.16924/riua.v0i30.233

- Sebastián Hernández Sierra, Víctor Manuel Sarria Muñoz and Manuel Salvador Rodriguez Susa: *Estudio del Tratamiento de Aguas Residuales de Tintorería por Medio de un Proceso Combinado Foto-Fenton y Lodos Activados*. Congreso Internacional Gestión Sostenible del Agua: Reutilización, Tratamiento y Evaluación de la Calidad - Memorias del Congreso, 07/2008. ISBN: 978-958-44-3709-9

- Sebastián Hernández Sierra and Francisco Perea: *Detección, promoción y formación de talentos tecnológicos*. En Contra de la Visión Convencional, Hoy se Puede Afirmar que la Inteligencia y el Talento se Desarrollan, edited by Julián De Zubiría, 02/2009: pages 153 - 176; Cooperativa Editorial Magisterio., ISBN: 9789582009748

Professional Conference Presentations (Oral/Poster)

- Sebastián Hernández, Dibakar Bhattacharyya, Lindell Ormsbee: *Hydrogel-nanoparticle composite membranes for degradation of chlorinated organic in water*. NIEHS Environmental Health Science FEST (December, 2016)

- Sebastián Hernández, Shi Lei, Rong Wang, Lindell Ormsbee, Dibakar Bhattacharyya: *Polymeric Nano-Metal Composite Membranes for Water Remediation*. Process Development Division, 2016 AIChE Annual Meeting (November, 2016)

- Sebastián Hernández: *Separation and Reaction Processes in Functional Nanostructured Porous Materials*. Meet the Faculty Candidate, 2016 AIChE Annual Meeting (November, 2016)

- Sebastián Hernández, Cassandra Porter, Xinyi Zhang, Yinan Wei and Dibakar Bhattacharyya: *Biomimetic Membranes by Incorporation of Porin Channels*. Ashland Inc. Distinguished Lectures & Symposium on Drug Discovery & Development (November, 2016)

- Sebastián Hernández: *Polymer-Nanoparticle Composite Membranes for Water Remediation*. Award presentation of the Materials and Chemical Engineering Graduate Student Association 2016 Spring Symposium at the University of Kentucky (May, 2016)

- Sebastián Hernández, Dibakar Bhattacharyya, Shi Lei, Rong Wang, and Lindell Ormsbee: *Iron Nanoparticle Immobilized Flat Sheet and Hollow Fiber Membranes for Water Remediation*. Advances in In Situ Pollutant Destruction by Nanoscale Zero Valent Iron & Other Engineered Nanoparticles at the 251st American Chemical Society National Meeting & Exposition (March, 2016)

- Sebastián Hernández, Lindell Ormsbee, Dibakar Bhattacharyya: *Synthesis and Evaluation of nanoparticle membrane-supported systems for Degradation of Trichloroethylene*. 2015 SUPERFUND RESEARCH PROGRAM Annual Meeting (November, 2015)

- Sebastián Hernández, Douglas Davenport, Minghui Gui, Lindell Ormsbee, Dibakar Bhattacharyya: *Advanced Polymer-Nanoparticle Composite Membranes for Water Detoxification*. Kentucky EPSCoR 2015 Annual Conference (May, 2015)

- Sebastián Hernández, Lindell Ormsbee, Dibakar Bhattacharyya: *Nanoparticle-Catalyzed Membranes for Water Detoxification*. RE^3 Workshop - Renewable Energy & Energy Efficiency (March, 2015)

- Sebastián Hernández, Minghui Gui, Doug Davenport, Lindell Ormsbee, Dibakar Bhattacharyya: *Nanocomposite Membranes for Water Purification*. Kentucky Water Resources Annual Symposium (March, 2015)

- Sebastián Hernández, Lindell Ormsbee, Dibakar Bhattacharyya: *Synthesis and Evaluation of nanoparticle membrane-supported systems for Degradation of Toxic Organic Contaminants*. Advanced Membrane Technology VI: Water, Energy, and New Frontiers (February, 2015)

- Sebastián Hernández, Joseph Papp, Dibakar Bhattacharyya: *Metal Catalyzed Hydrogel Synthesis in PVDF Membranes for Degradation of Toxic Organic Contaminants*. 2014 AIChE Annual Meeting (November, 2014)

- Sebastián Hernández, Lindell Ormsbee, Dibakar Bhattacharyya: *Evaluation of different nanoparticle support systems applied in the detoxification of chlorinated organic compounds*. 2014 SUPERFUND RESEARCH PROGRAM Annual Meeting (November, 2014)

- Sebastián Hernández, Dibakar Bhattacharyya: *Dechlorination of Trichloroethylene in Water by Membrane-Supported Fe/Pd Nanoparticles Directly Synthesized from Redox Polymerization Catalyst*. 2013 SUPERFUND RESEARCH PROGRAM Annual Meeting (October, 2013)

- Sebastián Hernández, Dibakar Bhattacharyya: *Evaluation of Trichloroethylene Dechlorination and Selenium Capture in Aqueous Phase Using Zero-Valent Iron Nanoparticles Synthesized In Situ From Exhausted Catalyst of Iron-Based Redox Polymerization*. Kentucky Water Resources Annual Symposium (March, 2013)

- Sebastián Hernández, Dibakar Bhattacharyya: *Iron-Based Redox Polymerization towards Nanoparticle Synthesis in Hydrogel*. 2012 AIChE Annual Meeting (October, 2012)

- Sebastián Hernández Sierra, Liliana Miranda, and Paola Villamil: *Configuration Assessment of the Drinking Water Supply Systems in Conditions of Emergency Applied to An Earthquake Scenario in the City of Bogota - Colombia*. 2010 AIChE Annual Meeting (November, 2010)

- Víctor Manuel Sarria Muñoz, Manuel Salvador Rodríguez Susa, Sebastián Hernández Sierra: *Mejoramiento de la Biotratabilidad de Aguas Residuales de Tintorería a Través de un Proceso de Oxidación Avanzada*. Simposio Latinoamericano Procesos Avanzados de Oxidación y sus Combinaciones con otros Procesos: Principios y Aplicaciones (November, 2008)